The University Of Sheffield.

INSIGNEO Institute for *in silico* Medicine

Gaussian process emulators for 1D vascular models

a dissertation presented
by
Alessandro Melis
to
The Department of Mechanical Engineering
The University of Sheffield
Sheffield, UK

in partial fulfillment of the requirements
for the degree of
Doctor of Philosophy

Supervisor: Dr. Alberto Marzo
CoSupervisor: Prof. Richard H. Clayton
Internal Examiner: Dr. Andrew Narracott
External Examiner: Dr. Jordi Alastruey

August 2017

This thesis was typeset using XeLaTeX, originally developed by Jonathan Kew and based on Donald Knuth's TeX. The text is set in 12 pt Windsor, Neuton and Alegreya fonts, designed by Eleisha Pechey, Brian Zick and Huerta Tipográfica, and hosted on FontZone and Google Fonts, respectively. The template, used to format the thesis with this look and feel, was forked from the Harvard Thesis template by Jordan Suchow (released under MIT license).

Acknowledgments

Firstly, I would like to express my sincere gratitude to my supervisor Dr. Alberto Marzo for the continuous support and related research, for his patience, motivation, and expertise. His guidance always helped me through the professional problems I have encountered during these three years. I could not have imagined having a better guide. I'm very grateful.

I would like to thank my second supervisor Prof. Richard H. Clayton for his insightful comments and encouragement during these years. I appreciate his advice and the research discussions we had. Thanks for the patience and the presence.

I immensely thank all my INSIGNEO colleagues and friends from PLB C+/E for the numerous coffee breaks, the walks in the Peak, the photo challenges, and the chess games. I will be missing all of you very much.

Last but not the least, I would like to thank my family and Claudia for the support throughout my studies and the writing of this thesis.

Abstract

One-dimensional numerical models of the arterial vasculature are capable of simulating the physics of pulse wave transmission and reflection. These models are computationally efficient and represents and ideal choice with great translational opportunities in healthcare. However, the use of these models in a patient-specific scenario is hampered by the difficulty in measuring the model inputs (parameters, boundary conditions, and initial conditions) in the clinical setting. As a result, most of the model inputs are noisy or missing, and the inputs uncertainty is transmitted to the model outputs. A fundamental step in the model development consists in performing a sensitivity and uncertainty analysis aimed at understanding how variations on the inputs affect the output variability, with the final aim of instruct the measurement process. A typical sensitivity analysis conducted by means of Monte Carlo sampling is computationally expensive due to the large number of runs required. A novel approach aimed at reducing the computational time consists in using a statistical emulator capable of mimicking mean and variance behaviours of the 1D deterministic model. In this study, emulators built through Gaussian process method are used to predict outcomes of a 1D finite-volume solver for networks of elastic vessels. The 1D model is discussed and validated showing good agreement with published results. The emulator approach for sensitivity analysis is validated against Monte Carlo sampling and a $99.9\ \%$ reduction in computational time is obtained. This methodology is further applied in the context of cerebral vasospasm where the sensitivity analysis results are used to identify new biomechanical metrics for this pathology. The novel biomarkers are effective at detecting the cerebral vasospasm better than the currently used one. In particular, the progression of the disease is characterised from an early onset even when the vasospasm is occurring at some distance away from the measurement location.

Contents

List of Figures

List of Tables

Declaration

A substantial part of the material presented in this thesis is published work or is currently under preaparation:

- Part of the material presented in Chapter 7 has been included in:

  Melis A, Clayton RH, Marzo A. A more efficient approach to perform sensitivity analyses in 0D/1D cardiovascular models. Computational & Mathematical Biomedical Engineering Proceedings. 2015 Jul:806-809.

- Part of the material presented in Chapter 8 has been included in:

  Melis A, Clayton RH, Marzo A. Bayesian sensitivity analysis of a 1D vascular model with Gaussian process emulators. International Journal for Numerical Methods in Biomedical Engineering. 2017 Mar 24.

- Part of the material presented in Chapter 9 has been included in:

  Melis A, Moura F, Larrabide I, Clayton RH, Narata AP, Marzo A. Improved biomechanical metrics of cerebral vasospasm identified via sensitivity analysis of a cerebral circulation model. In preparation.

Written permission was obtained from all the co-authors.

1 Introduction

The blood is pumped through the cardiovascular system, a complex network of compliant arteries and veins, by the cyclic contraction of the heart. This pulsatile regime and the vessels elasticity cause blood pressure to propagate through arteries as waves. The pressure waves move through the network and are deflected due to the presence of mechanical discontinuities such as bifurcations and bends. Cardiovascular pathologies, including vessel stenoses, aneurysms, and atherosclerosis could additionally modify these patterns. The pressure wave observed at a specific location is the result of the sum of incident and reflected waves. The study of this superimposition allows to infer the mechanical features of the vascular network upstream and downstream of the measurement point.

Numerical vascular models are aimed at better understanding of the blood circulation. Many of the hæmodynamics models are based on the Navier-Stokes equations (NSEs), which describes the macroscopic behaviour of fluids. One dimensional (1D) models are based on a reduction of the NSEs along with a constitutive relation describing the vessel-wall radial displacement. In a 1D model, each vessel is an elastic tube whose features can vary along the longitudinal direction.

Compared to three-dimensional (3D) simulations, 1D simulations are computationally cheaper and need a less detailed description of the network geometries and boundaries. This comes at the expense of accuracy in the proximity of bifurcations and valves, where flow recirculation may occur. Nevertheless, 1D models are detailed enough to simulate the mechanism of forward and backward waves superimposition, and have been successfully used to simulate the hæmodynamics of large vascular networks, i.e. the entire systemic and venous circulation, the pulmonary circulation, the brain vasculature, and the blood flow within the coronary arteries.

Despite being computationally less demanding than 3D simulations, 1D models still require a considerable number of parameters to represent a vascular network. For instance a systemic network including 103 large arteries requires about 500 parameters to be specified: in a patient-specific scenario, the measurement of all these parameters is infeasible. However, not all the model parameters have a significant effect on the clinically relevant output (e.g. the systolic pressure in the ascending aorta). Only the most influential parameters are those whose uncertainty must be

reduced, i.e. they should be measured as accurately as possible. Conversely, the parameters whose variation has little effect on the output can be fixed to nominal values. In general, the inputs can be ranked according to their influence in the view of informing the measurement process. The input ranking and fixing is the outcome of performing a sensitivity analysis of the 1D model.

The state-of-the-art sensitivity technique consists in the calculation of variance-based global sensitivity indices which assess the output sensitivity to the variation of individual inputs or combination of inputs. The inputs contributing more to the output variation will score higher sensitivity indices than the inputs whose variation affects the output value less significantly. The sensitivity indices can be computed by means of the Monte Carlo sampling method which tipically requires 1000 runs for each input parameter. Each simulation is run on a different set of inputs randomly drawn from a distribution over the input space. As the number of simulations grows, the model response at different input-space locations is investigated. Ideally, it would be desirable to draw an infinite number of input points, but in practice a sampling of order $\mathcal{O}(d \times 10^3)$ is enough, where d is the number of input parameters.

The computational time required for the $d \times 10^3$ simulations rises as d increases. The sensitivity analysis can be made more efficient by introducing an approximation of the physically-based model, i.e. an emulator. The emulator is a statistical tool that can be trained to infer the deterministic model global behaviour from a set of simulation runs. The number of simulation runs needed to train the emulator is usually smaller than $d \times 10^3$. Once trained, the emulator can predict the determinist model outcome for each of the $d \times 10^3$ input points required for the sensitivity analysis in few seconds. The Gaussian process (GP) method is a popular emulation technique in Machine Learning and it has been employed in this thesis to predict 1D blood flow model outcomes for sensitivity analysis purposes.

1.1 Aim and objectives

The aim of this study is to develop a novel numerical approach that will allow the identification of waveform-derived biomechanical metrics for an effective subject-specific diagnosis of cardiovascular pathologies.

The aim is achieved through the following objectives:

1. development of a 1D numerical model of blood pulse wave propagation and reflection within networks of elastic arteries;
2. validation of the 1D model against state-of-the-art benchmarks;
3. training of Gaussian process emulator to mimic the 1D model behaviour and to reduce the computational running time;
4. validation of the Gaussian process approach against the Monte Carlo sampling outcomes;
5. assessment of how Gaussian process method accuracy scales when trained over models of increasing complexity;
6. use of Gaussian process technique to perform 1D model sensitivity analysis and quantify the effect of uncertain, missing, and noisy data;
7. use of sensitivity analysis results to identify more effective biomarkers of a specific cardiovascular condition and to quantify the effect of uncertain data.

1.2 Thesis outline

The thesis is organised in two main parts: methodology and clinical applications as outlined in contents. The study objectives are achieved and described in the various chapters as follows:

- In Chapter 2, the project background is reported. This consists of an introduction of the cardiovascular system, its main functions and its mechanical description. This is followed by a review of the modelling approaches used to study the physics of wave propagation focusing on the numerical methods for 1D models. The chapter concludes with a description of the concepts and use of sensitivity analysis and statistical model emulators.
- Chapter 3 gives a description of the mathematical model used in this study (Objective 1).

- In Chapter 4, the sensitivity analysis method is introduced and discussed. This is reviewed as a generic modelling tool and not described in the context of cardiovascular modelling.

- In Chapter 5, the Gaussian process method is discussed. The problems of kernel selection and optimisation is described and a strategy for building covariance functions is presented. Finally, a sampling method suitable for sensitivity analysis purpose is presented.

- In Chapter 6, the developed numerical scheme for the 1D blood flow model is validated against a frequency-domain analytical solution and against other numerical solutions published in the literature. Additionally, experimental in-vivo and in-vitro measurements, also published in the literature, are used to assess the numerical solver accuracy (Objective 2).

- In Chapter 7, the application of Gaussian process as a data generator for sensitivity analysis of a cardiovascular model is presented (Objectives 3 and 4).

- In Chapter 8, the methodology is applied to four networks of increasing complexity. This study shows how the methodology performance in terms of computational time scales with the network size (Objectives 5 and 6).

- In Chapter 9, the methodology is employed to study an unmet clinical problem, the selection of more effective biomechanical metrics indicative of a specific cardiovascular condition, the cerebral vasospasm (Objective 7).

- In Chapter 10, the study conclusions are reported along with its limitations and future prospects.

2 Literature review

Summary

In this chapter, the project background is reported. First, the cardiovascular system and its mechanical properties are presented. This is followed by a literature review on vascular modelling with a particolar focus on 1D models. Finally, the concepts of statistical emulator and sensitivity analysis are introduced.

2.1 The cardiovascular system

The cardiovascular system comprises the heart, the two circulations - systemic and pulmonary - and the blood. The heart is a four chamber pump which contracts due to electrical stimulation and drives the blood through the systemic and the pulmonary circulations. The systemic, or greater, circulation distributes blood in all the body tissues except for the lungs which are served separately by the pulmonary circulation. The two networks are comprised of arteries and veins. Arteries bring blood from the heart to the capillaries; the veins link capillaries to the heart and close the circulation loop.

In this thesis, only the main large arteries of the systemic circulation are taken into consideration (Figure 2.1.1). The systemic circulation begins at the ascending aorta, which is directly connected to the heart left ventricle through the aortic valve. The aorta branches in a tree-like configuration and the daughter vessels progressively decrease in size[1].

The arteries are made of muscular compliant tissue and can actively control the blood flow by expanding and contracting to accomodate a varying volume of blood. The mechanical properties of the vascular wall change along the arterial tree: large vessels are elastic and compliant whereas peripheral arteries are narrow and stiff.

[1] The change in arteries internal radius (the lumen, R_0) at a bifurcation is described by Murray's power law: $R^3_{0p} = R^3_{0d_1} + R^3_{0d_2}$, where the subscripts p, d_1, and d_2 indicate the parent and the two daughter vessels, respectively.

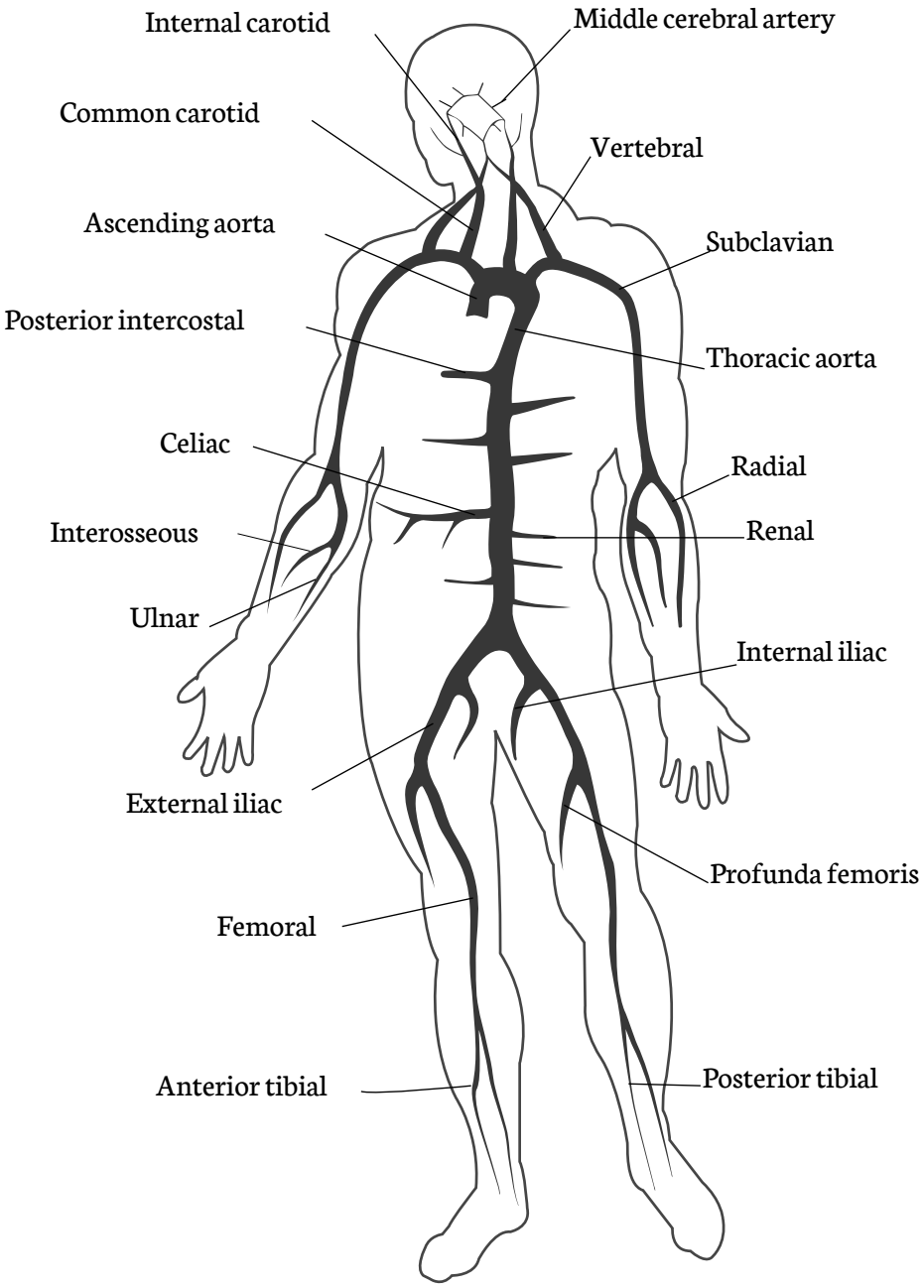

Figure 2.1.1: Main arteries in the systemic circulation. Circulation diagram based on (Reymond et al., 2009).

The two heart phases, systole and diastole, determine the pulsatile nature of blood flow [2], and the flow properties (e.g., volumetric flow rate[3] and pressure[4]) propagate in the system as waves. The travelling wave is partially reflected backwards by mechanical discontinuities in the arterial network (e.g., bifurcations, sudden changes in elasticity, or the capillary bed). Reflected waves superimpose with the forward wave, generating pressure and flow waveforms (Figure 2.1.3a). Depending on where waves are observed, the superimposition timing changes and as a result the pulse waveforms present different shapes along the arterial tree (Figure 2.1.3b).

The cardiovascular system duties consist in the transport of nutrients and gases, removal of waste products, and in maintaining an appropriate thermal environment all over the body. The exchange of nutrients between the blood an the tissues occurs at the capillary level where the flow must be steady and slow. Indeed as the blood flows through the circulation, the mean arterial pressure progressively falls from 100 mmHG to $\sim$ 2 mmHg in the capillary bed. This pressure drop is due to the vascular resistance that the blood has to overcome while flowing along arteries.

The flow resistance[5] has been experimentally studied in the case of steady laminar flow in pipes by Hagen (1839) and Poiseuille (1844) who described the parabolic radial velocity profile. In the case of parabolic profile, Hagenbach (1860) showed that the flow resistance is inversally proportional to the fourth power of the pipe internal radius[6]. In the arterial tree, vessel lengths change slowly and blood viscosity can be considered constant, therefore the resistance is mainly controlled by the lumen radii. Therefore an abrupt change in radius can greatly decrease/increase the mean arterial pressure and the volumetric flow rate to a specific area of the circulation.

In the case of a pulsatile dynamic condition, the velocity profile assumes a configuration other than parabolic (Figure 2.1.2). The exact shape of the velocity profile depends on blood viscosity and vessel geometry. The flow within an elastic vessel has been studied and described by Hale et al. (1955); Womersley (1955) who de-

[2]The first description of the pulsatile nature of the blood flow dates back to Aristoteles (384-322 BC) (Parker, 2009a), but the discovery of the circulation as a closed loop occurred only later by Harvey (1928) and Malpighi in the 17^{th} century.

[3]Volume of blood that passes a given point of the circulation in the unit of time, and it is measured in $\mathrm{ml}\cdot\mathrm{s}^{-1}$ ($1\ \mathrm{ml}\cdot\mathrm{s}^{-1} = 10^{-6}\ \mathrm{m}^3\cdot\mathrm{s}^{-1}$).

[4]Blood pressure is the force exerted by the blood against any unit area of the vessel wall, and it is clinically measured in mmHg (Avolio et al., 2010), where 1 mmHg $\simeq$ 133.332 Pa, e.g., $P = 50$ mmHg means that the force exerted is sufficient to push a column of mercury against gravity up to 50 mm high in a sphygmomanometer. The maximum pressure reached along the cardiac cycle, the systolic pressure, is tipically 120 mmHg.

[5]The vascular resistance is defined as the ratio $\mathcal{R} = {}^{Q}/_{\Delta P}$, and it is measured in $\mathrm{ml}\cdot\mathrm{s}^{-1}\cdot\mathrm{mmHg}^{-1}$.

[6]This law, taking into account also the fluid dynamic viscosity and the pipe length (μ and ℓ, respectively), is known as Poiseuille's pipe law: $\Delta P = Q\left({}^{8\mu\ell}/_{\pi R_0^4}\right)$.

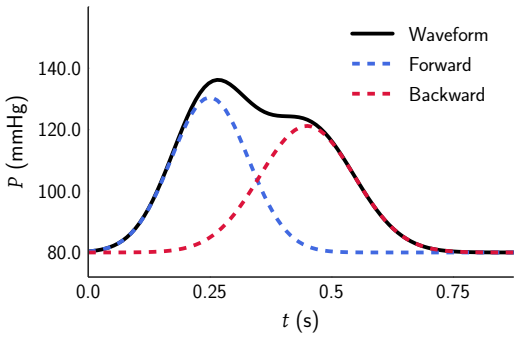

(a)

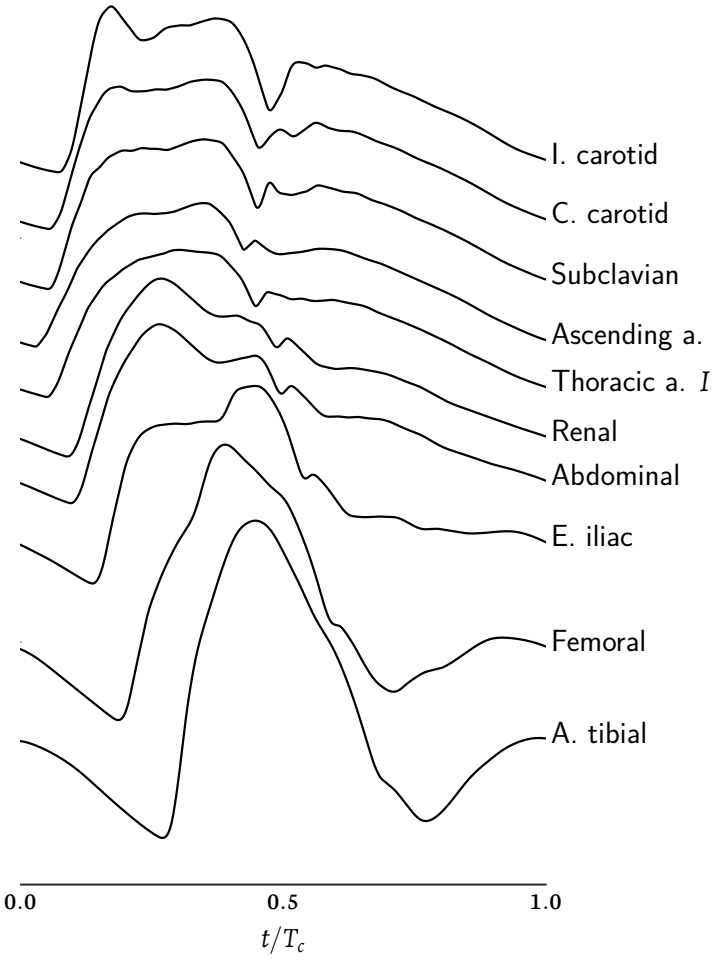

(b)

Figure 2.1.2: (a) Waveform superimposition mechanism. (b) Pressure waveforms calculated at different locations in the arterial tree with the numerical scheme described in Chapter 3. Based on (Avolio, 1980) with permission.

veloped the mathematical framework explaining the experimental observations of McDonald (1952, 1955) about back-flow, and phase lag between pressure and flow waves measured in large arteries.

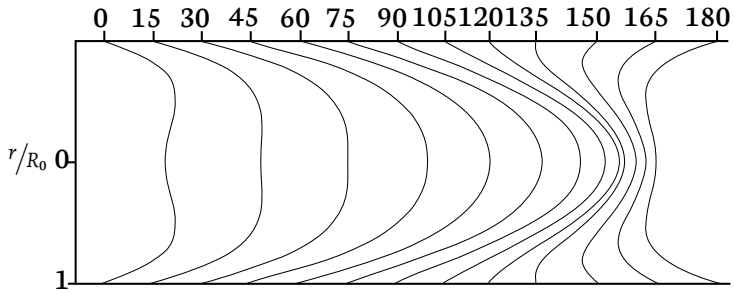

Figure 2.1.3: Radial velocity profile against the fractional radius (r/R_0) in the case of a periodic pressure gradient ($\propto \cos(\omega t)$, $\omega \in [0, 180]^\circ$). Based on experimental measurements by Helps and McDonald (1953).

The arterial wall

Arterial walls consist of three tissue layers or tunicæ: the inner tunica intima that is in contact with the blood flow, the middle tunica media, and the outer tunica adventitia (Figure 2.1.4). The tunica intima is a single layer of endothelial cells surrounded by a thin layer of elastin and collagen fibres. The tunica media - the thickest layer - is made of smooth muscle cells and elastin fibres which dictate the elastic properties of the vessel. The tunica adventitia consists of collagen and elastin merging onto the surrounding connective tissues. The tunica adventita mechanical properties are not relevant for flow.

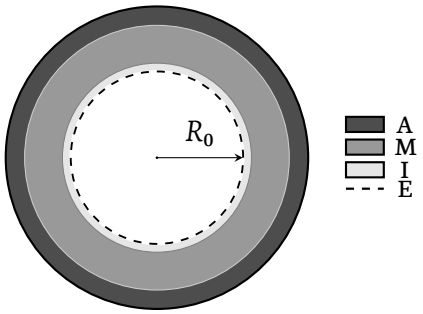

Figure 2.1.4: Artery cross section with lumen radius R_0 and wall layers: tunica adventitia (A), media (M), intima (I), and endothelium (E).

Arteries have strong muscular walls which help to maintain a tubular shape even in absence of flow. From large arteries to capillaries, passing by small arteries and arterioles, the artery lumen diameter decreases. Along with the lumen radius drop, there is a stiffening of the walls. Large arteries are close to the heart and contain a higher percentage of elastin and collagen than smaller muscular vessels.

In response to the tissue needs, walls expand/contract so that the right amount of flow is released. The vessel compliance is the ability of vessel walls to deform and accomodate a variable volume of blood[7]; peripheral vessels which are stiffer and less able to deform, constitute the major source of resistance in the circulation, while larger arteries in which the resistance is small, have a high compliance.

The arterial elasticity is responsible for converting the pulsatile flow exiting the heart in a constant and slow stream within the capillaries. This is the windkessel effect whose name originated from the analogy with a fire engine air chamber (*windkessel* in German) made by Hales (1964) and Borelli (1989) in the 17th century[8]. In a fire engine (Figure 2.1.5), the water is driven by a rotary pump and it is constantly sprinkled throughout the hose due to the air expansion chamber. The chamber accommodates a varying volume of water depending on the pump piston position. The outflow from the chamber is driven by the air inside the chamber that is compressed and slowly expands when the inflow from the pump stops. The mathematical description of the windkessel model is reported in Section 3.4.2.

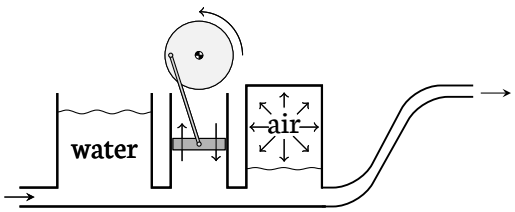

Figure 2.1.5: Windkessel effect analogy. The water (blood) is cyclically suctioned from a reservoir (left atrium) to the air chamber or windkessel (large arteries), by the rotary pump (heart). The air in the windkessel is compressed by the water (systole) and, as the pump action stops (diastole), the air expands (the arteries contract) and pushes the water out the windkessel towards the fireman hose (capillaries). The air expansion is not instantaneous but delayed; this causes a constant outflow to the hose (stable and continuous blood flow in capillaries).

The blood and its rheology

The blood is a suspension of red cells, white cells and platelets in plasma, a fluid with water-like mechanical properties. The relative proportion of volume occupied by red blood cells with respect to overall blood volume is the hæmatocrit and it varies depending on age, altitude, bodily activity, and blood pathologies. The blood

[7] The vascular compliance ($\mathcal{C}$) is defined as the volume of blood that can be accomodated in a given portion of the circulation for each mmHg pressure rise, $\mathcal{C} = {}^{\Delta V}/_{\Delta P}$.

[8] The windkessel mathematical description will be proposed two centuries later by Frank (1899).

red cells are flexible and their micro-structure dictates the whole blood mechanical properties. They are capable of stretching and of binding between each other, and, as a result, the blood viscosity changes depending on the flow properties (non-Newtonian behaviour). Conversely, the blood density is constant at $1050 \pm 10\,\mathrm{kg \cdot m^{-3}}$ (Kenner, 1989; Kenner et al., 1977).

For a non-Newtonian fluid, the dynamic viscosity depends on the shear-rate. In the case of blood, the viscosity decreases in a hyperbolic fashion as the shear-rate increases (Figure 2.1.6), and it becomes independent of the shear-rate for large γ values. In large arteries, the average shear-rate at the walls is $> 100\,\mathrm{s^{-1}}$ and for practical modelling applications the blood is usually considered a Newtonian fluid (Fung, 2010; Guyton and Hall, 2006; Nichols and O'Rourke, 2011; Pedley, 1980; Zamir, 2000, 2005).

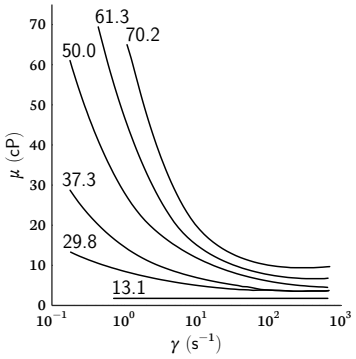

Figure 2.1.6: Blood dynamic viscosity against shear-rate for different hæmatocrit values. The blood behaves as a non-Newtonian fluid for $\gamma < 100\,\mathrm{s^{-1}}$ as the viscosity decreases for increasing shear-rate. The viscosity remains constant for $\gamma > 100\,\mathrm{s^{-1}}$ (Nichols and O'Rourke, 2011).

The effect of ageing on the cardiovascular system

Arterial tree mechanical properties have been observed to change due to ageing (Ferrari et al., 2003; Nichols and O'Rourke, 2011). Ageing effects in the heart are minor and can be attributed to the increasing load due to a change in arterial properties (Lakatta and Levy, 2003). Blood viscosity, which is related to the blood red cells count, also increases with age (Ajmani et al., 2000) (Figure 2.1.7c).

Structural changes due to ageing are spread uniformly over the entire arterial tree and concern primarily vessel local properties rather than the global topology. There is a general increase in vessel radius (Nichols et al., 1985) (Figure 2.1.7a), in media and intima thickness (Virmani et al., 1991), and in overall Young's modulus (Gozna et al., 1974) (Figure 2.1.7b). As a result, pulse wave velocity increases with

age (van de Vosse and Stergiopulos, 2011) while arterial compliance decreases (Redheuil et al., 2010).

Arteriosclerosis is a common cardiovascular condition, which consists of a vessel hardening, and occurs naturally with age. External factors, such as fat deposition on arteries walls, contribute to the local stiffening of arteries and are referred to as atherosclerosis (Mackenzie et al., 2002). The arteries stiffening has also been associated with an increase of systolic pressure (Benetos et al., 2002).

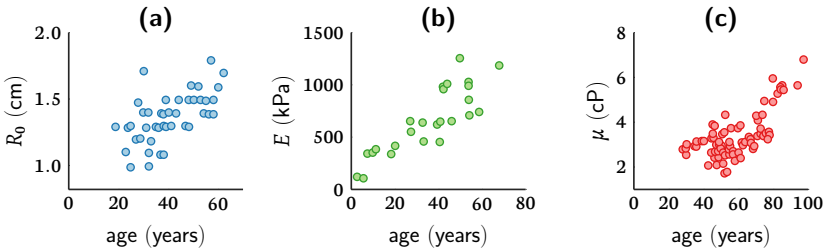

Figure 2.1.7: Changes in ascending aorta mean lumen radius (Nichols et al., 1985) (a), wall elastic modulus (Gozna et al., 1974) (b), and blood viscosity (Ajmani et al., 2000) (c) with age.

2.2 Vascular modelling

The history of vascular models is closely related to the studies on pipe flow. The 1D flow equations in an elastic tube were first derived by Euler (1844), while Young (1800) recognised the wave nature of the pulsatile flow, and, by making an analogy with the propagation of sound in compressible gas, derived a pulse wave velocity formula. A thorough theoretical and experimental description of the wave speed in elastic tubes was given later by Moens (1877), Korteweg (1878), and the Weber brothers (Weber and Weber, 1825; Weber, 1892). These studies, along with the experimental observations of Hagen (1839) and Poiseuille (1844), set the basis for the mathematical work of Womersley et al. on the blood velocity profile as a function of the vessel radius (Hale et al., 1955; Womersley, 1955).

As the measurement techniques became accurate enough to measure blood pressure waveforms, two different methods have been developed depending on the approach used to analyse the waveform. The analysis in the frequency-domain by means of Fourier transform (Fourier, 1822) is usually referred to as impedence analysis (IA) (Westerhof and Noordergraaf, 1970). Conversely, the wave intensity analysis (WIA), introduced by Parker and Jones (1990), stems directly from the application of the method of characteristics in the time-domain (Riemann, 1876). A thorough comparison of the two techniques is given in (Parker, 2009b).

In IA, the vascular network is represented as an electric circuit in which each feature of the circulation is represented by an electric component. The hydraulic resistance is an electric resistance, the wall compliance is a capacitance, the flow inertia is taken into account by inductances, and the flow rate and pressure are electric current and potential, respectively. The models built upon the electric analogy are referred to as 0D or lumped-parameter as spatial information is lost during the dimensionality reduction process (Shi et al., 2011).

In the time-domain, the conservative laws governing the blood flow are written in terms of a system of non-linear hyperbolic partial differential equations (PDEs) (Čanic et al., 2006; Čanic and Kim, 2003). The numerical solution of hyperbolic PDEs has been a crucial research topic in the 20^{th} century due to its application to gas dynamics (LeVeque, 2002). The fundamental studies on numerical analysis carried out by Courant, Friedrichs, and Lewy (Courant et al., 1928), Godunov (1959), and van Leer (1979) paved the way to several numerical hæmodynamic studies (Anliker et al., 1971; Hisland and Anliker, 1973; Lambert, 1958; Raines et al., 1971; Skalak, 1972; Stergiopulos et al., 1992; Stettler et al., 1981a,b).

The undeniable difficulty in performing in-vivo pressure waveform measurement led to the development of in-vitro models (Segers et al., 1998). The measurements performed on in-vitro models are still used as ground-truth to validate new numerical schemes and their implementations (Xiao et al., 2014). The electric circuit analogy was exploited to build analog models of the circulation (Noordergraaf et al., 1963; Westerhof et al., 1969, 1971), and the frequency-domain analysis was further developed to take into account vessels of several sizes, from large arteries to the whole capillary bed (Jager et al., 1965; Toy et al., 1985; Westerhof and Noordergraaf, 1970). These lumped-parameter segments can be assembled in large networks (i.e. mimicking the analog physical models) and solved by numerical means (Avolio, 1980; Broomé et al., 2013; Snyder et al., 1968). Brown (1996) employed the transmission line theory to study the changes in impedance within fractal like networks, while Milišic and Quarteroni (2004) proved that the 0D solution tends to the 1D one as the number of segments increases.

In recent times, there has been a re-flourish of theoretical works on the blood flow governing equations (Figure 2.2.1). In particular, the building of multi-scale models triggered the problem of coupling 3D , 1D , and 0D models. Formaggia et al. (1999) proposed a preliminary analysis of the coupling between 3D , 1D , and 0D models and compared 3D /1D and 2D/1D coupling (Formaggia et al., 2001). Fernández et al. (2005) proved the existence and uniqueness of the solution for 0D /1D coupling problem. Formaggia et al. (2006) coupled a lumped parameter model of the heart with a 1D arterial tree. Reymond et al. (2011, 2009) developed a 1D model of the coronary, systemic, and cerebral circulation with a varying elastance model of the heart, Womersley velocity profile, and implicit numerical solver with 0D

outlet boundary conditions; this model was validated in both patient-generic and patient-specific cases. Alastruey et al. studied the effect of 0D outlet boundary conditions (Alastruey et al., 2008) and model parameters (in a visco-elastic formulation) (Alastruey et al., 2012) on the waveforms computed in a complete arterial tree. Blanco et al. (2010) studied the effect of heart rate on a 3D -1D -0D model of the arterial tree. Formaggia et al. (2003) proposed the introduction of dissipation functions at bifurcation nodes to take into account the effect of branching angle; however due to the difficulty on selecting the dissipation parameter, bifurcations are treated as ideal in most of the works in literature.

The multi-scale strategy allows to build complex networks of varying spatial accuracy, and it has been successfully adopted to study the entire systemic circulation (Azer and Peskin, 2007; Olufsen, 1999; Olufsen et al., 2000; Sherwin et al., 2003b), the coronaries (Huo and Kassab, 2007), the cerebral vasculature (Alastruey et al., 2007; Mulder et al., 2011; Viedma et al., 1997), and the pulmonary circulation (Clavica et al., 2010; Lungu et al., 2014). Mulder et al. (2011) built a 1D model of the cerebral circulation. Alastruey et al. (2007) studied by means of a 1D model the effect of circle of Willis variation on cerebral flow. Marchandise et al. (2009) proposed the use of a 1D model to aid the planning of peripheral vascular bypass surgery. Vennin et al. (2015) proposed the first noninvasive estimation of pressure pulse waveform from measurements of blood velocity.

1D models are further classified depending on the numerical scheme used to solve the PDEs system (Table 2.2.1). The hyperbolic conservation laws can be written in three equivalent forms: integral, strong (or differential), and weak integral. The finite volume (FV) scheme is based on the integral form, whereas the finite difference (FD) and the finite element (FE) schemes are applied to the differential and weak forms, respectively. Recently, the benchmark study by Boileau et al. (2015) proved that all the numerical schemes are capable of achieving the same accuracy in terms of computed waveforms. The differences between schemes consist in the execution time and the numerical stability.
FD and FV scheme stability depends on Δt being small enough to capture wave propagation (the stability is ensured by the CFL condition). Conversely, the FE stability is not affected by the choice of Δt.

Azer and Peskin (2007) used the Womersley pulsatile theory to compute friction and convection terms and solved the 1D system by using a FD scheme. Casulli et al. (2012) proposed a semi-implicit FV solver for compliant arteries and Dumbser et al. (2015) improved the method by including an explicit calculation of the radial velocity profile.

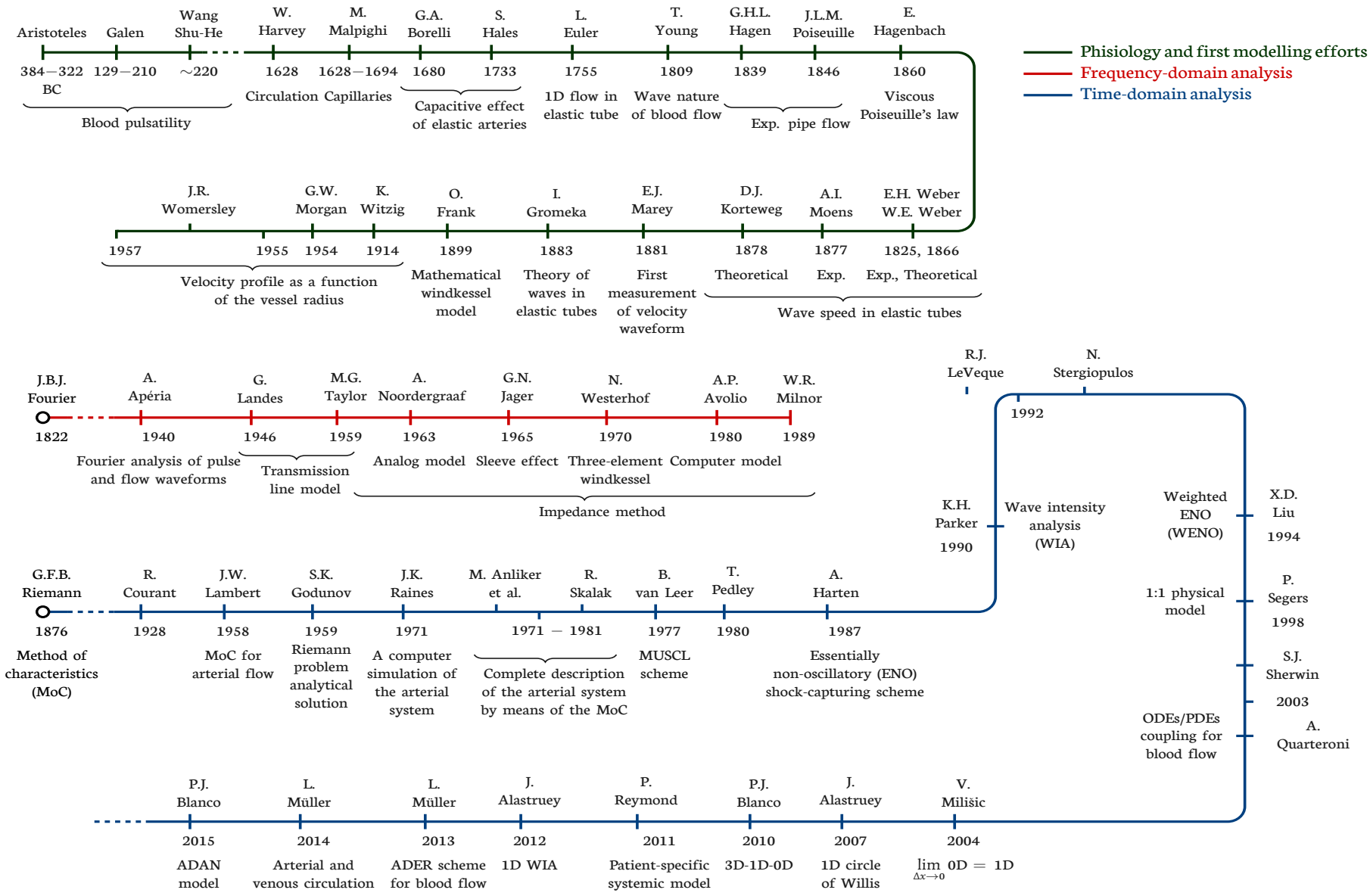

Figure 2.2.1: Vascular modelling timeline

	Type	Method	H	B	C	P	V	VE	Validation
Noordergraaf et al. (1963)	0D	–∿∿–							
Snyder et al. (1968)	0D	–∿∿–	●		●				CD
Westerhof et al. (1969)	0D	–∿∿–							CD
Westerhof et al. (1971)	0D	–∿∿–	●			●			in vivo
Avolio (1980)	0D	IA		●				●	
Balar et al. (1989)	1D	FE							
Stergiopulos et al. (1992)	1D	FD			●				
Sun et al. (1997)	0D	IA	●		●	●	●	●	CD
Olufsen (1999)	1D	FD	●					●	in vivo, CD
Cassot et al. (2000)	1D	Analytical		●					
Olufsen et al. (2000)	1D	FD							in vivo
Sherwin et al. (2003b)	1D	DG							
Formaggia et al. (2006)	1D	FE	●						
Azer and Peskin (2007)	1D	FD_i							Analytical
Huo and Kassab (2007)	1D	FD_i			●				in vivo, CD
Alastruey et al. (2007)	1D	DG		●					in vivo, CD
Reymond et al. (2009)	1D	FD_i	●	●	●	●		●	in vivo, CD
Mulder et al. (2011)	1D /3D	FV	●	●	●				
Reymond et al. (2011)	1D	FD_i		●				●	in vivo
Alastruey et al. (2011)	1D	DG						●	in vitro
Huberts et al. (2012)	1D	DG					●	●	in vivo
Low et al. (2012)	1D	FE	●	●	●				in vivo
Casulli et al. (2012)	1D	FV							
Gaddum et al. (2013)	1D	DG							in vivo
Müller and Toro (2013)	1D	FV							
Müller and Toro (2014)	1D	FV	●	●	●	●	●		in vivo
Blanco et al. (2015)	1D	FV	●	●	●	●	●		in vivo
Flores et al. (2016)	1D	Analytical							in silico

Table 2.2.1: Selection of blood flow models in literature and their main features. Analog model (–∿∿–), impedence analysis (IA), finite element (FE), finite-difference (FD), implicit FD (FD_i), finite-volume (FV), discontinuous Galerkin (DG), heart (H), brain circulation (B), coronary vessels (C), pulmonary circulation (P), venous system (V), arterial wall visco-elasticity (VE), clinical data (CD).

The FV method is also known as shock-capturing because it is capable of dealing with sharp gradients in the solution (known as *shocks* in gas-dynamics) (Harten et al., 1987; Shu and Osher, 1988). The shock-capturing feature is a direct consequence of the use of the integral form and makes FV schemes more stable than FD when dealing with the sudden change in pressure typical of pressure waveforms (Toro, 2001).

In the case of the venous system, where vessels can collapse and the lumen cross-sectional area can go to zero, FE schemes do not converge and become unstable. In

this scenario, ad-hoc FV solution schemes have been developed to deal with the arising numerical instabilities (Müller et al., 2012, 2013; Müller and Toro, 2014; Toro and Siviglia, 2013), Blanco et al. (2015) developed a detailed arterial network including over 2000 vessels. Sherwin et al. (2003a) analysed the wave propagation in vessels with variable mechanical properties, and Müller and Toro (2013) developed a higher-order FV scheme for the same application. This solver was later employed to calculate waveforms in a complete model of the circulation including the venous system (Müller and Toro, 2014).

In the view of developing a flexible and robust solver, the FV formulation has been used in this work. This scheme is stable under the CFL condition and converges also in presence of discontinuities in the solution, making it suitable to be extended for solving venous hæmodynamics in the future.

2.3 Sensitivity analysis

Arterial flow models are based on the selection of many parameters quantifying the cardiovascular physiology. Ideally, all these parameters would be directly and accurately measured, but in practice this is not always feasible. There are locations not reachable via non-invasive techniques and the measurements are always affected by noise. Consequently, the uncertainty in the inputs translates in an uncertainty in the output. The assessment of how much uncertainty is transferred from the inputs to the output is the aim of the uncertainty analysis (UA) (Xu and Gertner, 2008).

The Mathematical models are approximations of the physical processes under investigation and therefore there is also the model intrinsic uncertainty to be taken in to account in addition to the uncertainty brought by the input values. The model inputs have different influence on the final outcome, but the uncertainty embedded in the mathematical formulation makes it difficult to attribute to each input a portion of the output variation. The assignment of portions of the output uncertainty to each input is the focus of the sensitivity analysis (SA) (Saltelli et al., 2000). The SA constitutes an important step in the modelling practice and it has disparate applications (Janssen et al., 1990) such as the analysis of a chemical reaction system (Saltelli et al., 2005; Turányi, 1990), the engineering risk-assessment modelling (Cárdenas et al., 2014; Helton, 1993) and the heart valves design (Becker et al., 2011).

The SA helps in expanding the knowledge on the underlying physical system by ranking the input parameters with respect to their influence on the outcome. The less influential parameters can be eliminated from the modelling process, resulting in a reduction of the model complexity. The most influential parameters are those whose uncertainty must be reduced to obtain reliable results. The uncertainty is reduced by improving the input value estimation and the measurement process takes

advantage from the parameter prioritisation resulting from the SA. The SA process requires a meticulous evaluation of the model output all over the input space. These multiple evaluations can be exploited for optimisation and calibration purposes. Eventually, the SA provides an insight to input interactions that are difficult to observe in non-linear models.

The SA methods are grouped in two main classes: local and global SA methods. The local methods employ the one-at-a-time (OAT) approach in which one input is varied in a small range around its nominal value while keeping the others constant. This method effectively compares the effect of single inputs on the output, but it is not capable of capturing the effect of input interactions (Cukier et al., 1973). The OAT strategy has been adopted in a number of cardiovascular modelling studies (Broomé et al., 2013; Mohiuddin et al., 2012; Reymond et al., 2009; Sun et al., 1997; Westerhof et al., 2007). Conversely, the global methods also take into account the interactions by observing the output distribution over the whole input space.

The global SA methods are typically conducted by means of Monte Carlo (MC) method. The simulator is run several times by randomly changing the input parameters within fixed ranges. The number of simulations to be done (N) is linked to the number of input features in the model (d), and generally $N = \mathcal{O}(d \times 10^3)$ (Saltelli, 2002). Therefore, the global SA method can be used when the model evaluation computational cost is small.

This method has been applied in various fields (Iooss and Lemaître, 2015), such as hydrological modelling (Song et al., 2015), biological systems modelling (Kiparissides et al., 2009; Wu et al., 2012), and waste-water plant optimisation (Sin et al., 2011).

The global SA method has been used to study the arterial network (Chen et al., 2013; Eck et al., 2015b; Sankaran and Marsden, 2011; Xiu and Sherwin, 2007), the brain circulation (Grinberg et al., 2011), the arm arteries (Leguy et al., 2011), the ventricular mechanics (Osnes and Sundnes, 2012). However, the number of studies employing global SA methods is a small portion of the total number of papers aimed at using modelling as a clinical decision-making tool (Eck et al., 2015a) often due to computational cost limitations. A recent example consists in the study made to support the decision making process for arterio-venous fistula surgery (Huberts et al., 2013a,b). The struggle to include the global SA into the diagnosis process was mainly due to the computational cost which is high and can hardly be justified in a patient-specific scenario.

2.4 Gaussian process

Outside the cardiovascular field it is common practice to replace the mechanistic model with an approximation of it. This approximation - the emulator - is used

to quickly estimate the output continuous distribution over the input space and to perform the SA (Ratto et al., 2012; Sacks et al., 1989; Santner et al., 2013; Welch et al., 1992).

The problem of inferring input-output relationships from a set of observations is commonly referred to as a supervised learning problem (Bishop, 2006). A subcategory of supervised learning is regression. In a regression problem, the output to be predicted is a continuous variable and the input consists in a vector of values. The outputs of a mechanistic model are noise-free and the regression function can be seen as an interpolating function. A first approach in selecting the interpolation function consists in restricting the search to a specific class of functions such as linear interpolation, cubic splines, or Bézier curves. This approach works well when the interpolating function is of the same class of the mechanistic model, otherwise the fitting and the predictions may be poor (Williams and Rasmussen, 2006). An alternative approach (Bayesian) consists in taking into consideration all the functions passing through the observations and giving them a probability distribution (O'Hagan and Forster, 2004). This probability distribution denotes our prior knowledge about the data and it usually favours functions smoothly interpolating the training dataset. This approach allows to avoid restrictions in choosing a single interpolating function class and is more flexible than classical interpolation methods (Williams, 1998).

The Gaussian process (GP) method consists in giving a probability distribution over the infinite set of interpolating functions (Williams and Rasmussen, 1996). An example of the GP method is given in Figure 2.4.1. The goal is to mimic the behaviour of the deterministic model (simulator) in the interval $\mathcal{I} = [-1, 1]$. When there is no information on the simulator behaviour, only general properties for the interpolating function are chosen, e.g. to be smooth in $\mathcal{I}$ (Figure 2.4.1(a)). As soon as two observations are given (Figure 2.4.1(b)), only the functions passing by those points are considered. At each $x \in \mathcal{I}$ the mean and the standard deviation of all the $f(x)$ are calculated. Note, the uncertainty in the prediction is small close to the observations and it increases far away. By further increasing the number of observations (Figure 2.4.1(c, d)), the prediction uncertainty decreases as the mean function changes shape.

The GP is one of the so-called kernel methods. Historically, the concept of a kernel was introduced by Aizerman et al. in 1964 (Aizerman et al., 1964) and since then it has been adopted for different applications. The GP is know as kriging in geostatistics (Cressie, 1993), it can be seen as the generalisation of the Kalman filter (Reece and Roberts, 2010) and of the radial basis networks (Powell, 1987). It has also been proved that neural networks tend to a GP as the number of hidden layers goes to infinity (Neal, 2012). In the machine learning literature, GP reviews are found in (MacKay, 1998, 2003; Rasmussen, 1996; Williams, 1998).

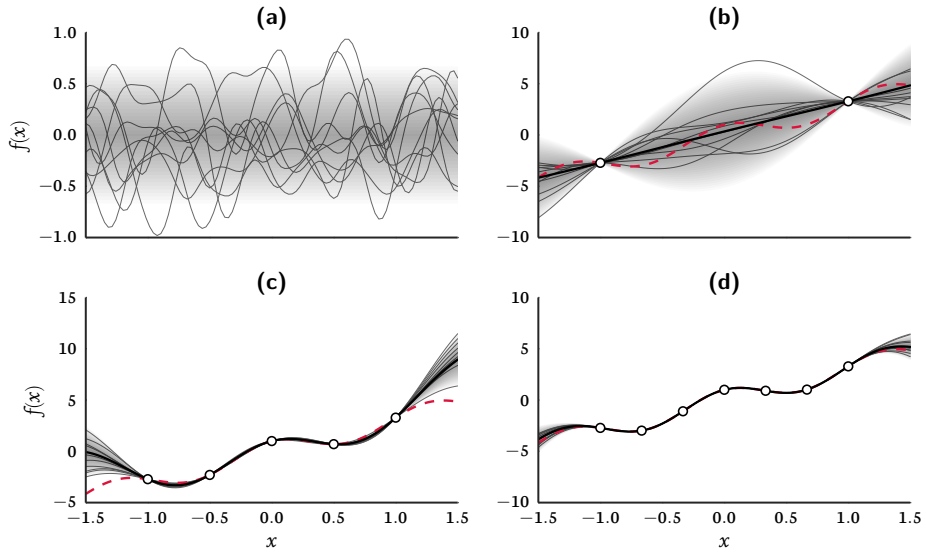

Figure 2.4.1: One-input and one-output (x and $y = f(x)$, respectively) Gaussian process example. (a) Samples from the prior distribution. Samples from the posterior distribution after two (b), five (c), and seven (d) data points (white marker) have been observed. Simulator (dashed) and emulator mean (thick line). Twice the standard deviation at each x is shown by the shaded area.

Emulators are well-known tools in both applied maths and statistics, where the most used techniques are polynomial chaos expansions (PCE) and GP, respectively (O'Hagan, 2013). Both tools aim to infer the simulator global behaviour starting from observed simulator runs. The main advantage of GP over the PCE technique resides in the availability of uncertainty information. This directly descends from the probabilistic nature of a GP, which allows embedding of uncertainty and explicit treatment of model parameters as uncertain quantities. This enables the impact of missing, uncertain, or noisy measurements on model outputs to be quantified. For a detailed analysis of the differences between the two techniques see (Hussain et al., 2002; O'Hagan, 2013). PCE has been successfully used for sensitivity analysis in the cardiovascular field, see for example (Donders et al., 2015; Ellwein et al., 2008; Huberts et al., 2014; Olsen et al., 2015). Despite the use of GP for SA being widely investigated outside of the cardiovascular field (Oakley and O'Hagan, 2004; O'Hagan, 2006), to the author's knowledge GP has never been used to predict 1D blood flow model outcomes for SA purposes.

Methodology

3 Vascular modelling

Summary

In this chapter the blood flow solution methodology is presented (Figure 3.0.1). Initially, the assumptions behind the derivation of the 1D mechanistic model for pulse and volumetric flow wave propagation in the cardiovascular system are presented (the derivation is reported and commented in Appendix A). The 1D system can be linearised and written in the 1D wave form (Section 3.1.2) for which an analytical solution exists (Appendix B). The analytical solution is used as a first validation of the numerical implementation (Section 6.1). The 1D wave equation is further integrated to the lumped-parameter form where the hydraulic/electric circuit analogy is introduced (Section 3.1.3). The lumped-parameter form is used to set the peripheral boundary conditions for the numerical scheme (Section 3.4). The 1D system numerical solution is achieved by means of a finite-volume algorithm (Section 3.3), which is based on the application of the method of characteristics (Section 3.2). This method is applied to the 1D model and the characteristic solution is derived in terms of Riemann invariants. The Riemann invariants are used to define compatibility conditions to close the set of numerical boundary conditions at inlet and outlets (Section 3.4). The electric analogy is used to derive a simplified model of capillary perfusion, which is used as outlet boundary condition for the vascular network.

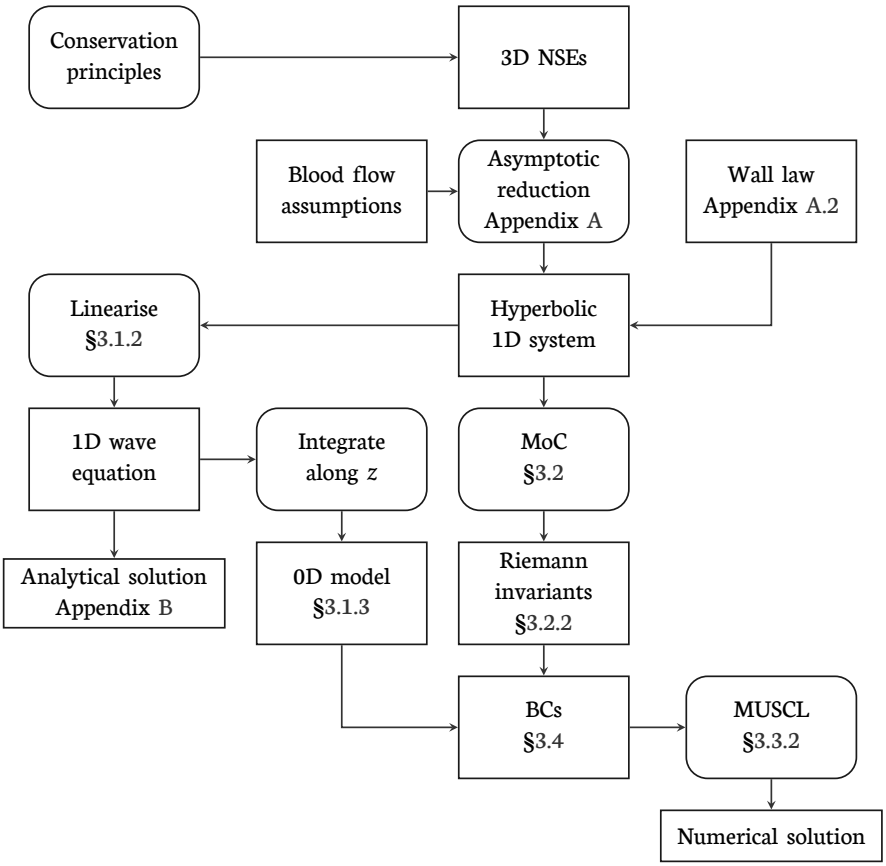

Figure 3.0.1: Methodology diagram. The 1D hyperbolic system of PDEs obtained from the reduction of 3D Navier-Stokes equations (NSEs) is used as a starting point. Further manipulations return the 1D wave equation and the lumped-parameter 0D model. The method of characteristics (MoC) is used to calculate the system Riemann invariants which, in turn, are used to set the system boundary conditions (BCs). Eventually, a finite volume numerical scheme (MUSCL) is used to compute the flow and pressure waveforms.

3.1 Flow through elastic vessels equations

3.1.1 Blood flow model assumptions

The blood flow model derivation is based on the following assumptions:

1. the blood flows in narrow and long circular vessels;
2. the vessels are straight and have linearly elastic compliant walls;
3. small displacements in the radial direction are allowed whereas the longitudinal displacement is neglected;
4. the blood is an incompressible Newtonian fluid.

Under these assumptions (Appendix A), the 1D equations read

$$\begin{cases} \dfrac{\partial A}{\partial t} + \dfrac{\partial Q}{\partial z} = 0, \\ \dfrac{\partial Q}{\partial t} + \dfrac{\partial}{\partial z}\left(\alpha \dfrac{Q^2}{A}\right) + \dfrac{A}{\rho}\dfrac{\partial P}{\partial z} = -2\dfrac{\mu}{\rho}(\gamma_v + 2)\dfrac{Q}{A}, \\ P(A) = P_{ext} + \beta\left(\sqrt{\dfrac{A}{A_0}} - 1\right), \quad \beta = \sqrt{\dfrac{\pi}{A_0}}\dfrac{Eh_0}{1-\nu^2}, \end{cases} \tag{3.1}$$

where t is time, z is the longitudinal coordinate, $A(z,t)$ is the vessel cross-sectional area, $Q(z,t)$ is the volumetric flow rate, α is the Coriolis' coefficient, ρ is the blood density, $P(z,t)$ is the blood pressure, μ is the blood dynamic viscosity, γ_v is a parameter defining the shape of the radial velocity profile, P_{ext} is the vessel external pressure, $E(z)$ is the vessel wall Young's modulus, ν is the Poisson's ratio, $A_0(z)$ is the reference cross-sectional area, and $h_0(z)$ is the reference wall thickness.

3.1.2 Linearised equations

The 1D system (3.1) is non-linear and it is solved by means of numerical methods (see Section 3.3). However, the 1D linearised system has the form of the 1D wave equation which has an analytical solution (reported in Appendix B). The analytical solution can be used as a first benchmark for the numerical solution of the non-linear system (see Section 6.1).

The 1D system (3.1) can be written in terms of (P, Q) variables and linearised around the unloaded zero flow state $(A, u) = (A_0, \mathbf{0})$. This leads to

$$\begin{cases} \dfrac{\partial P}{\partial t} + \dfrac{\beta}{2A_0}\dfrac{\partial Q}{\partial z} = \mathbf{0}, \\ \dfrac{\partial Q}{\partial t} + \dfrac{A_0}{\rho}\dfrac{\partial P}{\partial z} = -K_\nu Q, \end{cases} \tag{3.2}$$

where

$$K_\nu = 2(\gamma_\nu + 2)\frac{\mu}{\rho A_0}. \tag{3.3}$$

By differentiating the continuity equation with respect to t and by multiplying it by ρ/A_0, and by differentiating the momentum equation with respect to z and by subsituting in the continuity equation, we have

$$\frac{\partial^2 P}{\partial t^2} - \frac{\beta}{2\rho}\frac{\partial^2 P}{\partial z^2} + \frac{K_\nu}{A_0}\frac{\partial P}{\partial t} = \mathbf{0}, \tag{3.4}$$

which is a 1D wave equation, of speed $c = \sqrt{\beta/2\rho}$, modified by a viscous resistance component $\frac{K_\nu}{A_0}\frac{\partial P}{\partial t}$. Note that (3.4) could be similarly expressed in terms of Q.

3.1.3 RLC circuit analogy

In order to derive the windkessel equations, the linearised system (3.2) can be alternatively written as

$$\begin{cases} \mathcal{C}\dfrac{\partial P}{\partial t} + \dfrac{\partial Q}{\partial z} = \mathbf{0}, \\ \mathcal{L}\dfrac{\partial Q}{\partial t} + \dfrac{\partial P}{\partial z} = -\mathcal{R}Q, \end{cases} \tag{3.5}$$

where

$$\mathcal{C} = \frac{2A_0}{\beta\sqrt{\pi}}, \quad \mathcal{L} = \frac{\rho}{A_0}, \quad \mathcal{R} = \frac{\rho K_\nu}{A_0^2}. \tag{3.6}$$

The equations can be integrated along the vessel length and expressed by means

of average quantities

$$\begin{cases} \mathcal{C}\dfrac{d\overline{P}}{dt} + Q_\ell - Q_0 = 0, \\ \\ \mathcal{L}\dfrac{d\overline{Q}}{dt} + P_\ell - P_0 = -\mathcal{R}\overline{Q}\,, \end{cases} \qquad \overline{P} = \frac{1}{\ell}\int_0^\ell P dz, \quad \overline{Q} = \frac{1}{\ell}\int_0^\ell Q dz \tag{3.7}$$

where the subscripts 0 and ℓ indicate the inlet and the outlet of the vessel, respectively. By expressing the mean quantities $\overline{P}$ and $\overline{Q}$ in terms of the inlet and outlet quantities, respectively the system (3.7) reads

$$\begin{cases} \mathcal{C}\dfrac{dP_\ell}{dt} + Q_\ell - Q_0 = 0, \\ \\ \mathcal{L}\dfrac{dQ_0}{dt} + P_\ell - P_0 = -\mathcal{R}Q_0\,, \end{cases} \qquad \overline{P} = P_\ell, \qquad \overline{Q} = Q_0\,. \tag{3.8}$$

Note, the spatial information has been eliminated by the integration step, therefore the equations (3.8) are said to be zero-dimensional (0D). Similarly, by imposing $\overline{P} = P_0$ and $\overline{Q} = Q_\ell$, the 0D equations read

$$\begin{cases} \mathcal{C}\dfrac{dP_0}{dt} + Q_\ell - Q_0 = 0, \\ \\ \mathcal{L}\dfrac{dQ_\ell}{dt} + P_\ell - P_0 = -\mathcal{R}Q_\ell\,. \end{cases} \tag{3.9}$$

The system (3.9) is regarded as the mathematical description of an electric RLC system also known as L-circuit (Milišic and Quarteroni, 2004; Peiró and Veneziani, 2009) in which the volumetric flow rate Q corresponds to the electric current and the pressure P corresponds to the electric potential, whereas the flow viscous resistance corresponds to the electric resistance $\mathcal{R}$, the blood inertia to the inductance $\mathcal{L}$, and the wall compliance to the conductance $\mathcal{C}$ (Figure 3.1.1). Similarly, the system (eq:zero-dimensional) is known as inverse L-circuit (or L^{-1}-circuit) for which flow and pressure are prescribed at inlet and outlet, respectively.

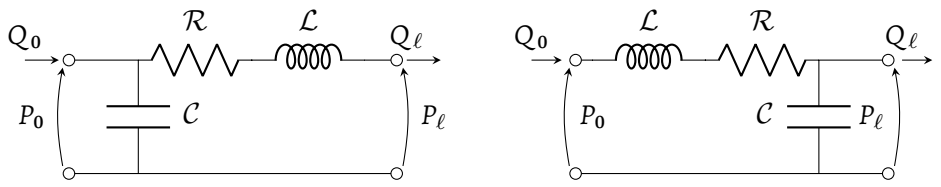

Figure 3.1.1: (left) L^{-1}-circuit and (right) L-circuit schemes

The RLC analogy can be exploited to model the behaviour of several parts of the cardiovascular system. By neglecting the inductance $\mathcal{L}$, the two-element windkessel is obtained. This is well-suited to represent the capillary bed where the inertial effects are negligible. The two-element windkessel model is usually modified to accommodate an additional impedance $\mathcal{Z}$ in series with the resistance $\mathcal{R}$. This is needed when coupling the windkessel to another vascular model (i.e. a 1D model). The coupling method (Section 3.4) may generate unrealistic wave reflections that can be avoided by matching the two models interface impedances. The impedance has the units of a resistance and it is defined as

$$\mathcal{Z} = \rho \frac{c}{A_0}, \tag{3.10}$$

where c is the local pulse wave velocity, ρ is the blood density, and A_0 is the vessel reference cross-sectional area.

The circuit containing the inlet impedance $\mathcal{Z}$ is the three-element windkessel model (Figure 3.1.2), whose equation reads

$$Q_i \left(1 + \frac{\mathcal{Z}}{\mathcal{R}}\right) + \mathcal{C}\mathcal{Z}\frac{\partial Q_i}{\partial t} = \frac{P_i - P_v}{\mathcal{R}} + \mathcal{C}\frac{\partial P_i}{\partial t}. \tag{3.11}$$

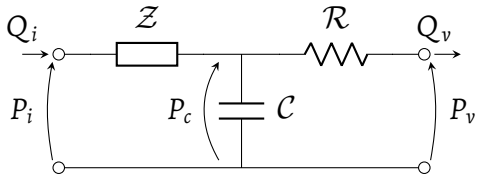

Figure 3.1.2: Three-element windkessel circuit. Quantities with subscript i refer to capillaries entrance; quantities with subscript v refer to the capillaries-veins interface. P_c is the pressure across the compliance C_s. The relative pressure at the end of the capillaries, P_v is set equal to zero. $\mathcal{R}$ and $\mathcal{C}$ are the peripheral viscous resistance and peripheral compliance respectively. Inertial forces within the capillaries are negligible.

3.2 Method of Characteristics

The solution of hyperbolic conservation laws can be studied by means of invariant quantities (Persico, 1952). These are quantities that do not change along preferential trajectories in the phase plane $t - x$ known as characteristic curves. The value of a quantity U is determined at any point (x, t) by following the characteristic trajectories and keeping constant the invariant quantities.

Consider a general one-dimensional hyperbolic equation in quasi-linear form, for a general variable U

$$\frac{\partial U}{\partial t} + \lambda \frac{\partial U}{\partial x} = S. \tag{3.12}$$

We want to find the change in U observed when travelling at speed u. Consider a small time step δt, so that $\delta x = u\delta t$, thus

$$\delta U = \frac{\partial U}{\partial t}\delta t + \frac{\partial U}{\partial x}\delta x = \left(\frac{\partial U}{\partial t} + u\frac{\partial U}{\partial x}\right)\delta t. \tag{3.13}$$

As the observer is in motion, his location is defined by $u = {}^{dx}/_{dt}$ and U is function of only time. Moreover,

$$\lim_{\delta t \to 0} \frac{\partial U}{\partial t} = \frac{dU}{dt} \quad \text{for } \frac{dx}{dt} = u, \tag{3.14}$$

and if $u = \lambda$, it results that

$$\frac{dU}{dt} = S \quad \text{for } \frac{dx}{dt} = \lambda, \tag{3.15}$$

which is the characteristic form of the hyperbolic conservation law. The equation ${}^{dx}/_{dt} = \lambda$ describes the characteristic curve and λ is the characteristic wave speed. In the homogeneous case $S = 0$,

$$\frac{dU}{dt} = 0 \quad \text{for } \frac{dx}{dt} = \lambda, \tag{3.16}$$

and U is constant for $\frac{dx}{dt} = \lambda$. Hence, U is invariant to the observer moving at speed λ and it is called Rieman invariant. The speed λ is the velocity at which the information about U propagates in space, which is different from the speed of U itself.

The characteristic solution can be drawn in the $x - t$ plane and it consists of a family of parallel curves with slope λ (Figure 3.2.1). A specific curve is identified by the initial condition $(x_0, 0)$ and, given the initial profile $U(x, 0)$, the solution is translated forward with velocity λ if $\lambda > 0$ and backwards if $\lambda < 0$.

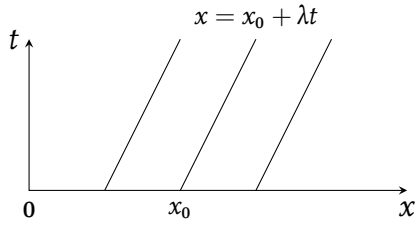

Figure 3.2.1: Family of parallel characteristic curves with slope $\lambda > 0$. The initial condition identify the curve passing by $(x_0, t_0 = 0)$.

The value of U does not change along the characteristic curve, but it differs between different characteristic curves. Hence, the value of U changes across the characteristic curve, and the characteristic curve can be seen as a discontinuity in U values propagating at finite speed λ.

An initial value problem with discontinuous initial condition (Figure 3.2.2a) is a Riemann problem

$$\begin{cases} \dfrac{\partial U}{\partial t} + \lambda \dfrac{\partial U}{\partial x} = 0, \\ \\ U(x,0) = \begin{cases} U_L, & x < 0, \\ \\ U_R, & x > 0. \end{cases} \end{cases} \tag{3.17}$$

The solution of (3.17) consists in propagating the initial configuration of a distance λt after time t. The characteristic curve $x = \lambda t$ (obtained for $x_0 = 0$) subdivides the $x - t$ plane in two sub-planes. The curves on the left side have solution U_L, whereas the curves on the right side take value U_R (Figure 3.2.2b).

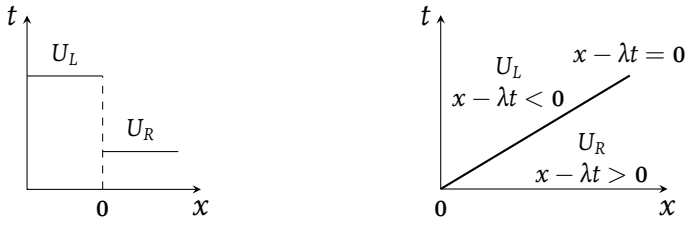

(a) **(b)**

Figure 3.2.2: (a) Discontinuous initial condition. (b) Characteristic solution of the initial value problem with discontinuous initial condition.

3.2.1 Hyperbolic system

In the case of a hyperbolic system, the quasi-linear form is written in terms of the Jacobian matrix $\mathbf{H}$

$$\frac{\partial \mathbf{U}}{\partial t} + \mathbf{H}\frac{\mathbf{U}}{\partial x} = \mathbf{S}. \tag{3.18}$$

For a hyperbolic system, $\mathbf{H} \in \mathbb{R}^{m\times m}$ has m distinct eigenvalues and eigenvectors, λ_i and $\mathbf{r}_i$, $i = 1, \ldots, m$, respectively. The diagonal matrix $\mathbf{\Lambda}$ contains the eigenvalues and the right-eigenvector matrix $\mathbf{R}$ is defined such that

$$\mathbf{LHR} = \mathbf{\Lambda}, \quad \mathbf{L} = \mathbf{R}^{-1}, \tag{3.19}$$

where $\mathbf{L}$ is the left-eigenvectors matrix. To calculate the Riemann invariants, we first left-multiply the quasi-linear form by $\mathbf{L}$

$$\mathbf{L}\frac{\partial \mathbf{U}}{\partial t} + \mathbf{LH}\frac{\mathbf{U}}{\partial x} = \mathbf{LS}, \tag{3.20}$$

and

$$\mathbf{L}\frac{\partial \mathbf{U}}{\partial t} + \mathbf{LHR}\,\mathbf{L}\frac{\mathbf{U}}{\partial x} = \mathbf{LS}, \tag{3.21}$$

leads to

$$\mathbf{L}\frac{\partial \mathbf{U}}{\partial t} + \mathbf{\Lambda L}\frac{\mathbf{U}}{\partial x} = \mathbf{LS}. \tag{3.22}$$

We define

$$d\,\mathbf{W} = \mathbf{L}\,d\,\mathbf{U}, \quad \mathbf{Z} = \mathbf{LS}, \tag{3.23}$$

so that

$$\frac{\partial \mathbf{W}}{\partial t} + \mathbf{\Lambda}\frac{\partial \mathbf{W}}{\partial x} = \mathbf{Z}, \tag{3.24}$$

which is the characteristic form and it is equivalent to a system of ODEs whose ith component reads

$$\frac{\partial W_i}{\partial t} + \lambda_i\frac{\partial W_i}{\partial x} = Z_i, \quad \forall i = 1, \ldots, m. \tag{3.25}$$

For each ith component

$$\frac{dW_i}{dt} = Z_i, \quad \text{for } \frac{dx}{dt} - \lambda_i, \tag{3.26}$$

and, for $\mathbf{Z} = \mathbf{0}$,

$$W_i = \text{const.} \quad \text{for } \frac{dx}{dt} = \lambda_i. \tag{3.27}$$

When the Riemann invariants $\mathbf{W}$ are known, $\mathbf{U}$ can be determined by integrating

$$d\,\mathbf{U} = \mathbf{R}\, d\,\mathbf{W}. \tag{3.28}$$

Conversely, if $\mathbf{U}$ is known at (x, t), the $\mathbf{W}$ are obtained by integrating

$$d\,\mathbf{W} = \mathbf{L}\, d\,\mathbf{U}. \tag{3.29}$$

The Riemann problem for the hyperbolic system reads

$$\begin{cases} \dfrac{\partial \mathbf{U}}{\partial t} + \mathbf{H}\dfrac{\partial \mathbf{U}}{\partial x} = \mathbf{0}, \\ \mathbf{U}(x, \mathbf{0}) = \begin{cases} \mathbf{U}_L, & x < \mathbf{0}, \\ \mathbf{U}_R, & x > \mathbf{0}, \end{cases} \end{cases} \tag{3.30}$$

The general solution structure (Figure 3.2.3) consists of two waves originating in $x = 0$. Each curve represents a discontinuity propagating at velocity λ_i. The solution of (3.30) consists in finding the value of $\mathbf{U}$ in the star region, $\mathbf{U}^*$.

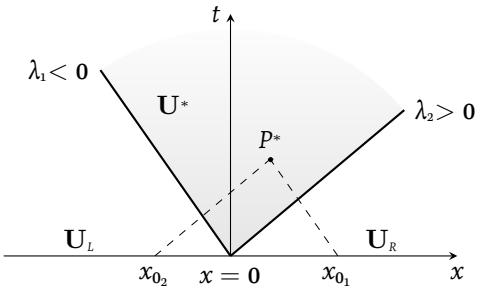

Figure 3.2.3: Riemann problem solution scheme

From the homogeneous form of (3.24) it results that the two linearly independent right eigenvectors $\mathbf{R} = [\mathbf{r}_1, \mathbf{r}_2]^T$ can be used to expand the left and right constant states as

$$\mathbf{U}_L = \sum_{i=1}^{2} \alpha_i\, \mathbf{r}_i, \quad \mathbf{U}_R = \sum_{i=1}^{2} \beta_i\, \mathbf{r}_i, \tag{3.31}$$

where α and β are constant coefficients. Let us now trace the characteristic curves through P^*, a generic point inside the star region. These two curves pass by the initial points $x_{0_{1,2}}$ in the right and left regions, respectively, and we can use the known values $\mathbf{U}_L$ and $\mathbf{U}_R$ to find α_i and β_i in (3.31). The solution in P^* is

$$\mathbf{U}^* = \sum_{i=1}^{2} \eta_i \, \mathbf{r}_i, \quad \eta_i = \text{const.} \tag{3.32}$$

Let us now take a point in the left region, (x_L, t^*), whose known solution is

$$\mathbf{U}_L = \mathbf{U}(x_L, t^*) = \alpha_1 \, \mathbf{r}_1 + \alpha_2 \, \mathbf{r}_2. \tag{3.33}$$

As we shift forward, across the first wave $dx/dt = \lambda_1$, the quantity $x - \lambda t$ becomes positive, α_1 changes to β_1, and the solution in the star region results

$$\mathbf{U}^* = \eta_1 \, \mathbf{r}_1 + \eta_2 \, \mathbf{r}_2 = \beta_1 \, \mathbf{r}_1 + \alpha_2 \, \mathbf{r}_2. \tag{3.34}$$

The same result would be obtained starting from a point in the right region and moving backwards across the second wave $dx/dt = \lambda_2$.

3.2.2 1D flow system Riemann invariants

Take $\alpha = 1$ (plug-flow) and express the system (3.1) in terms of (A, Au)

$$\begin{cases} \dfrac{\partial A}{\partial t} + \dfrac{\partial (Au)}{\partial z} = 0, \\ \dfrac{\partial (Au)}{\partial t} + \dfrac{\partial (Au^2)}{\partial z} + \dfrac{A}{\rho} \dfrac{\partial P}{\partial z} = -2 \dfrac{\mu}{\rho} (\gamma_v + 2) u. \end{cases} \tag{3.35}$$

Note that for $\alpha = 1, \gamma_v \to \infty$ as shown in Figure A.1.2. Therefore, to compute the viscous term in (3.35), $\gamma_v = 9$ is used as an approximation of the plug-flow profile. The system (3.35) is the called conservative form of the 1D system because it stems naturally from the application of the conservation laws (Formaggia et al., 2010). By defining $\mathbf{U} = [A, Au]^T$, the conservative form of the system can be written along the single vessel with initial and boundary conditions as

$$\begin{cases} \dfrac{\partial \mathbf{U}}{\partial t} + \dfrac{\partial \mathbf{F}(\mathbf{U})}{\partial z} = \mathbf{S}(\mathbf{U}), \quad z \in [0, \ell], \\ \mathbf{U}(z, 0) = \mathbf{U}^{(0)}(z), \quad t > 0, \\ \mathbf{U}(0, t) = \mathbf{U}_L(t), \quad \mathbf{U}(\ell, t) = \mathbf{U}_R(t), \end{cases} \tag{3.36}$$

$$\mathbf{U} = \left\{ \begin{array}{c} A \\ Au \end{array} \right\}, \tag{3.37}$$

$$\mathbf{F}\left(\mathbf{U}\right) = \left\{ \begin{array}{c} Au \\ Au^2 + \gamma A^{3/2} \end{array} \right\}, \tag{3.38}$$

$$\mathbf{S}\left(\mathbf{U}\right) = \left\{ \begin{array}{c} 0 \\ f_s \end{array} \right\}, \tag{3.39}$$

$$\gamma = \frac{\beta}{3\rho\sqrt{A_0}}, \tag{3.40}$$

$$f_s = -\frac{1}{\rho}\left[\frac{\partial P}{\partial A_0}\frac{\partial A_0}{\partial z} + \frac{\partial P}{\partial \beta}\frac{\partial \beta}{\partial z} + 2\mu\left(\gamma_v + 2\right)\frac{u}{A}\right] \tag{3.41}$$

where $\mathbf{F}$ is the flux term, and $\mathbf{S}$ is the source term. The flux Jacobian reads

$$\frac{\partial \mathbf{F}}{\partial \mathbf{U}} = \mathbf{H} = \begin{bmatrix} 0 & 1 \\ \frac{3}{2}\gamma\sqrt{A} - u^2 & 2u \end{bmatrix}, \tag{3.42}$$

which, under the assumption $A > 0$, has two eigenvalues

$$\lambda_{1,2} = u \mp c, \qquad c = \sqrt{\frac{3}{2}\gamma\sqrt{A}} = \sqrt{\frac{\beta}{2\rho}}A^{1/4}, \tag{3.43}$$

where c is the wave speed. In arteries, under physiological conditions, $u << c$ always, $\lambda_1 < 0$ and $\lambda_2 > 0$. Thus, the system (3.35) is said to be strictly hyperbolic as $\mathbf{H}$ has two distinct real eigenvalues and a corresponding set of two linearly independent right eigenvectors $\mathbf{R} = \left[\mathbf{r}_1, \mathbf{r}_2\right]^T$ (Sherwin et al., 2003b). The right eigenvectors are obtained by solving

$$\mathbf{HR} = \mathbf{\Lambda R}, \qquad \mathbf{\Lambda} = \mathrm{diag}(\lambda_1, \lambda_2), \tag{3.44}$$

$$\mathbf{R} = \begin{bmatrix} -A/c & A/c \\ 1 & 1 \end{bmatrix}, \tag{3.45}$$

and the left eigenvectors follow

$$\mathbf{L} = \mathbf{R}^{-1} = \begin{bmatrix} -c/A & 1 \\ c/A & 1 \end{bmatrix}. \tag{3.46}$$

The hyperbolic system characteristic curves (W_1, W_2) are obtained by solving

$$\frac{\partial \mathbf{W}}{\partial \mathbf{U}} = \mathbf{L}, \tag{3.47}$$

$$\frac{\partial W_1}{\partial A} = -\frac{c}{A}, \quad \rightarrow \quad \int dW_1 = \int -\frac{c}{A} dA, \tag{3.48}$$

$$W_{1_A} = -\sqrt{\frac{\beta}{2\rho}} \int \frac{A^{1/4}}{A} dA = -4\sqrt{\frac{\beta}{2\rho}} A^{1/4} + c_0 = -4(c - c_0), \tag{3.49}$$

$$\frac{\partial W_1}{\partial u} = 1, \quad \rightarrow \quad W_{1_u} = u - u_0, \tag{3.50}$$

hence

$$W_1 = u - u_0 - 4(c - c_0), \tag{3.51}$$

and, similarly

$$W_2 = u - u_0 + 4(c - c_0). \tag{3.52}$$

One can also express the primitive variables (A,u) in terms of the characteristic variables as

$$A = \left(\frac{W_2 - W_1}{4}\right)^4 \left(\frac{2\rho}{\beta}\right)^2, \quad u = W_1 + W_2. \tag{3.53}$$

The Riemann invariants $W_{1,2}$ will be employed to set the system boundary and interface conditions (Section 3.4). The solution along the vessel was achieved by numerical means. The application of the finite-volume method to the 1D system is presented in the following section.

3.3 Finite volume method

The generic one-dimensional homogeneous conservative law in integral form reads (LeVeque, 2002)

$$\frac{\partial}{\partial t} \int_{x_1}^{x_2} q(x,t) dx = f(q(x_1,t)) - f(q(x_2,t)), \tag{3.54}$$

where q is a generic quantity and x_1 and x_2 are the boundaries of the control volume Ω. The treatment of the source term is presented in Section 3.3.3. The conservation law states that the change of q within Ω is due to the amount of q that crosses the

boundary, i.e. the flux f of q. Let us now subdivide the time-space domain in M cells I_i (Figure 3.3.1a). The domain length is equal to ℓ, and cell length is given by Δx. The total simulation time T defines domain height, hence cell height is given by Δt. In each cell I_i three points are defined: centre point x_i, left extreme $x_{i-1/2}$, and right extreme $x_{i+1/2}$ (Figure 3.3.1b).

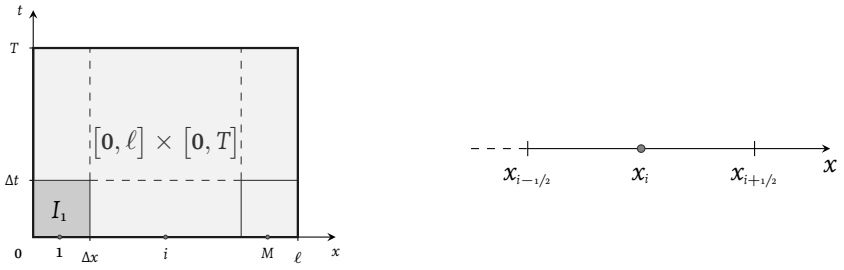

(a) **(b)**

Figure 3.3.1: (a) Computational domain scheme; each cell has dimensions $\Delta x \times \Delta t$. (b) A single cell is centred on a node i and has boundaries at $\mp\frac{1}{2}\Delta x$ on the two sides, $i - \frac{1}{2}$ and $i + \frac{1}{2}$, respectively.

3.3.1 Godunov's scheme

The finite-volume method (Guinot, 2012) computes the time evolution of the average values within each cell i at time n, U_i^n, and assigns this value to each cell midpoint x_i. The idea is that as $\Delta x \to 0$, the average solution tends to the exact solution (LeVeque, 1992). Hence

$$U_i^n \underset{\Delta x \to 0}{=} \frac{1}{\Delta x} \int_{x_i - \frac{\Delta x}{2}}^{x_i + \frac{\Delta x}{2}} q(x, t_n) dx, \tag{3.55}$$

and knowing the flux at the boundaries of the cell, the conservation law becomes

$$\frac{\partial}{\partial t} U_i^n + \frac{1}{\Delta x}\left(F_{i+1/2}^n - F_{i-1/2}^n\right) = 0. \tag{3.56}$$

This can be solved at each time-step within a single cell with a time-stepping method (Toro, 2001) along with a method to compute $F_{i\pm1/2}^n = F\left(U(x_{i\pm1/2}, t_n)\right)$.

At each boundary, there are two local constant solutions: the left solution U_L and the right solution U_R. A problem in which we have constant initial conditions, except for a discontinuity, is known as Riemann problem (Toro, 2009). The Riemann problem can be solved exactly in particular cases, or it can be approximated.

A widely used numerical flux is the Lax-Friedrichs flux

$$F^n_{i+1/2} = \frac{1}{2}\left(F^n_L + F^n_R\right) - \frac{\Delta x}{\Delta t}\left(U^n_{i+1} - U^n_i\right). \tag{3.57}$$

The use of a piecewise constant distribution (Figure 3.3.2(a)) for the solution of conservative laws was first proposed by Godunov (Godunov, 1959). The Godunov's method is first-order accurate and it presents a high degree of numerical diffusion, i.e. sharp gradients tend to be smoothed by the numerical process. This is due to the piecewise constant reconstruction of the solution (Toro, 1989).

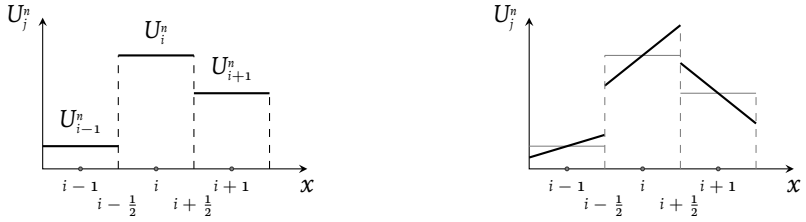

Figure 3.3.2: Piecewise distributions: constant (a) and linear (b)

3.3.2 MUSCL scheme

The MUSCL (monotonic upstream-centred scheme for conservation laws) scheme (van Leer, 1979) substitutes the solution within each cell with a linear piecewise approximation (Figure 3.3.2(b))

$$U(x, t_n) = U^n_i + \sigma^n_i (x - x_i), \tag{3.58}$$

where U^n_i is the Godunov's average and σ^n_i is the cell slope ($\sigma^n_i = 0$ returns the Godunov's scheme) at the time t_n. The switch to the linear piecewise reconstruction may introduce oscillations in the solution (Gibbs phenomenon) for too steep slopes which may lead to unrealistic values of the solution variables (LeVeque, 2002). This is avoided by introducing a slope limiter such as the superbee limiter

$$\sigma_i = \text{maxmod}\left[\text{minmod}(\Delta U^-, 2\Delta U^+), \text{minmod}(2\Delta U^-, \Delta U^+)\right], \tag{3.59}$$

where

$$\Delta U^- = \frac{U_i - U_{i-1}}{\Delta x}, \qquad \Delta U^+ = \frac{U_{i+1} - U_i}{\Delta x}, \tag{3.60}$$

$$\text{maxmod}(a,b) = \frac{1}{2}\Big[\text{sgn}(a) + \text{sgn}(b)\Big] \max\Big\{|a|, |b|\Big\}, \tag{3.61}$$

and

$$\text{minmod}(a,b) = \frac{1}{2}\Big[\text{sgn}(a) + \text{sgn}(b)\Big] \min\Big\{|a|, |b|\Big\}. \tag{3.62}$$

We then compute the values at the two sides of the cell as

$$U^L_{i+1/2} = U_i + \sigma_i \frac{\Delta x}{2}, \quad U^R_{i-1/2} = U_i - \sigma_i \frac{\Delta x}{2}, \tag{3.63}$$

where the time superscript has been dropped to ease the notation.

The evolution from time n to the successive time-step $n+1$ is performed as

$$\begin{cases} U^*_i = U^n_i + \dfrac{\Delta t}{\Delta x}\Big(F^n_{i-1/2} - F^n_{i+1/2}\Big), \\ \\ U^{n+1}_i = \dfrac{1}{2}U^n_i + \dfrac{1}{2}\left[U^*_i + \dfrac{\Delta t}{\Delta x}\Big(F^*_{i-1/2} - F^*_{i+1/2}\Big)\right]. \end{cases} \tag{3.64}$$

The MUSCL method can be generalised to higher dimensions by applying the scheme given in (3.64) to each dimension (Shu and Osher, 1988).

3.3.3 Source term

The hyperbolic conservation system with source term reads

$$\begin{cases} \dfrac{\partial \mathbf{U}}{\partial t} + \dfrac{\partial \mathbf{F}(\mathbf{U})}{\partial x} = \mathbf{S}(\mathbf{U}), \quad x \in \big[\mathbf{0}, \ell\big], \\ \\ \mathbf{U}(x, \mathbf{0}) = \mathbf{U}^{(\mathbf{0})}(x), \quad t > \mathbf{0}, \\ \\ \mathbf{U}(\mathbf{0}, t) = \mathbf{U}_L(t), \quad \mathbf{U}(\ell, t) = \mathbf{U}_R(t), \end{cases} \tag{3.65}$$

which can be split in the homogeneous problem (3.30) and the ODE source problem

$$\frac{d\,\mathbf{U}}{dt} = \mathbf{S}(\mathbf{U}). \tag{3.66}$$

The split problem solution is achieved in two steps

$$\begin{cases} \dfrac{\partial \mathbf{U}}{\partial t} + \dfrac{\partial \mathbf{F}(\mathbf{U})}{\partial x} = \mathbf{0} \\ \\ \mathbf{U}(x, t^n) = \mathbf{U}^n, \end{cases} \quad \rightarrow \quad \overline{\mathbf{U}}^{n+1}, \tag{3.67}$$

$$\begin{cases} \dfrac{d\,\mathbf{U}}{dt} = \mathbf{S}(\mathbf{U}), \\ \\ \overline{\mathbf{U}}^{n+1}, \end{cases} \qquad \rightarrow \qquad \mathbf{U}^{n+1}, \tag{3.68}$$

In the case of (3.35), the source term is

$$\mathbf{S}\left(\mathbf{U}\right) = \left\{ \begin{array}{c} \mathbf{0} \\ f_s \end{array} \right\}, \tag{3.69}$$

where

$$f_s = -\frac{\mathbf{1}}{\rho}\left[\frac{\partial P}{\partial A_0}\frac{\partial A_0}{\partial x} + \frac{\partial P}{\partial \tau}\frac{\partial \beta}{\partial x} + 2\mu\left(\gamma_v + 2\right)\frac{u}{A}\right], \tag{3.70}$$

$$\tau = \beta\sqrt{A_0}, \qquad P = P_{ext} + \tau\left(\sqrt{A} - \sqrt{A_0}\right), \tag{3.71}$$

and

$$\frac{\partial P}{\partial A_0} = -\frac{\beta}{\mathbf{2}}, \quad \frac{\partial P}{\partial \tau} = \sqrt{A} - \sqrt{A_0}. \tag{3.72}$$

By assuming a linear tapering of the lumen radius form a proximal radius R_p to a distal radius R_d for $x = \mathbf{0}$ and $x = \ell$, respectively,

$$A_0 = \pi R_0(x)^2, \qquad R_0(x) = \frac{R_d - R_p}{\ell}x + R_p, \tag{3.73}$$

$$\frac{\partial A_0}{\partial x} = 2\pi R_0\frac{\partial R_0}{\partial x} = 2\pi R_0\frac{R_d - R_p}{\ell}, \tag{3.74}$$

and

$$\frac{\partial \tau}{\partial x} = \frac{\mathbf{4}}{\mathbf{3}}\sqrt{\pi}E\left[\frac{h_0}{R_0} + R_0\left(abe^{bR_0} + cde^{dR_0}\right)\right]\frac{R_d - R_p}{\ell}, \tag{3.75}$$

where we used an estimate for the vessel wall thickness (Avolio, 1980)

$$\frac{h_0}{R_0} = \left(ae^{bR_0} + ce^{dR_0}\right). \tag{3.76}$$

The Crank-Nicholson scheme was employed to evolve the source problem from t_n to t^{n+1} as

$$\mathbf{U}^{n+1} = \mathbf{U}^n + \frac{\mathbf{1}}{\mathbf{2}}\left(\mathbf{C} + \mathbf{N}\right), \tag{3.77}$$

where

$$\begin{cases} \mathbf{C} = \Delta t\, \mathbf{S}\left(t^n, \mathbf{U}^n\right) \\ \mathbf{N} = \Delta t\, \mathbf{S}\left(t^n + \Delta t, \mathbf{U}^n + C\right). \end{cases} \tag{3.78}$$

3.3.4 CFL condition

The finite-volume scheme is stable and converges as the spatial grid is refined if it respects the Courant-Friedrichs-Lewy (CFL) condition (Courant et al., 1928, 1967). This introduces the concept of numerical speed $\Delta x/\Delta t$ alongside the characteristic physical speed λ. In order to have a stable numerical scheme, the numerical speed must be strictly greater than the physical speed. In particular, each computational cell must verify

$$\frac{\Delta x}{\Delta t} > S_{max}, \quad S_{max} = \max_{i=1,\dots,M} \left\{ |\lambda_{i_{1,2}}| \right\}. \tag{3.79}$$

The Δx is usually left to be user-defined to control the scheme spatial accuracy. Hence, the CFL condition is written as a condition on the Δt

$$\Delta t \leq C_{CFL} \frac{\Delta x}{S_{max}}, \quad C_{CFL} \in (0, 1), \tag{3.80}$$

where C_{CFL} is the Courant's number. This can be freely chosen in the range $(0, 1)$ by bearing in mind that as $C_{CFL} \to 1$ the scheme becomes unstable. In this work the value was set to $C_{CFL} = 0.9$ which represent a good compromise between numerical stability and computational time.

In the MUSCL scheme, the CFL condition is easily linked to the Riemann problem solution. The computational cells should be defined such that the inner values depend only on neighbouring cells (Figure 3.3.3a). Failing that, in a Δt, the information travelling along a characteristic curve would end further than one Δx away (Figure 3.3.3b). The numerical solution would fail in tracking the waves propagation resulting in an accumulation of numerical errors.

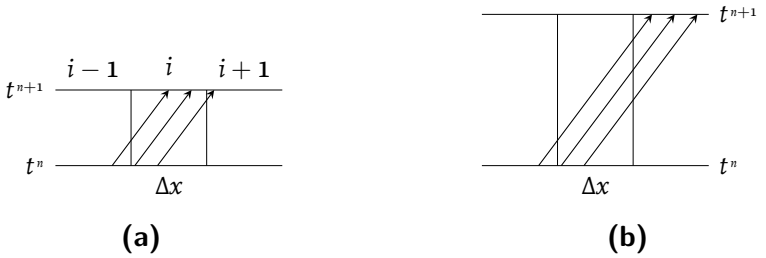

Figure 3.3.3: Illustration of the CFL condition. (a) The Δt should be small enough to capture the wave travelling one cell further. (b) The Δt is too large and the wave is not captured.

3.4 Boundary and interface conditions

Inlet and outlet boundary conditions (BCs) are applied at the beginning and at the ending of each time step, respectively. The BCs are usually specified in terms of Q and/or P, and the 1D system primitive variables are u and A. Thus, at each time step, we need to convert the assigned (Q, P) to (A, u) values.

3.4.1 Inlet

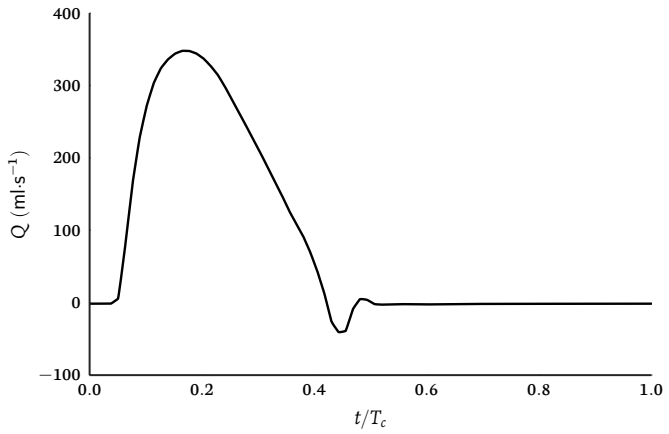

Figure 3.4.1: Ascending aorta volumetric flow rate as function of time normalised on the cardiac cycle period T_c. This is a typical example of time-function used as boundary condition at the inlet of a vascular network.

Consider the system inlet where the BC is applied to the first node of the network root vessel, and it is usually assigned through a volumetric flow rate time-function

(Figure 3.4.1). By simply assigning $Q = Au$, there is ambiguity on the values (A, u), and to uniquivocally set these values, we need another relation.

Compatibility relations are used to compute the quantity not directly assigned by boundary conditions. These relations are derived by using a technique called extrapolation of characteristics (EoC) (Peiró and Veneziani, 2009) which is depicted in Figure 3.4.2.

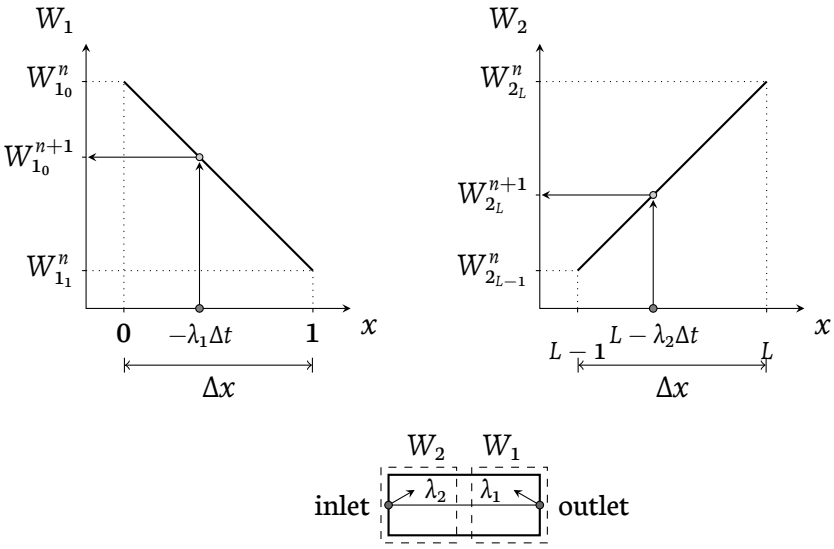

Figure 3.4.2: Extrapolation of characteristics diagram at inlet and outlet nodes (left and right schemes, respectively). The unknown Reimann invariants are calculated by extrapolating back in time the characteristic curves associated to $\lambda_{1,2}$.

The EoC exploits the hyperbolic nature of the 1D system and the Riemann invariants W calculated in Section 3.2 (Quarteroni and Veneziani, 2003). Recall that W are constant quantities along the characteristic curves, for an observer travelling at characteristic speed $\lambda_{1,2}$. At each point x_i there are two characteristic curves: one travelling forward at speed λ_1 and one travelling backwards at speed λ_2.

At the inlet, Riemann invariants

$$W_{1,2} = u \mp 4c, \quad c = \sqrt{\frac{3}{2}\gamma\sqrt{A}}. \tag{3.81}$$

are computed at the first node (W_{1_0}) and at the second node (W_{2_0}) for the current

time step n. The new invariants are extrapolated with a linear law

$$\begin{cases} W_{1_0}(t) = Q_{in}(t), \\ W_{2_0}^{n+1} = W_{2_0}^{n}\Big(L - \lambda_2(L)\Delta t\Big), \end{cases} \tag{3.82}$$

where $Q_{in}(t)$ indicates that at the inlet, the flow value at each time step is assigned by a user-defined time function.

The same procedure can be applied in the case one wants to apply a pressure time-function to the system inlet.

3.4.2 Outlet

At the outlet the same EoC procedure yields

$$\begin{cases} W_{2_L}^{n+1} = W_{2_L}^{n} + \dfrac{W_{2_{L-1}}^{n} - W_{2_L}^{n}}{\Delta x}\left(u_L^n + c_L^n\right)\Delta t, \\ W_{1_L}^{n+1} = W_{1_L}^{0} - R_t\left(W_{1_L}^{n+1} - W_{2_L}^{0}\right), \end{cases} \tag{3.83}$$

where R_t is a reflection coefficient $\in [-1, 1]$, when $R_t = 0$ there are no reflections and incident waves are free to leave the vessel without being reflected.

A more physiologically representative BC is given by the coupling of a three-element windkessel 0D model. Three element windkessel simulates the perfusion of downstream vessels coupled with system outlets (Figure 3.4.3). The 0D model is coupled to 1D model terminal branches via the solution of a Riemann problem at the 0D /1D interface (Fernández et al., 2005; Formaggia et al., 2006).

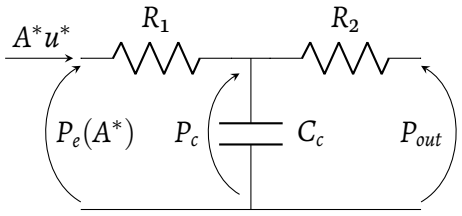

Figure 3.4.3: Three-element windkessel model. R_1 is the proximal resistance, R_2 is the peripeheral reisistance, C_c is the peripheral compliance, P_c is the pressure across the peripheral compliance, P_{out} is the pressure at the artery-vein interface, P_e is the pressure at the 0D /1D interface.

At capillary level, the pressure is assumed to be zero, i.e. $P_{out} = 0$ and the coupling is performed by assuming that an intermediate state (A^*, u^*) generates from (A_l, u_l)

(1D outlet) and (A_r, u_r) (0D inlet) (Alastruey et al., 2008). This intermediate state must satisfy the windkessel equation

$$A^* u^* \left(1 + \frac{R_1}{R_2}\right) + C_c R_1 \frac{\partial (A^* u^*)}{\partial t} = \frac{P_e - P_{out}}{R_2} + C_c \frac{\partial P_e}{\partial t}, \tag{3.84}$$

where P_c is initialised to zero and, at each time step, computed as

$$C_c \frac{\partial P_c}{\partial t} = A^* u^* - \frac{P_c - P_{out}}{R_2}. \tag{3.85}$$

We consider β and A_0 to be the same on both sides of the 0D /1D interface. This yields the non-linear equation

$$f(A^*) = A^* R_1 \left(u_l + 4c_l\right) - 4A^* R_1 c^* - \frac{\beta}{A_0}\left(\sqrt{A^*} - \sqrt{A_0}\right) + P_c, \tag{3.86}$$

where c_l and c^* are the wave speeds calculated with A_l and A^* respectively. A^* is initialised to A_l and $f(A^*) = 0$ is solved iteratively by means of Newton's method. Once A^* is found, u^* reads

$$u^* = \frac{P_e^* - P_{out}}{A^* R_1}, \tag{3.87}$$

where $P_e^* = P_e(A^*)$.

3.4.3 Junctions

Interface conditions are needed for junctions, i.e. when connecting two (conjunction) or three vessels (bifurcation or anastomosis).

Conjunction

A conjunction is defined as two vessels connected in series (Figure 3.4.4) and it is solved by imposing the conservations of mass and total pressure (Bernoulli's principle) at the interface node j.

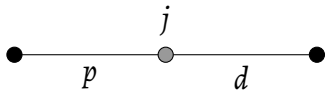

Figure 3.4.4: Conjunction schematics. The parent vessel (p) outlet is linked to the daughter vessel (d) inlet by node j.

Two additional relations are obtained by extrapolating the outgoing characteristics from the two vessels. From the parent vessel outlet we have

$$W_1 = u_1 + 4c_1, \tag{3.88}$$

and for the daughter vessel inlet we have

$$W_2 = u_2 - 4c_2. \tag{3.89}$$

The the principle of conservation of mass in mathematical terms can be expressed as $A_1 u_1 - A_2 u_2 = 0$, and the total pressure conservation requires $P_{t_1} = P_{t_2}$. By defining the unknown vector $\mathbf{q}_c$ as

$$\begin{gathered} \mathbf{q}_c = \{q_{c_i}\} = \left[u_1, \quad u_2, \quad A_1^{1/4}, \quad A_2^{1/4}\right]^T, \\ i = 1, \ldots, 4, \end{gathered} \tag{3.90}$$

the four relations read

$$\mathbf{f}_c = \{f_{c_i}\} = \begin{cases} q_{c_1} + 4k_1 q_{c_3} - W_1^* = 0, \\ q_{c_2} - 4k_2 q_{c_4} - W_2^* = 0, \\ q_{c_1} q_{c_3}^4 - q_{c_2} q_{c_4}^4 = 0, \\ \beta_1 \left(\dfrac{q_{c_3}^2}{A_{01}^{1/2}} - 1 \right) + \dfrac{1}{2}\rho q_{c_1}^2 - \beta_2 \left(\dfrac{q_{c_4}^2}{A_{02}^{1/2}} - 1 \right) - \dfrac{1}{2}\rho q_{c_2}^2 = 0, \end{cases} \tag{3.91}$$

where $c_i = k_i A_i^{1/4}$, $k_i = \sqrt{\dfrac{3}{2}\gamma_i}$. Relation $\mathbf{f}_c(\mathbf{q}_c) = \mathbf{0}$ is solved iteratively with Newton's method

$$\begin{cases} \mathbf{J}_c \cdot \delta \mathbf{q}_c = -\mathbf{f}_c(\mathbf{q}_c), \\ \mathbf{q}_c^{n+1} = \mathbf{q}_c + \delta \mathbf{q}_c, \end{cases} \tag{3.92}$$

where $\mathbf{J}_c$ is the Jacobian

$$\mathbf{J}_c = \begin{bmatrix} 1 & 0 & 4k_1 & 0 \\ 0 & 1 & 0 & -4k_2 \\ q_{c_3}^4 & -q_{c_4}^4 & 4q_{c_1}q_{c_3}^3 & -4q_{c_2}q_{c_4}^3 \\ \rho q_{c_1} & -\rho q_{c_2} & 2\beta_1 \dfrac{q_{c_3}}{A_{01}^{1/2}} & -2\beta_2 \dfrac{q_4}{A_{02}^{1/2}} \end{bmatrix}. \tag{3.93}$$

Bifurcation

A bifurcation (Figure 3.4.5) cannot be solved by Bernoulli's principle as the assumption of a single streamline bifurcating at node b would yield to the generation of energy rather than a redistribution of it. Thus, the bifurcation is solved by imposing conservation of mass and of static pressure only at the bifurcation node b.

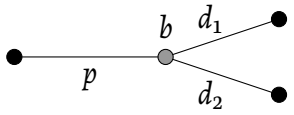

Figure 3.4.5: Bifurcation schematics. A parent vessel (p) is linked to two daughter vessels $(d_{1,2})$ by node b.

Three additional relations are obtained by extrapolating the three outgoing characteristics. The solution process is the same described for the conjunction case. $\mathbf{q}_b$ and $\mathbf{f}_b$ vectors read

$$\mathbf{q}_b = \{q_{b_i}\} = \left[u_1, \quad u_2, \quad u_3, \quad A_1^{1/4}, \quad A_2^{1/4}, \quad A_3^{1/4}\right]^T, \qquad i = 1, ..., 6, \tag{3.94}$$

$$\mathbf{f}_b = \{f_{b_i}\} = \begin{cases} q_{b_1} + 4k_1 q_{b_4} - W_1^* = 0, \\ q_{b_2} - 4k_2 q_{b_5} - W_2^* = 0, \\ q_{b_3} - 4k_3 q_{b_6} - W_3^* = 0, \\ q_{b_1} q_{b_4}^4 - q_{b_2} q_{b_5}^4 - q_{b_3} q_{b_6}^4 = 0, \\ \beta_1 \left(\dfrac{q_{b_4}^2}{A_{01}^{1/2}} - 1 \right) - \beta_2 \left(\dfrac{q_{b_5}^2}{A_{02}^{1/2}} - 1 \right) = 0, \\ \beta_1 \left(\dfrac{q_{b_4}^2}{A_{01}^{1/2}} - 1 \right) - \beta_3 \left(\dfrac{q_{b_6}^2}{A_{03}^{1/2}} - 1 \right) = 0, \end{cases} \tag{3.95}$$

and the Jacobian reads

$$\mathbf{J}_b = \begin{bmatrix} 1 & 0 & 0 & 4k_1 & 0 & 0 \\ 0 & 1 & 0 & 0 & -4k_2 & 0 \\ 0 & 0 & 1 & 0 & 0 & -4k_3 \\ q_{b_4}^4 & -q_{b_5}^4 & -q_{b_6}^4 & 4q_{b_1} q_{b_4}^3 & -4q_{b_2} q_{b_5}^3 & -4q_{b_3} q_{b_6}^3 \\ 0 & 0 & 0 & 2\beta_1 \dfrac{q_{b_4}}{A_{01}^{1/2}} & -2\beta_2 \dfrac{q_{b_5}}{A_{02}^{1/2}} & 0 \\ 0 & 0 & 0 & 2\beta_1 \dfrac{q_{b_4}}{A_{01}^{1/2}} & -2\beta_2 \dfrac{q_{b_5}}{A_{02}^{1/2}} & 0 \end{bmatrix}. \tag{3.96}$$

This approach does not take into accounts the bifurcation geometry, i.e. the bifurcation angle. This can be introduced by means of an empirical loss factor in equations (3.95) (Formaggia et al., 2003). However, due to the difficulty of assigning suitable loss coefficients, the bifurcation has been treated as a perfect conjunction of three vessels.

Anastomosis

The anastomosis is a reversed bifurcation, i.e. there are two inlet parent vessels ($p_{1,2}$) and one outlet daughter vessel (d) (Figure 3.4.6).

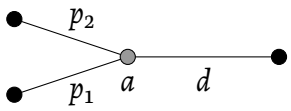

Figure 3.4.6: Anastomosis schematics. A daughter vessel is linked to two parent vessels by node a.

The anastomosis is solved as a bifurcation by means of few iteration of the Newton's methods. The vectors $\mathbf{q}_a$ and $\mathbf{f}_a$ are

$$\mathbf{q}_a = \{q_{a_i}\} = \left[u_1, \quad u_2, \quad u_3, \quad A_1^{1/4}, \quad A_2^{1/4}, \quad A_3^{1/4}\right]^T, \qquad i = 1, ..., 6, \tag{3.97}$$

$$\mathbf{f}_a = \{f_{a_i}\} = \begin{cases} q_{a_1} + 4k_1 q_{a_4} - W_1^* = 0, \\ q_{a_2} + 4k_2 q_{a_5} - W_2^* = 0, \\ q_{a_3} - 4k_3 q_{a_6} - W_3^* = 0, \\ q_{a_1} q_{a_4}^4 + q_{a_2} q_{a_5}^4 - q_{a_3} q_{a_6}^4 = 0, \\ \beta_1 \left(\dfrac{q_{a_4}^2}{A_{01}^{1/2}} - 1 \right) - \beta_3 \left(\dfrac{q_{a_6}^2}{A_{03}^{1/2}} - 1 \right) = 0, \\ \beta_2 \left(\dfrac{q_{a_5}^2}{A_{02}^{1/2}} - 1 \right) - \beta_3 \left(\dfrac{q_{a_6}^2}{A_{03}^{1/2}} - 1 \right) = 0, \end{cases} \tag{3.98}$$

and the Jacobian reads

$$\mathbf{J}_a = \begin{bmatrix} 1 & 0 & 0 & 4k_1 & 0 & 0 \\ 0 & 1 & 0 & 0 & 4k_2 & 0 \\ 0 & 0 & 1 & 0 & 0 & -4k_3 \\ q_{a_4}^4 & q_{a_5}^4 & -q_{a_6}^4 & 4q_{a_1}q_{a_4}^3 & 4q_{a_2}q_{a_5}^3 & -4q_{a_3}q_{a_6}^3 \\ 0 & 0 & 0 & 2\beta_1 \dfrac{q_{a_4}}{A_{01}^{1/2}} & 0 & -2\beta_3 \dfrac{q_{a_6}}{A_{03}^{1/2}} \\ 0 & 0 & 0 & 0 & 2\beta_2 \dfrac{q_{a_5}}{A_{02}^{1/2}} & -2\beta_3 \dfrac{q_{a_6}}{A_{03}^{1/2}} \end{bmatrix}. \tag{3.99}$$

3.5 Concluding remarks

In this chapter, the mathematical and numerical methods employed for the solution of blood flow were reported. The 1D model was derived from the 3D Navier-Stokes equation by means of asymptotic analysis, and the three-element windkessel model was obtained through linearisation of the 1D equations. The method of characteristics was employed to develop the MUSCL scheme and to obtain the numerical solution in terms of Riemann invariants. Compatibility relations for vessel inlet and outlets were defined to express the model boundary conditions in terms of invariant quantities. Interface conditions were defined at bifurcations, junctions, and anastomosis, where flow quantities are computed by means of Newton-Raphson method. At network outlets, the lumped-parameter formulation was used to model capillary perfusion.

In Chapter 6, the proposed numerical model is validated against state-of-the-art solvers from literature. In the following chapter, the fundamental concepts of uncertainty and sensitivity analysis are reported. Sensitivity analysis techniques based on graphical and variance methods are shown by means of a numerical example.

4 Sensitivity analysis

Summary

The construction of patient specific 1D models is difficult because the model inputs are difficult or expensive to measure in the clinical setting. It is therefore important to ensure that model predictions and biomarkers are robust under a range of model inputs. Moreover, in order to take into consideration the uncertainty in measurements, the sensitivity of each output of interest to the variability of each model parameter should be assessed. This chapter presents the sensitivity analysis techniques employed. First, the graphical methods based on scatterplots are applied to a toy example (Section 4.1). Then the ANOVA decomposition is discussed (Section 4.2). This is applied to generate the main-effect plots and to derive the sensitivity indices (sections 4.2.1 and 4.2.2, respectively).

4.1 Scatterplots and correlations

A popular graphical SA method consists in plotting each input against the output of interest. Inputs causing a large variation of the output are directly determined by a visual inspection of the plots.

Let us take into consideration the model $y = f(x_1, x_2, x_3)$, relating the output y to the three inputs x_j, $j = 1, 2, 3$. The scatterplots (Figure 4.1.1) show three different behaviours of y with respect to x_j. The first scatterplot suggests that y is not sensitive to x_1 as the points are scattered along the entire solution space and they do not show a definite trend. Conversely, a linear and a non-linear trend are noticed in the second and third plot, respectively.

A simple correlation coefficient between inputs and output is given by Pearson product moment formula (Pearson, 1895)

$$r = \frac{\sum_{i=1}^{N}(x_{ij} - \overline{\mathrm{x}}_j)(y_i - \overline{\mathrm{y}})}{\sqrt{\sum_{i=1}^{N}(x_{ij} - \overline{\mathrm{x}}_j)^2}\sqrt{\sum_{i=1}^{N}(y_i - \overline{\mathrm{y}})^2}}, \tag{4.1}$$

where x_{ij} is the i-th point of the j-th input, and

$$\overline{\mathbf{x}}_j = \frac{1}{N}\sum_{i=1}^{N} x_{ij}, \quad \overline{\mathbf{y}} = \frac{1}{N}\sum_{i=1}^{N} y_i, \tag{4.2}$$

are the mean values for the input x_j and the output y, respectively. The r value varies in $[-1, 1]$ with 0 indicating no correlation. For $r = \pm 1$, an exact linear correlation is implied.

In the example, the correlation coefficients are $r = (0.04, 0.98, -0.84)$ for the three cases, respectively. The correlation coefficient indicates only whether y is linearly associated to x_j, but it does not capture non-linear relationships. The scatterplots are more informative than correlation values but they do not provide any insight on the possible interactions between inputs.

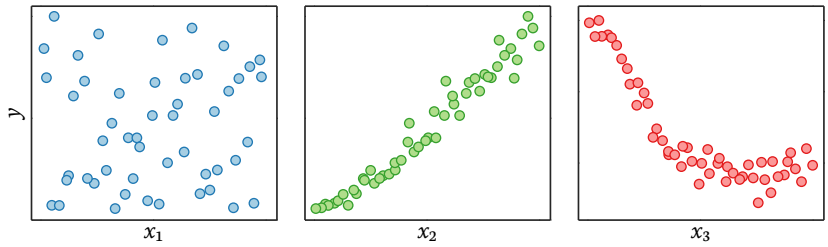

Figure 4.1.1: Example of inputs-output scatterplots. (left) The points scattered across the model domain indicate a weak relationship between y and x_1. (center) The data shows an increasing trend and the points are closely scattered along a line. This is a sign of a strong linear correlation as remarked by the correlation coefficient $r = 0.98$. (right) The points show a non-linear trend but this is not captured by $r = -0.84$ which implies only a negative linear correlation.

4.2 Variance-based sensitivity analysis

The analysis of variances (ANOVA) type decomposition consists in representing $y = f(\mathbf{x})$ as a sum of components of different dimensions. Define the d-dimensional unit hypercube $\mathcal{I}^d$ as the hyperspace containing the d-dimensional input vectors,

$\mathbf{x} \in \mathcal{I}^d = [\mathbf{0}, \mathbf{1}]^d$. Then, y can be rewritten as the sum

$$y = y_0 + \sum_{i=1}^{d} f_i(x_i) + \sum_{1 \le i < j \le d} f_{ij}(x_i, x_j) + \cdots + f_{1,2,\ldots,d}(\mathbf{x}), \quad y_0 = \text{const.}, \tag{4.3}$$

if

$$\int_{\mathcal{I}^d} f_{i_1,\ldots,i_z}(x_{i_1}, \ldots, x_{i_z}) dx_{i_p} = \mathbf{0}, \quad \forall \mathbf{1} \le p \le z. \tag{4.4}$$

A decomposition satisfying (4.4) has orthogonal components, i.e. for any two $f_{i_{1,\ldots,z}}$ and $f_{j_{1,\ldots,w}}$,

$$\int_{\mathcal{I}^d} f_{i_{1,\ldots,z}}(x_{i_{1,\ldots,z}}) f_{j_{1,\ldots,w}}(x_{j_{1,\ldots,w}}) d\mathbf{x} = \mathbf{0}, \quad (i_{1,\ldots,z}) \neq (j_{1,\ldots,w}), \tag{4.5}$$

where y_0 is the mean of $y(\mathbf{x})$

$$y_0 = \int_{\mathcal{I}^d} f(\mathbf{x}) d\mathbf{x}. \tag{4.6}$$

The first-order terms $f_i(x_i)$ are obtained by integrating (4.3) over all the inputs except the ith, i.e.

$$f_i(x_i) = \int_{\mathcal{I}^d} f(\mathbf{x}) d\mathbf{x}_z - y_0, \quad z \in [\mathbf{1}, \ldots, d] : z \neq i. \tag{4.7}$$

The second-order terms $f_{ij}(x_i, x_j), i \neq j$, read

$$\begin{aligned} f_{ij}(x_i, x_j) = \int_{\mathcal{I}^d} f(\mathbf{x}) d\mathbf{x}_{zw} - y_0 - f_i(x_i) - f_j(x_j), \\ z, w \in [\mathbf{1}, \ldots, d] : z \neq i, w \neq j, \end{aligned} \tag{4.8}$$

and the higher-order terms follow

$$\begin{aligned} f_{ij\ldots k}(x_i, x_j, \ldots, x_k) = \int_{\mathcal{I}^d} f(\mathbf{x}) d\mathbf{x}_{zw\ldots b} - y_0 - f_i(x_i) - \cdots - f_k(x_k), \\ z, w, \ldots, b \in [\mathbf{1}, \ldots, d] : z \neq i, \ldots, b \neq k. \end{aligned} \tag{4.9}$$

The hyper-integrals in (4.7-4.9) can be approximated as hyper-series when the number of data points is large enough, and it was estimated that the integrals evaluation requires a number of points of order $\mathcal{O}(d \times 10^3)$ (Saltelli, 2002).

4.2.1 Main effect plots

This is a visualisation technique exploiting ANOVA decomposition, and it can assess the non-linearity of the output sensitivity to an individual input or a couple of inputs variation.

The ith main-effect plot draws $(x_i, f_i(x_i))$ points that are calculated by means of (4.7). These integrals can be numerically computed by approximating a continuous distribution of points with a uniform discrete sampling (sampling techniques are discussed in Section 5.3). In the case of three input variables x_i, each $f_i(x_i)$ is calculated as the average over 1000 points.

The three inputs are normalised dimension-wise to $[0, 1]$ by subtracting the mean $\overline{x}_i$ and by dividing by the standard deviation $\text{std}(x_i)$,

$$\hat{x}_{ki} = \frac{x_{ki} - \overline{x}_i}{\text{std}(x_i)}. \tag{4.10}$$

The use of normalised points places all the x_i on a common scale.

The main-effect plot presents a curve for each normalised input $\hat{x}_i$. The output sensitivity is directly assessed by observing the plot: the greater the $f_i(x_i)$ curve variability, the higher the output sensitivity to the input x_i change.

The model output is not sensitive to the first input as the main-effect plot shows a constant f_1 value along the whole x_1 range (Figure 4.2.1). Conversely, f_2 and f_3 exhibit a wider distribution over $\hat{x}$ range. The former has a linear reponse, whereas the latter does not. These observations are in agreement with the SA result obtained by graphical means in Section 4.1.

In order for the interactions between the inputs to be taken into account, (4.8) is used to plot the points $(\hat{x}, f_{ij}(x_i, x_j))$. These are obtained by fixing two inputs and averaging the outcomes computed by varying the remaining input values over their ranges (Figure 4.2.2).

The interaction plot for the pairs (x_1, x_2) and (x_1, x_3) shows a zero constant value meaning that the parameter x_1 does not influence the outcome y when it is combined with the others. This is not observed for the pair (x_2, x_3) as the interaction plot varies greatly over the $\hat{x}$ range. The $f_{23}(x_2, x_3)$ curve steeply increases for $\hat{x} < 0.5$ and slowly decreases for $\hat{x} > 0.5$.

Similarly, higher-order interactions between more than two inputs can be computed via (4.9), but the visualisation becomes cumbersome due to the increased number of dimensions. Thus, higher-order interactions are better studied by means of the sensitivity indices.

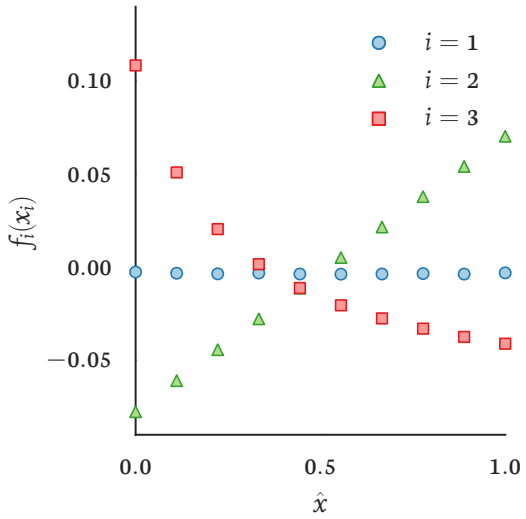

Figure 4.2.1: Main-effect plots $(x_i, f_i(x_i))$, $i = 1, 2, 3$. The higher the plot variability the greater the output sensitivity to the input variation.

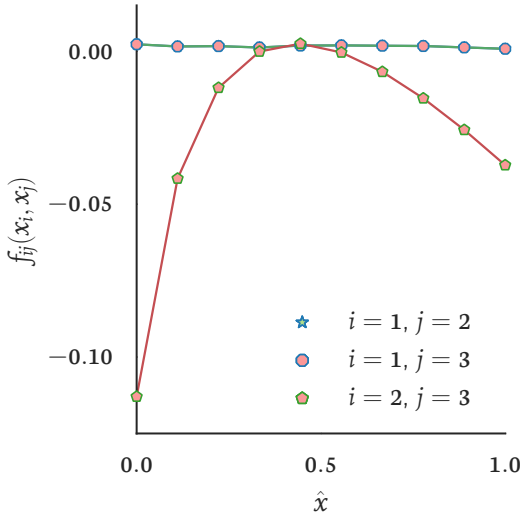

Figure 4.2.2: Interaction plots for all the pairs (i, j), $i, j = 1, 2, 3$, $i \neq j$. The curves for pairs (x_1, x_2) and (x_1, x_3) are superimposed and constant around zero, meaning that the interaction between these inputs is negligible. A high degree of interaction is shown by the pair (x_2, x_3) as the corresponding curve varies in the $\hat{x}$ range in non-linear fashion.

4.2.2 Sensitivity indices

Define the variance of $y = f(\mathbf{x})$ as

$$V_f = \int_{\mathcal{I}^d} f(\mathbf{x})^2 d\mathbf{x} - y_0^2, \tag{4.11}$$

and, by means of the ANOVA decomposition (4.3), the partial variances read

$$\begin{aligned} V_{i_1,\dots,i_z} &= \int_{\mathcal{I}^d} f_{i_1,\dots,i_z}(\mathbf{x})^2 d\mathbf{x}, \\ z = 1,\dots,d, \quad & 1 \le i_1 < \cdots < i_z \le d. \end{aligned} \tag{4.12}$$

Integrating (4.12) over $\mathcal{I}^d$, it results

$$V_f = \sum_{i=1}^{d} V_i + \sum_{1 \le i < j \le d} V_{ij} + \cdots + V_{1,\dots,d}, \tag{4.13}$$

where the output total variance V_f is expressed in terms of the partial variances $V_i, V_{ij}, \dots, V_{1\dots d}$. The quantities

$$\begin{aligned} \mathbb{S}_{i_1,\dots,i_z} &= \frac{V_{i_1,\dots,i_z}}{V_f}, \\ z = 1,\dots,d, \quad & 1 \le i_1 < \cdots < i_z \le d, \end{aligned} \tag{4.14}$$

are the sensitivity indices or Sobol's indices.

The sensitivity indices are the ratio between the total and partial variances. They express the contribution of each input (or combination of inputs) to the global variance. The index $\mathbb{S}_i$ is a first-order index and it takes into account the effect of a single input on the output variance. Similarly, $\mathbb{S}_{ij}$ is a second-order index and it expresses the interaction degree between a pair of inputs. The quantitative knowledge provided by first- and second-order indices is similar to the qualitative insight given by main-effect and interaction plots, respectively.

Introduce the total-effect sensitivity indices

$$\mathbb{T}_i = \mathbb{S}_i + \sum_{j>i} \mathbb{S}_{ij} + \sum_{j<i} \mathbb{S}_{ji} + \cdots + \mathbb{S}_{1,\dots,d}, \tag{4.15}$$

which are the sum of all the sensitivity indices related to the ith input. Hence, the higher-order effects can be directly measured as $\mathbb{T}_i - \mathbb{S}_i$. The sensitivity indices

can be converted to percent values indicating the fraction of the total variance due to single or combination of inputs.

First-order indices can be used to rank inputs and to decide which has the strongest individual influence on the model outputs. Eventually, by highlighting input collaborations, total-effect sensitivity indices assess the inputs that can be fixed to nominal values.

The first- and second-order indices calculated for the toy-example are reported as percent luminance values in the heat-map of Figure 4.2.3. The heat-map main diagonal contains $\mathbb{S}_i$ indices ant the $\mathbb{S}_{ij}$ indices are in the lower triangular matrix. The first-order and the total-effect indices are reported in Table 4.2.1.

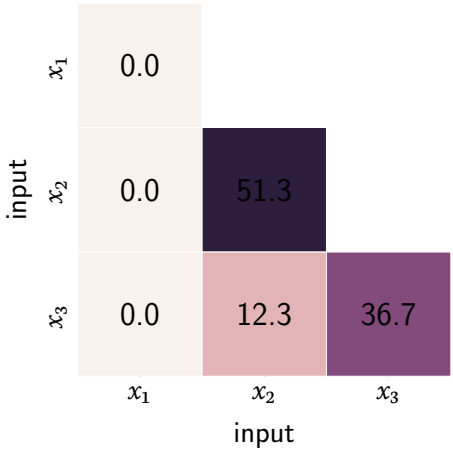

Figure 4.2.3: Sensitivity indices heat-map for the example from Figure 4.1.1. $\mathbb{S}_i$ indices are reported on the main diagonal and $\mathbb{S}_{ij}$ indices on the lower triangular matrix.

	$\mathbb{S}_i\,\%$	$\mathbb{T}_i\,\%$
x_1	1.70×10^{-5}	1.53×10^{-3}
x_2	51.3	62.7
x_3	36.7	49.4

Table 4.2.1: First-order and total-effect sensitivity indices for the three inputs.

The $\mathbb{S}_1$ value is about zero, i.e., the output is not sensitive to x_1 variations, and $\mathbb{S}_{12}$ and $\mathbb{S}_{13}$ zero values confirm the absence of interaction between x_1 and both x_2 and

x_3. The large values of $\mathbb{S}_2$ and $\mathbb{S}_3$ indices indicate the dominant influence of x_2 and x_3 on y variation. The interaction between these two model parameters is moderate as $\mathbb{S}_{23} \simeq 12\%$.

4.3 Concluding remarks

In this chapter, the sensitivity analysis method was introduced and discussed as a generic modelling tool rather than in the context of vascular modelling. The benefit of performing a global sensitivity analysis were shown by analysing a test dataset. First, scatter-plots used for a visual inspection and to assess the poor level of information provided by simple correlation methods. Then, the analysis of variance method was introduced to generate main effect plots. These plots take into considerations the interactions between inputs and provide a better insight on the system non-linearities. Eventually, sensitivity indices were derived from ANOVA decomposition. The Sobol indices were used to quantify the sensitivity of outputs to individual and combined inputs.

The global sensitivity analysis techniques explained in this chapter will be used in the applications to study non-linearities in vascular network of different complexity. The next chapter deals with Gaussian process theory and sampling techniques for the generation of datasets for sensitivity analysis purposes.

5 Gaussian process

Summary

Sensitivity analysis techniques are subject to the availability of large datasets reporting the variation of outputs and inputs. A comprehensive exploration of the model input space is computationally intensive, but is more tractable if a fast-running statistical emulator replaces the model. A Gaussian process emulator can be trained on a relatively small number of model runs. In this chapter, the mathematical framework underlying the Gaussian process method is presented. The various kernel function used to build the emulators are revised, and the techniques used to generate new ones are discussed (Section 5.1). Then, the GP training and optimisation phases are analysed (Section 5.2). Finally, the input space sampling problem is addressed, and the Latin hypercube algorithm is reported (Section 5.3).

Consider a set of N d-dimensional inputs $\mathbf{X} = \{\mathbf{x}_1, \dots, \mathbf{x}_N\}$ and N corresponding observations (outputs) $\mathbf{y} = \{y_1, \dots, y_N\}$. The set of N inputs and outputs is the training dataset $\mathcal{D} = \{\mathbf{X}, \mathbf{y}\}$. The task of learning the input-output mapping f (Figure 5.0.1), from observed data is a regression problem (MacKay, 1998) and, once the mapping is found, it can be employed to predict outputs $\hat{\mathbf{y}}$ for new, unseen, inputs $\hat{\mathbf{X}}$.

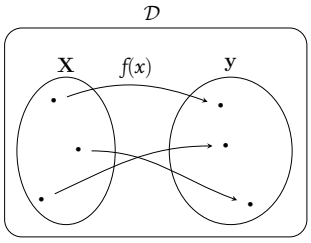

Figure 5.0.1: Inputs-outputs mapping within a generic training dataset $\mathcal{D}$

The GP is defined as a set of random variables representing the values $f(\mathbf{X})$ whose subsets have a joint normal probability distribution (O'Hagan and Kingman, 1978).

This joint probability distribution is fully described by a mean function m and a covariance function (kernel) k. The standard notation for a GP reads

$$f(\mathbf{x}) \sim \mathcal{GP}\Big(m(\mathbf{x}), k(\mathbf{x}, \tilde{\mathbf{x}})\Big), \tag{5.1}$$

$$m(\mathbf{x}) = \mathbb{E}\big[f(\mathbf{x})\big], \tag{5.2}$$

$$k(\mathbf{x}, \mathbf{x}') = \mathbb{E}\Big\{\Big[f(\mathbf{x}) - m(\mathbf{x})\Big]\Big[f(\tilde{\mathbf{x}}) - m(\tilde{\mathbf{x}})\Big]\Big\}, \tag{5.3}$$

where $\tilde{\mathbf{x}} \in \mathcal{D}$ and $\mathbb{E}\big[f(\mathbf{x})\big]$ denotes the expected value of f at $\mathbf{x}$. It is always possible to pre-process $\mathcal{D}$ to have zero mean, i.e., $m(\mathbf{x}) = \mathbf{0}, \forall\, \mathbf{x} \in \mathcal{D}$.

The kernel function is used to build the covariance matrix $\mathbf{K}$,

$$\mathbf{K}_{i,j} = k(\mathbf{x}_i, \mathbf{x}_j), \quad i, j = \mathbf{1}, \ldots, N, \tag{5.4}$$

and it is to be chosen such that, for similar $\mathbf{x}_i$ and $\mathbf{x}_j$, the corresponding $f(\mathbf{x}_i)$ and $f(\mathbf{x}_j)$ are strongly correlated (MacKay, 1998). A widely used kernel is the squared exponential function (Abrahamsen, 1997)

$$k_{SE}(\mathbf{x}, \tilde{\mathbf{x}}) = \vartheta_\sigma^2 \exp\left(-\frac{||\mathbf{x} - \tilde{\mathbf{x}}||^2}{2\vartheta_\ell^2}\right), \tag{5.5}$$

where the hyper-parameters ϑ_σ and ϑ_ℓ are the signal variance and length-scale, respectively. Several kernel functions can be used for GP training, and their hyper-parameters can be optimised to increase the prediction accuracy (see Section 5.2).

By definition, the prior probability has zero mean, it is normally distributed, and it is described by the covariance $\mathbf{K}$,

$$p(f) = \mathcal{N}(\mathbf{0}, \mathbf{K}), \tag{5.6}$$

where $\mathbf{0}$ is the zero vector. The (5.6) is a probability distribution over functions and it can be sampled to obtain random Gaussian vectors. Samples $\mathbf{s} \sim \mathcal{N}(\mathbf{m}, \mathbf{C})$ from a multivariate normal distribution of mean $\mathbf{m}$ and covariance $\mathbf{C}$ are generated in three steps (Williams and Rasmussen, 2006):

1. decompose the covariance matrix by means of the Cholesky decomposition: $\mathbf{C} = \mathbf{L}\mathbf{L}^T$, where $\mathbf{L}$ is a lower triangular matrix called Cholesky factor;
2. generate $\mathbf{u} \sim \mathcal{N}\big(\mathbf{0}, \mathbf{I}\big)$ by multiple calls of a scalar random Gaussian generator;
3. compute $\mathbf{s} = \mathbf{m} + \mathbf{L}\mathbf{u}$.

In Figure 5.0.2(a) few samples from the prior built through (5.5) were plotted against the input x.

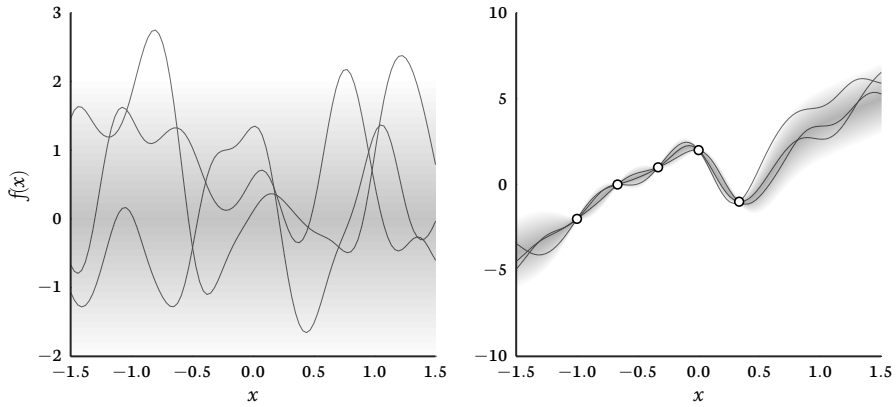

Figure 5.0.2: Functions drawn from the prior and conditional distributions on left and right, respectively. The white markers represent the training data upon which the conditional distributions are sampled; 94% confidence interavals are shown by the shadowed areas.

Take into consideration the training data $\mathcal{D}$ along with a new and unseen set of test inputs $\mathbf{X}_t$ for which we want to predict the outputs $\mathbf{y}_t$. By definition of GP, the joint distribution of $p\left(\mathbf{y}, \mathbf{y}_t\right)$ is normally distributed,

$$p\left(\mathbf{y}, \mathbf{y}_t\right) = \mathcal{N}\left(\mathbf{0}, \mathbf{K}_{N+t}\right), \tag{5.7}$$

$$\begin{aligned} \mathbf{K}_{N+t} &= \begin{bmatrix} \mathbf{K}_N & \mathbf{K}_{Nt} \\ \mathbf{K}_{Nt}^T & \mathbf{K}_t \end{bmatrix}, \\ \mathbf{K}_{Nt} &= k(\mathbf{x}_i, \mathbf{x}_j), \qquad i = 1, \ldots, N, \\ \mathbf{K}_t &= k(\mathbf{x}_j, \mathbf{x}_\ell), \qquad j, \ell = N+1, \ldots, N+t. \end{aligned} \tag{5.8}$$

The predictions on $\mathbf{X}_t$ are done by evaluating the conditional distribution (Seeger, 2004)

$$p(\mathbf{y}_t|\mathbf{y}) = \mathcal{N}\left(\mathbf{y}_t|\mathbf{0}, \mathbf{K}_{N+t}\right), \tag{5.9}$$

where

$$\mathbf{y}_t|\mathbf{0} = m\left(\mathbf{X}_{N+t}\right) = \mathbf{K}_{Nt}^T \mathbf{K}_N^{-1} \mathbf{y}_N, \tag{5.10}$$

and

$$\mathbf{K}_{N+t} = \mathbf{K}_t - \mathbf{K}_{Nt}^T \mathbf{K}_N^{-1} \mathbf{K}_{Nt}. \tag{5.11}$$

The conditional distribution (5.9) is the results of conditioning the prior with the observed values and it is called posterior distribution (Figure 5.0.2(b)).

5.1 Kernels

The prediction accuracy of a GP regressor depends on the kernel selection and its optimisation (Abrahamsen, 1997). This section deals with the former problem, the latter task is presented in Section 5.2.

A two-arguments function calculating the similarity between its arguments is called covariance function or kernel, $k(\mathbf{x}, \tilde{\mathbf{x}})$ (Yaglom, 2004). The kernel is used to build the covariance matrix $\mathbf{K}$, a symmetric positive semi-definite matrix. The symmetry requirement implies:

$$k(\mathbf{x}, \tilde{\mathbf{x}}) = k(\tilde{\mathbf{x}}, \mathbf{x}). \tag{5.12}$$

The matrix $\mathbf{K}$ is positive semi-definite if $\mathbf{v}^T \mathbf{K} \mathbf{v} \geq 0, \forall\, \mathbf{v} \in \mathbb{R}^N$, and the kernel is positive semi-definite (von Mises, 2014) if and only if

$$k(\mathbf{x}, \tilde{\mathbf{x}}) \geq \mathbf{0}, \quad \forall (\mathbf{x}, \tilde{\mathbf{x}}) \in \mathbb{R}^N. \tag{5.13}$$

Kernels are said stationary (Genton, 2001) if they are function of the difference between the arguments, $k(\mathbf{x}, \tilde{\mathbf{x}}) = k(\mathbf{x} - \tilde{\mathbf{x}})$. Stationary kernels are invariant to translation within the input space. If the kernel depends on the distance between inputs, $k(\mathbf{x}, \tilde{\mathbf{x}}) = k\left(||\mathbf{x} - \tilde{\mathbf{x}}||\right)$, the kernel is also homogeneous (or isotropic). Non-stationary kernels, on the other hand, let the GP model adapt to changes in smoothness within the input space (Paciorek and Schervish, 2004).

Among the stationary homogeneous kernels (Matheron, 1973), standard covariance functions include the squared exponential (SE) kernel (5.5), for which the hyperparameter ϑ_ℓ determines the function length-scale, i.e. as ϑ_ℓ decreases the function frequency increases (Figure 5.1.1).

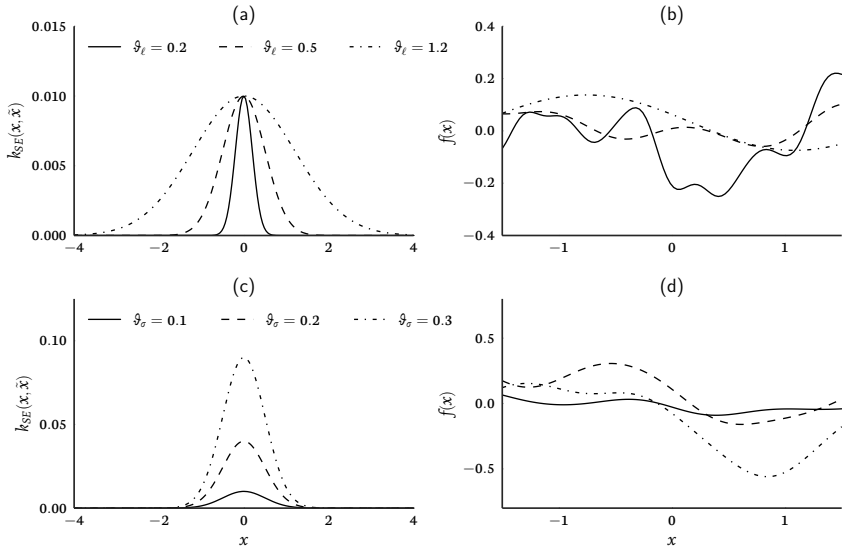

Figure 5.1.1: Squared exponential kernel for different values of the length-scale hyperparameter ϑ_ℓ (a) and variance ϑ_σ (c). All kernels are multiplied by ϑ_σ, the variance, which scales the kernel and regulates the functions distance from their mean values. (b,d) Prior distribution samples drawn for the different values of ϑ_ℓ and ϑ_σ, respectively.

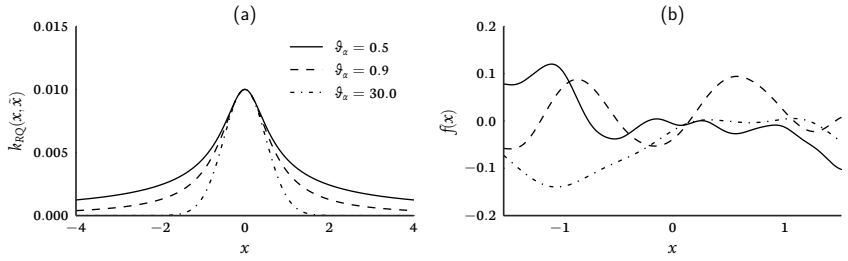

Figure 5.1.2: (a) Rational quadratic kernel for different values of the hyper-parameter ϑ_α. (b) Prior distribution samples drawn for the different values of ϑ_α.

The rational quadratic kernel (Figure 5.1.2)

$$k_{RQ}(\mathbf{x}, \tilde{\mathbf{x}}) = \vartheta_\sigma^2 \left(1 + \frac{||\mathbf{x} - \tilde{\mathbf{x}}||^2}{2\vartheta_\alpha \vartheta_\ell^2}\right)^{-\vartheta_\alpha}, \tag{5.14}$$

results from an infinite sum of SE kernels and ϑ_α is weighting factor setting the relative importance of large length-scales over small length-scales. Note that

$$\lim_{\vartheta_\alpha \to \infty} k_{RQ} = k_{SE}. \tag{5.15}$$

The periodic kernel

$$k_P(\mathbf{x}, \tilde{\mathbf{x}}) = \vartheta_\sigma^2 \exp\left[-\frac{2}{\vartheta_\ell^2} \sin\left(\pi \frac{||\mathbf{x} - \tilde{\mathbf{x}}||}{\vartheta_p} \right) \right], \tag{5.16}$$

can be employed in the case of functions repeating exactly with a fixed period, and the hyperparameter ϑ_P sets the repetition distance (Figure 5.1.3).

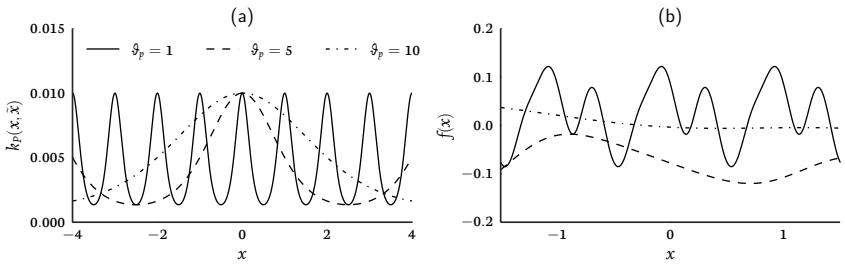

Figure 5.1.3: (a) Periodic kernel for different values of the hyperparameter ϑ_P. (b) Prior distribution samples drawn for the different values of ϑ_P.

The Matérn class of kernels (Figure 5.1.4) (Matérn, 2013)

$$k_{M\nu}(\mathbf{x}, \tilde{\mathbf{x}}) = \vartheta_\sigma^2 \frac{2^{1-\nu}}{\Gamma(\nu)} \left(\frac{\sqrt{2\nu}}{\vartheta_\ell} ||\mathbf{x} - \tilde{\mathbf{x}}|| \right)^\nu I_\nu \left(\frac{\sqrt{2\nu}}{\vartheta_\ell} ||\mathbf{x} - \tilde{\mathbf{x}}|| \right), \tag{5.17}$$

where $\Gamma(\cdot)$ is the Gamma function, $I_\nu(\cdot)$ is a modified Bessel function, and ν is a positive parameter which controls the smoothness of the kernel function Stein (2012). Note that $\lim_{\nu \to \infty} k_{M\nu} = k_{SE}$.

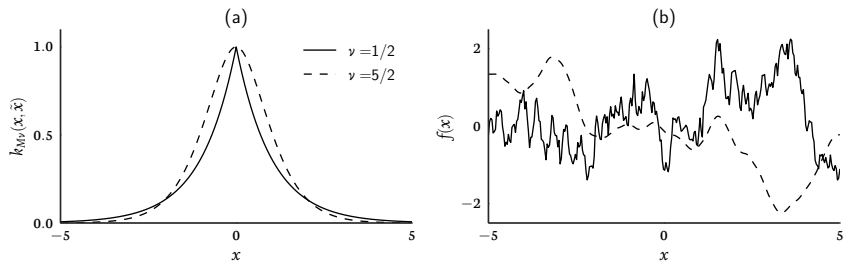

Figure 5.1.4: (a) Matérn class kernel for different values of the hyperparameter ϑ_ν. (b) Prior distribution samples drawn for the different values of ϑ_ν.

The linear kernel (Figure 5.1.5)

$$k_L(\mathbf{x}, \tilde{\mathbf{x}}) = \vartheta_b^2 + \vartheta_\sigma^2 \left(\mathbf{x} - \vartheta_c\right)\left(\tilde{\mathbf{x}} - \vartheta_c\right), \tag{5.18}$$

is non-stationary and defines a family of straight lines with an offset from the origin which is specified by the two hyperparameters $(\vartheta_c, \vartheta_b)$.

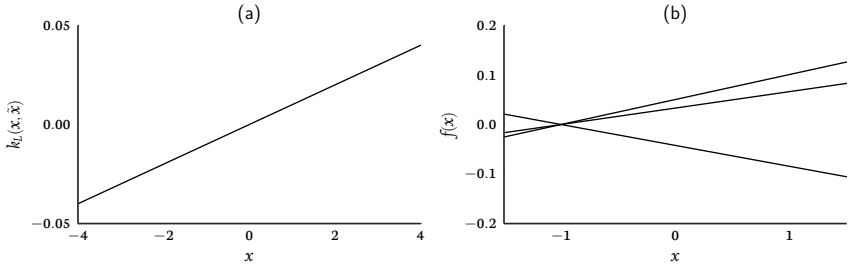

Figure 5.1.5: (a) Linear kernel. (b) Three samples drawn from the prior distribution informed by the linear kernel with $\vartheta_b = 0$ and $\vartheta_c = -1$.

5.1.1 Kernels combination

The most used kernels for GP regression are reported in Table 5.1.1. These functions fulfil requirements (5.12, 5.13) and can be used to build the covariance matrix (5.4). New kernels can be built by using functions in Table 5.1.1 as building blocks. The rules for building a new kernel $k(\mathbf{x}, \tilde{\mathbf{x}})$ starting from two valid kernels k_1, k_2 read (Bishop, 2006)

$$
\begin{aligned}
&k = ck_1, \quad c = \text{const.} > 0,\\
&k = k_1 + k_2,\\
&k = k_1 \cdot k_2,\\
&k = \exp(k_1),\\
&k = \mathbf{x}^T \mathbf{A} \tilde{\mathbf{x}},\\
&k = f(\mathbf{x}) \cdot k_1 \cdot f(\tilde{\mathbf{x}}),
\end{aligned}
\tag{5.19}
$$

where $\mathbf{A}$ is a symmetric positive semi-definite matrix and $f(\mathbf{x})$ is any function. These rules can be applied to mix together kernels with different length-scales, and thus to obtain interpolating functions capable of mimicking complex non-linear functions.

kernel	$k(\mathbf{x}, \tilde{\mathbf{x}})$
Linear, k_L	$\vartheta_b^2 + \vartheta_\sigma^2 (\mathbf{x} - \vartheta_c)(\tilde{\mathbf{x}} - \vartheta_c)$
Polynomial, k_{Pl}	$\left(\mathbf{x} \cdot \tilde{\mathbf{x}} + \vartheta_\sigma^2\right)^p$
SE, k_{SE}	$\exp\left(-r^2/2\vartheta_\ell^2\right)$
γ-exponential, $k_{\gamma E}$	$\exp\left(-r/\vartheta_\ell\right)^\gamma$
Rational quadratic, k_{RQ}	$\left(1 + r^2/2\vartheta_\alpha\vartheta_\ell^2\right)^{-\vartheta_\alpha}$
Periodic, k_P	$\exp\left[-2/\vartheta_\ell^2 \sin\left(r\pi/\vartheta_p\right)\right]$
Mν, $k_{M\nu}$	$2^{1-\nu}/\Gamma(\nu)\left(r\sqrt{2\nu}/\vartheta_\ell\right)^\nu I_\nu\left(r\sqrt{2\nu}/\vartheta_\ell\right)$

Table 5.1.1: Typically used covariance functions for GP regression. All the stationary kernels, expressed in terms of $r = ||\mathbf{x} - \tilde{\mathbf{x}}||$, must be multiplied by the variance hyperparameter ϑ_σ.

The kernel $k_{MSE} = k_{M\nu} + k_{SE}$ (Figure 5.1.6) uses the Mν length-scale (twice than the SE one) to adjust the low frequency response of the prior distribution, whereas the high frequency wiggling is regulated by the SE kernel.

In the case of periodic function slightly changing over time, as most of physiological signals, the multiplication of the periodic kernel k_P by the k_{SE} returns the locally periodic kernel, $k_{LP} = k_P \cdot k_{SE}$ (Figure 5.1.7). The prior distribution is periodic and controlled by ϑ_p, but the shape changes slowly over time because of the SE and its characteristic length.

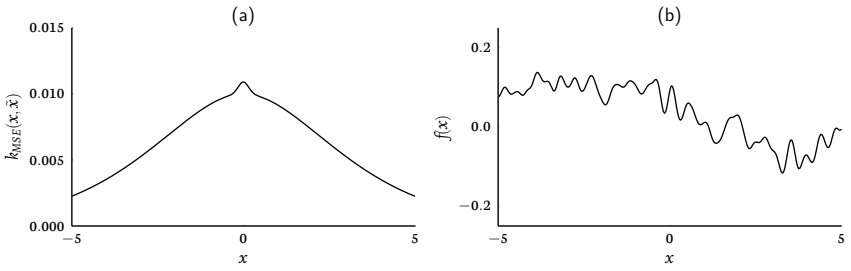

Figure 5.1.6: Matérn plus squared exponential, $\vartheta_{\sigma,\ell} = (0.1, 0.3)$ and $\vartheta_{\sigma,\ell} = (0.03, 0.15)$.

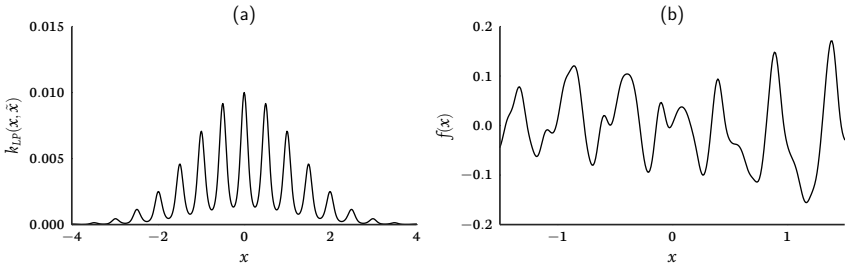

Figure 5.1.7: (a) Locally periodic kernel calculated as the product of the periodic kernel and the squared exponential kernel with hyperparameters $\vartheta_{p,\ell} = (0.5, 1.0)$ and $\vartheta_{\ell} = 1.2$, respectively. (b) The sample from the prior distribution has an overall period of 0.5 and slowly changes over x because of the effect of the squared exponential length-scale.

5.2 Model selection

The GP method is very flexible but, as remarked in (Duvenaud et al., 2013), the kernel selection and its hyperparameters adjustment may at first appear as a black art. In the one-dimensional case, the general characteristic of the kernel (e.g. stationary or non-stationary) can be directly inferred from the observation of the training data, but for higher dimensional data the model selection must rely on an optimisation process.

The optimisation process follows a cross-validation strategy: the training dataset is partitioned in s subsets, $(s-1)$ of them are used for training and the remaining set, the validation set, is used to assess the model performance (Bishop, 2006).

We can use Bayes' rule to make inference about the hyperparameters set $\boldsymbol{\Theta} = \{\vartheta_\cdot\}$ in the training phase (Seeger, 2000). The assumptions about $\boldsymbol{\Theta}$ are embedded in the prior $p(\boldsymbol{\Theta})$ and the effect of the training dataset is captured by the conditional probability $p(\mathbf{y}|\boldsymbol{\Theta})$. Bayes' rule reads

$$p(\boldsymbol{\Theta}|\mathbf{y}) = \frac{p(\mathbf{y}|\boldsymbol{\Theta})p(\boldsymbol{\Theta})}{p(\mathbf{y})}, \tag{5.20}$$

the likelihood $p(\mathbf{y}|\boldsymbol{\Theta})$ indicates how likely it is to observe $\mathbf{y}$ given different configurations of $\boldsymbol{\Theta}$. The denominator $p(\mathbf{y})$ is a normalisation constant which ensures that the posterior $p(\boldsymbol{\Theta}|\mathbf{y})$ is a probability density i.e., $\int p(\boldsymbol{\Theta}|\mathbf{y})d\mathbf{y} = 1$.

The Bayes' rule can be re-stated as

$$p(\boldsymbol{\Theta}|\mathbf{y}) \propto p(\mathbf{y}|\boldsymbol{\Theta})p(\boldsymbol{\Theta}), \tag{5.21}$$

in the view of maximising the posterior probability for a fixed prior (i.e. the kernel function), the optimisation problem reduces to the maximisation of the likelihood function, which translates in finding the $\boldsymbol{\Theta}$ maximising $p(\mathbf{y}|\boldsymbol{\Theta})$ (Mardia and Marshall, 1984). This is done by choosing an error (or loss) function to be minimised. There are not restrictions to the choice of the error function, and it is common practice to use the negative logarithm of the likelihood function (Williams and Rasmussen, 1996). This is because the negative log is a monotonically decreasing function, and the minimisation of the negative log is equivalent to the minimisation of the function itself.

Assume that our dataset is independent and identically distributed, the Gaussian likelihood reads

$$p(\mathbf{y}|\boldsymbol{\Theta}) = \prod_{n=1}^{N} \mathcal{N}(y_n|\boldsymbol{\Theta}), \tag{5.22}$$

and, by taking the log, the product of probabilities turns into the sum of log probabilities, and the log likelihood $\mathcal{L}$ reads

$$\mathcal{L} = \ln p(\mathbf{y}|\boldsymbol{\Theta}) = -\frac{1}{2}\ln|\mathbf{K}_N| - \frac{1}{2}\mathbf{y}\mathbf{K}_N^{-1}\mathbf{y} - \frac{N}{2}\ln(2\pi). \tag{5.23}$$

The minimisation of $\mathcal{L}$ can be efficiently done by means of the conjugate-gradient method (Nocedal and Wright, 2006); the gradient of $\mathcal{L}$ reads

$$\frac{\partial\mathcal{L}}{\partial\vartheta_i} = -\frac{1}{2}\mathrm{Tr}\left[\left(\mathbf{a}\mathbf{a}^T - \mathbf{K}_N^{-1}\right)\frac{\partial\mathbf{K}}{\partial\vartheta_i}\right], \qquad \mathbf{a} = \mathbf{K}^{-1}\mathbf{y}, \tag{5.24}$$

where $\mathrm{Tr}(\mathbf{A}) = \sum_{i=1}^{N} a_{ii}$, $\mathbf{A} \in \mathbb{R}^{N\times N}$, is the matrix trace.

The hyperparameter search is done by running a parameter sweep over suitable ranges. To avoid local optima, the process is restarted several times by randomly picking the initial vector (Press, 2007). Eventually, the set of trained hyperparameters is the one for which the negative $\mathcal{L}$ is the lowest.

5.3 Sampling

In order to compute the output either to inform a SA or to train a GP emulator, we need to select a set of input points. The selection process - the experimental design - should not affect the final analysis. We are only interested in how the model response changes as we move within the domain, but not in changes due to the sampling method, i.e. the final outcome must be independent of the experimental design. Let us define the generic design $\mathcal{D}$ as the set of N d-dimensional input points $\mathbf{x}_i, i = 1, \ldots, N$, where $\mathbf{x}_i = \{x_{i1}, \ldots, x_{id}\}$, and $x_{ij}, j = 1, \ldots, d$ are the input point features.

The experimental design selection for the sensitivity analysis of computer models is based on two principles: randomisation and orthogonality. The former consists in selecting data points at random in the view of eliminating systematic errors due to the user-biased manual action. The experimenter may be biased in conducting simulations in a particular order or in focusing more on a certain domain area without noticing. A well-defined randomisation process effectively eliminates the experimenter bias. The orthogonality requirement derives from the necessity of studying the effect of input interactions. An orthogonal design is built such that input features are not correlated, so that we can independently observe the effect of a single feature. A design based on orthogonality and randomisation principles is optimal if it also does not replicate observations, i.e. all the input points differ for at least one feature value.

The GP prediction error at any domain location is conditioned by the data point density in that area, the larger the number of data points the higher the prediction accuracy. This is a direct consequence of the probabilistic approach adopted. The prediction confidence increases as we train the GP on a more detailed dataset. The training datasets containing evenly spread points - space-filling datasets - are used to limit the prediction error all-over the domain. The space-filling designs are characterised by an even points density and can be both randomised and orthogonal.

5.3.1 Latin hypercube

The Latin hypercube sampling (LHS) is a method to generate homogeneous orthogonal datasets. Consider the two-dimensional unit square $\mathcal{I}^{[0,1]\times[0,1]}$. The LHS algorithm to generate N samples for the pair $(x_1, x_2) \in \mathcal{I}$ develops in three steps:

1. Subdivide the $[0, 1]$ ranges in N equal intervals, resulting in N^2 cells.

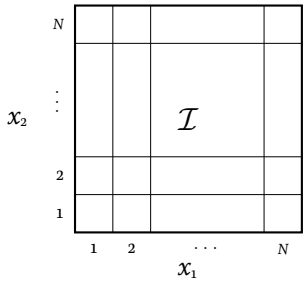

2. Each cell is unequivocally determined by a pair (i, j), $i, j \in \{1, 2, \ldots, N\}$. The pairs (i, j) are generated as random distinct permutations of the ordered sequence $1, 2, \ldots, N$. The matrix containing one permutation in each column is the $LHS_{2,N}$ sampling matrix.

i	j
2	5
3	1
6	3
1	2
5	4
4	6

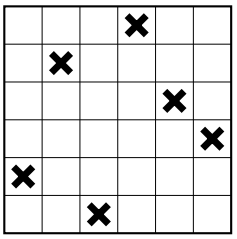

Figure 5.3.1: (left) Permutations matrix $LHS_{2,6}$ for $N = 6$. (right) Cells selected by the permutation matrix are indicated by the black crosses.

3. For each cell, draw samples (x_1, x_2) as

$$x_1 = F_{x_1}^{-1}\left(\frac{i - 1 + \eta_{x_1}}{N}\right), \quad x_2 = F_{x_2}^{-1}\left(\frac{j - 1 + \eta_{x_2}}{N}\right), \tag{5.25}$$

where $\eta_{x_1}, \eta_{x_2} \in [0, 1]$ are randomly generated numbers, and F_{x_1,x_2}^{-1} are the inverse cumulative probability distribution functions of x_1 and x_2, respectively (Figure 5.3.2). This is equivalent to pick a random point within each cell in the permutation matrix.

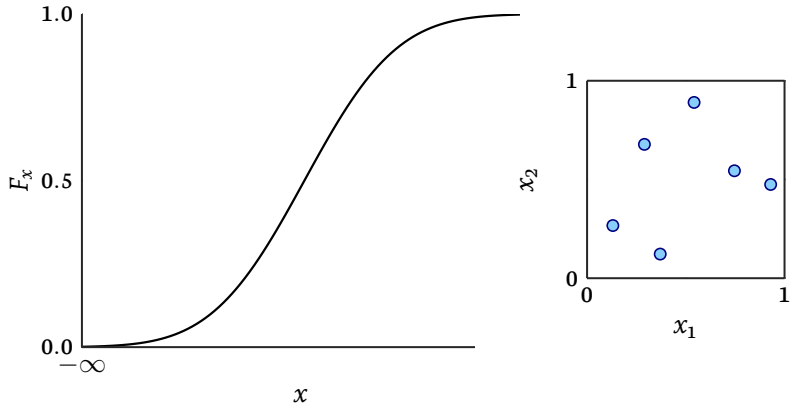

Figure 5.3.2: (left) Cumulative probability distribution function. (right) Six points sampled by means of the LHS method in $\mathcal{I}^2$.

Note, the LHS algorithm can be easily generalised for a d-dimensional hyperspace $\mathcal{D}^d$ by computing the sampling matrix $LHS_{d,N}$.

The LHS ensures an even coverage of the input hyperspace even for a small sample size. Conversely, a simple random sample does not cover the full domain (Figure 5.3.3). As the sample size increases, the LHS and the random sampling tend to cover the domain in the same way (Figure 5.3.4).

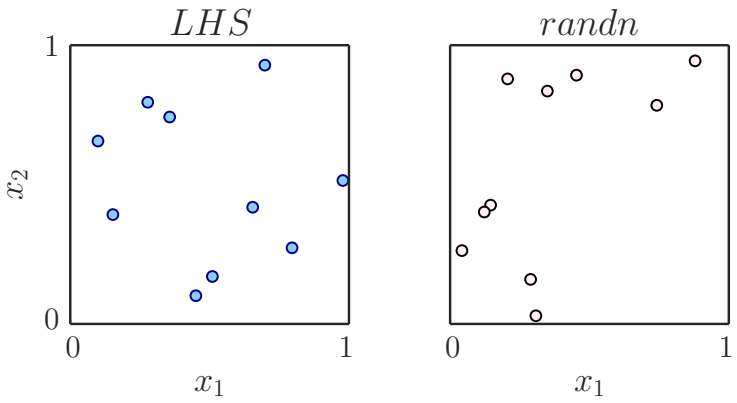

Figure 5.3.3: Comparison for $N = 10$ of (left) the Latin hypercube sampling and (right) the random sampling from a normal distribution. The random sampling fails to cover the entire domain while the LHS spreads evenly the sample points.

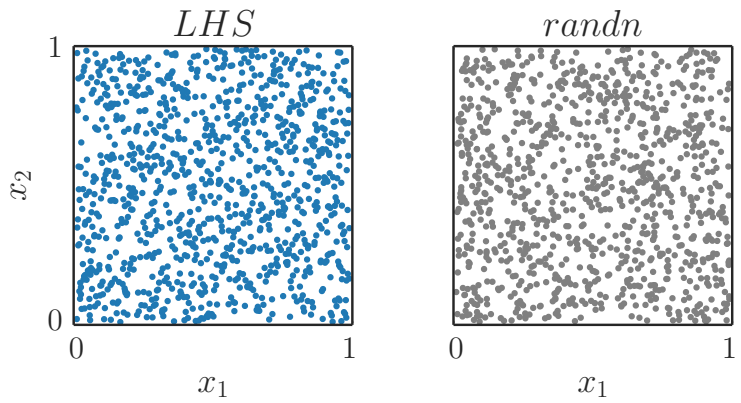

Figure 5.3.4: Comparison for $N = 1024$ of (left) the Latin hypercube sampling and (right) the random sampling from a normal distribution. The two point distributions are similar as samples are evenly drawn.

5.4 Concluding remarks

In this chapter, the mathematical basis for the Gaussian process method were reported. The construction of the Gaussian process emulator, which is based on the selection of the covariance function, was shown with examples of distributions sampled from different kernels. The covariance function optimisation was achieved with a Bayesian approach. This approach can be generalised to find optimal hyperparameters for different combinations of kernels. Eventually, the problem of input space sampling was introduced and the popular method of Latin hypercube was described. The Latin hypercube sampling method minimises the number of sample points for an homogeneous coverage of the input space.

The introduction of the Gaussian process emulator can reduce significantly the computational time required by a robust sensitivity analysis. Such a thorough description of the model and the effects of its parameters would not be possible by running the source model alone. This has particular relevance in a potential scenario where use of these modelling approaches could be used in a clinical setting to support patient-specific diagnosis and predictions of certain cardiovascular conditions.

In the following chapters, the application of the reported methodology will be shown in different scenarios. First, the numerical model is validated against published data. Then, the scalability of the Gaussian process approach will be shown on networks of increasing complexity. Finally, the sensitivity analysis through Gaussian process emulation will be applied to the problem of cerebral vasospasm.

Applications

6 Numerical model validation

Summary

In this chapter, the validation of the numerical model is presented. First, the numerical solver is compared to the analytical solution for an elastic straight tube (reported in Appendix B). In addition to the analytical solution, the numerical model validation is performed by comparing the 1D results with different 1D and 3D simulations published in the literature, and experimental measurements (in-vivo and in-vitro). Finally, the limitations of the models are analysed and further improvements are discussed.

The MUSCL numerical scheme described in Section 3.3.2 was implemented into the computational library **openBF**, an open-source blood flow solver developed as part of this PhD study (Melis, A, 2017). **openBF** was written in Julia, a high-level programming language designed for high-performance scientific computing (Bezanson et al., 2014), and it was released under Apache-2.0 free software license.

In this section, the validation of **openBF** code is presented. The validation strategy relied on data published in the literature. The numerical implementation of the MUSCL scheme (oBF-1D) was tested on: the analytical solution for a straight elastic tube (Brown et al., 2012; Wang et al., 2015); the 1D finite volume (FV-1D) and 3D fluid structure interaction numerical solution of the upper thoracic aorta, the common carotid artery, and the iliac bifurcation reported in (Boileau et al., 2015; Xiao et al., 2014); the in-vitro measurements on a 37-vessel network proposed by (Matthys et al., 2007); the FV-1D numerical solution of a 56-vessel network presented in (Blanco et al., 2014, 2015); and the 1D numerical solution of the circle of Willis compared with in-vivo measurements from (Alastruey et al., 2007).

6.1 Analytical solution

The numerical scheme was validated against the analytical solution (3.4) in the case of a straight elastic vessel, modelled using mechanical properties of a generic as-

cending aorta, coupled with a three-element windkessel model at the outlet (Table 6.1.1).

ℓ	R_0	$E \cdot h_0$	$\mathcal{R}_1$	$\mathcal{R}_2$	$\mathcal{C}_p$
(cm)	(cm)	(kPa·m)	(Pa·s·m^{-3})	(Pa·s·m^{-3})	(m^3·Pa^{-1})
4	1.47	660.724	1.31×10^{7}	2.22×10^{7}	1.61×10^{-8}

Table 6.1.1: Ascending aorta and windkessel model parameters from (Wang et al., 2015) and (Brown et al., 2012), respectively. The blood was modelled as an incompressible, Newtonian fluid with ρ =1056 kg·m^{-3} and μ =3.5×10^{-3}Pa·s. The vessels were discretised using 40 elements with $\Delta x = 1$ mm and the variable Δt was calculated with $C_{CFL} = 0.9$.

The flow inlet boundary condition was manually extracted from (Brown et al., 2012), and reported in Figure 6.1.1(a). The pressure (P) and volumetric flow rate (Q) waveforms resulting from both the analytical solution and the numerical simulation are reported from two locations, the inlet and the outlet (Figures 6.1.1(b-d)). The results are in agreement as the waveforms computed by the numerical scheme match those obtained analytically.

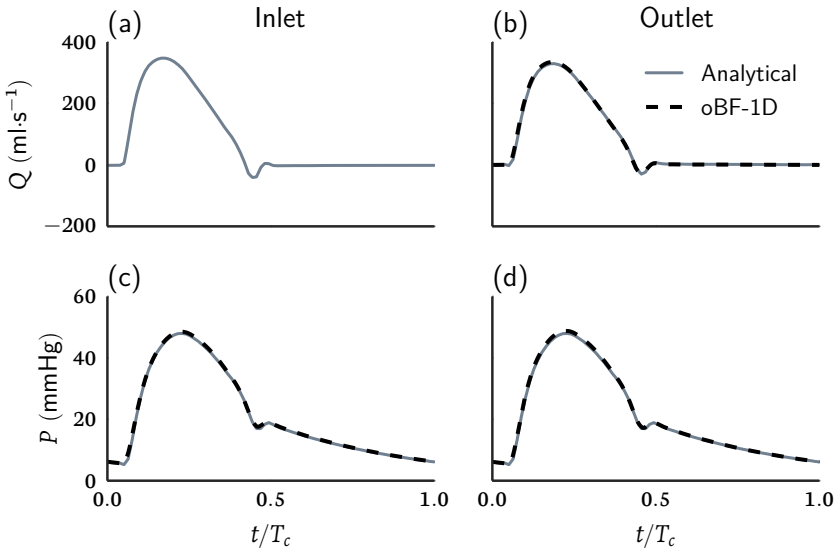

Figure 6.1.1: Analytical validation results. (a) The volumetric flow rate inlet boundary condition (Q_{in}). (b) Analytical (grey) and numerical (dashed) flow waveforms at the system outlet, i.e. at the 1D/0D coupling location. (c,d) Pressure waveforms at the inlet and outlet locations, respectively. Time was normalised with respect to the cardiac cycle period T_c.

6.2 Numerical benchmarks

In (Boileau et al., 2015), several numerical methods for 1D blood flow equations were tested on different vascular networks. These implementations were also compared with a 3D fluid-structure interaction simulation (Xiao et al., 2014). The finite-volume 1D scheme (FV-1D) used in (Boileau et al., 2015) was based on (Müller and Toro, 2013; Toro and Siviglia, 2013) and it is similar to the one implemented in this work. The 1D models are compared with 3D results and percentage errors are computed as in (Boileau et al., 2015)

$$\begin{aligned} \mathcal{E}_P^{\mathrm{RMS}} &= \sqrt{\frac{1}{N}\sum_{i=1}^{N}\left(\frac{p_i - P_i}{P_i}\right)^2}, & \mathcal{E}_P^{\mathrm{MAX}} &= \max_i \left|\frac{p_i - P_i}{P_i}\right|, \\ \mathcal{E}_P^{\mathrm{SYS}} &= \frac{\max p - \max P}{\max P}, & \mathcal{E}_P^{\mathrm{DIAS}} &= \frac{\min p - \min P}{\min P}, \end{aligned} \tag{6.1}$$

where p and P are the waveforms computed by the 1D and 3D models, respectively. Additionally,

$$\begin{aligned} \mathcal{E}_W^{\mathrm{RMS}} &= \sqrt{\frac{1}{N}\sum_{i=1}^{N}\left(\frac{w_i - W_i}{\max_i W_i}\right)^2}, & \mathcal{E}_W^{\mathrm{MAX}} &= \max_i \left|\frac{w_i - W_i}{\max_i W_i}\right|, \\ \mathcal{E}_W^{\mathrm{SYS}} &= \frac{\max w - \max W}{\max W}, & \mathcal{E}_W^{\mathrm{DIAS}} &= \frac{\min w - \min W}{\max W}, \end{aligned} \tag{6.2}$$

where w and W can be either Q, ΔP, or Δr quantities for the 1D and 3D models, respectively.

6.2.1 Single artery models

The first two benchmarks were evaluated on single straight vessels: the upper thoracic aorta (UTA) and the common carotid artery (CCA). These two vessels have different diameters, thus different radial velocity profile shape. Both vessels were coupled to a three-element windkessel model (Table 6.2.1).

For each numerical method (3D, FV-1D, and oBF-1D), the pressure P, volumetric flow-rate Q, and radius change Δr waveforms at the midpoint of the vessel were reported along with the pressure difference ΔP between outlet and inlet (UTA and CCA in Figures 6.2.1a and 6.2.1b, respectively).

	ℓ (cm)	R_0 (mm)	h_0 (mm)	E (kPa)	$\mathcal{R}_1$ (Pa·s·m^{-3})	$\mathcal{R}_2$ (Pa·s·m^{-3})	C_p (m^3·Pa^{-1})	R_d (mm)	γ_ν
UTA	24.14	9.87	0.82	400	1.17×10^{7}	1.12×10^{8}	1.0163×10^{-8}	1.19	9
CCA	12.60	2.65	0.24	700	2.48×10^{8}	1.87×10^{9}	1.75×10^{-10}	2.98	2

Table 6.2.1: Upper thoracic aorta (UTA) and common carotid artery (CCA) model parameters (Boileau et al., 2015). The diastolic lumen radius R_d was used as reference to compute Δr within the cardiac cycle. The radial velocity profile shape is set as either plug-flow like or parabolic for γ_ν =9 or γ_ν =2, respectively. Blood properties were taken as ρ =1060 kg·m^{-3} and μ =4×10^{-3}Pa·s.

The FV-1D and oBF-1D results are in agreement as the difference in errors w.r.t. the 3D solution is within 6% (Table 6.2.2).

		UTA		CCA	
		FV-1D	oBF-1D	FV-1D	oBF-1D
$\mathcal{E}^{\text{RMS}}$	P	1.14	1.83	0.28	0.37
	ΔP	7.14	7.94	4.21	5.01
	Q	2.17	2.96	0.29	0.60
	Δr	2.44	3.05	1.07	1.44
$\mathcal{E}^{\text{MAX}}$	P	3.18	6.01	0.66	0.80
	ΔP	29.13	35.55	15.6	19.62
	Q	7.07	11.25	1.07	1.49
	Δr	7.20	11.26	2.28	2.48
$\mathcal{E}^{\text{SYS}}$	P	-0.71	-0.38	-0.29	-0.26
	ΔP	-8.53	-10.77	-14.83	-16.97
	Q	-5.29	-5.03	-0.58	-0.53
	Δr	-2.86	-4.11	-1.68	-2.32
$\mathcal{E}^{\text{DIAS}}$	P	0.99	1.17	0.28	0.05
	ΔP	6.37	10.53	4.45	5.05
	Q	3.48	3.31	0.24	0.27
	Δr	2.05	1.18	0.12	1.49

Table 6.2.2: Single vessel simulation percentage relative errors w.r.t 3D solution. FV-1D values are reported from (Boileau et al., 2015).

The oBF-1D model also shows the main features of the 3D simulation but underestimates of 35% the maximum ΔP needed to drive the blood flow within the vessel. This is also evident at peak systole and diastole, when the inertial forces are predominant in the system and the absolute error is 10%. Here is where the system non-linearity comes into play and the oBF-1D assumptions result in the ΔP underestimation. The $\leq$ 11% discrepancy in the Δr plot is due to the small-displacement

assumption made in the derivation of the oBF-1D constitutive equation. In fact, these discrepancies are more evident (11% for maximum pressure) for the large aorta (Figure 6.2.1a.d) but not for the carotid (Figure 6.2.1b.d) which is less compliant ($\leq 2.5\%$ for maximum pressure).

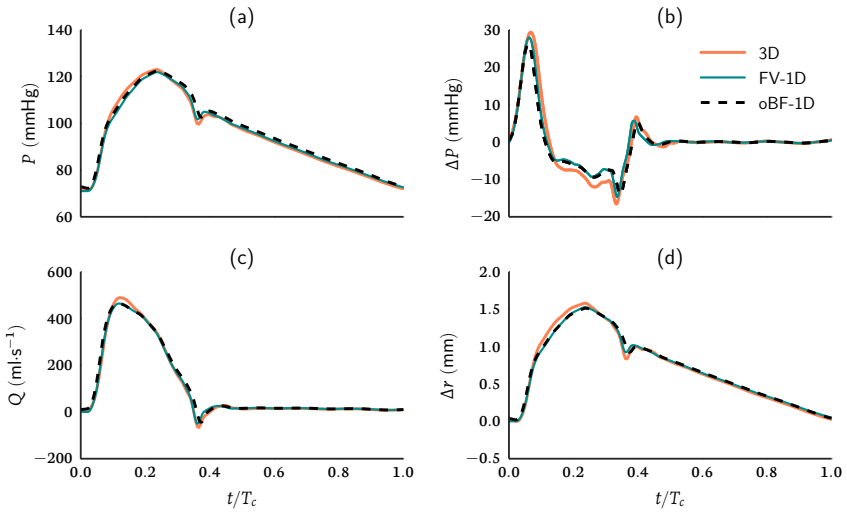

(a) Upper thoracic aorta

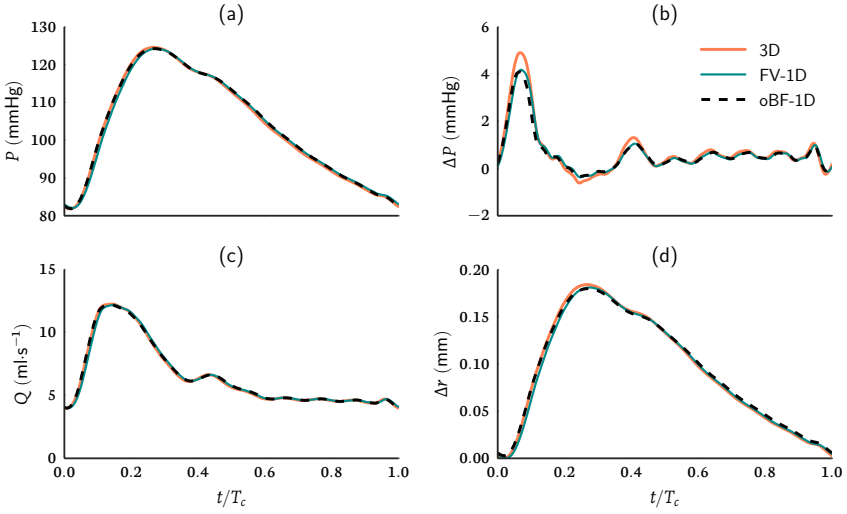

(b) Common carotid artery

Figure 6.2.1: Single vessel simulation results. (a, c, d) Pressure, flow, and radius change at the midpoint of the vessel. (b) Pressure difference between the vessel ends. FV-1D (Boileau et al., 2015), 3D (Xiao et al., 2014)

6.2.2 Iliac bifurcation

	ℓ (cm)	R_0 (mm)	h_0 (mm)	E (kPa)	$\mathcal{R}_1$ (Pa·s·m^{-3})	$\mathcal{R}_2$ (Pa·s·m^{-3})	$\mathcal{C}_p$ (m^3·Pa^{-1})	R_d (mm)	γ_v
Aorta	8.60	7.58	0.90	500	-	-	-	8.44	9
Iliac	8.50	5.49	0.68	700	6.81×10^{7}	3.10×10^{9}	3.67×10^{-10}	5.91	9

Table 6.2.3: Iliac bifurcation model parameters (Boileau et al., 2015). Blood properties were taken as ρ =1060 kg·m^{-3} and μ =4×10^{-3}Pa·s.

The bifurcation is a reflection location and it is a fundamental building block for complex networks; its validation was performed on a three-vessel symmetric (i.e. the two daughter vessels are equal) model of the iliac bifurcation (Table 6.2.3 and Figure 6.2.2). Both outlet vessels were coupled with a windkessel model and a flow waveform was imposed at the inlet.

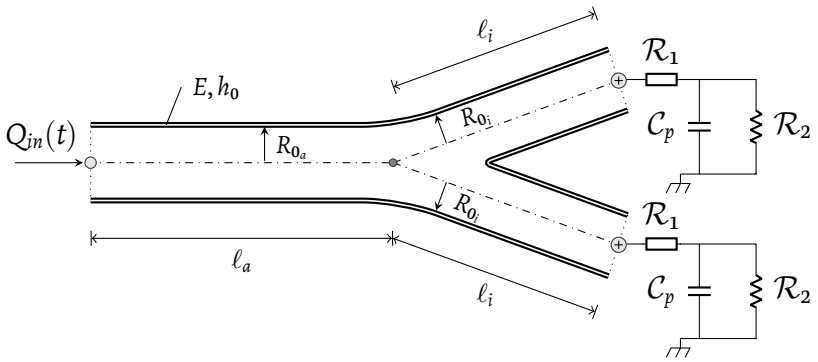

Figure 6.2.2: Iliac bifurcation scheme

Flow, pressure, and radius change at the aorta midpoint/outlet, and at the iliac artery midpoint were reported in Figure 6.2.3, numerical errors w.r.t. 3D simulations in Table 6.2.4. The 1D numerical models are capable of simulating the wave reflections caused by the bifurcation as the flow and pressure waveforms match the 3D ones. The error difference between FV-1D and oBF-1D solutions are within 1% for pressure and flow waveforms. In the case of Δr, the oBF-1D error w.r.t. 3D solution is $\leq$ 10% whereas that is $\leq$ 5% for the FV-1D solution. This is due the use of a visco-elastic constitutive equation in the latter against the linear-elastic formulation used in this study.

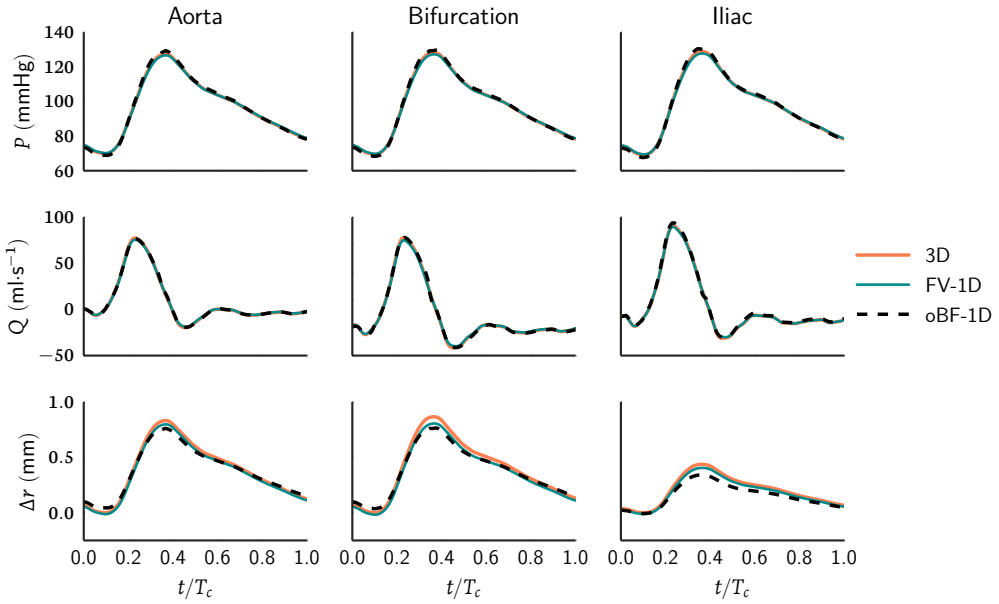

Figure 6.2.3: Iliac bifurcation simulation results FV-1D (Boileau et al., 2015), 3D (Xiao et al., 2014).

		Aorta		Bifurcation		Iliac	
		FV-1D	oBF-1D	FV-1D	oBF-1D	FV-1D	oBF-1D
$\mathcal{E}^{\text{RMS}}$	P	0.40	0.31	0.44	0.31	0.47	0.31
	Q	0.81	0.45	1.08	0.45	0.68	0.44
	Δr	2.49	4.30	4.08	4.20	4.31	4.40
$\mathcal{E}^{\text{MAX}}$	P	0.68	0.91	0.80	0.91	0.92	0.92
	Q	2.44	1.71	3.28	1.13	1.80	1.10
	Δr	4.01	10.20	6.95	10.30	7.48	11.0
$\mathcal{E}^{\text{SYS}}$	P	-0.55	0.04	-0.72	0.04	-0.85	0.04
	Q	-2.44	-0.11	-3.26	-0.11	-1.58	-0.09
	Δr	-4.00	-4.60	-6.88	-7.33	-7.31	-18.0
$\mathcal{E}^{\text{DIAS}}$	P	0.53	-0.9	0.57	-0.15	0.57	-0.83
	Q	1.16	-0.91	1.74	0.25	1.18	-0.80
	Δr	-1.35	-9.20	-1.89	-10.00	-2.35	-8.00

Table 6.2.4: Iliac bifurcation simulation percentage relative errors w.r.t 3D solution. FV-1D values are reported from (Boileau et al., 2015).

6.2.3 Systemic circulation

The blood flow in the large systemic arteries was simulated on *a detailed anatomical* (ADAN) model (Blanco et al., 2014, 2015). This is a 61-segment network of the 56 major arteries (Figure 6.2.4) whose mechanical properties and boundary conditions are based on physiological human data (Table 6.2.5 and 6.2.6).

A typical adult individual flow waveform was imposed at the aorta inlet and a three-element windkessel model was coupled to each of the 31 outlets. The Young's modulus was set as $E = 225$ kPa for each vessel (Boileau et al., 2015), and the wall thickness as

$$h_0(x) = R_0(x)\left(ae^{-bR_0(x)} + ce^{-dR_0(x)}\right), \tag{6.3}$$

where $a = 0.2802$, $b = 5.053\,\mathrm{cm}^{-1}$, $c = 0.1324$, and $d = 0.1114\,\mathrm{cm}^{-1}$ (Avolio, 1980). The lumen radius tapering was assumed to be linear between the proximal and the distal radii R_{0p} and R_{0d}, respectively. Blood properties were set as $\rho = 1060\,\mathrm{kg{\cdot}m}^{-3}$ and $\mu = 4 \times 10^{-3}$ Pa·s.

In the case of ADAN56 model, Boileau et al. (2015) reports also the numerical solution obtained with finite-elements (FE-1D), finite-difference (FD-1D), and simplified trapezium (STM-1D) methods. The simplified trapezium method is based on a full linearisation of the flow equations solved by means of the trapezium rule; the resulting scheme is second-order accurate in space. All the solution waveforms were reported for comparison with oBF-1D solution (Figures 6.2.5 and 6.2.6); errors were computed w.r.t. FV-1D solution (Table 6.2.7).

Qualitatively, all the numerical models solve correctly the wave propagation and reflection problem. Waveforms overlap along the cardiac cycle and there is no difference between FV-1D , FE-1D , and FD-1D as these were high-order non-linear solvers with a visco-elastic constitutive equation. The flow waveforms generated by the oBF-1D model underestimated the FV-1D ones at peak systole of 10%, when the inertial forces become predominant and the non-linear terms solution gain importance. The pressure waveforms computed by the oBF-1D are in close agreement with the higher-order models with errors $\leq 6\%$ overall. The FV-1D scheme is based on the Arbitrary DERivative (ADER) approach which includes higher-order terms resulting in greater accuracy than MUSCL in space and time. The waveforms shape is similar meaning that the reflection at bifurcation and outlet sites was represented adequately. Note that FV-1D scheme directly imposes the conservation of the total pressure at bifurcations, whereas the dynamic pressure was not considered in the oBF-1D implementation.

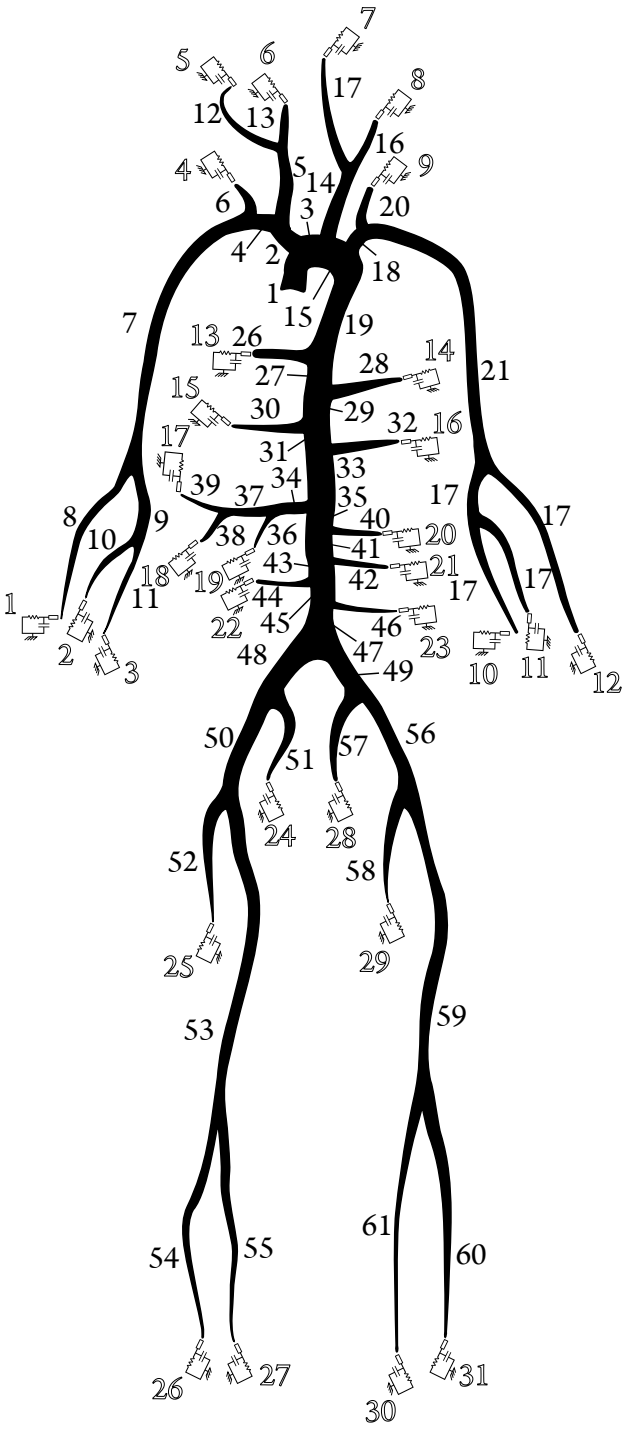

Figure 6.2.4: Diagram of the ADAN56 model, based on (Blanco et al., 2014, 2015). The inlet boundary condition is applied to the root vessel (1). The 31 outlet vessels are coupled to windkessel models. Each vessel is numbered for reference.

	Name	ℓ (cm)	R_{0p} (mm)	R_{0d} (mm)	$\mathcal{R}_1$ (10^9Pa·s·m^{-3})	$\mathcal{R}_2$ (Pa·s·m^{-3})	$\mathcal{C}$ (10^{-11}m^3·Pa^{-1})
1	AA I	7.44	15.95	12.95	-	-	-
2	BrA trunk	4.74	6.73	6.16	-	-	-
3	AA II	0.96	12.95	12.57	-	-	-
4	SA R I	1.57	4.90	4.18	-	-	-
5	Comm. CA R	8.12	4.48	3.33	-	-	-
6	Vertebral R	20.45	1.34	1.34	1.81	7.24	3.13
7a	SA R II	4.11	4.18	2.30	-	-	-
7b	Axillary R	12.00	2.30	2.08	-	-	-
7c	Brachial R	22.31	2.08	1.83	-	-	-
8	Radial R	30.09	1.38	1.38	1.15	4.62	4.91
9	Ulnar R I	2.98	1.41	1.41	-	-	-
10a	Comm. interosseous R	1.63	0.96	0.96	-	-	-
10b	Ulnar R II	23.93	1.41	1.41	1.17	4.70	4.82
11	Post. interosseous R	23.06	0.68	0.68	4.78	19.13	1.18
12	Ext. CA R	6.09	2.27	2.27	0.94	3.76	6.03
13	Int. CA R	13.21	2.77	2.77	0.58	2.30	9.83
14	Comm. CA L	12.13	4.48	3.33	-	-	-
15	AA III	0.70	12.57	12.28	-	-	-
16	Ext. CA L	6.09	2.27	2.27	0.94	3.77	6.01
17	Int. CA L	13.21	2.77	2.77	0.58	2.31	9.80
18	SA L I	4.94	4.90	3.48	-	-	-
19a	AA IV	4.31	12.28	10.55	-	-	-
19b	Vertebral L	20.42	1.34	1.34	1.92	7.70	2.94
20	SA L II	4.11	3.48	2.30	-	-	-
21a	Axillary L	12.00	2.30	2.08	-	-	-
21b	Brachial L	22.31	2.08	1.83	-	-	-
21c	Radial L	31.09	1.38	1.38	1.13	4.53	5.00
22	Ulnar L I	2.98	1.41	1.41	-	-	-
23	Comm. interosseous L	1.63	0.96	0.96	-	-	-
24a	Ulnar L II	23.93	1.41	1.41	1.20	4.79	4.73
24b	Post. interosseous L	23.06	0.68	0.68	4.80	19.19	1.18
25	Tor. aorta I	0.99	10.55	10.36	-	-	-
26	Post. intercostal R	19.69	1.40	1.40	24.91	99.65	0.23
27	Tor. aorta II	0.79	10.36	10.22	-	-	-
28	Post. intercostal L	17.80	1.40	1.40	25.56	102.23	0.22
29	Tor. aorta III	1.56	10.22	9.92	-	-	-
30	Post. intercostal R	20.16	1.55	1.55	23.24	92.97	0.24
31	Toracic aorta IV	0.53	9.92	9.82	-	-	-

Table 6.2.5: ADAN56 model parameters (part 1) (Boileau et al., 2015). Aortic arch (AA), brachiocephalic artery (BrA), subclavian artery (SA), carotid artery (CA).

	Name	ℓ (cm)	R_{0p} (mm)	R_{0d} (mm)	$\mathcal{R}_1$ (10^9Pa·s·m^{-3})	$\mathcal{R}_2$ (Pa·s·m^{-3})	$\mathcal{C}$ (10^{-11}m^3·Pa^{-1})
32	Post. intercostal L	18.52	1.55	1.55	23.44	93.77	0.24
33a	Toracic aorta V	12.16	9.82	7.54	-	-	-
33b	Toracic aorta VI	0.32	7.54	7.49	-	-	-
34	Celiac trunk	1.68	3.35	3.21	-	-	-
35	Abd. aorta I	1.40	7.49	7.32	-	-	-
36	Comm. hepatic	6.66	2.69	2.69	0.33	1.34	16.92
37	Splenic I	0.39	2.17	2.17	-	-	-
38	Gastric L	9.29	1.51	1.51	34.34	137.36	0.16
39	Splenic II	6.44	2.17	2.17	0.47	1.89	11.97
40	Sup. mesenteric	21.64	3.93	3.93	0.22	0.87	0.26
41	Abd. aorta II	0.43	7.32	7.26	-	-	-
42	Renal L	2.18	2.71	2.71	0.23	0.91	25.03
43	Abd. aorta III	1.20	7.26	7.11	-	-	-
44	Renal R	3.77	3.10	3.10	0.23	0.91	24.95
45	Abd. aorta IV	5.41	7.11	6.43	-	-	-
46	Inf. mesenteric	9.02	2.08	2.08	2.39	9.57	2.37
47	Abd. aorta V	4.22	6.43	5.90	-	-	-
48	Comm. iliac R	7.64	4.50	4.09	-	-	-
49	Comm. iliac L	7.40	4.50	4.09	-	-	-
50a	Ext. iliac R	10.22	3.38	3.19	-	-	-
50b	Int. iliac R	7.25	2.82	2.82	0.41	1.66	13.66
51	Femoral R I	3.16	3.19	3.14	-	-	-
52	PFA R	23.84	2.14	2.14	0.34	1.37	16.53
53a	Femoral R II	31.93	3.14	2.69	-	-	-
53b	Popliteal R I	13.20	2.69	2.37	-	-	-
54	Ant. tibial R	38.62	1.17	1.17	2.45	9.81	2.31
55a	Popliteal R II	0.88	2.37	2.35	-	-	-
55b	Tibiofibular trunk R	3.62	2.35	2.35	-	-	-
55c	Post. tibial R	38.29	1.23	1.23	2.12	8.46	2.68
56a	Ext. iliac L	10.22	3.38	3.19	-	-	-
56b	Int. iliac L	7.25	2.82	2.82	0.42	1.66	13.62
57	Femoral L I	3.16	3.19	3.14	-	-	-
58	PFA L	23.84	2.14	2.14	0.34	1.37	16.52
59a	Femoral L II	31.93	3.14	2.69	-	-	-
59b	Popliteal L I	13.20	2.69	2.37	-	-	-
60	Aant. tibial L	38.62	1.17	1.17	2.45	9.81	2.31
61a	Popliteal L II	0.88	2.37	2.35	-	-	-
61b	Tibiofibular trunk L	3.62	2.35	2.35	-	-	-
61c	Post. tibial L	38.29	1.23	1.23	2.12	8.47	2.68

Table 6.2.6: ADAN56 model parameters (part 2) (Boileau et al., 2015). Posterior femoral artery (PFA).

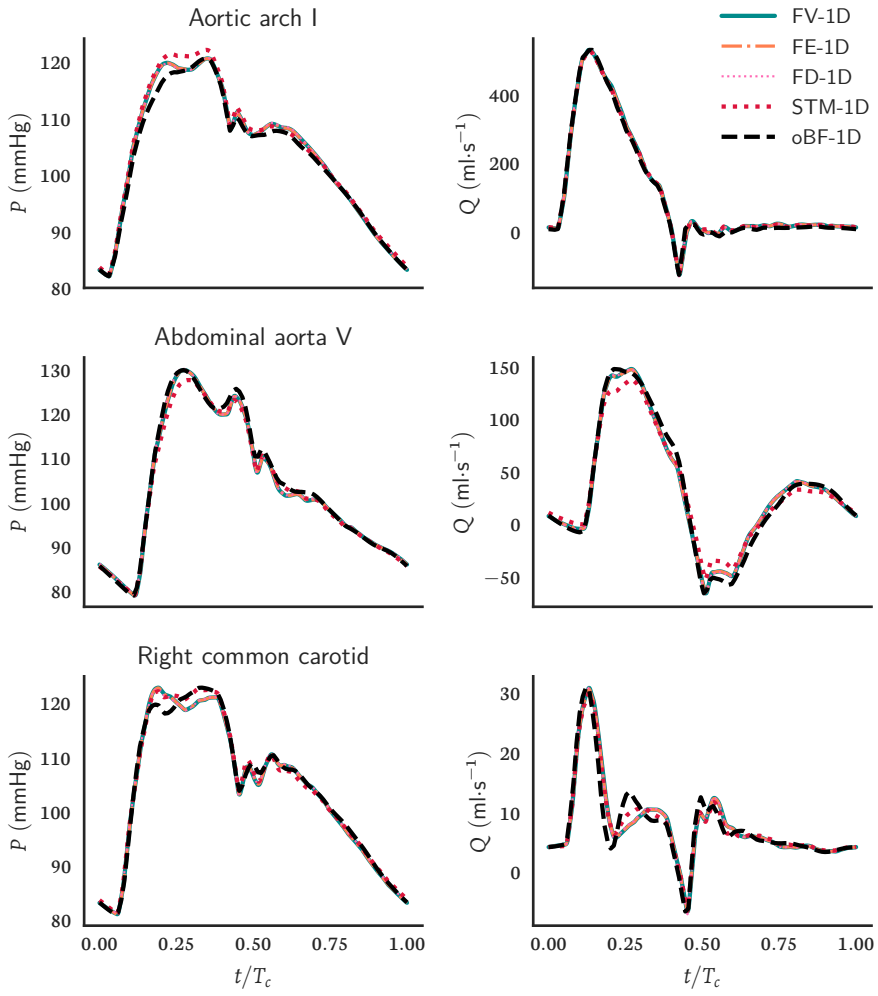

Figure 6.2.5: Aortic arch I (1), Abdominal aorta V (33a), Right common carotid (5). FV-1D, FE-1D, FD-1D, and STM-1D waveforms reported from (Boileau et al., 2015).

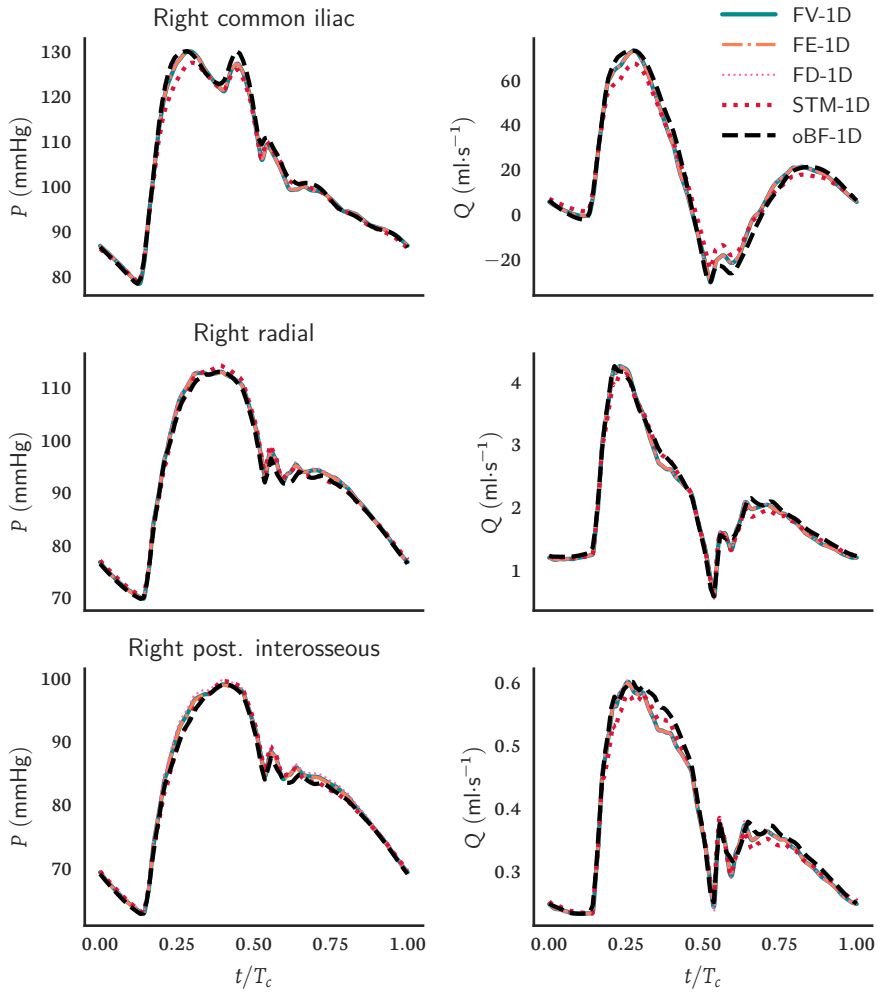

Figure 6.2.6: Right common iliac (48), Right radial (8), Right posterior interosseous (11). FV-1D, FE-1D, FD-1D, and STM-1D waveforms reported from (Boileau et al., 2015).

	P				Q			
	$\mathcal{E}^{\text{RMS}}$	$\mathcal{E}^{\text{MAX}}$	$\mathcal{E}^{\text{SYS}}$	$\mathcal{E}^{\text{DIAS}}$	$\mathcal{E}^{\text{RMS}}$	$\mathcal{E}^{\text{MAX}}$	$\mathcal{E}^{\text{SYS}}$	$\mathcal{E}^{\text{DIAS}}$
Aortic arch I	1.57	3.53	-0.66	3.53	2.25	11.31	0.03	-1.97
Abd. aorta V	2.22	5.65	-3.32	4.65	3.91	11.28	-8.82	8.05
Comm. carotid R	1.96	4.58	-2.01	3.70	7.60	23.04	2.54	-1.34
Comm. iliac R	2.30	5.88	-3.40	4.66	3.66	11.97	-10.25	7.08
Radial R	2.54	6.06	0.49	5.73	2.85	8.59	-4.75	0.85
Post. interosseous R	2.28	5.63	0.11	5.44	2.84	9.61	-5.62	3.26

Table 6.2.7: ADAN56 simulation percentage errors w.r.t. FV-1D solution from (Boileau et al., 2015)

6.3 Experimental measurements

6.3.1 In-vitro model

Flow and pressure measurements in an in-vitro model (Matthys et al., 2007) have been used for comparison with FV-1D and oBF-1D numerical results.

The model consists of 37 tapered vessels (Figure 6.3.1) representing the main arteries in the systemic circulation. For each vessel, the pulse wave velocity (c) measurements are given in (Matthys et al., 2007); these were used to calculate the Young's modulus of each vessel as

$$E = \frac{3}{2}\frac{\rho R_0}{\sqrt{\pi}h_0}c^2. \tag{6.4}$$

The outlets in FV-1D were coupled to a single-resistance lumped-parameter model; instead, in the case of oBF-1D model, the outlets were coupled with a three-element windkessel. The peripheral resistances were set as $\mathcal{R}_1 + \mathcal{R}_2 = \mathcal{R}$, where $\mathcal{R}$ is the peripheral resistance from (Matthys et al., 2007). The peripheral compliances were assumed to be the same for all the windkessels and equal to $\mathcal{C} = 1 \times 10^{-13}$ m^3·Pa^{-1}. Vessels parameters are reported in Table 6.3.1.

The calculated numerical waveforms (P and Q) and the in-vitro measurements at four locations in the network, are reported in Figure 6.3.2; the errors of oBF-1D and FV-1D w.r.t. the experimental measurements are reported in Table 6.3.2.

The pressure waveforms are close in shape and amplitude at all the four locations and all the errors are $\leq$ 15%. The largest errors are found in distal arteries (i.e. ulnar and splenic) for the maximum pressure value, that is 14.72% and 15.66%, respectively. The oBF-1D pressure absolute errors are similar to FV-1D ones as the maximum difference between the two solvers is 10% in the splenic artery. The flow waveforms computed by both FV-1D and oBF-1D models return errors as high as 60% for the maximum flow value. A visual inspection of the waveforms reveals

that even though the mean behaviour is the similar (RMS values $\leq$ 26%), the reflection pattern is different and large oscillations occur. In the in-vitro and FV-1D models, the distal vessels are coupled with a single resistance which causes unrealistic and non-physiological waveforms. The three-element windkessel used in the oBF-1D model effectively dampens these spurious oscillations.

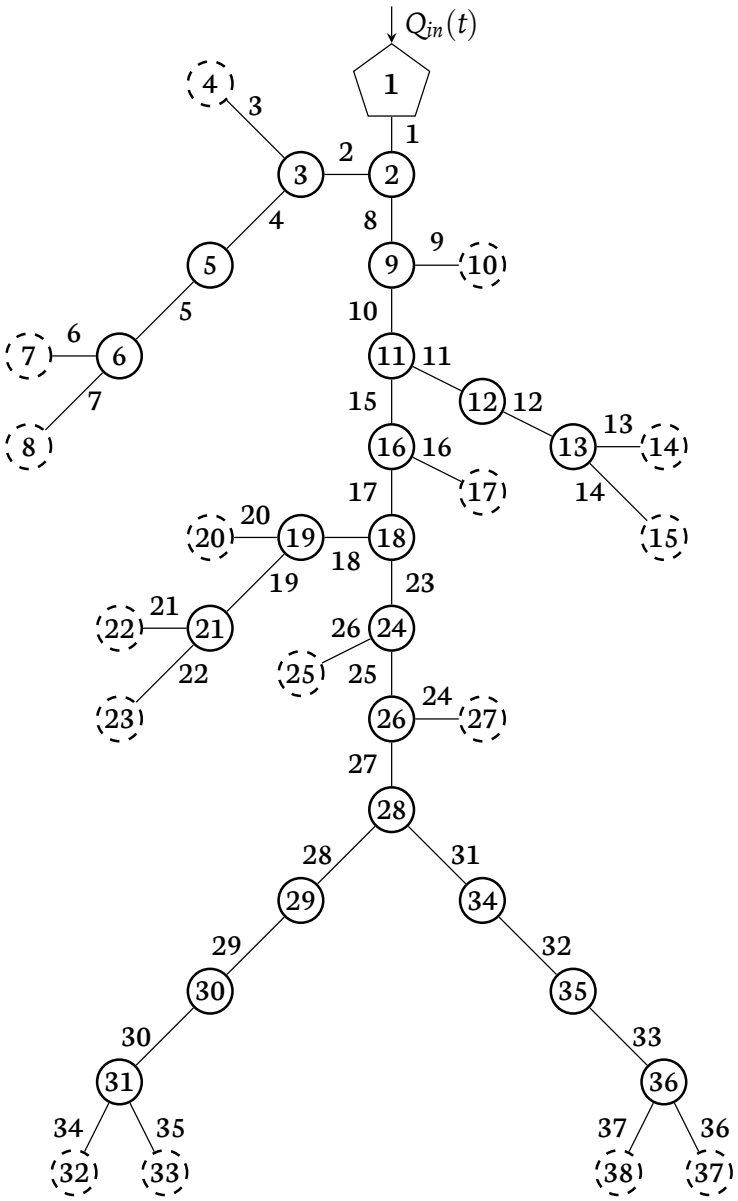

Figure 6.3.1: Inlet node (1), bifurcation nodes (circular), outlet nodes (dashed circles), and vessel IDs, based on (Matthys et al., 2007).

	Artery	ℓ (cm)	R_{0p} (cm)	R_{0d} (cm)	E (kPa)	$\mathcal{R}_1 + \mathcal{R}_2$ (10^9 Pa·s·m^{-3})
1	Ascending aorta	3.60	1.440	1.300	683.224	-
2	Brachiocephalic	2.80	1.100	0.729	689.627	-
3	Carotid R	14.5	0.537	0.386	701.344	2.67
4	Subclavian R I	21.8	0.436	0.334	685.437	-
5	Subclavian R II	16.5	0.334	0.278	672.370	-
6	Radial R	23.5	0.207	0.207	676.958	3.92
7	Ulnar R	17.7	0.210	0.210	689.695	3.24
8	Aortic arch I	2.10	1.300	1.250	676.746	-
9	Carotid L	17.8	0.558	0.373	706.203	3.11
10	Aortic arch II	2.90	1.250	1.180	671.553	-
11	Subclavian L I	22.7	0.442	0.339	698.554	-
12	Subclavian L II	17.5	0.339	0.284	698.549	-
13	Radial L	24.5	0.207	0.207	684.480	3.74
14	Ulnar L	19.1	0.207	0.207	694.061	3.77
15	Thoracic aorta I	5.60	1.108	1.100	683.145	-
16	Intercostals	19.5	0.412	0.322	684.853	2.59
17	Thoracic aorta II	7.20	1.100	0.926	675.178	-
18	Celiac I	3.80	0.397	0.397	678.030	-
19	Celiac II	1.30	0.431	0.431	680.213	-
20	Splenic	19.1	0.183	0.183	655.677	3.54
21	Gastric	19.8	0.192	0.192	702.496	4.24
22	Hepatic	18.6	0.331	0.289	679.062	3.75
23	Abdominal aorta I	6.20	0.926	0.801	675.509	-
24	Renal L	12.0	0.259	0.259	661.516	3.46
25	Abdominal aorta II	7.00	0.790	0.790	681.713	-
26	Renal R	11.8	0.255	0.255	684.061	3.45
27	Abdominal aorta III	10.4	0.780	0.588	687.436	-
28	Iliac R I	20.5	0.390	0.338	692.444	-
29	Iliac R II	21.6	0.338	0.231	714.263	-
30	Iliac R III	20.6	0.231	0.210	665.179	-
31	Iliac L I	20.1	0.402	0.334	688.672	-
32	Iliac L II	19.5	0.334	0.226	713.776	-
33	Iliac L III	20.7	0.226	0.212	688.122	-
34	Ant. tibial R	16.3	0.155	0.155	658.738	5.16
35	Post. tibial R	15.1	0.153	0.153	676.978	5.65
36	Post. tibial L	14.9	0.158	0.158	667.185	4.59
37	Ant. tibial L	12.6	0.155	0.155	676.820	3.16

Table 6.3.1: Vessel parameters for the 37-artery network. Based on (Boileau et al., 2015; Matthys et al., 2007)

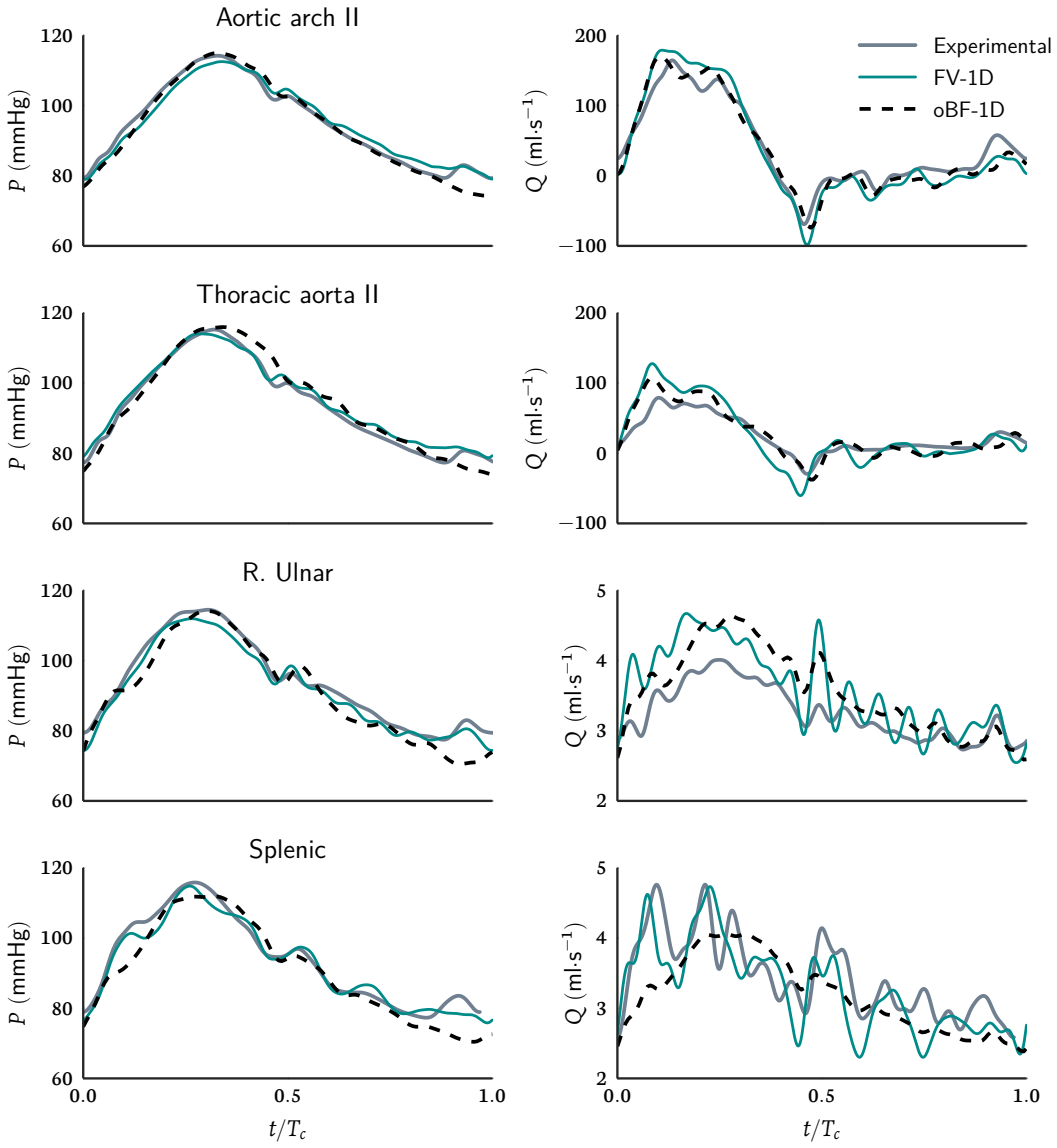

Figure 6.3.2: In-vitro experimental measurements from (Matthys et al., 2007).

		P				Q			
	Scheme	$\mathcal{E}^{\text{RMS}}$	$\mathcal{E}^{\text{MAX}}$	$\mathcal{E}^{\text{SYS}}$	$\mathcal{E}^{\text{DIAS}}$	$\mathcal{E}^{\text{RMS}}$	$\mathcal{E}^{\text{MAX}}$	$\mathcal{E}^{\text{SYS}}$	$\mathcal{E}^{\text{DIAS}}$
A. arch II	oBF-1D	2.97	9.53	0.65	-6.33	10.08	26.77	3.72	-4.03
	FV-1D	1.87	3.72	-1.46	-0.30	12.11	29.13	8.75	-17.93
Thoracic a. II	oBF-1D	3.06	7.87	0.61	-4.48	17.82	61.80	35.49	-10.84
	FV-1D	2.44	5.57	-1.03	1.81	25.43	65.69	61.59	-39.26
R. Ulnar	oBF-1D	5.14	14.72	-0.31	-8.99	10.18	19.97	15.57	-3.65
	FV-1D	2.49	6.32	-2.20	3.92	11.62	30.93	16.50	-4.60
Splenic	oBF-1D	5.51	15.66	-3.38	-8.93	10.59	31.30	-14.77	-4.14
	FV-1D	2.33	5.57	-0.97	-0.19	9.04	23.30	-1.47	-5.21

Table 6.3.2: In-vitro model simulation percentage relative errors w.r.t. measured waveforms for FV-1D and oBF-1D numerical schemes

6.3.2 Circle of Willis

In (Alastruey et al., 2007), results of a one-dimensional numerical model were compared to in-vivo measurements of the blood flow velocity in the subclavian, brachiocephalic, and carotid arteries. The arterial network consisted of 37 straight vessels including a full representation of the circle of Willis. This brain circulation network has been used to validate the oBF-1D model in the case of small arteries.

The solution of the circle of Willis required the introduction of anastomosis in the network. In order to ease the numerical procedure, a conventional positive flow direction was set for each vessel. This is the direction towards which the blood is mainly supposed to flow during the simulation. Each junction in the network was appointed as either a bifurcation or an anastomosis. A bifurcation has one vessel positively flowing inwards, whereas an anastomosis has two inward vessels (Figure 6.3.3). By declaring the type of conjunction, the numerical scheme directly employs the correct set of equations (either (3.95) or (3.98)) and numerical instabilities are avoided.

Vessel parameters and inflow function were taken from (Alastruey et al., 2007) and they are reported in Table 6.3.3. Blood properties were set as $\rho = 1050\ \text{kg}\cdot\text{m}^{-3}$ and $\mu = 4.5 \times 10^{-3}\ \text{Pa}\cdot\text{s}$. Outlets were coupled with three-element windkessel models whose peripheral resistance was reported as $\mathcal{R} = \mathcal{R}_1 + \mathcal{R}_2$ in (Alastruey et al., 2007). The winkdkessel inlet impedance $\mathcal{R}$ was adaptively set at each time step to match the outlet vessel impedance, thus reducing spurious numerical oscillations due to the coupling.

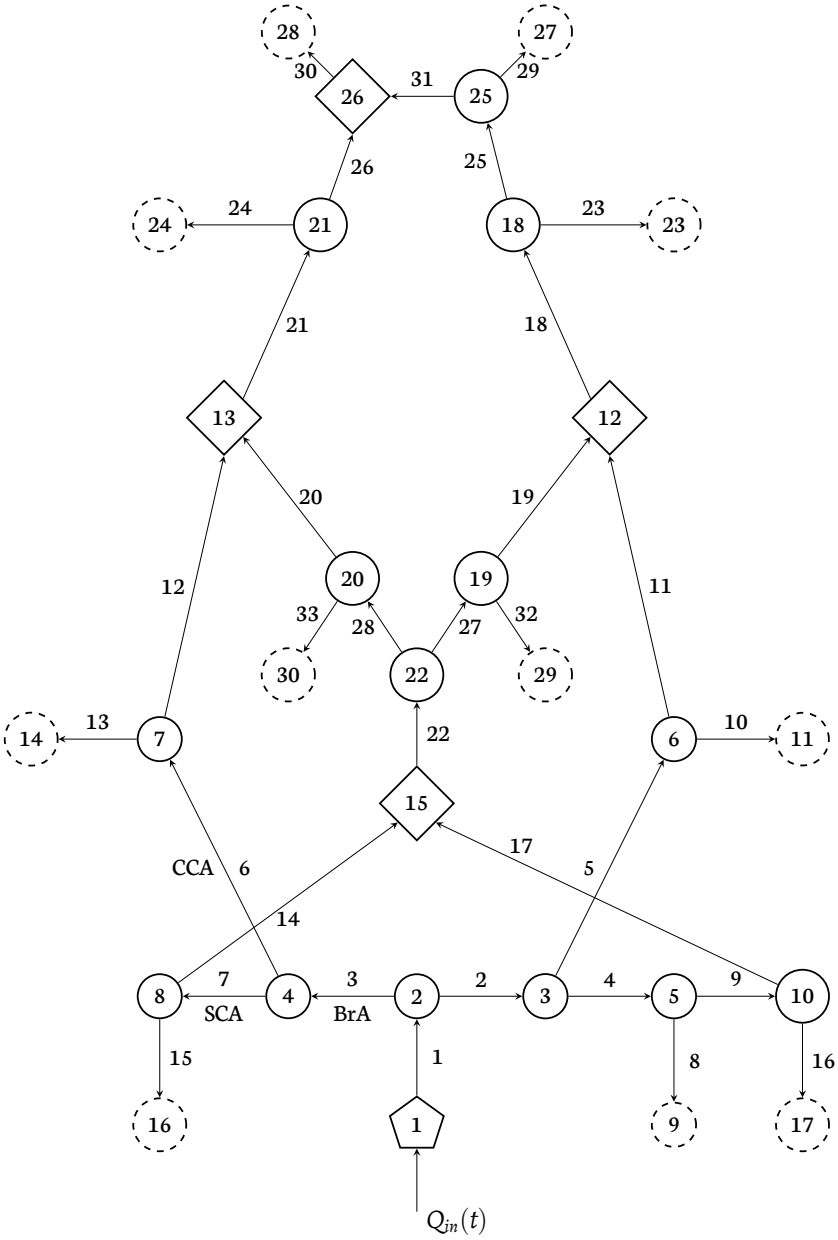

Figure 6.3.3: Circle of Willis network diagram based on (Alastruey et al., 2007). Inlet node (pentagon, 1), bifurcation nodes (circular), anastomosis nodes (squared), outlet nodes (dashed circle). The positive flow direction is indicated by the arrows.

	Artery	ℓ (cm)	R_0 (cm)	E (kPa)	$\mathcal{R}_1 + \mathcal{R}_2$ (10^9 Pa·s·m^{-3})	$\mathcal{C}_p$ (10^{-10} m^3·Pa^{-1})
1	Ascending aorta	4.00	1.200	400	–	–
2	Aortic arch I	2.00	1.120	400	–	–
3	Brachiocephalic	3.40	0.620	400	–	–
4	Aortic arch II	3.90	1.070	400	–	–
5	Common carotid L	20.8	0.250	400	–	–
6	Common carotid R	17.7	0.250	400	–	–
7	Subclavian R	3.40	0.423	400	–	–
8	Thoracic aorta	15.6	0.999	400	0.180	38.7
9	Subclavian L	3.40	0.423	400	–	–
10	Ext. carotid L	17.7	0.150	800	5.430	1.27
11	Int. carotid L I	17.7	0.200	800	–	–
12	Int. carotid R I	17.7	0.200	800	–	–
13	Ext. carotid R	17.7	0.150	800	5.430	1.27
14	Vertebral R	14.8	0.136	800	–	–
15	Brachial R	42.2	0.403	400	2.680	2.58
16	Brachial L	42.2	0.403	400	2.680	2.58
17	Vertebral L	14.8	0.136	800	–	–
18	Int. carotid L II	0.50	0.200	1600	–	–
19	PCoA L	1.50	0.073	1600	–	–
20	PCoA R	1.50	0.073	1600	–	–
21	Int. carotid R II	0.50	0.200	1600	–	–
22	Basilar	2.90	0.162	1600	–	–
23	MCA L	11.9	0.143	1600	5.970	1.16
24	MCA R	11.9	0.143	1600	5.970	1.16
25	ACA L I	1.20	0.117	1600	–	–
26	ACA R I	1.20	0.117	1600	–	–
27	PCA L I	0.50	0.107	1600	–	–
28	PCA R I	0.50	0.107	1600	–	–
29	ACA L II	10.3	0.120	1600	8.480	0.82
30	ACA R II	10.3	0.120	1600	8.480	0.82
31	ACoA	0.30	0.074	1600	–	–
32	PCA L II	8.60	0.105	1600	11.08	0.62
33	PCA R II	8.60	0.105	1600	11.08	0.62

Table 6.3.3: Posterior communicating artery (PCoA), middle cerebral artery (MCA), anterior cerebral artery (ACA), posterior cerebral artery (PCA), anterior communicating artery (ACoA) (Alastruey et al., 2007).

The velocity waveforms computed by the 1D models (oBF-1D and FV-1D) at the three measurement locations are reported in Figure 6.3.4. The results are in good agreement as the velocity waveforms overlap at each of the three locations. In (Alastruey et al., 2007), the comparison with Doppler measurements was only a quali-

tative one. This was due to the lack of patient-specific information (network mechanical properties and boundary conditions) to inform the 1D model. In a healthy subject, the flow in the CCA is always positive during the cardiac cycle, so that the brain is regularly supplied with blood. Instead, in the BrA and SCA there is a period of back-flow at the beginning of the diastolic phase. These two observations, assisted by measurements published in (Oates, 2008), were made also on the waveform computed by the FV-1D model.

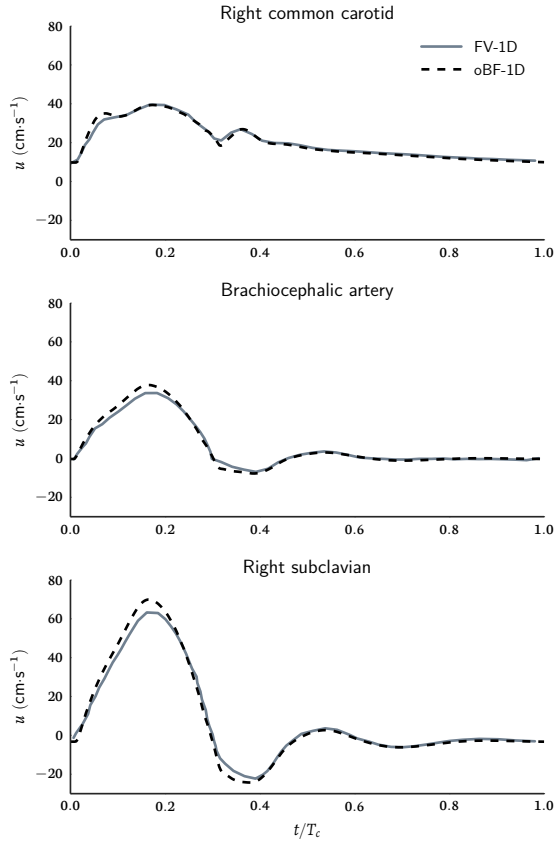

Figure 6.3.4: Velocity waveforms comparison with data from (Alastruey et al., 2007) with permission.

6.4 Discussion and conclusions

The 1D blood flow model was presented highlighting its hyperbolic nature and the need for specific numerical solution schemes. This led to the introduction of the method of characteristics and its application in the finite volume numerical method.

The 1D equations were further linearised and integrated, resulting in the three-element windkessel model used as an outlet boundary condition for the vascular network.

The proposed numerical solution was validated against an analytical solution and against studies published in literature providing numerical and experimental data. The 1D models is capable of representing the physics of pulse wave transmission and reflection within complex arterial networks. Its accuracy, measured on state-of-the-art benchmarks, was close to other finite volume solvers with errors $\leq 10\%$ is the case of the complete ADAN56 model.

6.4.1 Limitations and Future Improvements

The solver was designed to be complex enough to represent the main characteristics of the blood pulse wave propagation. In this view, some features, present in other implementations, were not included. These are herein summarised and will be added to a future version of the solver aimed at simulating also the venous circulation.

- The vascular network inlet boundary condition was set by means of a user provided time-function (volumetric flow rate or pressure). In the case of the complete systemic circulation, the flow time-function resembles the waveform that can be measured at the left ventricle outlet. The boundary value is assigned at each time step and it is not influenced by the presence of the vascular network. As in the case of the outlets, the network impedance can differ from the impedance of the coupled boundary condition, resulting in non-physiological reflections. A deterministic model of the heart mechanics would prevent these oscillations by adapting the cardiac output with respect to the network impedance. A well-known left ventricle model is based on the time varying elastance function (Suga and Sagawa, 1974), but there are also lumped-parameter models taking into account the four chambers and the presence of valves (Sun et al., 1997).

- The radial velocity profile was assumed either parabolic or flat for narrow and large arteries, respectively. The velocity profile assumption was used in the dimensionality reduction process and it simplified the description of viscous losses. However, a better and more realistic representation of the hæmodynamics can be achieved by including a direct calculation of the velocity profile from Womersley's theory (Čanic et al., 2006; Womersley, 1955). The velocity profile calculation depends on the knowledge of the pressure gradient along the vessel, and this can be included by iterating until convergence within a single time-step.

- The mechanical behaviour of the arterial walls was assumed to be linearly elastic, resulting in the adoption of the transmural pressure

$$P(x,t) - P_{ext} = \sqrt{\frac{\pi}{A_0(x)}} \frac{E(x)h_0(x)}{1-\nu^2} \left(\sqrt{\frac{A(x,t)}{A_0(x)}} - 1 \right). \tag{6.5}$$

However, wave propagation is strongly influenced by arterial wall visco-elasticity and its mechanical representation. Therefore, this purely-elastic wall mechanics can be enhanced by a more realistic visco-elastic non-linear constitutive representation. Conversely, veins collapse under physiological conditions and require a different constitutive law (Figure 6.4.1). The venous transmural pressure is commonly described by

$$P(x,t) - P_{ext} = \frac{E(x)}{12(1-\nu^2)} \left(\frac{h_0(x)}{R_0(x)} \right)^3 \left[\left(\frac{A(x,t)}{A_0(x)} \right)^m - \left(\frac{A(x,t)}{A_0(x)} \right)^n \right], \tag{6.6}$$

where $m = 10$ and $n = -1.5$ are typical values for vein-like collapsible tubes (Müller and Toro, 2014; Shapiro, 1977).

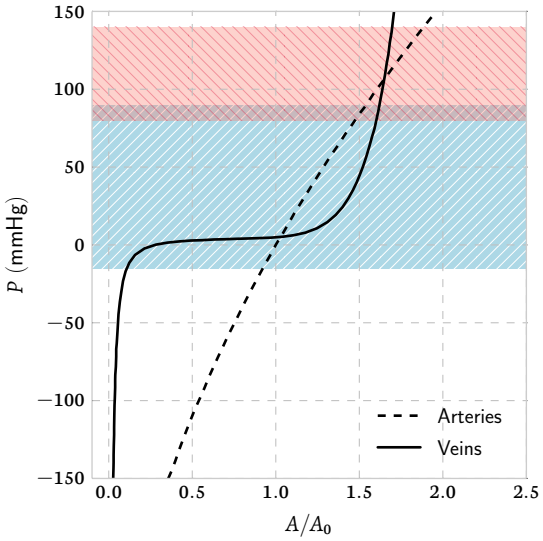

Figure 6.4.1: Pressure vs normalised cross-sectional area for the two tube laws (6.5, 6.6). The veins collapse (i.e. $A/A_0 < 1$) occur within their physiological range (blue area). The arteries behave linearly in physiological condition (red area). Adapted from (Müller and Toro, 2014) with permission.

- In the view of implementing the venous circulation, the tube law (6.6) should be adopted. This will in turn change the momentum equation requiring the derivation of new flux (3.38) and source (3.39) terms. Eventually, the characteristic solution will change with the addition of three characteristic curves.

- The body forces (such as the gravity) are neglected in the momentum equation. This is not a limiting assumption in the case of a vascular network in the supine position. However, for a standing subject, the gravitational effect increases and cannot be ignored. This is accentuated in the venous system where the pulse pressure does not drive the blood flow as in the arterial part.

- The vessels were represented as straight and narrow circular elastic tubes. However, actual arteries are often convoluted and asymmetric; for example, the ascending aorta presents a tight bend right after the left atrium. The effect of the bend is to cause a pressure loss in the system. A way to model the pressure loss is to subdivide the bend in small straight vessels and to introduce a loss function mimicking the conjunction of vessels at an angle $\beta \neq 0$ (Figure 6.4.2a).

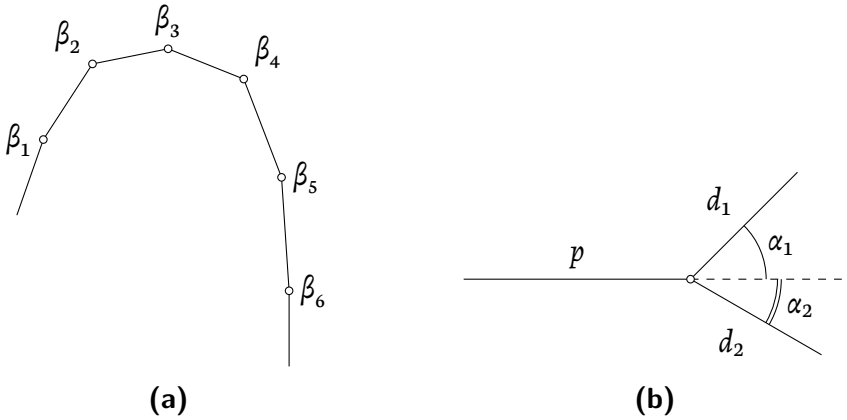

Figure 6.4.2: Pressure loss functions can be used to mimic realistic bends (a) and bifurcations (b)

- Similarly, the proposed bifurcations are ideal as the bifurcation angle is not taken into consideration (Figure 6.4.2b). More accurate interface conditions for bifurcating vessels are obtained by the introduction of a loss function taking into account the bifurcation angle. The issue arising by introducing the loss functions consists in the selection of the loss coefficient that should be linked to experimental measurements or to 3D fluid structure interaction simulations.

Part of this chapter has been included in:
Melis A, Clayton RH, Marzo A. A more efficient approach to perform sensitivity analyses in 0D /1D cardiovascular models. Computational & Mathematical Biomedical Engineering Proceedings. 2015 Jul:806-9.

7 Wave propagation through a vascular bifurcation

Summary

In this chapter, the proposed sensitivity analysis technique is applied to a cerebral bifurcation model. Few runs of the vascular model were used to train a GP emulator that, once trained, mimicked the vascular model behaviour across its parameter space. The GP explored the input space with significantly shorter running times. Predicted values were used to compute Sobol sensitivity indices. The introduction of the Gaussian process emulator allowed to perform the sensitivity analysis in approximately 0.4% of the total time required for the Monte Carlo analysis. The emulator error on predicting Monte Carlo simulations outcomes was less than 1%. The sensitivity indices computed with the two techniques were similar and differed by less than 3%.

7.1 Introduction

The Monte Carlo (MC) method is a simple approach to compute sensitivity indices, as it consists in running the mechanistic model several thousand times. For each simulator run a different set of inputs are randomly drawn from a distribution of points. This distribution covers the entire input space. Ideally, the distribution contains infinite points, hence by obtaining a result for each point, the model global behaviour would be known. In practice, an infinite distribution cannot be achieved, and MC sampling requires a number of runs of the order of $\mathcal{O}(d \times 10^6)$, where d is the number of input parameters. Saltelli et al. (Saltelli, 2002; Saltelli et al., 2010) introduced a MC-based technique to calculate sensitivity indices which requires a number of runs of order $\mathcal{O}(d \times 10^3)$, but this can still be an impractical number of runs for most applications.

When considering a large number of parameters, the computational time needed for the $d \times 10^3$ simulations becomes prohibitively high. This analysis can be made more efficient by introducing an approximation of the mechanistic model, i.e. an emulator.

The aim of this chapter is to show that the sensitivity analysis based on GP emulator is more efficient in terms of computational time than that based on Monte Carlo sampling. A patient-generic cerebral arterial bifurcation model was chosen to show the benefits of using of GP emulators for cardiovascular applications. Results were validated on the outcomes of the MC analysis.

7.2 Methodology

The vascular model was based on the reduced 1D form of the general continuity and Navier-Stokes equations for incompressible flows within narrow straight elastic tubes (Chapter 3). The vascular network taken into consideration consisted of a simplified bifurcation model (Figure 7.2.1). An inlet boundary condition was applied to the inlet of the root vessel in terms of a flow time-function. Outlet boundaries of peripheral bifurcating vessels were coupled to three-element windkessel models (Fernández et al., 2005); at capillary level, the last boundary condition was assigned by assuming the arterial-venous interface pressure equal to zero.

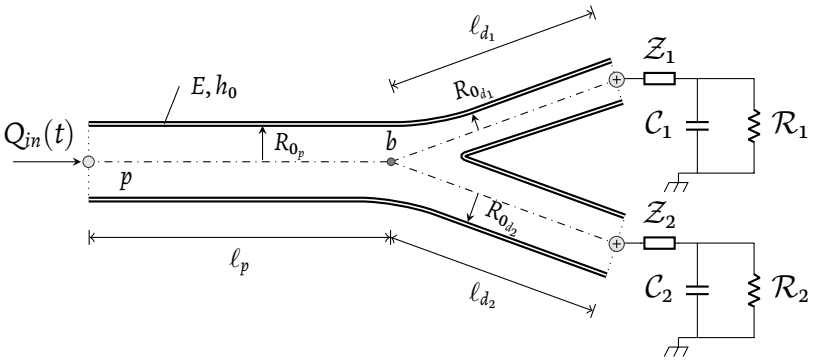

Figure 7.2.1: Bifurcation model scheme. The parent vessel p was connected to two daughter vessels, d_1 and d_2, at the bifurcation node b. Each vessel had its own mechanical properties: length ℓ, unstressed lumen radius R_0, unstressed thickness h_0, and wall Young's modulus E. The two windkessel models had independent values for each component: inlet impedance $\mathcal{Z}$, peripheral resistance $\mathcal{R}$, and peripheral compliance $\mathcal{C}$. Inlet flow boundary condition was applied at the root node as $Q_{in}(t)$.

Geometrical values, material properties, and inlet flow time function were based on data available for the middle cerebral artery bifurcation and each model parameter was varied within the reported physiological ranges (Reymond et al., 2009). The bifurcation mechanics was defined by 17 inputs (Table 7.2.1). Daughter vessel radii were set to satisfy Murray's law ($R_{0_p}^3 = R_{0_{d_1}}^3 + R_{0_{d_2}}^3$) and defined by the pa-

rameter $\varphi = {}^{R_{0_{d_1}}}/_{R_{0_p}}$. In order to avoid wave reflections induced by discontinuities caused by time-dependent changes in diameters at the bifurcation outlets, windkessel inlet impedances $\mathcal{Z}$ were calculated at each time step to match daughter vessel outlet impedance.

Analysis of the results was conducted by extracting 15 outputs (Table 7.2.1). The pressure waveforms were computed at each node of the system, and minimum and maximum values at the middle point of each vessel and at bifurcation node b were recorded, i.e. min and max $P_{p,d_1,d_2,b}$, respectively. Volumetric flow rate values were calculated and reported as normalised values with respect to flow through the parent vessel, i.e. ${}^{\bar{Q}_{d_i}}/_{\bar{Q}_p}$. Power losses between system inlet and each outlet, $PL_{p-1,2}$, were computed as the difference of total pressure times the local flow rate at the two locations. The pulse wave velocity within the three vessels was recorded as c_{p,d_1,d_2}. Outputs from 9 to 15 were time-averaged across the cardiac cycle.

ID_i	Name	Unit	Range
1	R_{0_p}	10^{-3} m	$[1.75, 3.25]$
2	φ	-	$[0.4, 0.796]$
3	E_p	10^3 Pa	$[184.701, 343.032]$
4	E_{d_1}	10^3 Pa	$[124.367, 230.967]$
5	E_{d_2}	10^3 Pa	$[124.367, 230.967]$
6	$\mathcal{R}_1$	10^9 Pa·s·m^{-3}	$[7.35, 13.65]$
7	$\mathcal{R}_2$	10^9 Pa·s·m^{-3}	$[7.35, 13.65]$
8	$\mathcal{C}_1$	10^{-14} m^3·Pa^{-1}	$[0.78, 1.38]$
9	$\mathcal{C}_2$	10^{-14} m^3·Pa^{-1}	$[0.78, 1.38]$
10	ρ	kg·m^{-3}	$[1000.0, 1100.0]$
11	μ	10^{-3} Pa·s	$[2.0, 7.0]$
12	ℓ_p	10^{-3} m	$[5.6, 10.4]$
13	ℓ_{d_1}	10^{-3} m	$[49.7, 92.3]$
14	ℓ_{d_2}	10^{-3} m	$[49.0, 91.0]$
15	h_p	10^{-3} m	$[0.7, 1.3]$
16	h_{d_1}	10^{-3} m	$[0.7, 1.3]$
17	h_{d_2}	10^{-3} m	$[0.7, 1.3]$

ID_o	Name	Unit
1	$\min(P_p)$	Pa
2	$\min(P_b)$	Pa
3	$\min(P_{d_1})$	Pa
4	$\min(P_{d_2})$	Pa
5	$\max(P_p)$	Pa
6	$\max(P_b)$	Pa
7	$\max(P_{d_1})$	Pa
8	$\max(P_{d_2})$	Pa
9	${}^{\bar{Q}_{d_1}}/_{\bar{Q}_p}$	-
10	${}^{\bar{Q}_{d_2}}/_{\bar{Q}_p}$	-
11	PL_{p-1}	W
12	PL_{p-2}	W
13	c_p	m·s^{-1}
14	c_{d_1}	m·s^{-1}
15	c_{d_2}	m·s^{-1}

Table 7.2.1: Input names and IDs, units, and ranges (left). Output names and IDs and units (right).

The GP model was implemented by using the GPy library (GPy, 2012). In order to avoid numerical problems due to bad conditioning of the covariance matrix, training inputs and training outputs were normalised dimension-wise, i.e. each dimension in the input space was separately normalised. The kernel function to compute the covariance matrix was obtained as the sum of a squared exponential kernel and a Matérn ${}^5/_2$ kernel. Hyperparameters optimisation was conducted by minimising the log-likelihood through the conjugate gradient descent method.

The sensitivity analysis was performed following a three steps strategy:

1. The mechanistic model was run with a small set of input values spanning

evenly the entire parameter space. Simulation inputs and outputs constituted the dataset $\mathcal{T}$ on which the GP emulators were trained. $\mathcal{T}$ was designed through orthogonal Latin hypercube sampling method to ensure an even coverage of the input space. In order to avoid an ill-conditioned covariance matrix, inputs and outputs were normalised.

2. The trained GP was then used to predict outcomes for a bigger set of inputs with size of order $\mathcal{O}(d \times 10^3)$.

3. Sobol's sensitivity indices were computed by means of ANOVA decomposition. Inputs were ranked accordingly to first-order indices. The largest first-order indices indicated those inputs which mainly affect the outcome. Any differences between first-order and total sensitivity indices indicated that the outcome variance could be ascribed to covariance of more than one input.

7.3 Gaussian process emulator verification

In order to assess the GP prediction error, a MC analysis was performed on the vascular model. This consisted in running 17000 simulations on a fine grid covering the entire 17-dimension input space. The 17000 inputs and the 17000×15 outputs constituted the GP dataset. A portion of the dataset was randomly sampled and saved for diagnostic purpose. The GP model was trained on the remaining part.

The training sample was varied in size to assess the relation between the prediction error and the sample size. Three diagnostics were used to verify GP model predictions Bastos and O'Hagan (2009):

1. Normalised GP model predictions were compared with normalised vascular model outputs (Figure 7.3.1a). Points lying on the dashed line of equality indicate a good agreement between emulator and simulator.

2. The differences between simulator outputs and emulator mean predictions were quantified by means of the standardised prediction error. The emulator is claimed to be able to represent properly the simulator when its error distribution is normally distributed (Figure 7.3.1b). The normal distribution having mean and standard deviation computed from the error distribution is plotted over the actual error distribution. A visual inspection of the error distribution confirms the similarity between the two distributions.

3. The mean average prediction error (MAPE) was computed between emulator predictions and simulator outputs for each output of interest

(Figure 7.3.1c) for a different input sample size. This index scored values less than 1% for all outputs for a sample size greater than 70 points.

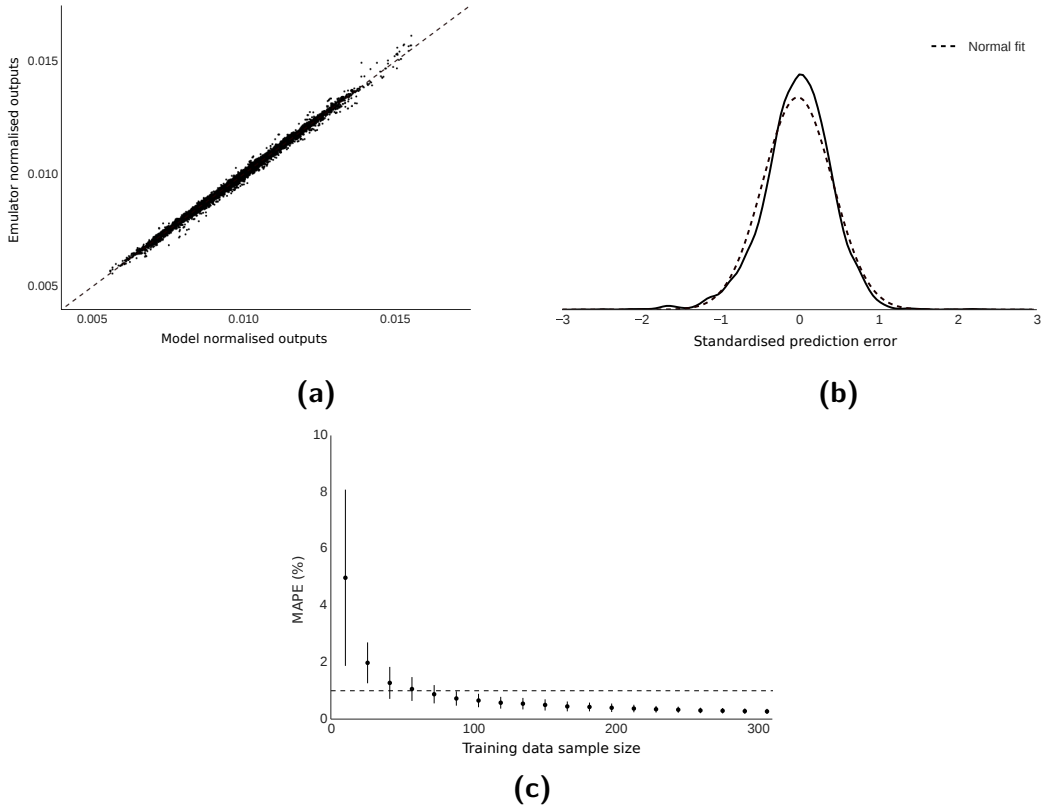

Figure 7.3.1: Gaussian process validation diagnostics. (a) Graphical comparison between emulator and simulator. (b) Prediction error distribution. (c) A MAPE lower than 1% was achieved for a sample size of about 70 points.

7.4 Results and discussion

The trained GP emulator was used to predict results for all the 17000 input points needed for the sensitivity analysis. These input points were chosen to explore thoroughly the input hyperspace. The computational running times of both the numerical vascular model and the GP emulator are reported in Table 7.4.1. The predictions made by the numerical model on the $N = 70$ training set took about 1.42 hours of computational time on a standard Linux workstation. Whereas it took about 15.3 days of computational time to run all the 17000 simulations in the MC analysis. The GP computational time for both training and prediction phases took

in total 15.73 seconds. Thus, by coupling the numerical model with the GP regression model, the bulk of the computational time was taken by numerical simulations on the $N = 70$ dataset used for training. Predictions for $N = 17000$ dataset were made in a relatively short time by the GP emulator. By using the GP emulator, the production of the sensitivity analysis dataset took about 0.4% of the MC computational time.

	$N = 70$	$N = 17000$
MC	1.42 hours	15 days 3 hours
GP	1.42 hours	

Table 7.4.1: Elapsed computational time comparison between numerical vascular model and GP emulator for training ($N = 70$) and MC analysis ($N = 17000$) set of input points. The GP running time includes both training and prediction phases.

The ensemble of input points and predicted outputs was used to compute Sobol's sensitivity indices. The first order and total effect indices were converted to luminance values and plotted in heat maps (see figures 7.4.1a and 7.4.1b, respectively). The second order indices were plotted in lower triangular matrices whose x- and y-axes range all model inputs (Figure 7.4.2).

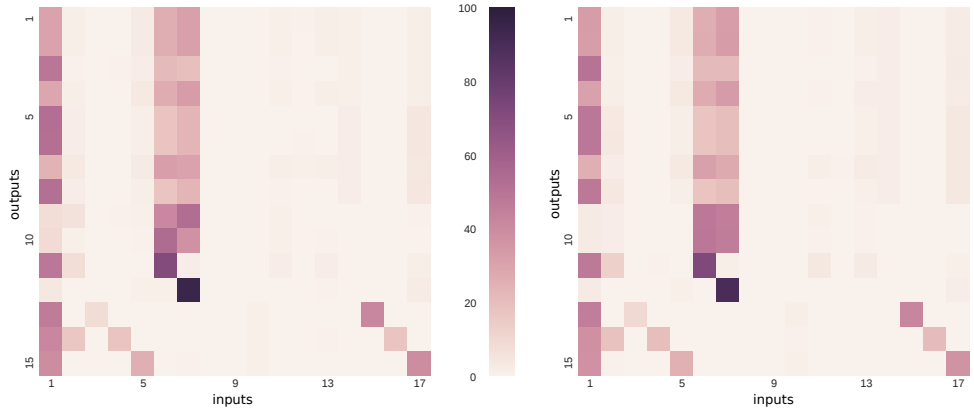

#	1	2	3	4	5	6	7	8	9	10	11	12	13	14	15	16	17
input	R_{0_p}	φ	E_p	E_{d_1}	E_{d_2}	$\mathcal{R}_1$	$\mathcal{R}_2$	$\mathcal{C}_1$	$\mathcal{C}_2$	ρ	μ	ℓ_p	ℓ_{d_1}	ℓ_{d_2}	h_p	h_{d_1}	h_{d_2}
output	$\min(P_p,$	$P_b,$	$P_{d_1},$	$P_{d_2})$	$\max(P_p,$	$P_b,$	$P_{d_1},$	$P_{d_2})$	$\bar{Q}_{d_1}/\bar{Q}_p$	$\bar{Q}_{d_2}/\bar{Q}_p$	PL_{p-1}	PL_{p-2}	c_p	c_{d_1}	c_{d_2}		

Figure 7.4.1: First-order (a) and total effect (b) sensitivity indices. The higher the sensitivity index the darker the square. Inputs and outputs numbers and labels are reported in the bottom table.

The inputs whose first-order indices (Figure 7.4.1a) were larger than 40% are

those which mainly affect output variances. The parent vessel radius R_{0_p} (input 1) is the main geometrical parameter and its variation had an important effect ($\sim$ 50%) on the maximum pressure values (outputs 5 - 8). Pressure values and flow distribution (outputs 1 - 10) were affected by changes in peripheral resistance (input 6 and 7) to an extent of 70 - 90%. According to the physics of waves propagation, pulse wave velocities (outputs 13 - 15) were affected by vessels' Young's modulus (inputs 3 - 5) and their wall thickness (inputs 15 - 17) by about 40%.

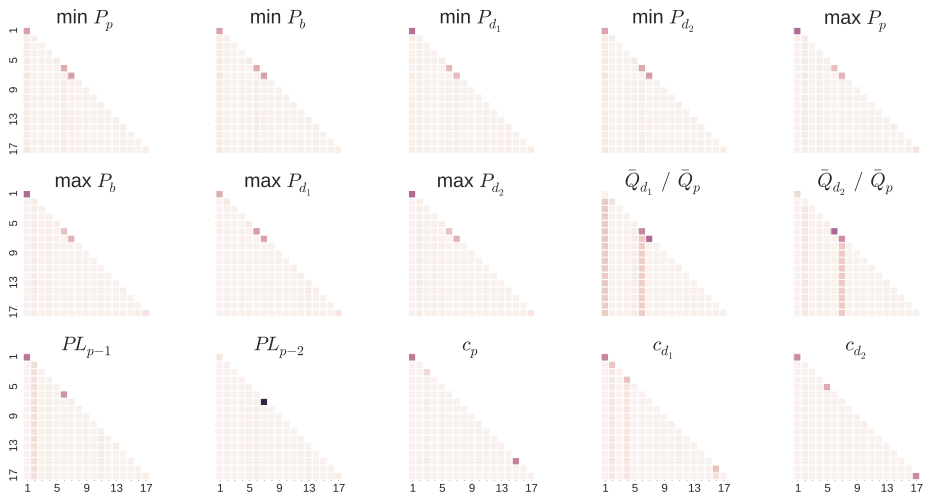

Figure 7.4.2: Second-order indices S_{ij} are plotted for each output in lower diagonal matrices. Principal diagonal elements are first-order indices S_i. Outputs are indicated above each matrix.

Peripheral compliance, blood density, and vessel length (inputs 8 - 10 and 11 - 14) scored low first-order sensitivity indices (less than 15%). The analysis of total effect indices (Figure 7.4.1b) confirmed R_{0_p}, E_p, h_p, $\mathcal{R}_1$, and $\mathcal{R}_2$ as the input parameters whose variation most affected output variation. These were the input parameters worth to be prioritisied in a patient-specific scenario. The remaining inputs can be fixed to literature reference values. The magnitude of second-order indices were small in comparison to the magnitude of first-order and total effect indices, indicating the covariance of inputs had little effect on output variance (Figure 7.4.2).

Finally, the sensitivity analysis was performed on the 17000 simulator runs from the Monte Carlo approach, and the sensitivity indices obtained were compared with those computed from GP predictions (Figure 7.4.3). Figure 7.4.3b shows that the computed percentage error was always smaller than 3%.

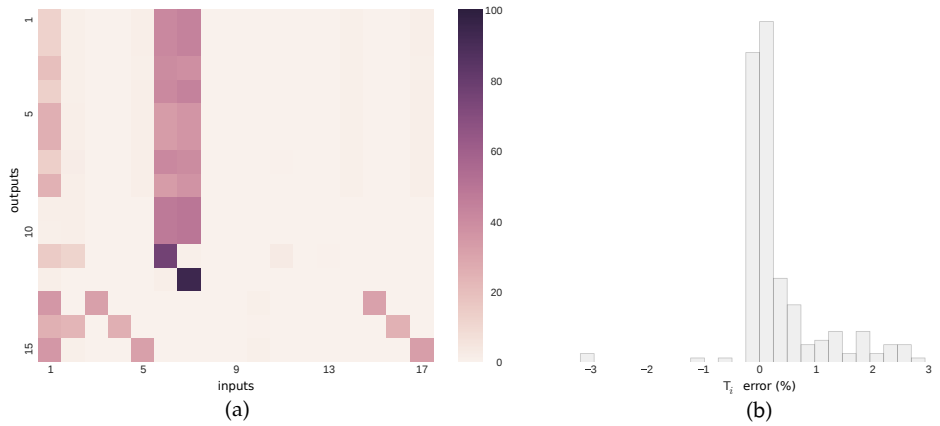

Figure 7.4.3: (a) Total effect sensitivity indices computed from MC analysis results. (b) The error in computing sensitivity indices starting from GP predictions rather than from actual simulations ranged between -3 and 3%.

7.5 Conclusions

A reduced number of model simulations were used to train a Gaussian process regression model. This emulator was able to mimic the vascular numerical model with a mean average percentage error lower than 1% when compared to the actual model runs. The emulator running time was also much shorter than the simulator one. More specifically, the adoption of a Gaussian process emulator in the sensitivity analysis framework allowed for a reduction of computational time by 99.6% compared to Monte Carlo analysis. Sensitivity indices computed with Gaussian process predictions differed by 3% from those computed with results from the Monte Carlo analysis.

This framework was tested on a simple vascular model of the middle cerebral artery bifurcation, whose physics can be easily interpreted. As expected, parent vessel radius was the main influential parameter, whereas vessel length did not have an effect on monitored outputs. Vessel mechanical properties influenced pulse wave velocity but not the waveforms minimum and maximum values. The peripheral resistance had a major effect on the flow distribution and on the systolic pressure. Blood viscosity had a small effect on pressure waveform shape, whereas blood density showed no effect. The interactions between inputs were described in terms of second-order sensitivity indices. These indices gave an insight of the non-linear behaviour of the mechanistic model, e.g. the amount of flow entering the first daughter vessel was not directly affected by R_{0_p}, but by the interaction of R_{0_p} with all other inputs.

The conclusions drawn from sensitivity analysis are not novel, but they confirm

that the developed framework is sound, and it is capable of capturing the intrinsic non linear behaviour of flows through an elastic bifurcation. Total running times were drastically reduced when using the emulator approach, which allowed a thorough sensitivity analysis with comparable accuracy to a Monte Carlo approach. The study of model sensitivity indices gave an insight of input interactions and could be used to study how input uncertainty propagated to the outputs.

Part of this chapter has been included with permission from:
Melis A, Clayton RH, Marzo A. Bayesian sensitivity analysis of a 1D vascular model with Gaussian process emulators. International Journal for Numerical Methods in Biomedical Engineering. 2017.

8 Scalability study

Summary

In order to analyse the scalability of the methodology adopted in Chapter 7, this was tested on four vascular networks of increasing complexity. The scalability study showed that the number of mechanistic simulations needed to train a Gaussian process for sensitivity analysis was of the order $\mathcal{O}(d)$, rather than $\mathcal{O}(d \times 10^3)$ needed for Monte Carlo analysis (where d is the number of parameters in the model). In the case of a complete network of 61 vessels, the computational time needed to perform the sensitivity analysis with an emulator was reduced by the 99.96% compared to a Monte Carlo approach. A substantial part of this chapter has been included in (Melis et al., 2017).

8.1 Introduction

The aim of this chapter is to compare sensitivity analysis of a 1D cardiovascular model based on GP emulators with the traditional approach based on Monte Carlo sampling. We have also shown how the GP properties scale with the vascular network complexity. Four patient-generic arterial networks of increasing size were employed to demonstrate the benefits of using GP emulators for cardiovascular applications. Results were validated on the outcomes of a Monte Carlo analysis.

8.2 Methodology

In order to show how the computational time, the accuracy, and the convergence of the proposed methodology scales with the mechanistic model complexity, four vascular networks were analysed (Figure 8.2.1). These represent the iliac bifurcation (8 arteries), the ascending and the upper thoracic aorta (7 arteries), the thoracic aorta and the right arm (15 arteries), and a more complete cardiovascular system (61 arteries). Geometrical values (lumen radius R_0 and vessel length ℓ), material properties (wall Young's modulus E), inlet flow time function, and Windkessel parameters (peripheral resistance $\mathcal{R}$ and peripheral compliance $\mathcal{C}$) were based on data

published in (Boileau et al., 2015; Brown et al., 2012; Xiao et al., 2014). Uncertainty domains for all the parameters were set as in (Huberts et al., 2013c) (Table 8.2.1).

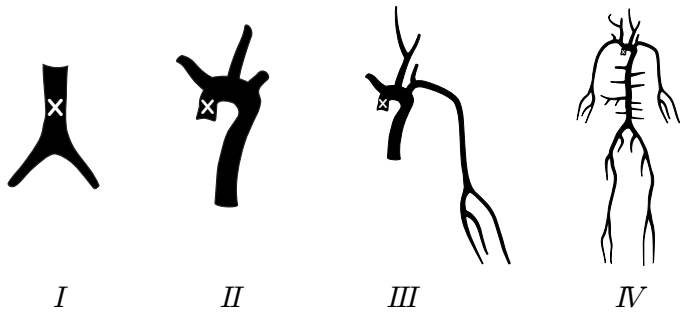

Figure 8.2.1: Diagrams of the four vascular networks used in the scalability study: (*I*) iliac bifurcation (Xiao et al., 2014), (*II*) ascending and thoracic aorta (Brown et al., 2012), (*III*) thoracic aorta and right arm (Boileau et al., 2015; Brown et al., 2012), (*IV*) complete model of the main 61 arteries adapted from (Boileau et al., 2015). The deterministic model outputs were extracted at the middle point of the root vessel of each network (white $\times$ marker).

$\ell\,(\%)$	$R_0\,(\%)$	$E\,(\%)$	$\mathcal{R}\,(\%)$	$\mathcal{C}\,(\%)$
$-10, 10$	$-10, 10$	$-20, 20$	$-25, 25$	$-50, 50$

Table 8.2.1: Simulation parameters uncertainty domain (Huberts et al., 2013c): ℓ vessel length, R_0 lumen radius, E wall Young's modulus, $\mathcal{R}$ peripheral resistance, and $\mathcal{C}$ peripheral resistance.

Analysis of the results was conducted by extracting two outputs: the pressure waveforms were computed at each node of the system, and minimum and maximum values at the middle point of the root vessel (i.e. the vessel to which the inlet boundary condition is applied) were recorded (Figure 8.2.2(b)).

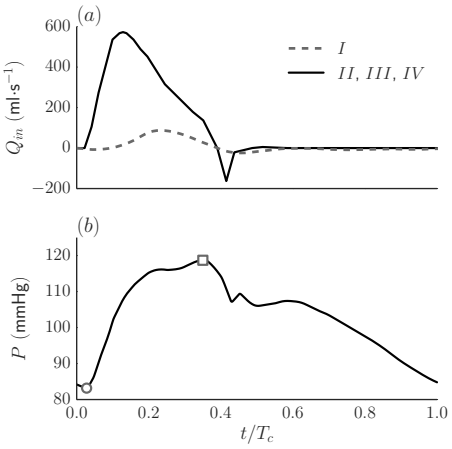

Figure 8.2.2: (a) Typical inlet flow time functions used as inlet boundary condition for the four networks, taken from (Boileau et al., 2015). (b) Example of computed pressure waveform at the middle point of the root vessel of network IV. The waveforms are reported as a function of the time normalised with respect to the cardiac cycle period T_c. The minimum (circle) and the maximum (square) pressure values are the waveform features taken as outputs of the deterministic model.

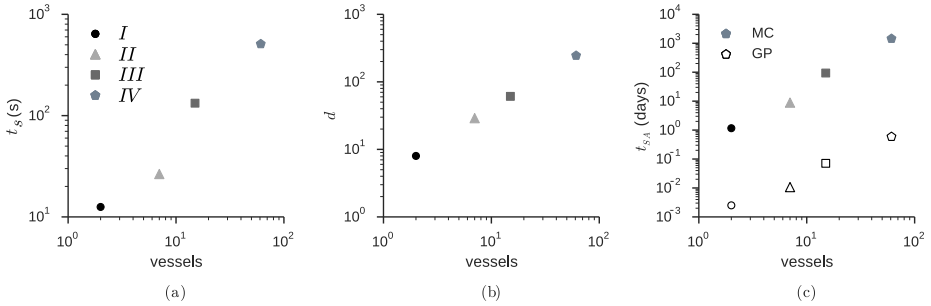

Figure 8.2.3: (a) Computational time required by the mechanistic solver to compute the flow solution for each of the four networks ($I - IV$). The computational time increases as more vessels are added to the network. (b) Number of input parameters in the vascular model to be studied with the sensitivity analysis as the number of vessels increases. (c) Total computational time required to compute all the $d \times \mathbf{10^3}$ simulation for the sensitivity analysis by both the Monte Carlo (MC, filled markers) and the Gaussian process (GP, empty markers) methods.

The GP prediction error was assessed by performing a Monte Carlo (MC) analysis on the vascular models. This consisted of running $d \times 10^3$ simulations by sampling

the d-dimensional input space. The $d \times 10^3$ inputs and the $d \times 10^3 \times 2$ outputs constituted the GP design data $\mathcal{D}$. A portion of the dataset was randomly sampled and saved for diagnostic purposes. The GP model was trained on the remaining part. The MC analysis was performed for the networks I, II, and III, but not for the complete model IV, as the computational time required would have been prohibitive and estimated around 9 years and 4 months (Figure 8.2.3).

The training sample was varied in size to assess the relation between the prediction error and the sample size. Three diagnostics (Bastos and O'Hagan, 2009) were used to verify GP model predictions: graphical analysis (Figure 8.2.4a-c), standardised prediction error (Figure 8.2.4d-f), and mean average prediction error (MAPE) (Figure 8.2.5). In case IV, for which the MC method was not applicable, the MAPE was computed on a reduced dataset of 1000 simulator runs.

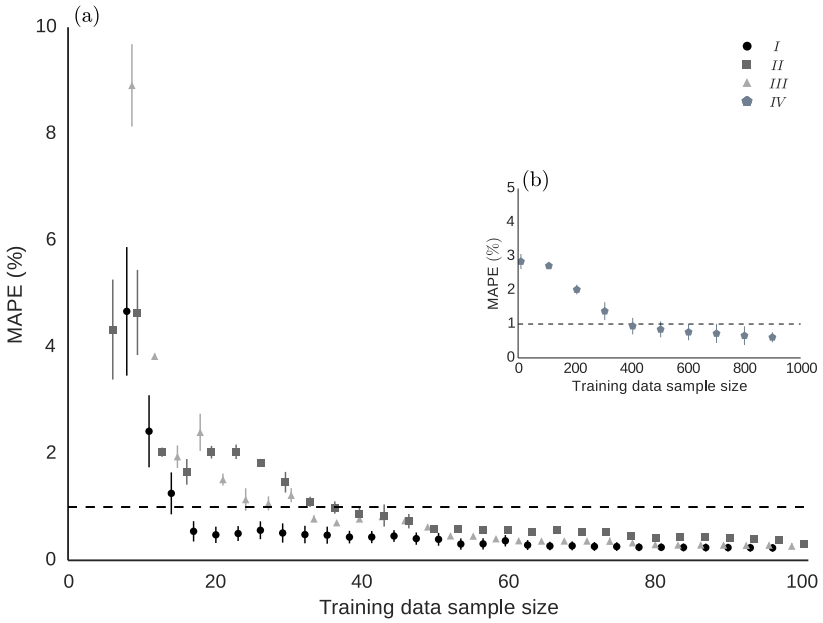

Figure 8.2.5: Mean average prediction error (MAPE) between emulator predictions and simulator outputs for each input of interest on the first three networks (a) and for the complete model (b). The MAPE decreases as the number of points in the training sample increases.

The sensitivity analysis for parameter fixing and prioritisation was performed in the three step strategy of section 7.2.

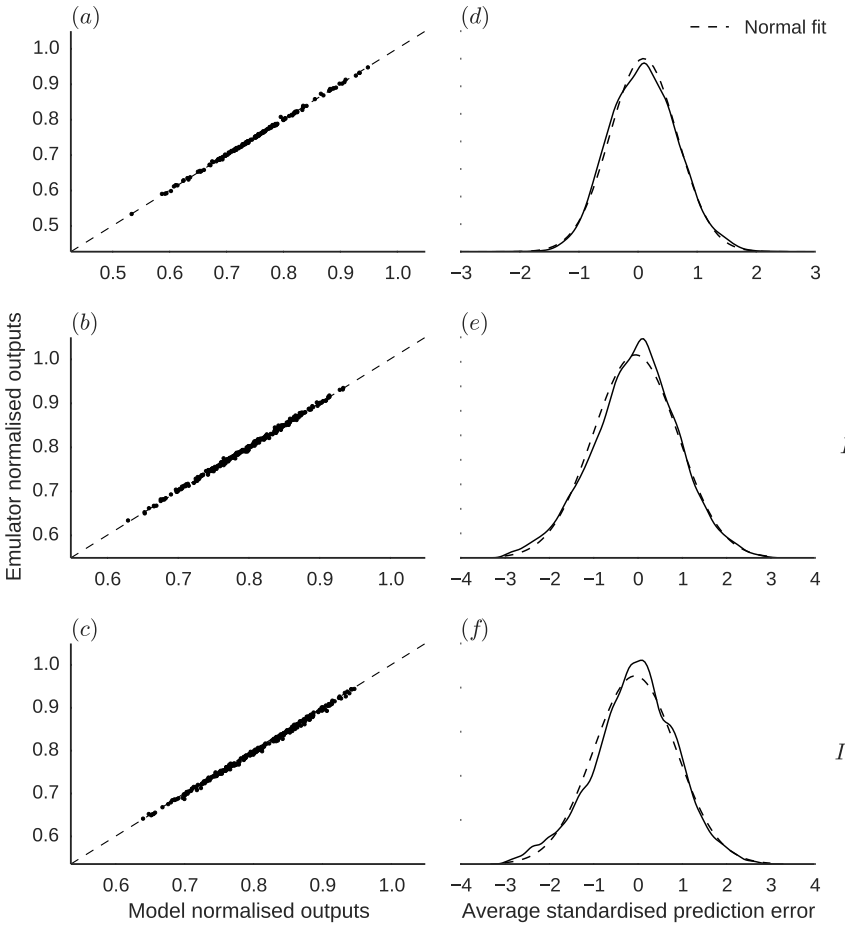

Figure 8.2.4: Gaussian process validation diagnostics for the first three vascular networks ($I-III$). (a-c) Graphical comparison between emulator predictions and simulator outputs; points lying on the dashed line of equality indicate a good agreement between the two techniques. (d-f) A properly trained emulator is expected to have standardised prediction errors normally distributed.

8.3 Results and discussion

The time spent to run a single simulation with the mechanistic solver, t_s, for each network is reported in Figure 8.2.3a. The trained GP emulators were used to predict results for all the $d \times 10^3$ input points needed for the sensitivity analysis (Figure 8.2.3b). These input points were chosen to explore thoroughly the input hyperspace. The sensitivity analysis computational running times, t_{SA}, of both the numerical vascular model and the GP emulator are reported in Figure 8.2.3c. The computational time in the MC analysis added up to 2.5 days for the single bifurcation, and it was estimated to scale up to about 9 years in the case of the complete vascular model. The GP computational time for both training and prediction phases increased as the number of vessels in the network increased. The t_{SA} was always four orders of magnitude smaller with respect to the MC approach. By coupling the numerical model with the GP regression model, the bulk of the computational time was taken by numerical simulations on the dataset used for training (Table 8.3.1), e.g. 14 hours for the 61 arteries model. Predictions for the $d \times 10^3$ datasets were made in 0.42 seconds by the GP emulator. Therefore, the sensitivity analysis on the complete model was performed in 14 hours.

	d	N_{GP}	N_{MC}	$t_{SA_{MC}}\,(\%)$
I	8	17	8000	0.216
II	29	34	29000	0.120
III	61	47	61000	0.075
IV	245	500	245000	0.040

Table 8.3.1: Gaussian process and Monte Carlo training sample size (N_{GP}, N_{MC}) for the four vascular network. The time needed by the GP method to perform the sensitivity analysis predictions is reported as percent of the time taken by the MC, $t_{SA_{MC}}\%$. For each network, its complexity is reported in terms of the number of input parameters d.

The GP prediction error decreased as the number of points in the training sample increased (Figure 8.2.5). The number of training points needed to score a MAPE lower than 1% was always lower than the number of points needed to perform the MC analysis (Table 8.3.1). These results indicated that the number of points needed to train the GP is of the order $\mathcal{O}(d)$.

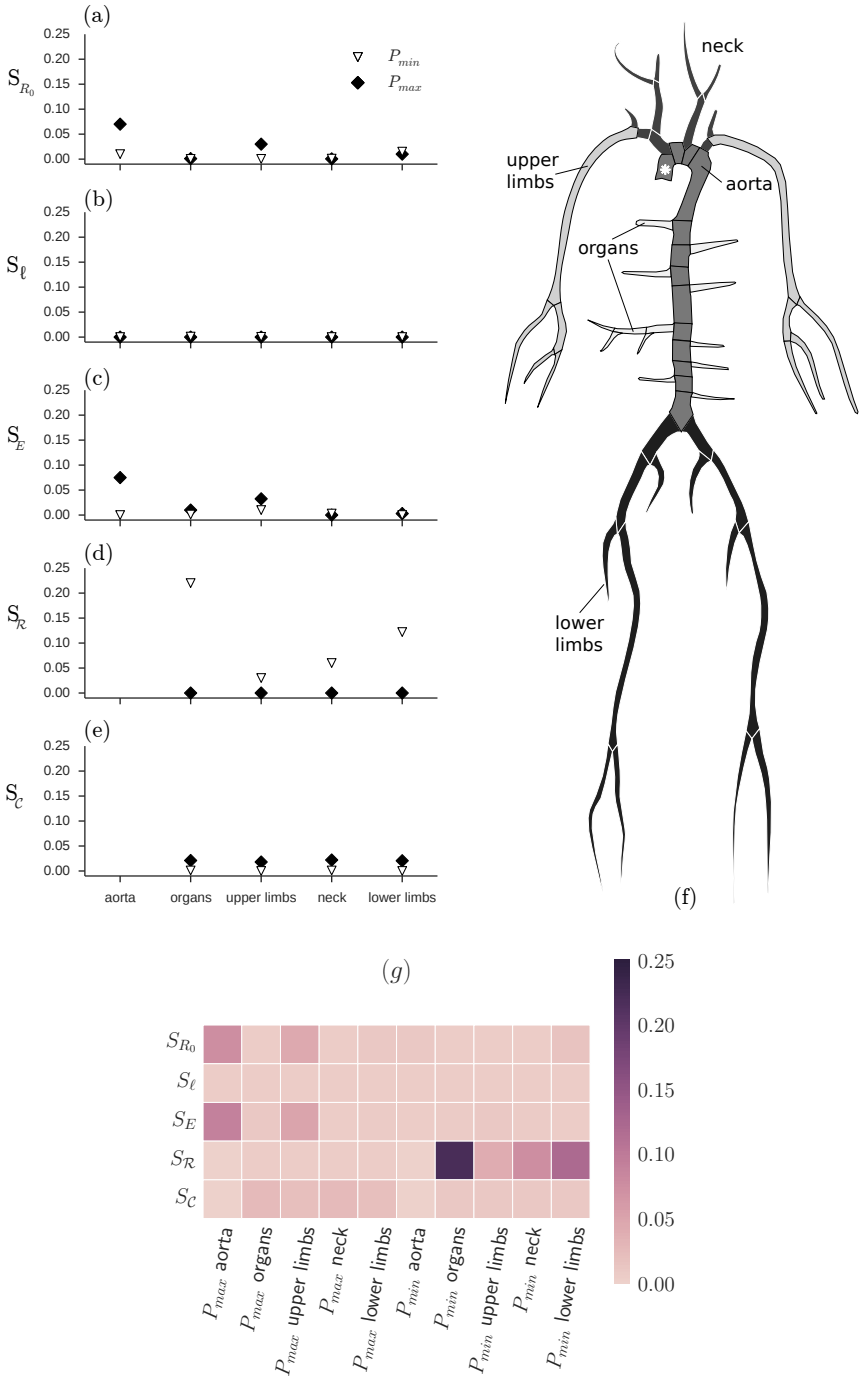

Figure 8.3.1: (a-e, g) First-order sensitivity indices (S_i) relating the variation of minimum and maximum pressure (the outputs of the deterministic model, P_{min} and P_{max}, respectively) at the ascending aorta location ($*$ marker in (f)) with the variation of the lumen radius, vessel length, Young's modulus, peripheral resistance and compliance for the five groups of arteries in (f).

In the case of the complete model, the ensemble of input points and predicted outputs was used to compute first-order Sobol' sensitivity indices (Figure 8.3.1a-e). To ease the analysis, the indices were subdivided in five sets depending on the vessel location as in (Eck et al., 2015b) (areas are indicated in Figure 8.3.1f). The vessel length and the peripheral compliance (ℓ and $\mathcal{C}$, respectively) scored low first-order sensitivity indices (less than 0.02, Figure 8.3.1b,e). Upper limbs vessel radii and Young's moduli slightly affected ($S_{R_0,E} \sim 0.05$) the maximum pressure in the ascending aorta whereas they had no effect on the minimum pressure (Figure 8.3.1a,c). Aorta vessel radii and Young's moduli were the topological parameters to have the most effect on the maximum pressure ($S_{R_0,E} \sim 0.1$). The peripheral resistance ($\mathcal{R}$) variation at organ vessels affected the variation of the maximum and minimum pressure ($S_{\mathcal{R}} \sim 0.25$), whereas the upper part of the network (upper limbs and neck vessels) has a slightly lower effect ($0.05 < S_{\mathcal{R}} < 0.15$) on both minimum and maximum pressure at the ascending aorta (Figure 8.3.1d). In order to show the sensitivity indices in a qualitative way, these were converted to luminance values and plotted in a heat map (Figure 8.3.1g).

The choice of different inlet boundary conditions for the networks investigated did not seem to affect the main outcome of the study, as computational time reduced linearly with the number of vessels for all networks regardless of the conditions set at their inlets (Figure 8.2.3(c)). In addition, the same prediction accuracy, as measured by the MAPE (Figure 8.2.5), was achieved for a sample size proportional to the number of vessels rather than to the type of flow time-function used. Nonetheless, the inlet boundary condition is a source of uncertainty due to its large variability between individuals. In future studies aimed at finding clinical bio-mechanical markers, the inlet flow function will be included as a GP input.

8.4 Conclusions

One-dimensional models of the cardiovascular system provide an accurate description of the physics of wave transmission in blood and can be used to provide realistic or patient-specific pulse and flow rate waveforms. Their mathematical description relies on the specification of a large number of parameters, which are often not readily available as typical or patient-specific values. Many of these cannot be specified as a constant value either, as they will vary within the physiological envelope of an individual. In this context, ranking and fixing of parameters through sensitivity analysis has been previously proposed as a way to focus on the most influential model inputs or simply to quantify input uncertainty on variables of interest. However, these operations may require many simulations, resulting in large or infeasible computational time.

A time efficient approach to sensitivity analysis is proposed in this chapter. A

reduced number of model simulations were used to train a GP regression model. This emulator was able to mimic the vascular numerical model with a percentage error lower than 1% when compared to the actual model runs. The emulator running time was also much shorter than the simulator: the GP prediction phase for network IV took 0.19 s as opposed to an average of 197 s required for a single run of the deterministic model. More in general, the adoption of a GP emulator in the sensitivity analysis framework allowed for a minimum reduction of computational time by 99.96% compared to Monte Carlo analysis.

This framework scalability was tested by developing four vascular models of increasing complexity, i.e. starting from a single bifurcation, the number of vessels was increased up to 61 in the case of a complete vascular model. In all the four cases, by introducing the GP, the simulator runs needed for the sensitivity analysis is reduced from $d \times 10^3$ to $\mathcal{O}(d)$.

The analysis of sensitivity indices allowed us to identify the location in the network of model parameters affecting maximum and minimum pressures in the ascending aorta. In particular, the minimum pressure was affected by changes in the peripheral resistance of organ arteries. The maximum pressure was sensitive to changes in the aorta Young's modulus as well as in the upper limbs arteries.

The introduction of a GP regression model as an output generator for a mechanistic model is a novel approach in the cardiovascular research community. The conclusions drawn from sensitivity analysis are not novel, but they confirm that the developed framework is sound, and it is capable of capturing the intrinsic non linear behaviour of flows through a vascular network. Running times were drastically reduced when using the emulator approach, which allowed a thorough sensitivity analysis with comparable accuracy to a much more time consuming approach. The study of model sensitivity indices gave an insight into how the inputs interact and could be used to study how input uncertainty propagates through to the outputs. The same approach has the potential to improve efficiency in the analysis of more complex and complete models of the cardiovascular systems.

Part of this chapter will be included in:
Melis A, Moura F, Larrabide I, Clayton RH, Narata AP, Marzo A. Improved biomechanical metrics of cerebral vasospasm identified via sensitivity analysis of a cerebral circulation model. In preparation.

9 Cerebral vasospasm

Summary

In this chapter, the time efficient method to perform the sensitivity analysis of numerical vascular models was applied to identify clinical biomechanical metrics (referred to from here onwards as a biomarker) for a specific vascular condition, cerebral vasospasm. Cerebral vasospasm is the progressive narrowing of intracranial arteries following cerebral hæmorrhage. In current clinical practice, the primary non-invasive diagnostic method is transcranial echo-doppler that detects increases in blood velocity from baseline values following the vessels narrowing. This is effective when the vasospasm affects large vessels at accessible locations, but it has low sensitivity when the narrowing occurs in the peripheral vasculature. The study presented in this chapter had the aim of identifying novel cerebral vasospasm biomarkers through sensitivity analysis. The biomarkers were selected by analysing pulse waveforms simulated by means of a 1D model of the cerebral circulation. Sobol's indices were used to identify the waveform descriptors most sensitive to vessel narrowing. The identified biomarker, the maximum rate of pressure change over time, resulted to be sensitive to both local and peripheral vasospasm. The sensitivity analysis was performed in 5% of the computational time required by the Monte Carlo method.

9.1 Introduction

Cerebral vasospasm (CVS) is the progressive narrowing of intracranial arteries and a severe complication of sub-arachnoid haemorrhage (SAH) (Fehnel et al., 2014; Macdonald, 2016). Amongst the complications of SAH, CVS has been regarded as the major cause of delayed cerebral ischemia (Kolias et al., 2009). Arterial narrowing begins days after SAH and reaches its peak after typically one week when symptoms of cerebral ischemia become evident. Worldwide around 10 out of 100,000 patients have SAH each year and, of the 70% who survive the initial rupture, approximately 70% go on to suffer CVS, which often results in additional disability or death (Pluta et al., 2009).

The economic costs of CVS-related morbidity are also disproportionately high, as it tends to affect younger people who often require long-term health care and are

unable to return to work. Unfortunately, the mechanisms of SAH-induced CVS remain incompletely understood from both pathogenic and therapeutic perspectives. Many pathological processes have been proposed to explain the contraction, the inflammatory and/or immunological responses of the vascular wall (Lin et al., 2014). In current clinical practice, the primary diagnostic method is Transcranial Doppler (TCD) due to the non-invasive nature of this technique compared to X-ray irradiation imaging methods (Kumar et al., 2015). TCD assessment detects an increase in blood velocity from baseline values following the narrowing of affected vessels (Aaslid et al., 1984; Fontana et al., 2015; Harders and Gilsbach, 1987). This biomarkers can be effective when detecting CVS at accessible locations in larger arteries, but velocity measurements have low sensitivity when the condition affects the more peripheral intracranial vasculature, or vessels 'hidden' behind thick bone tissue. For these reasons, and for the scarce confidence in current biomarkers, CVS is often diagnosed by excluding other possible concomitant causes, thus limiting the effectiveness of its direct management.

Pressure waves in the cardiovascular system originate from the periodic contraction of the heart and propagate through the elastic vessels of the cardiovascular system reflecting at points of mechanical discontinuity, such as branches, bends or sudden narrowings, including those caused by CVS. As they travel along the cardiovascular system, pressure waves collect a rich set of information about blood vessel geometry, making them potentially useful as diagnostic indicators. Computer models, in particular 1D and 0D-distributed models, have been used to describe the physics of these waves (Alastruey et al., 2007; Reymond et al., 2009).

To better understand the cause-effect mechanisms governing CVS, computational models have been proposed (Baek et al., 2007; Humphrey et al., 2007; Lodi and Ursino, 1999; Robinson et al., 2010), where the CVS was assumed to occur in the middle cerebral artery (MCA). However, these studies mainly focus on the biomarker currently used to identify CVS, blood flow maximum velocity, and show its increase in the vessel affected by the condition. To the authors' knowledge, there is no evidence in the literature of studies attempting to correlate different types of CVS (including those affecting the smaller peripheral vessels) to waveform features, at proximal and accessible locations that could signal the presence of the condition.

The effect on waveforms may be hampered by other influencing factors not necessarily related to pathology. For example, changes in vessel compliance with age, patient-specific variations in cardiovascular anatomy, and other physiological factors such as heart rate, peripheral vasodilation secondary to higher metabolic demand or activity levels. The influence of these concomitant factors on waveforms is not fully understood and has hampered the full exploitation of these models in the clinic.

The aim of the study reported in this chapter was to develop a 1D numerical mech-

anistic model of CVS to show the limitations of currently used biomarkers. Moreover, it was proposed the use of GP emulators to identify effective biomarkers capable of characterising and stratifying different types (location and severity) of CVS in presence of uncertain, noisy, or missing data.

9.2 Methodology

The study was organised into the following tasks:

- *Deterministic model*: implementation of a model of a typical cerebral cardiovascular network affected by CVS.

- *Biomarker pool identification*: identification of a comprehensive number of pressure and flow rate waveform descriptors (biomarkers pool).

- *Sensitivity analysis (SA) for CVS biomarker selection*: identification of a GP emulator using a reduced number of model runs using Latin hypercube sampling to ensure an optimal coverage of the parameter space. The identified GP was then used to run a complete sensitivity analysis of the model outputs of interest (waveform biomarkers pool) to the input parameters of interest, i.e. vessel radii reduction. This allowed the identification of those waveform features (CVS biomarkers) that were most sensitive to a change in lumen radius.

- *Vasospasm characterisation*: once these biomarkers (i.e. the waveform features) were identified, the 1D model was employed to simulate different types of CVS (location and severity). The results of this second set of simulations were then analysed to establish a relation between biomarkers and CVS properties, and their sensitivity when compared with traditional biomarkers.

These tasks are further explained below.

9.2.1 Deterministic model

The idealised brain circulation network model chosen for this study consists of 17 vessels connected in a tree-like configuration (Figure 9.2.1). It starts from the internal carotid artery (ICA) and bifurcates into the anterior cerebral artery (ACA), and the MCA and its distal vessels. The ACA was included to consider the effect of flow redistribution caused by the CVS.

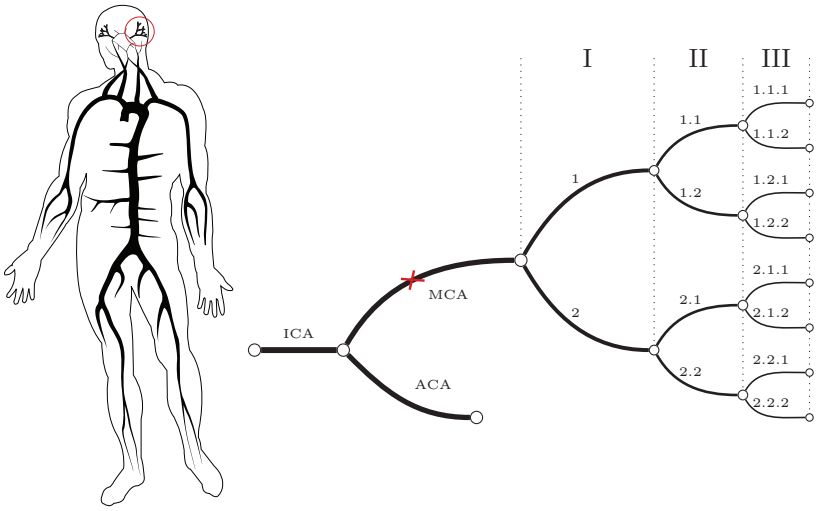

Figure 9.2.1: Diagram of the vascular network model (right); the vascular model location is indicated in the systemic circulation diagram (left). The network starts from the internal carotid artery (ICA) and branches into the middle cerebral artery (MCA) and in the anterior cerebral artery (ACA). Three generations (I, II, and III) of arteries branch out the MCA. They are identified by a numeric code following the branching pattern as the upper branches are indicated by 1 and the lower branches are indicated by 2. The point at which waveforms were monitored in the MCA is indicated by the cross marker.

The mechanical properties of the arteries were taken from (Reymond et al., 2009) and are representative of a typical young, healthy individual. Additionally, the effect of ageing was considered by changing vessels elasticity to resemble individuals of 10, 40, and 80 years old, as reported in (Gozna et al., 1974; Hayashi et al., 1980). The network develops through three generations of arteries (I-II-III in Figure 9.2.1), with radii following the Murray's law, $R_p^3 = R_{d_1}^3 + R_{d_2}^3$, where for each bifurcation, R_p is the parent vessel radius and $R_{d_{1,2}}$ are the daughter vessels radii. The branching was assumed to be symmetrical, i.e. $R_{d_1} = R_{d_2}$.

The inlet boundary condition at ICA root was set as a typical volumetric flow rate waveform taken from (Reymond et al., 2009), and the outlet boundary conditions were set by coupling the 1D model with three-element windkessel models of the peripheral vasculature with typical peripheral resistance and compliance values taken from (Reymond et al., 2009).

9.2.2 Biomarker pool identification

The biomarkers pool included minimum (min), maximum (max), and time average (mean) flow rate (Q), pressure (P) and velocity (u) values, as well as their first (∂_t) and second derivatives (∂_{tt}) with respect to time (t). These features are easy to extract from the waveforms and commonly used in the literature to calculate more complex metrics (e.g. pulsatility index and augmentation index).

9.2.3 Sensitivity analysis for CVS biomarker selection

The CVS biomarkers were found by performing a SA of the 1D numerical model outputs (Santner et al., 2013), where the SA identified the set of outputs most sensitive to a change of each single input of the numerical model. The CVS biomarkers were assumed to be those outputs sensitive to changes in lumen radius. Since the vascular system is highly non-linear, its outputs may be sensitive to more than one input. Hence, to ensure that only those waveform features sensitive to changes in vessel radius were selected, inputs other than R_0 were also included in the SA. In particular, the inputs considered in the SA study were the lumen radius R_0, the wall Young's modulus E, the vessel length ℓ, as well as the peripheral resistances R_p and the peripheral compliance C_p of the three-element windkessel models.

All values were initially set to a reference value (Table 9.2.1). The SA was performed by changing the inputs within $\pm 50\%$ of their reference value as such variation is to be expected in the CVS scenario (Findlay et al., 2015). A homogeneous coverage of the input space was ensured by the use of the Latin hypercube sampling method as explained in (Melis et al., 2017; Santner et al., 2013).

The SA was done by means of the analysis of variance decomposition from which the Sobol's sensitivity indices were computed (Saltelli et al., 2010; Sobol, 2001). Two types of sensitivity indices were computed: the total-order sensitivity index ($\mathbf{T}_i$) measures the contribution to the output variance of the input i, and of the interactions with other inputs; the higher-order indices ($\mathbf{H}_{ij}$) measure only the output variance due to inputs i and j interaction. The SA indices were computed by means of a GP regression model (Bishop, 2006; Oakley and O'Hagan, 2004; O'Hagan, 2006; Williams and Rasmussen, 2006) and a more detailed description of GP application to SA is reported in chapters 7 and 8.

Vessel	R_0 (mm)	E (kPa)	ℓ (mm)	R_p $(\mathrm{GPa{\cdot}s{\cdot}m^{-3}})$	C_c $(\times 10^{-3}\mathrm{m^3{\cdot}GPa^{-1}})$
ICA	2.50	509.998	132.0		
ACA	1.97	525.033	14.0	4.60	60.316
MCA	2.00	523.892	4.0		
1	1.58	544.749	4.0		
2	1.58	544.749	4.0		
1.1	1.26	573.941	4.0		
1.2	1.26	573.941	4.0		
2.1	1.26	573.941	4.0		
2.2	1.26	573.941	4.0		
1.1.1	1.00	612.726	4.0	35.51	4.769
1.1.2	1.00	612.726	4.0	35.51	4.769
1.2.1	1.00	612.726	4.0	35.51	4.769
1.2.2	1.00	612.726	4.0	35.51	4.769
2.1.1	1.00	612.726	4.0	35.51	4.769
2.1.2	1.00	612.726	4.0	35.51	4.769
2.2.1	1.00	612.726	4.0	35.51	4.769
2.2.2	1.00	612.726	4.0	35.51	4.769

Table 9.2.1: Reference values for vessel lumen radius (R_0) and length (ℓ), wall Young's modulus (E), and peripheral windkessel resistance (R_p) and compliance (C_p). Based on (Reymond et al., 2009). Vessel names refer to the network diagram in Figure 9.2.1.

The SA for CVS biomarkers selection was performed in four steps:

1. The 1D numerical model was run on a set of 50 input points evenly covering the parameter space defined by $\pm 50\%$ of the reference values. In order to avoid ill-defined calculations, the simulation inputs and outputs were normalised before being used to train the GP emulator.

2. The GP emulator, based on the squared exponential kernel, was implemented and trained by using GPy library (GPy, 2012). The GP training and optimisation was achieved by means of the gradient descent method.

3. The predictions on the $\mathcal{O}(d \times 10^3)$ input set were generated by the trained GP.

4. Sobol's sensitivity indices were computed by means of ANOVA decomposition and converted to percent values. The members of the biomarker pool were ranked accordingly to their indices with respect to the radius. A threshold at 90% was set, i.e. the outputs scoring less than 90% were filtered out. In addition, the higher-order indices were computed and outputs scoring more than 5% were filtered out. This was to ensure that only outputs sensitive to radius changes alone were selected.

9.2.4 Cerebral vasospasm simulations

The propagation and narrowing levels of CVS was decided in consultation with two fully trained Interventional Neuroradiologists from Hôpitaux de Tours, France. Different CVS types were considered, describing increasing areas of progression of the condition, either propagating from the MCA towards the peripheral vessels (forward CVS) or from the peripheral vessels towards the MCA (backward CVS) in a symmetric or asymmetric fashion as depicted in Figure 9.2.2. For each type, the narrowing was gradually set in six steps from 0% (baseline condition without CVS) to 60% (severe CVS) of vessel narrowing calculated as a percentage in diameter reduction with respect to the baseline value.

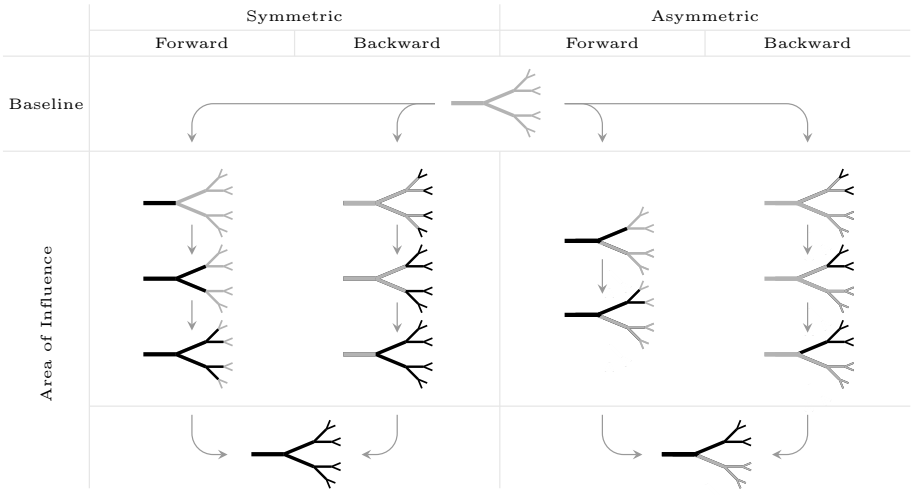

Figure 9.2.2: Diagrams of CVS types in the network starting from the MCA. The vessels affected by the CVS are coloured in black. The vessels not affected by the CVS are coloured in gray. The CVS is subdivided in symmetric (left) and asymmetric (right) types. In the symmetric cases, the CVS propagates along upper and lower branches of the tree. In the asymmetric cases, the CVS affects only the upper main branch of the system. Within these two types (symmetric and asymmetric), we simulate the CVS propagating either from left to right (forward) or from right to left (backward). The global configurations are those in which the CVS affects the entire network (last line).

9.2.5 TCD measurements comparison

The methodology adopted to simulate CVS onset and propagation was tested against experimental TCD measurements. These were available from the literature (Harders and Gilsbach, 1987) and constisted in repeated measurements of blood velocity at MCA location in subjects affected by SAH. The initial measurement (i.e. at the rupture of SAA) was taken as reference value; all the subsequent measurements were normalised w.r.t. the first measurement to highlight the percentage deviation from initial conditions. In the literature study, imaging data was used to link the percentage lumen reduction w.r.t. velocity measurements.

9.3 Results

9.3.1 Numerical model and emulator validations

The 1D numerical model was first validated (Figure 9.3.1a) by comparing its predicted velocity values time-averaged over the cardiac cycle in the MCA, and in pres-

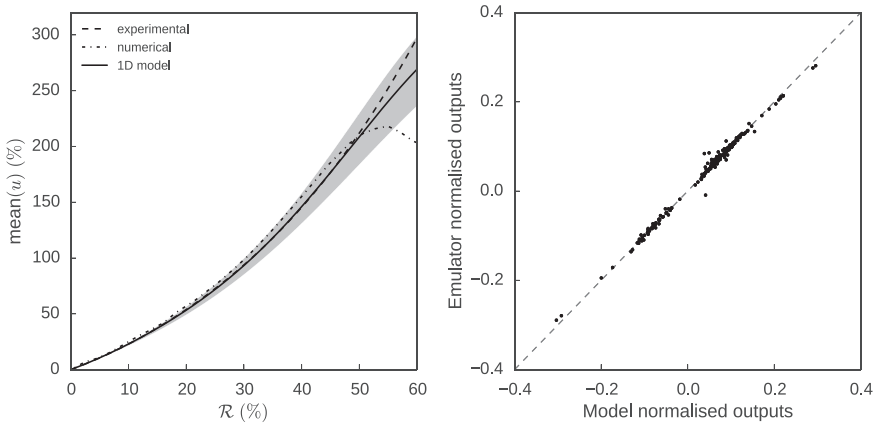

Figure 9.3.1: (a) Computed mean velocity change in the MCA (in percentage with respect to the pre-vasospasm value) versus percentage changes in lumen radius. The gray shaded area indicates the confidence interval of the numerical results of the present work; dashed lines: published measurements (Harders and Gilsbach, 1987); dash-dotted line: numerical results from another published study (Lodi and Ursino, 1999). (b) Comparison between the numerical simulator outputs and the GP emulator outputs. Points lying close to the dashed line (line of equality) indicate good agreement between the two methods. The computed predictions mean average error is 3.53%.

ence of CVS, with published measurements from SAH subjects and with the results from another numerical study on CVS, published in (Harders and Gilsbach, 1987) and (Lodi and Ursino, 1999), respectively. The reported curve (continuous line) was obtained by time averaging the results from CVS simulations at different ages. The grey area indicates the result variability due to age, i.e., the change in Young's modulus. The proposed numerical model is in good agreement with both results from the literature. The difference between the curves are within 2% for radius narrowing $\leq$50%. Further narrowing makes both numerical models diverge from the experimental measurements, reaching 20% difference at 60% radius narrowing. Despite the divergence of the model results from the experimental, these are still within the elastance-induced variance of the 1D numerical model data for all degrees of CVS simulated.

The GP emulator was trained upon 50 simulator runs, where the number of sample points was taken proportional to the number of SA parameters ($d = 5$) (Melis et al., 2017). For validation purposes, an additional test set of 200 simulation was run. Numerical outputs and GP predictions on the test set are plotted against each

other in Figure 9.3.1b. The two methods are in good agreement as the points are scattered close to the diagonal line of equality. The MAPE obtained for the test set was 3.53%, which is small with respect to the 300% whole biomarker variation within the CVS range.

The simulations on the 50 sample points dataset were performed on a standard Linux workstation and took 31 hours to complete. The GP model (implemented by means of the GPy library (GPy, 2012)) training and the predictions on the larger $d \times 10^3$ dataset needed for the sensitivity analysis were completed in 10.4 seconds. The estimated computational time to perform a complete Monte Carlo (MC) analysis using the deterministic model is of 612 hours. Thus, the generation of the dataset for the SA by means of GP took the 5% of the MC computational time.

9.3.2 Sensitivity analysis and CVS biomarkers selection

The total effect ($\mathbf{T}$) and higher-order ($\mathbf{H}$) sensitivity indices were converted to percentage luminance values and reported in heat maps (Figure 9.3.2). For instance, the SA indicates that the mean flow rate (Q) waveform is more sensitive to interaction between inputs (large $\mathbf{H}$ indices) than to a single input. The velocity and pressure waveforms have features sensitive to the change in radius only. The CVS biomarkers were selected by filtering out all the outputs whose $\mathbf{T}$ is smaller than 90% and whose $\mathbf{H}$ relative to the lumen radius (R_0) is larger than 5%. These features were identified as CVS biomarkers. The list of the eight CVS biomarkers is ranked with respect to the total effect index and reported in Figure 9.3.2. In the following, the results for average velocity (mean(u)) and maximum pressure gradient (max($\partial_t P$)) are analysed. These were chosen because related to two different quantities (velocity and pressure), highly sensitive to changes in radius (high $\mathbf{T}$ index), and less affected by parameter interactions (low $\mathbf{H}$ index).

9.3.3 CVS simulations

Results are here presented as the percent change of the selected eight CVS biomarkers with respect to the pre-CVS value ($\mathcal{C}\%$). As the lumen narrows, the $\mathcal{C}\%$ was computed as

$$\mathcal{C}(x) = 100\frac{x_{\text{CVS}} - x_{\text{REF}}}{x_{\text{REF}}},$$

where x_{CVS} is the value of the CVS biomarker as the CVS is occurring (i.e. the narrowing is $>0\%$) and x_{REF} is the value of the CVS biomarker in the pre-CVS configuration.

The results in terms of time average velocity biomarker for the symmetric CVS for a typical individual are reported in Figure 9.3.3. In the forward CVS case, the

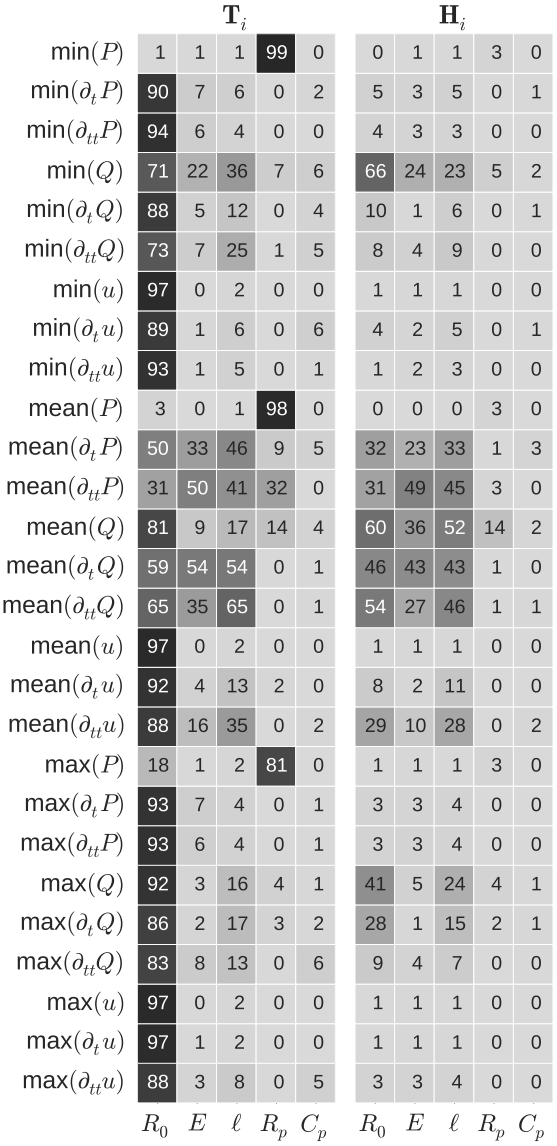

CV biomarker	$\mathbf{T}_{R_0}$	$\mathbf{H}_{R_0}$
mean(u)	97.43	0.82
max(u)	97.28	0.84
min(u)	97.23	0.93
max($\partial_t u$)	96.83	0.90
min($\partial_{tt} P$)	93.76	3.62
max($\partial_{tt} P$)	93.05	3.35
min($\partial_{tt} u$)	92.98	1.16
max($\partial_t P$)	92.52	3.18

Figure 9.3.2: (left) Total effect ($\mathbf{T}_i$) and higher-orders ($\mathbf{H}_i$) sensitivity heat maps. The darker the cell the higher the sensitivity of the output (row) to the variation of the related input (column). The rounded percentage values of the sensitivity indices are reported inside each cell. (right) Selected CVS biomarkers sensitivity indices are ranked in descending order with respect to the total effect index $\mathbf{T}_{R_0}$ and reported in the table.

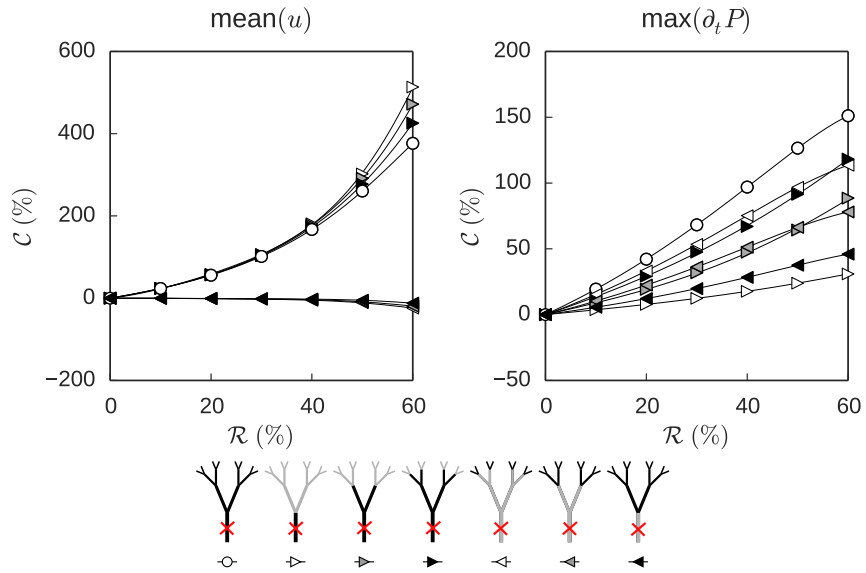

Figure 9.3.3: Percent change of CVS biomarkers as the lumen radius decreases in the case of symmetric CVS occurring in an adult generic subject. The CVS biomarker is reported above each plot and the lumen radius reduction location is indicated by the markers shape and colour.

mean velocity (mean(u)) monotonically increases as the lumen radius narrows. In the backward CVS case, the values remain close to zero $\mathcal{C}$%, even for large lumen reductions ($\mathcal{R}$ =60%). This suggests that time average velocity is an effective biomarker only when measured at locations affected by vessel narrowing. When the narrowing occurs far from the measurement point (backward CVS), the same biomarker shows less sensitivity to vessel narrowing.

For all the symmetric CVS cases, the pressure biomarker increases as the vessels narrow. In the global case, severe CVS (60% lumen reduction) causes the pressure biomarker to rise by 150%. The pressure biomarker increase is linear with the vessel narrowing in all the CVS cases. In the case of severe backward CVS, the pressure biomarker change is 100% when only the outermost vessels are involved (white marker), and it decreases as the CVS propagates toward the MCA (black marker).

In the case of asymmetric CVS (Figure 9.3.4), the velocity biomarker behaviour is quantitatively similar to the symmetric case one. The mean(u) increases by 475% when a severe lumen reduction occurs in the MCA, and it remains close to the baseline value for the distal CVS case. Conversely, the pressure biomarker increases linearly in both proximal and distal CVS cases. The max($\partial_t P$) increases up to the 60% for the global asymmetric CVS configuration, whereas the CVS occurring only in

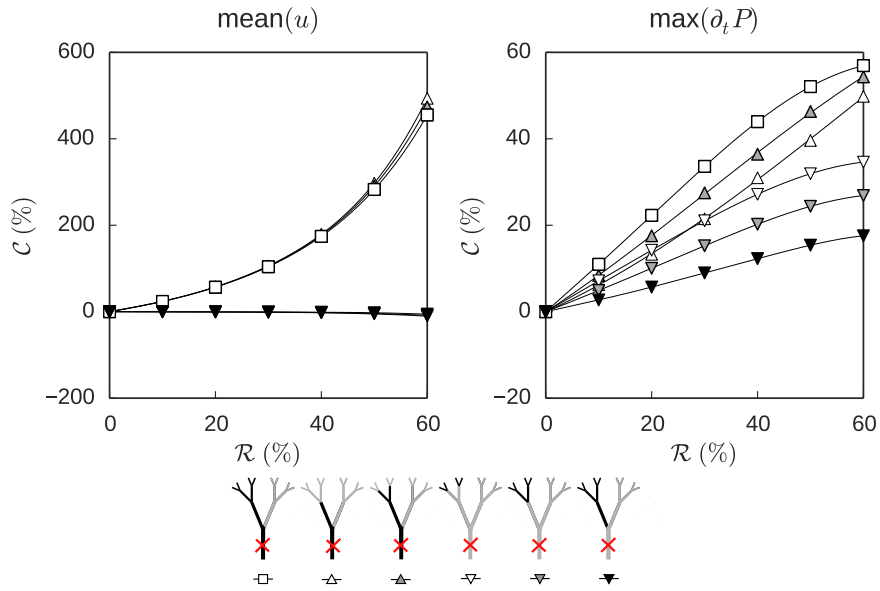

Figure 9.3.4: Percent change of CVS biomarkers as the lumen radius decreases in the case of asymmetric CVS occurring in an adult generic subject. The CVS biomarker is reported above each plot and the lumen radius reduction location is indicated by the markers shape and colour.

generations I, II, and III causes a small (20%) increase.

In Figure 9.3.5, the velocity and pressure biomarkers are reported for the three age groups studied, in the case of symmetric and asymmetric global CVS. The numerical solution failed to converge in the case of 60% radius reduction for the elder subject due to numerical instabilities caused by the presence of thin and stiff peripheral vessels. In all the cases, the velocity biomarker increases quadratically as the vessel radii decrease. Symmetric and asymmetric curves have the same behaviour for lumen reduction between 0 and 50%, when the increase in mean velocity is of the 275%. The maximum change in mean(u), 475%, is obtained for the severe symmetric CVS (60% reduction) case, whereas in the severe asymmetric case the maximum mean(u) change is of the 400%. The distinction between symmetric and asymmetric cases is clear for the pressure biomarker. The biomarker increase is linear with the lumen radius reduction for all the ages, but the rate of change depends on the CVS case. Symmetric CVS causes the pressure biomarker to increase faster than the asymmetric one, e.g., 20% radius reduction causes 50% and 20% change of the pressure biomarker in the symmetric and asymmetric cases, respectively. In the case of severe CVS, the difference between the two cases is more evident, as the CVS causes an increase of 120% and 50% for the symmetric and asym-

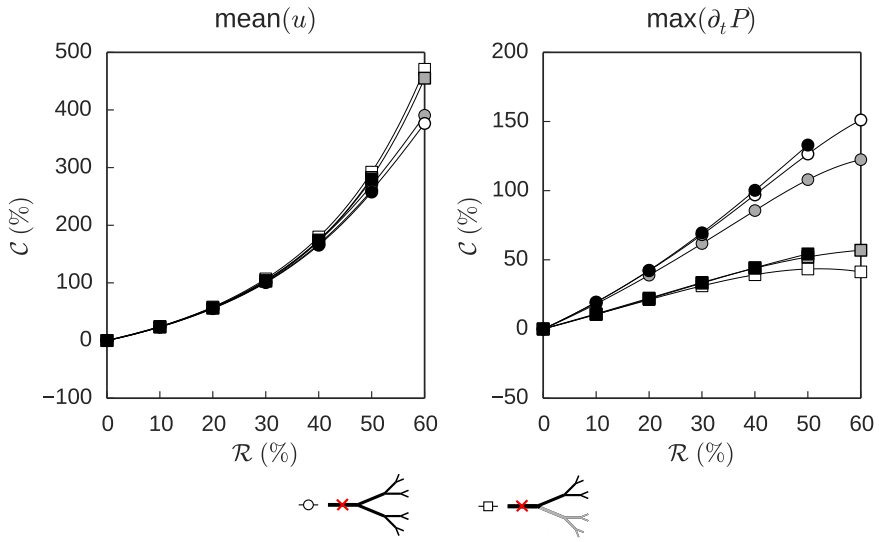

Figure 9.3.5: Percent change of three CVS biomarkers against the percent change of lumen radius. Each curve is related to a different age group: young (white), adult (gray), and old (black). The symmetric CVS results are indicated by round markers and the asymmetric CVS ones are indicated by the squared markers.

metric cases, respectively. However, the increase rate does not depend on the age group as the age effect is small in comparison to the variation due to the change of CVS configuration. This, as also reported in (Inagawa, 2016), indicates that the age does not play an important role in the case of SAH.

9.4 Discussion and Conclusions

CVS is the progressive narrowing of intracranial arteries following SAH. Currently, the mechanism of CVS is not fully understood and the diagnosis process relies on TCD measurements of mean blood velocity repeated in time. The velocity biomarker is capable of detecting CVS in the case of TCD measurements directly performed on the narrowing vessel. In the case of peripheral narrowing, the velocity biomarker prediction ability is lost and the CVS is not detected until the condition becomes severe. The aim of this study was to identify more efficient biomarkers capable of detecting and characterising different CVS typologies.

A mechanistic 1D model of the cerebral circulation was developed to characterise blood pressure waveforms. A pool of CVS biomarkers was identified through SA on waveform features. The sought biomarkers are all those waveform features whose

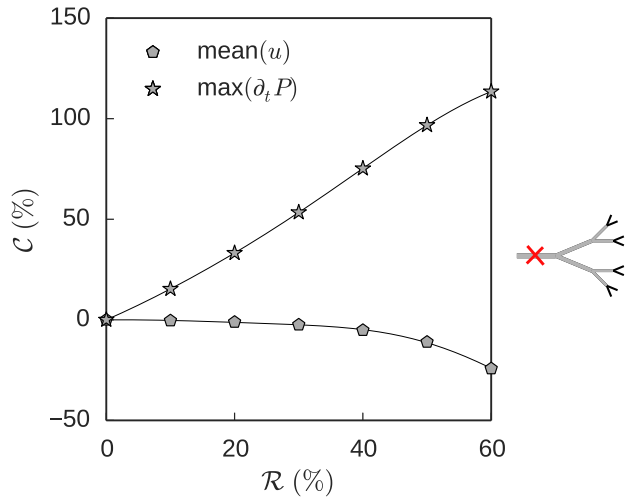

Figure 9.4.1: Comparison between the time-average velocity biomarker and the pressure maximum-gradient biomarker in the case of peripheral cerebral vasospasm for the adult-generic subject. The pressure biomarker is responsive to small changes in radius (>10%) whereas the velocity biomarker starts changing only in the case of severe vasospasm (>40%).

variation is caused by changes in mechanical properties due to CVS. A computationally efficient exploration of the parameter space in a 1D model of the cerebral circulation was performed by means of GP emulation, that reduced of the 95% computational cost of the analysis with respect to a Monte Carlo analysis.

A CVS occurring at the measurement location caused an increase (more than 450%) of the velocity biomarker. However, when the CVS occurred more peripherally (Figure 9.4.1), the velocity biomarker was only marginally affected by the vessel lumen reduction (mean(u) decreased by approximately 20% when vessel narrowing was 60%). The decrease was due to the increase in peripheral resistance and, in turn, to the flow diversion towards the ICA. Therefore, biomarkers related to the velocity waveform are not good predictors for CVS in distal arteries. Conversely, the maximum gradient of the pressure waveform was sensitive to CVS in both proximal and distal arteries. Increase (up to 150%) of this biomarker occurred for all the CVS configurations tested. Furthermore, the newly identified CVS biomarker, max($\partial_t P$), was only marginally influenced by changes in Young's modulus within a physiological range representative of an ageing healthy individual.

Velocity biomarker results were in agreement with previously published numerical and experimental works, where an increase in mean(u) was associated with decrease in MCA lumen radius (Harders and Gilsbach, 1987; Lodi and Ursino, 1999).

However, while the numerical model accurately predicted the velocity biomarkers, the analysis was limited to the MCA and the surrounding cerebral network. In addition, the numerical model lacks a representation of the auto-regulation system, therefore a further improvement of the numerical model would consist in the development of a larger vascular network, including the whole circle of Willis, both sides of the cerebral circulation, and a representation of the auto-regulation mechanism. This network could be used to identify better measurement locations for monitoring early CVS onset. Alongside, the numerical results can be used as hypothesis to inform novel clinical diagnostic approaches and technology development, and to validate the newly found biomarker prediction accuracy.

10 Conclusions

The aim of this project was to develop an efficient framework for performing the sensitivity analysis of 1D numerical vascular models. The computational benefit of using Gaussian process emulators to generate the dataset required for the sensitivity analysis was shown. The main contribution of this thesis is the novel application of GP approach and the identification of the GP training dataset size required to perform a sensitivity analysis with 1% error from the Monte Carlo simulation. An application was presented where this technique was applied to the case of cerebral vasospasm and enabled the early onset detection and classification of the pathology.

The 1D vascular model presented in Chapter 3 was solved by means of a finite-volume algorithm. The numerical solver was validated against other numerical solution and experimental measurements published in the literature. The developed solver matched the literature results in the case of simple arterial networks (single vessel and single bifurcation). In the case of the complete model (ADAN56) the results are in agreement and the differences between the waveforms are due to the use of different constitutive equations: linear-elastic in the case of the present study and visco-elastic for the results from the literature. The comparison with the in-vitro model showed a good agreement between the waveforms mean behaviour. The in-vitro model employed simply resistive outlet that caused wide oscillations; in the proposed numerical model these oscillations were avoided by using a three element windkessel model as outlet boundary condition. The comparison with the Circle of Willis model showed a good agreement in terms of the waveforms computed by the two studies. The numerical solutions were qualitatively identical to the waveforms measured in-vivo.

In Chapters 4 and 5 the sensitivity analysis and Gaussian process methodologies were reported. In particular, the sensitivity analysis methods based on graphical and variance analysis were shown by means of a simple example. The Gaussian process methodology was reported with particular regards on the concepts of kernel and its optimisation. Eventually, the problem of sampling was presented and the Latin hypercube method was introduced.

A first application of the Gaussian process for sensitivity analysis of the 1D vas-

cular model was reported in Chapter 7. The sensitivity of waveform features to inputs variation was studied in the case of a single cerebral bifurcation. The process of emulator training and verification was shown and the results in terms of computational efficiency were reported. The sensitivity analysis results were consistent with those obtained from the Monte Carlo analysis.

In Chapter 8, the scalability of the proposed methodology was analysed. In particular four vascular networks of increasing complexity were modelled. The Gaussian process outcomes were compared with the Monte Carlo analysis results to identify the sample size required to achieve a prediction error lower than 1%. As a result, the sample size is of the same order of the number of parameters in the network. This reduced the computational time needed by the sensitivity analysis of the 99.96%. The scalability study was published in (Melis et al., 2017).

In Chapter 9, the proposed mechanistic model was used to describe pressure waveforms in cerebral circulation affected by cerebral vasospasm. This model was used to identify a more sensitive cerebral vasospasm biomarker than those currently used in clinical practice. In particular, the mean velocity measured by trans-cranial Doppler does not detect distal cerebral vasospasm whereas the maximum gradient of the pressure waveform is capable of differentiating between location and severity of cerebral vasospasm. The newly identified biomarker can be used as an additional diagnostic metric. The results suggest that cerebral vasospasm could be detected earlier even in the case of peripheral onset. The biomarkers were selected by means of the sensitivity analysis efficiently performed with Gaussian process emulators. As a future work, the numerical model will be expanded to include the whole cerebral circulation and a necessary step will consists in experimental testing of the new biomarker on patient specific measurements.

10.1 Key Findings

The thesis aim and objectives as stated in Section 1.1 were satisfied by the results reported in the Methodology and Applications part, and summarised in the previous paragraphs. The main contributions of this work to the research field of vascular modelling are outlined here:

The validated 1D numerical solver **openBF** has been released under Apache 2.0[1] open-source license and it is free for use, reproduction, and distribution. This was done in the view of foster collaboration within the vascular modelling community and to provide a starting point for future development of the solver. To the author knowledge this is the first open-source finite-volume solver to be released in the vascular modelling community.

[1] https://www.apache.org/licenses/LICENSE-2.0

The use of Gaussian process and statistical emulators in the vascular modelling field is novel. The computational time required to perform the sensitivity analysis of a full size model was reduced by 99.6% while maintaining the prediction error below the 1% with respect to the Monte Carlo analysis results.

The scalability study in Chapter 8 and published in (Melis et al., 2017) provides novel results also for the Machine Learning research community. The main result indicates that the training data sample size w.r.t. d the number of inputs in the deterministic model is $O(d)$. While not fundamental in the machine learning scenario, where training points are usually cheap to obtain, this result is relevant for computationally demanding deterministic simulations.

The fast training and reduced computational power required by the novel SA workflow proved to be useful when analysing pulse waveforms. The cerebral vasospasm study in Chapter 9 showed how waveform features can be extracted via a SA and these can be rich in information about peripheral areas of the vascular network.

10.2 Limitations

The mathematical model reported in Chapter 3 currently lacks several features. The most important are herein listed in order of significance:

1. A model of the heart providing the inlet boundary condition to the network root. The heart model would avoid spurious reflections due to the one-way coupling of the network with a fixed time-varying flow function. Moreover, a parameterised model heart would provide the possibility of adapting the cardiac output to cover the variability among subjects.

2. A constitutive equation describing visco-elastic and collapsible behaviour. The former would allow a better matching of the numerical solution with published results (Section 6.2.3). The latter is needed to describe the flow in veins and it would be the first step toward the implementation of a full closed loop of the systemic circulation.

3. The treatment of pressure losses due to bends and bifurcation angles. Although empirical laws can be applied, these require loss coefficients to be specified and possibly measured experimentally in-vitro.

4. The representation of gravitational effects on the blood flow. These are of crucial importance in the view of studying the effect of human movement on blood flow distribution.

10.3 Future works

The simulation of pulse wave propagation and reflection in vessel networks is a well-known tool in the biomechanical community. These methods have been proved useful to predict and describe the complex behaviour of blood waveforms in the clinical set-up. A limitation of these models consists in the large number of parameters to be measured on the subject to inform the computational analysis. The methodology described in this thesis allows to effectively perform the sensitivity analysis of the necessary parameters. The numerical model dimensionality can be reduced and the parameters measurement process can be efficiently guided. The proposed methodology based on Gaussian process emulators was aimed at the description of pulse waveform features. The computed emulators were not used to generate the full time-series. A further development of the methodology would explicitly take into account the time variable to represent the whole waveform rather than only its features. The reduced computational time allows to include in the numerical model additional physiological aspects. A multi-scale approach could be explored with the 1D model taking into account the wave propagation, 0D models describing the auto-regulation feedback loop, and 3D models solving the flow-structure-interaction in complex geometries. This multi-scale model could be used for a thorough parameter-sweep study considering the physiological ranges for each input. The outcomes of this study would be used to train a series of Gaussian process emulators able to predict waveforms for any physiological condition in a very short time. In a translational scenario, these emulators can provide a quick first assessment of the subject state without long computational wait time. In addition, the trained emulators can be used as exploration tool to test hypothesis and to guide the subsequent experimental and numerical studies.

Bibliography

Aaslid, R., Huber, P., and Nornes, H. (1984). Evaluation of cerebrovascular spasm with transcranial doppler ultrasound. *Journal of neurosurgery*, 60(1):37–41.

Abrahamsen, P. (1997). *A review of Gaussian random fields and correlation functions*. Norsk Regnesentral/Norwegian Computing Center.

Aizerman, M., Braverman, È., and Rozonoer, L. (1964). Probability problem of pattern recognition learning and potential functions method. *Avtomat. i Telemekh*, 25(9):1307–1323.

Ajmani, R., Metter, E., Jaykumar, R., Ingram, D., Spangler, E., Abugo, O., and Rifkind, J. (2000). Hemodynamic changes during aging associated with cerebral blood flow and impaired cognitive function. *Neurobiology of aging*, 21(2):257–269.

Alastruey, J., Khir, A., Matthys, K., Segers, P., Sherwin, S., Verdonck, P., Parker, K., and Peiró, J. (2011). Pulse wave propagation in a model human arterial network: assessment of 1-d visco-elastic simulations against in vitro measurements. *Journal of biomechanics*, 44(12):2250–2258.

Alastruey, J., Parker, K., Peiró, J., Byrd, S., and Sherwin, S. (2007). Modelling the circle of willis to assess the effects of anatomical variations and occlusions on cerebral flows. *Journal of biomechanics*, 40(8):1794–1805.

Alastruey, J., Parker, K., Peiró, J., and Sherwin, S. (2008). Lumped parameter outflow models for 1-d blood flow simulations: effect on pulse waves and parameter estimation. *Communications in Computational Physics*, 4(2):317–336.

Alastruey, J., Passerini, T., Formaggia, L., and Peiró, J. (2012). Physical determining factors of the arterial pulse waveform: theoretical analysis and calculation using the 1-d formulation. *Journal of Engineering Mathematics*, 77(1):19–37.

Anderson Jr., J. (1995). *Computational Fluid Dynamics*. McGraw-Hill Science/Engineering/Math, 1 edition.

Anderson Jr., J. (2001). *Fundamentals of Aerodynamics (Mcgraw-Hill Series in Aeronautical and Aerospace Engineering)*. McGraw-Hill Science/Engineering/Math, 3 edition.

Anderson Jr, J. (2010). *Fundamentals of aerodynamics*. Tata McGraw-Hill Education.

Andersson, M., Lantz, J., and Karlsson, M. (2011). Modeling of subject arterial segments using 3d fluid structure interaction and 1d-0d arterial tree network boundary condition.

Anliker, M., Rockwell, R., and Ogden, E. (1971). Nonlinear analysis of flow pulses and shock waves in arteries. *Zeitschrift für angewandte Mathematik und Physik ZAMP*, 22(2):217–246.

Avolio, A. (1980). Multi-branched model of the human arterial system. *Medical & biological engineering & computing*, 18(6):709–18.

Avolio, A., Butlin, M., and Walsh, A. (2010). Arterial blood pressure measurement and pulse wave analysis–their role in enhancing cardiovascular assessment. *Physiological measurement*, 31(1):R1–47.

Azer, K. and Peskin, C. (2007). A one-dimensional model of blood flow in arteries with friction and convection based on the womersley velocity profile. *Cardiovascular Engineering*, 7(2):51–73.

Baek, S., Valentin, A., and Humphrey, J. (2007). Biochemomechanics of cerebral vasospasm and its resolution: II. constitutive relations and model simulations. *Annals of biomedical engineering*, 35(9):1498–1509.

Balar, S., Rogge, T., and Young, D. (1989). Computer simulation of blood flow in the human arm. *Journal of biomechanics*, 22(6-7):691–697.

Barnard, A., Hunt, W., Timlake, W., and Varley, E. (1966). A theory of fluid flow in compliant tubes. *Biophysical journal*, 6(6):717.

Bastos, L. and O'Hagan, A. (2009). Diagnostics for gaussian process emulators. *Technometrics*, 51(4):425–438.

Becker, W., Rowson, J., Oakley, J., Yoxall, A., Manson, G., and Worden, K. (2011). Bayesian sensitivity analysis of a model of the aortic valve. *Journal of biomechanics*, 44(8):1499–1506.

Benetos, A., Waeber, B., Izzo, J., Mitchell, G., Resnick, L., Asmar, R., and Safar, M. (2002). Influence of age, risk factors, and cardiovascular and renal disease on arterial stiffness: clinical applications. *American journal of hypertension*, 15(12):1101–1108.

Bezanson, J., Edelman, A., Karpinski, S., and Shah, V. (2014). Julia: A fresh approach to numerical computing. *arXiv preprint arXiv:1411.1607*.

Bishop, C. (2006). *Pattern recognition and machine learning*. Springer.

Blanco, P., Urquiza, S., and Feijóo, R. (2010). Assessing the influence of heart rate in local hemodynamics through coupled 3d-1d-0d models. *International Journal for Numerical Methods in Biomedical Engineering*, 26(7):890–903.

Blanco, P., Watanabe, S., Dari, E., Passos, M., and Feijóo, R. (2014). Blood flow distribution in an anatomically detailed arterial network model: criteria and algorithms. *Biomechanics and modeling in mechanobiology*, 13(6):1303–1330.

Blanco, P., Watanabe, S., Passos, M., Lemos, P., and Feijóo, R. (2015). An anatomically detailed arterial network model for one-dimensional computational hemodynamics. *IEEE Transactions on Biomedical Engineering*, 62(2):736–753.

Boileau, E., Nithiarasu, P., Blanco, P., Müller, L., Fossan, F., Hellevik, L., Donders, W., Huberts, W., Willemet, M., and Alastruey, J. (2015). A benchmark study of numerical schemes for one-dimensional arterial blood flow modelling. *International journal for numerical methods in biomedical engineering*, 31(10).

Borelli, G. (1989). De motu animalium (1680). *Translated as on the movement of animals, translated by Maquet P) Springer-Verlag, Berlin*.

Broomé, M., Maksuti, E., Bjällmark, A., Frenckner, B., and Janerot-Sjöberg, B. (2013). Closed-loop real-time simulation model of hemodynamics and oxygen transport in the cardiovascular system. *Biomedical engineering online*, 12(1):1.

Brown, A., Shi, Y., Marzo, A., Staicu, C., Valverde, I., Beerbaum, P., Lawford, P., and Hose, D. (2012). Accuracy vs. computational time: translating aortic simulations to the clinic. *Journal of biomechanics*, 45(3):516–523.

Brown, D. (1996). Input impedance and reflection coefficient in fractal-like models of asymmetrically branching compliant tubes. *IEEE transactions on biomedical engineering*, 43(7):715–722.

Čanic, S., Hartley, C., Rosenstrauch, D., Tambača, J., Guidoboni, G., and Mikelic, A. (2006). Blood flow in compliant arteries: an effective viscoelastic reduced model, numerics, and experimental validation. *Annals of Biomedical Engineering*, 34(4):575–592.

Čanic, S. and Kim, E. (2003). Mathematical analysis of the quasilinear effects in a hyperbolic model blood flow through compliant axi-symmetric vessels. *Mathematical Methods in the Applied Sciences*, 26(14):1161–1186.

Cárdenas, I., Al-Jibouri, S., Halman, J., and Tol, F. (2014). Modeling risk-related knowledge in tunneling projects. *Risk analysis*, 34(2):323–339.

Cassot, F., Zagzoule, M., and Marc-Vergnes, J. (2000). Hemodynamic role of the circle of willis in stenoses of internal carotid arteries. an analytical solution of a linear model. *Journal of Biomechanics*, 33(4):395–405.

Casulli, V., Dumbser, M., and Toro, E. (2012). Semi-implicit numerical modeling of axially symmetric flows in compliant arterial systems. *International journal for numerical methods in biomedical engineering*, 28(2):257–272.

Chen, P., Quarteroni, A., and Rozza, G. (2013). Simulation-based uncertainty quantification of human arterial network hemodynamics. *International journal for numerical methods in biomedical engineering*, 29(6):698–721.

Clavica, F., Alastruey, J., Borlotti, A., Sherwin, S., and Khir, A. (2010). One-dimensional computational model of pulse wave propagation in the human bronchial tree. In *Engineering in Medicine and Biology Society (EMBC), 2010 Annual International Conference of the IEEE*, pages 2473–2476. IEEE.

Courant, R., Friedrichs, K., and Lewy, H. (1928). Über die partiellen differenzengleichungen der mathematischen physik. *Mathematische annalen*, 100(1):32–74.

Courant, R., Friedrichs, K., and Lewy, H. (1967). On the partial difference equations of mathematical physics. *IBM journal*, 11(2):215–234.

Cressie, N. (1993). Statistics for spatial data: Wiley series in probability and statistics. *Wiley-Interscience, New York*, 15:105–209.

Cukier, R., Fortuin, C., Shuler, K. E., Petschek, A., and Schaibly, J. (1973). Study of the sensitivity of coupled reaction systems to uncertainties in rate coefficients. i theory. *The Journal of chemical physics*, 59(8):3873–3878.

Donders, W., Huberts, W., van de Vosse, F., and Delhaas, T. (2015). Personalization of models with many model parameters: an efficient sensitivity analysis approach. *International Journal for Numerical Methods in Biomedical Engineering*.

Dumbser, M., Iben, U., and Ioriatti, M. (2015). An efficient semi-implicit finite volume method for axially symmetric compressible flows in compliant tubes. *Applied Numerical Mathematics*, 89:24–44.

Duvenaud, D., Lloyd, J., Grosse, R., Tenenbaum, J., and Ghahramani, Z. (2013). Structure discovery in nonparametric regression through compositional kernel search. In *ICML (3)*, pages 1166–1174.

Eck, V., Donders, W., Sturdy, J., Feinberg, J., Delhaas, T., Hellevik, L., and Huberts, W. (2015a). A guide to uncertainty quantification and sensitivity analysis for cardiovascular applications. *International journal for numerical methods in biomedical engineering*.

Eck, V., Feinberg, J., Langtangen, H., and Hellevik, L. (2015b). Stochastic sensitivity analysis for timing and amplitude of pressure waves in the arterial system. *International journal for numerical methods in biomedical engineering*, 31(4).

Ellwein, L., Tran, H., Zapata, C., Novak, V., and Olufsen, M. (2008). Sensitivity analysis and model assessment: mathematical models for arterial blood flow and blood pressure. *Cardiovascular Engineering*, 8(2):94–108.

Euler, L. (1844). Principia pro motu sanguinis per arterias determinando. *Opera posthuma mathematica et physica anno*, pages 814–823.

Fehnel, C., Wendell, L., Potter, N., Klinge, P., and Thompson, B. (2014). Severe cerebral vasospasm after traumatic brain injury. *Rhode Island Medical Journal*, 97(7).

Fernández, M., Milisic, V., and Quarteroni, A. (2005). Analysis of a geometrical multiscale blood flow model based on the coupling of odes and hyperbolic pdes. *Multiscale Modeling & Simulation*, 4(1):215–236.

Ferrari, A., Radaelli, A., and Centola, M. (2003). Invited review: aging and the cardiovascular system. *Journal of Applied Physiology*, 95(6):2591–2597.

Findlay, J., Nisar, J., and Darsaut, T. (2015). Cerebral vasospasm: a review. *Canadian Journal of Neurological Sciences/Journal Canadien des Sciences Neurologiques*, pages 1–18.

Flores, J., Alastruey, J., and Poiré, E. (2016). A novel analytical approach to pulsatile blood flow in the arterial network. *Annals of biomedical engineering*, 44(10):3047–3068.

Fontana, J., Wenz, H., Schmieder, K., and Barth, M. (2015). Impairment of dynamic pressure autoregulation precedes clinical deterioration after aneurysmal subarachnoid hemorrhage. *Journal of Neuroimaging*.

Formaggia, L., Gerbeau, J., Nobile, F., and Quarteroni, A. (2001). On the coupling of 3d and 1d navier–stokes equations for flow problems in compliant vessels. *Computer Methods in Applied Mechanics and Engineering*, 191(6):561–582.

Formaggia, L., Lamponi, D., and Quarteroni, A. (2003). One-dimensional models for blood flow in arteries. *Journal of engineering mathematics*, 47(3-4):251–276.

Formaggia, L., Lamponi, D., Tuveri, M., and Veneziani, A. (2006). Numerical modeling of 1d arterial networks coupled with a lumped parameters description of the heart. *Computer methods in biomechanics and biomedical engineering*, 9(5):273–288.

Formaggia, L., Nobile, F., Quarteroni, A., and Veneziani, A. (1999). Multiscale modelling of the circulatory system: a preliminary analysis. *Computing and visualization in science*, 2(2-3):75–83.

Formaggia, L., Quarteroni, A., and Veneziani, A. (2010). *Cardiovascular Mathematics: Modeling and simulation of the circulatory system*, volume 1. Springer Science & Business Media.

Fourier, J. (1822). *Theorie analytique de la chaleur, par M. Fourier*. Chez Firmin Didot, père et fils.

Frank, O. (1899). Die grundform des arteriellen pulses. *Z Biol*, 37(483-526):19.

Fung, Y. (2010). *Biomechanics: Circulation*. Springer, 2nd edition.

Gaddum, N., Alastruey, J., Beerbaum, P., Chowienczyk, P., and Schaeffter, T. (2013). A technical assessment of pulse wave velocity algorithms applied to non-invasive arterial waveforms. *Annals of biomedical engineering*, 41(12):2617–2629.

Genton, M. (2001). Classes of kernels for machine learning: a statistics perspective. *Journal of machine learning research*, 2(Dec):299–312.

Godunov, S. (1959). A difference method for numerical calculation of discontinuous solutions of the equations of hydrodynamics. *Matematicheskii Sbornik*, 89(3):271–306.

Gozna, E., Marble, A., Shaw, A., and Holland, J. (1974). Age-related changes in the mechanics of the aorta and pulmonary artery of man. *Journal of Applied Physiology*, 36(4):407–411.

GPy (since 2012). GPy: A gaussian process framework in python. `http://github.com/SheffieldML/GPy`.

Grinberg, L., Cheever, E., Anor, T., Madsen, J., and Karniadakis, G. (2011). Modeling blood flow circulation in intracranial arterial networks: a comparative 3d/1d simulation study. *Annals of biomedical engineering*, 39(1):297–309.

Guinot, V. (2012). *Wave propagation in fluids: models and numerical techniques*. John Wiley & Sons.

Guyton, A. and Hall, J. (2006). *Textbook of medical physiology*. Elsevier Saunders.

Hagen, G. (1839). Ueber die bewegung des wassers in engen cylindrischen röhren. *Annalen der Physik*, 122(3):423–442.

Hagenbach, E. (1860). Ueber die bestimmung der zähigkeit einer flüssigkeit durch den ausfluss aus röhren. *Annalen der Physik*, 185(3):385–426.

Hale, J., McDonald, D., and Womersley, J. (1955). Velocity profiles of oscillating arterial flow, with some calculations of viscous drag and the reynolds number. *The Journal of physiology*, 128(3):629–640.

Hales, S. (1964). *Statical essays, containing haemastaticks*. Number 22. Hafner Pub. Co.

Harders, A. and Gilsbach, J. (1987). Time course of blood velocity changes related to vasospasm in the circle of willis measured by transcranial doppler ultrasound. *Journal of neurosurgery*, 66(5):718–728.

Harten, A., Engquist, B., Osher, S., and Chakravarthy, S. (1987). Uniformly high order accurate essentially non-oscillatory schemes, iii. In *Upwind and High-Resolution Schemes*, pages 218–290. Springer.

Harvey, W. (1928). Exercitatio anatomica de motu cordis et sanguinis in animalibus. *Frankfurt am Main*, 1628.

Hayashi, K., Handa, H., Nagasawa, S., Okumura, A., and Moritake, K. (1980). Stiffness and elastic behavior of human intracranial and extracranial arteries. *Journal of biomechanics*, 13(2):175181–179184.

Helps, E. and McDonald, D. (1953). Systolic backflow in the dog femoral artery. In *Journal of Physiology*, volume 122, pages P73–P73. Cambridge University Press, New York, NY.

Helton, J. (1993). Uncertainty and sensitivity analysis techniques for use in performance assessment for radioactive waste disposal. *Reliability Engineering & System Safety*, 42(2-3):327–367.

Hisland, M. and Anliker, M. (1973). Influence of flow and pressure on wave propagation in the canine aorta. *Circulation research*, 32(4):524–529.

Huberts, W., Bode, A., Kroon, W., Planken, R., Tordoir, J., van de Vosse, F., and Bosboom, E. (2012). A pulse wave propagation model to support decision-making in vascular access planning in the clinic. *Medical engineering & physics*, 34(2):233–248.

Huberts, W., de Jonge, C., van der Linden, W., Inda, M., Passera, K., Tordoir, J., van de Vosse, F., and Bosboom, E. (2013a). A sensitivity analysis of a personalized pulse wave propagation model for arteriovenous fistula surgery. part b: Identification of possible generic model parameters. *Medical engineering & physics*, 35(6):827–837.

Huberts, W., de Jonge, C., van der Linden, W., Inda, M., Tordoir, J., van de Vosse, F., and Bosboom, E. (2013b). A sensitivity analysis of a personalized pulse wave propagation model for arteriovenous fistula surgery. part a: Identification of most influential model parameters. *Medical engineering & physics*, 35(6):810–826.

Huberts, W., de Jonge, C., van der Linden, W., Inda, M., Tordoir, J., van de Vosse, F., and Bosboom, E. (2013c). A sensitivity analysis of a personalized pulse wave propagation model for arteriovenous fistula surgery. part a: Identification of most influential model parameters. *Medical engineering & physics*, 35(6):810–826.

Huberts, W., Donders, W., Delhaas, T., and van de Vosse, F. (2014). Applicability of the polynomial chaos expansion method for personalization of a cardiovascular pulse wave propagation model. *International journal for numerical methods in biomedical engineering*, 30(12):1679–1704.

Humphrey, J., Baek, S., and Niklason, L. (2007). Biochemomechanics of cerebral vasospasm and its resolution: I. a new hypothesis and theoretical framework. *Annals of biomedical engineering*, 35(9):1485–1497.

Huo, Y. and Kassab, G. (2007). A hybrid one-dimensional/womersley model of pulsatile blood flow in the entire coronary arterial tree. *American Journal of Physiology-Heart and Circulatory Physiology*, 292(6):H2623–H2633.

Hussain, M., Barton, R., and Joshi, S. (2002). Metamodeling: radial basis functions, versus polynomials. *European Journal of Operational Research*, 138(1):142–154.

Inagawa, T. (2016). Risk factors for cerebral vasospasm following aneurysmal subarachnoid hemorrhage: A review of the literature. *World neurosurgery*, 85:56–76.

Iooss, B. and Lemaître, P. (2015). A review on global sensitivity analysis methods. In *Uncertainty Management in Simulation-Optimization of Complex Systems*, pages 101–122. Springer.

Jager, G., Westerhof, N., and Noordergraaf, A. (1965). Oscillatory flow impedance in electrical analog of arterial system: representation of sleeve effect and non-newtonian properties of blood. *Circulation research*, 16(2):121–133.

Janssen, P., Slob, W., and Rotmans, J. (1990). Sensitivity analysis and uncertainty analysis: an inventory of ideas, methods and techniques. *RIVM Report*, (958805001).

Kenner, T. (1989). The measurement of blood density and its meaning. *Basic research in cardiology*, 84(2):111–124.

Kenner, T., Leopold, H., and Hinghofer-Szalkay, H. (1977). The continuous high-precision measurement of the density of flowing blood. *Pflügers Archiv*, 370(1):25–29.

Kiparissides, A., Kucherenko, S., Mantalaris, A., and Pistikopoulos, E. (2009). Global sensitivity analysis challenges in biological systems modeling. *Industrial & Engineering Chemistry Research*, 48(15):7168–7180.

Kolias, A., Sen, J., and Belli, A. (2009). Pathogenesis of cerebral vasospasm following aneurysmal subarachnoid hemorrhage: putative mechanisms and novel approaches. *Journal of neuroscience research*, 87(1):1–11.

Korteweg, D. (1878). Ueber die fortpflanzungsgeschwindigkeit des schalles in elastischen röhren. *Annalen der Physik*, 241(12):525–542.

Kumar, G., Shahripour, R., and Harrigan, M. (2015). Vasospasm on transcranial doppler is predictive of delayed cerebral ischemia in aneurysmal subarachnoid hemorrhage: a systematic review and meta-analysis. *Journal of neurosurgery*, pages 1–8.

Lakatta, E. and Levy, D. (2003). Arterial and cardiac aging: major shareholders in cardiovascular disease enterprises part ii: the aging heart in health: links to heart disease. *Circulation*, 107(2):346–354.

Lambert, J. (1958). On the nonlinearities of fluid flow in nonrigid tubes. *Journal of the Franklin Institute*, 266(2):83–102.

Landau, L. and Lifshitz, E. (1959). Fluid mechanics (course of theoretical physics). *Vol. 6Pergamon, New York*.

Leguy, C., Bosboom, E., Belloum, A., Hoeks, A., and van de Vosse, F. (2011). Global sensitivity analysis of a wave propagation model for arm arteries. *Medical engineering & physics*, 33(8):1008–1016.

LeVeque, R. (1992). *Numerical methods for conservation laws*, volume 132. Springer.

LeVeque, R. (2002). *Finite volume methods for hyperbolic problems*, volume 31. Cambridge university press.

Lin, C., Dumont, A., Zhang, J., Zuccarello, M., and Muroi, C. (2014). Cerebral vasospasm after aneurysmal subarachnoid hemorrhage: mechanism and therapies. *BioMed research international*, 2014.

Lodi, C. and Ursino, M. (1999). Hemodynamic effect of cerebral vasospasm in humans: a modeling study. *Annals of biomedical engineering*, 27(2):257–273.

Low, K., van Loon, R., Sazonov, I., Bevan, R., and Nithiarasu, P. (2012). An improved baseline model for a human arterial network to study the impact of aneurysms on pressure-flow waveforms. *International journal for numerical methods in biomedical engineering*, 28(12):1224–1246.

Lungu, A., Wild, J., Capener, D., Kiely, D., Swift, A., and Hose, D. (2014). Mri model-based non-invasive differential diagnosis in pulmonary hypertension. *Journal of biomechanics*, 47(12):2941–2947.

Macdonald, R. (2016). Origins of the concept of vasospasm. *Stroke*, 47(1):e11–e15.

MacKay, D. (1998). Introduction to gaussian processes. *NATO ASI Series F Computer and Systems Sciences*, 168:133–166.

MacKay, D. (2003). *Information theory, inference and learning algorithms*. Cambridge university press.

Mackenzie, I., Wilkinson, I., and Cockcroft, J. (2002). Assessment of arterial stiffness in clinical practice. *Qjm*, 95(2):67–74.

Marchandise, E., Willemet, M., and Lacroix, V. (2009). A numerical hemodynamic tool for predictive vascular surgery. *Medical engineering & physics*, 31(1):131–144.

Mardia, K. and Marshall, R. (1984). Maximum likelihood estimation of models for residual covariance in spatial regression. *Biometrika*, 71(1):135–146.

Matérn, B. (2013). *Spatial variation*, volume 36. Springer Science & Business Media.

Matheron, G. (1973). The intrinsic random functions and their applications. *Advances in applied probability*, pages 439–468.

Matthys, K., Alastruey, J., Peiró, J., Khir, A., Segers, P., Verdonck, P., Parker, K., and Sherwin, S. (2007). Pulse wave propagation in a model human arterial network: assessment of 1-d numerical simulations against in vitro measurements. *Journal of biomechanics*, 40(15):3476–3486.

McDonald, D. (1952). The velocity of blood flow in the rabbit aorta studied with high-speed cinematography. *The Journal of physiology*, 118(3):328–339.

McDonald, D. (1955). The relation of pulsatile pressure to flow in arteries. *The Journal of physiology*, 127(3):533–552.

Melis, A., Clayton, R. H., and Marzo, A. (2017). Bayesian sensitivity analysis of a 1D vascular model with gaussian process emulators. *International Journal for Numerical Methods in Biomedical Engineering*, page e2882. cnm.2882.

Melis, A (since 2017). openBF: A simple Julia package for blood flow simulations within narrow elastic vessels. https://insigneo.github.io/openBF/.

Milišic, V. and Quarteroni, A. (2004). Analysis of lumped parameter models for blood flow simulations and their relation with 1d models. *ESAIM: Mathematical Modelling and Numerical Analysis-Modélisation Mathématique et Analyse Numérique*, 38(4):613–632.

Moens, A. (1877). Over de voortplantingssnelheid von den pols (on the speed of propagation of the pulse). *Acad. Profsch., Leiden*, 1:1–72.

Mohiuddin, M., Rihani, R., Laine, G., and Quick, C. (2012). Increasing pulse wave velocity in a realistic cardiovascular model does not increase pulse pressure with age. *American Journal of Physiology-Heart and Circulatory Physiology*, 303(1):H116–H125.

Moore, S., David, T., Chase, J., Arnold, J., and Fink, J. (2006). 3d models of blood flow in the cerebral vasculature. *Journal of biomechanics*, 39(8):1454–1463.

Morales, H., Larrabide, I., Geers, A., Aguilar, M., and Frangi, A. (2013). Newtonian and non-newtonian blood flow in coiled cerebral aneurysms. *Journal of biomechanics*, 46(13):2158–2164.

Mulder, G., Marzo, A., Bogaerds, A., Coley, S., Rongen, P., Hose, D., and van de Vosse, F. (2011). Patient-specific modeling of cerebral blood flow: geometrical variations in a 1d model. *Cardiovascular Engineering and Technology*, 2(4):334–348.

Müller, L., Montecinos, G., and Toro, E. (2012). Some issues in modelling venous haemodynamics. In *Numerical Methods for Hyperbolic Equations: Theory and Applications. An international conference to honour Professor EF Toro*, pages 347–354.

Müller, L., Parés, C., and Toro, E. (2013). Well-balanced high-order numerical schemes for one-dimensional blood flow in vessels with varying mechanical properties. *Journal of Computational Physics*, 242:53–85.

Müller, L. and Toro, E. (2013). Well-balanced high-order solver for blood flow in networks of vessels with variable properties. *International journal for numerical methods in biomedical engineering*, 29(12):1388–1411.

Müller, L. and Toro, E. (2014). A global multiscale mathematical model for the human circulation with emphasis on the venous system. *International journal for numerical methods in biomedical engineering*, 30(7):681–725.

Nardinocchi, P., Pontrelli, G., and Teresi, L. (2005). A one-dimensional model for blood flow in prestressed vessels. *European Journal of Mechanics-A/Solids*, 24(1):23–33.

Neal, R. (2012). *Bayesian learning for neural networks*, volume 118. Springer Science & Business Media.

Nichols, W. and O'Rourke, M. (2011). *McDonald's blood flow in arteries: theoretical, experimental, and clinical principles*. CRC Press.

Nichols, W., O'Rourke, M., Avolio, A., Yaginuma, T., Murgo, J., Pepine, C., and Conti, C. (1985). Effects of age on ventricular-vascular coupling. *The American journal of cardiology*, 55(9):1179–1184.

Nocedal, J. and Wright, S. (2006). *Numerical optimization*. Springer Science & Business Media.

Noordergraaf, A., Verdouw, P., and Boom, H. (1963). The use of an analog computer in a circulation model. *Progress in Cardiovascular Diseases*, 5(5):419–439.

Oakley, J. and O'Hagan, A. (2004). Probabilistic sensitivity analysis of complex models: a bayesian approach. *Journal of the Royal Statistical Society: Series B (Statistical Methodology)*, 66(3):751–769.

Oates, C. (2008). *Cardiovascular haemodynamics and Doppler waveforms explained*. Cambridge University Press.

O'Hagan, A. (2006). Bayesian analysis of computer code outputs: a tutorial. *Reliability Engineering & System Safety*, 91(10):1290–1300.

O'Hagan, A. (2013). Polynomial chaos: A tutorial and critique from a statistician's perspective, siam. *ASA J. Uncertain. Quantif.*

O'Hagan, A. and Forster, J. (2004). *Kendall's advanced theory of statistics, volume 2B: Bayesian inference*, volume 2. Arnold.

O'Hagan, A. and Kingman, J. (1978). Curve fitting and optimal design for prediction. *Journal of the Royal Statistical Society. Series B (Methodological)*, pages 1–42.

Olsen, C., Tran, H., Ottesen, J., Mehlsen, J., and Olufsen, M. (2015). Challenges in practical computation of global sensitivities with application to a baroreceptor reflex model. *PLOS Computational Biology (online)*.

Olufsen, M. (1999). Structured tree outflow condition for blood flow in larger systemic arteries. *American journal of physiology-Heart and circulatory physiology*, 276(1):H257–H268.

Olufsen, M., Peskin, C., Kim, W., Pedersen, E., Nadim, A., and Larsen, J. (2000). Numerical simulation and experimental validation of blood flow in arteries with structured-tree outflow conditions. *Annals of biomedical engineering*, 28(11):1281–1299.

Osnes, H. and Sundnes, J. (2012). Uncertainty analysis of ventricular mechanics using the probabilistic collocation method. *IEEE Transactions on Biomedical Engineering*, 59(8):2171–2179.

Paciorek, C. and Schervish, M. (2004). Nonstationary covariance functions for gaussian process regression. *Advances in neural information processing systems*, 16:273–280.

Parker, K. (2009a). A brief history of arterial wave mechanics. *Medical and Biological Engineering and Computing*, 47(2):111–118.

Parker, K. (2009b). An introduction to wave intensity analysis. *Medical & biological engineering & computing*, 47(2):175–188.

Parker, K. and Jones, C. (1990). Forward and backward running waves in the arteries: analysis using the method of characteristics. *Journal of biomechanical engineering*, 112(3):322–326.

Pearson, K. (1895). Note on regression and inheritance in the case of two parents. *Proceedings of the Royal Society of London*, 58:240–242.

Pedley, T. (1980). *The fluid mechanics of large blood vessels*, volume 1. Cambridge University Press Cambridge.

Peiró, J. and Veneziani, A. (2009). Reduced models of the cardiovascular system. In *Cardiovascular mathematics*, pages 347–394. Springer.

Persico, E. (1952). Introduzione alla fisica matematica.

Pluta, R., Hansen-Schwartz, J., Dreier, J., Vajkoczy, P., Macdonald, R., Nishizawa, S., Kasuya, H., Wellman, G., Keller, E., Zauner, A., et al. (2009). Cerebral vasospasm following subarachnoid hemorrhage: time for a new world of thought. *Neurological research*, 31(2):151–158.

Poiseuille, J. (1844). *Recherches expérimentales sur le mouvement des liquides dans les tubes de très-petits diamètres*. Imprimerie Royale.

Powell, M. (1987). Radial basis functions for multivariable interpolation: a review. In *Algorithms for approximation*, pages 143–167. Clarendon Press.

Press, W. (2007). *Numerical recipes 3rd edition: The art of scientific computing*. Cambridge university press.

Quarteroni, A. and Veneziani, A. (2003). Analysis of a geometrical multiscale model based on the coupling of ode and pde for blood flow simulations. *Multiscale Modeling & Simulation*, 1(2):173–195.

Raines, J., Jaffrin, M., and Shapiro, A. (1971). A computer simulation of the human arterial system. In *Proceedings of the 1971 Summer Computer Conference*, volume 2, pages 171–178.

Rasmussen, C. (1996). *Evaluation of Gaussian processes and other methods for non-linear regression*. PhD thesis, Citeseer.

Ratto, M., Castelletti, A., and Pagano, A. (2012). Emulation techniques for the reduction and sensitivity analysis of complex environmental models. *Environmental Modelling & Software*, 34:1–4.

Redheuil, A., Yu, W., Wu, C., Mousseaux, E., de Cesare, A., Yan, R., Kachenoura, N., Bluemke, D., and Lima, J. (2010). Reduced ascending aortic strain and distensibility earliest manifestations of vascular aging in humans. *Hypertension*, 55(2):319–326.

Reece, S. and Roberts, S. (2010). An introduction to gaussian processes for the kalman filter expert. In *Information Fusion (FUSION), 2010 13th Conference on*, pages 1–9. IEEE.

Reymond, P., Bohraus, Y., Perren, F., Lazeyras, F., and Stergiopulos, N. (2011). Validation of a patient-specific one-dimensional model of the systemic arterial tree. *American Journal of Physiology-Heart and Circulatory Physiology*, 301(3):H1173–H1182.

Reymond, P., Merenda, F., Perren, F., Rüfenacht, D., and Stergiopulos, N. (2009). Validation of a one-dimensional model of the systemic arterial tree. *American Journal of Physiology-Heart and Circulatory Physiology*, 297(1):H208–H222.

Riemann, B. (1876). *Gesammelte mathematische Werke und wissenschaftlicher Nachlass*, volume 1. BG Teubner.

Robinson, J., Walid, M., Hyun, S., O'Connell, R., Menard, C., and Bohleber, B. (2010). Computational modeling of hhh therapy and impact of blood pressure and hematocrit. *World neurosurgery*, 74(2):294–296.

Roloff, C., Bordás, R., Nickl, R., Mátrai, Z., Szaszák, N., Szilárd, S., and Thévenin, D. (2013). Investigation of the velocity field in a full-scale model of a cerebral aneurysm. *International Journal of Heat and Fluid Flow*, 43:212–219.

Sacks, J., Welch, W., Mitchell, T., and Wynn, H. (1989). Design and analysis of computer experiments. *Statistical science*, pages 409–423.

Saltelli, A. (2002). Making best use of model evaluations to compute sensitivity indices. *Computer Physics Communications*, 145(2):280–297.

Saltelli, A., Annoni, P., Azzini, I., Campolongo, F., Ratto, M., and Tarantola, S. (2010). Variance based sensitivity analysis of model output. design and estimator for the total sensitivity index. *Computer Physics Communications*, 181(2):259–270.

Saltelli, A., Chan, K., Scott, E., et al. (2000). *Sensitivity analysis*, volume 1. Wiley New York.

Saltelli, A., Ratto, M., Tarantola, S., and Campolongo, F. (2005). Sensitivity analysis for chemical models. *Chemical reviews*, 105(7):2811–2828.

Sankaran, S. and Marsden, A. (2011). A stochastic collocation method for uncertainty quantification and propagation in cardiovascular simulations. *Journal of biomechanical engineering*, 133(3):031001.

Sankaran, S., Moghadam, M., Kahn, A., Tseng, E., Guccione, J., and Marsden, A. (2012). Patient-specific multiscale modeling of blood flow for coronary artery bypass graft surgery. *Annals of biomedical engineering*, 40(10):2228–2242.

Santner, T., Williams, B., and Notz, W. (2013). *The design and analysis of computer experiments*. Springer Science & Business Media.

Seeger, M. (2000). Bayesian model selection for support vector machines, gaussian processes and other kernel classifiers. In *Proceedings of the 13th Annual Conference on Neural Information Processing Systems*, number EPFL-CONF-161324, pages 603–609.

Seeger, M. (2004). Gaussian processes for machine learning. *International journal of neural systems*, 14(02):69–106.

Segers, P., Dubois, F., De Wachter, D., and Verdonck, P. (1998). Role and relevancy of a cardiovascular simulator. *Cardiovascular Engineering*, 3:48–56.

Shapiro, A. (1977). Steady flow in collapsible tubes. *Journal of Biomechanical Engineering*, 99(3):126–147.

Sherwin, S., Formaggia, L., Peiró, J., and Franke, V. (2003a). Computational modelling of 1d blood flow with variable mechanical properties and its application to the simulation of wave propagation in the human arterial system. *International Journal for Numerical Methods in Fluids*, 43(6-7):673–700.

Sherwin, S., Franke, V., Peiró, J., and Parker, K. (2003b). One-dimensional modelling of a vascular network in space-time variables. *Journal of Engineering Mathematics*, 47(3-4):217–250.

Shi, Y., Lawford, P., and Hose, D. (2011). Review of zero-D and 1-D models of blood flow in the cardiovascular system. *Biomedical engineering online*, 10(1):33.

Shu, C. and Osher, S. (1988). Efficient implementation of essentially non-oscillatory shock-capturing schemes. *Journal of Computational Physics*, 77(2):439–471.

Sin, G., Gernaey, K., Neumann, M., van Loosdrecht, M., and Gujer, W. (2011). Global sensitivity analysis in wastewater treatment plant model applications: prioritizing sources of uncertainty. *Water research*, 45(2):639–651.

Skalak, R. (1972). Synthesis of a complete circulation. *Cardiovascular fluid dynamics*, 2:341–376.

Snyder, M., Rideout, V., and Hillestad, R. (1968). Computer modeling of the human systemic arterial tree. *Journal of Biomechanics*, 1(4):341–353.

Sobol, I. (2001). Global sensitivity indices for nonlinear mathematical models and their monte carlo estimates. *Mathematics and computers in simulation*, 55(1):271–280.

Song, X., Zhang, J., Zhan, C., Xuan, Y., Ye, M., and Xu, C. (2015). Global sensitivity analysis in hydrological modeling: Review of concepts, methods, theoretical framework, and applications. *Journal of hydrology*, 523:739–757.

Stein, M. (2012). *Interpolation of spatial data: some theory for kriging*. Springer Science & Business Media.

Stergiopulos, N., Young, D., and Rogge, T. (1992). Computer simulation of arterial flow with applications to arterial and aortic stenoses. *Journal of biomechanics*, 25(12):1477–1488.

Stettler, J., Niederer, P., and Anliker, M. (1981a). Theoretical analysis of arterial hemodynamics including the influence of bifurcations. *Annals of biomedical engineering*, 9(2):145–164.

Stettler, J., Niederer, P., Anliker, M., and Casty, M. (1981b). Theoretical analysis of arterial hemodynamics including the influence of bifurcations. part ii: critical evaluation of theoretical model and comparison with noninvasive measurements of flow patterns in normal and pathological cases. *Annals of biomedical engineering*, 9(2):165.

Suga, H. and Sagawa, K. (1974). Instantaneous pressure-volume relationships and their ratio in the excised, supported canine left ventricle. *Circulation research*, 35(1):117–126.

Sun, Y., Beshara, M., Lucariello, R., and Chiaramida, S. (1997). A comprehensive model for right-left heart interaction under the influence of pericardium and baroreflex. *American Journal of Physiology-Heart and Circulatory Physiology*, 272(3):H1499–H1515.

Toro, E. (1989). A fast riemann solver with constant covolume applied to the random choice method. *International Journal for Numerical Methods in Fluids*, 9(9):1145–1164.

Toro, E. (2001). *Shock-capturing methods for free-surface shallow flows*. Wiley.

Toro, E. (2009). *Riemann solvers and numerical methods for fluid dynamics: a practical introduction*. Springer Science & Business Media.

Toro, E. and Siviglia, A. (2013). Flow in collapsible tubes with discontinuous mechanical properties: mathematical model and exact solutions. *Communications in Computational Physics*, 13(02):361–385.

Toy, S., Melbin, J., and Noordergraaf, A. (1985). Reduced models of arterial systems. *IEEE transactions on biomedical engineering*, (2):174–176.

Turányi, T. (1990). Sensitivity analysis of complex kinetic systems. tools and applications. *Journal of Mathematical Chemistry*, 5(3):203–248.

van de Vosse, F. and Stergiopulos, N. (2011). Pulse Wave Propagation in the Arterial Tree. *Annual Review of Fluid Mechanics*, 43(1):467–499.

van Leer, B. (1979). Towards the ultimate conservative difference scheme. v. a second-order sequel to godunov's method. *Journal of computational Physics*, 32(1):101–136.

Vennin, S., Mayer, A., Li, Y., Fok, H., Clapp, B., Alastruey, J., and Chowienczyk, P. (2015). Noninvasive calculation of the aortic blood pressure waveform from the flow velocity waveform: a proof of concept. *American Journal of Physiology-Heart and Circulatory Physiology*, 309(5):H969–H976.

Viedma, A., Jimenez-Ortiz, C., and Marco, V. (1997). Extended willis circle model to explain clinical observations in periorbital arterial flow. *Journal of Biomechanics*, 30(3):265–272.

Virmani, R., Avolio, A., Mergner, W., Robinowitz, M., Herderick, E., Cornhill, J., Guo, S., Liu, T., Ou, D., and O'Rourke, M. (1991). Effect of aging on aortic morphology in populations with high and low prevalence of hypertension and atherosclerosis. comparison between occidental and chinese communities. *The American journal of pathology*, 139(5):1119.

von Mises, R. (2014). *Mathematical theory of probability and statistics*. Academic Press.

Wang, X., Fullana, J., and Lagrée, P. (2015). Verification and comparison of four numerical schemes for a 1d viscoelastic blood flow model. *Computer methods in biomechanics and biomedical engineering*, 18(15):1704–1725.

Weber, E. and Weber, W. (1825). *Wellenlehre auf Experimente gegründet oder über die Wellen tropfbarer Flüssigkeiten mit Anwendung auf die Schall-und Lichtwellen. Von den Brüdern Ernst Heinrich Weber... und Wilhelm Weber...* bei Gerhard Fleischer.

Weber, W. (1892). Theorie der durch wasser oder andere inkompressibele flüssigkeiten in elastischen röhren fortgepflanzten wellen. In *Wilhelm Weber's Werke*, pages 548–552. Springer.

Welch, W., Buck, R., Sacks, J., Wynn, H., Mitchell, T., and Morris, M. (1992). Screening, predicting, and computer experiments. *Technometrics*, 34(1):15–25.

Westerhof, B., Guelen, I., Stok, W., Wesseling, K., Spaan, J., Westerhof, N., Bos, W., and Stergiopulos, N. (2007). Arterial pressure transfer characteristics: effects of travel time. *American Journal of Physiology-Heart and Circulatory Physiology*, 292(2):H800–H807.

Westerhof, N., Bosman, F., De Vries, C., and Noordergraaf, A. (1969). Analog studies of the human systemic arterial tree. *Journal of biomechanics*, 2(2):121–143.

Westerhof, N., Elzinga, G., and Sipkema, P. (1971). An artificial arterial system for pumping hearts. *Journal of applied physiology*, 31(5):776–781.

Westerhof, N. and Noordergraaf, A. (1970). Arterial viscoelasticity: a generalized model: effect on input impedance and wave travel in the systematic tree. *Journal of Biomechanics*, 3(3):357–379.

Williams, C. (1998). Prediction with gaussian processes: From linear regression to linear prediction and beyond. In *Learning in graphical models*, pages 599–621. Springer.

Williams, C. and Rasmussen, C. (1996). Gaussian processes for regression.

Williams, C. and Rasmussen, C. (2006). Gaussian processes for machine learning. *the MIT Press*, 2(3):4.

Womersley, J. (1955). Method for the calculation of velocity, rate of flow and viscous drag in arteries when the pressure gradient is known. *The Journal of physiology*, 127(3):553–563.

Wu, Q., Cournède, P., and Mathieu, A. (2012). An efficient computational method for global sensitivity analysis and its application to tree growth modelling. *Reliability Engineering & System Safety*, 107:35–43.

Xiao, N., Alastruey, J., and Alberto Figueroa, C. (2014). A systematic comparison between 1-d and 3-d hemodynamics in compliant arterial models. *International journal for numerical methods in biomedical engineering*, 30(2):204–231.

Xiu, D. and Sherwin, S. (2007). Parametric uncertainty analysis of pulse wave propagation in a model of a human arterial network. *Journal of Computational Physics*, 226(2):1385–1407.

Xu, C. and Gertner, G. (2008). Uncertainty and sensitivity analysis for models with correlated parameters. *Reliability Engineering & System Safety*, 93(10):1563–1573.

Yaglom, A. (2004). *An introduction to the theory of stationary random functions*. Courier Corporation.

Young, T. (1800). The croonian lecture. on the functions of the heart and arteries. In *Abstracts of the Papers Printed in the Philosophical Transactions of the Royal Society of London*, volume 1, pages 314–316. The Royal Society.

Zamir, M. (2000). *The physics of pulsatile flow*, volume 3. Springer.

Zamir, M. (2005). *The physics of coronary blood flow*, volume 30. Springer.

Appendices

A Blood flow equations

A.1 Mathematical model

The blood vessel was modelled as a straight, narrow and long tube with compliant walls (Figure A.1.1) (Čanic and Kim, 2003; Nardinocchi et al., 2005). The flow was assumed axisymmetric and a cylindrical coordinates system, (z, r, φ), was defined having the z -axis along the vessel centreline.

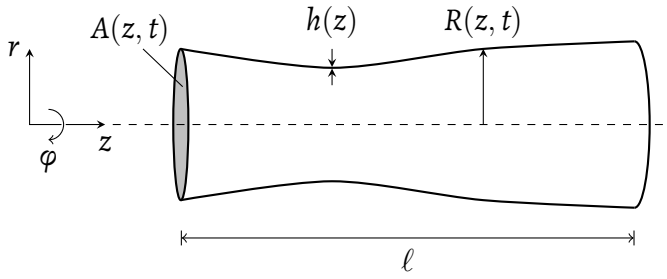

Figure A.1.1: One-dimensional axisymmetric vessel geometry. The vessel has a constant length ℓ, a time and space varying cross-sectional area $A = \pi R^2$, and the wall thickness h that can vary along the longitudinal direction

The flow model was developed by applying two fundamental conservation principles: the conservation of mass and the conservation of momentum. For a generic fluid, these two principles can be mathematically expressed in compact vectorial form (Anderson Jr, 2010) as

$$\frac{\partial \rho}{\partial t} + \nabla \cdot (\rho \mathbf{v}) = \mathbf{0}, \tag{A.1}$$

$$\frac{\partial \mathbf{v}}{\partial t} + (\mathbf{v} \cdot \nabla)\,\mathbf{v} = -\frac{1}{\rho}\nabla P + \frac{\mu}{\rho}\Delta \mathbf{v} + \mathbf{F}, \tag{A.2}$$

where t is the time variable, ρ is the fluid density, $\mathbf{v} = [v_z, v_r, v_\varphi]^T$ is the velocity

vector field, P is the pressure, μ is the fluid dynamic viscosity, and $\mathbf{F}$ represents all the body forces (e.g. gravitational force) acting on the fluid system.

The gravity affects the hydrostatic pressure acting on the blood flowing along each single vessel. In a network, this effect is important when studying the distribution of blood volume. This is relevant for veins which are more deformable than arteries and, depending on the subject posture, they contain up to 70% of whole blood volume. Here we will consider only arteries in supine subjects and the gravitational effect will be ignored.

The energy equation, which expresses the principle of conservation of energy, was not included. This is because the blood is assumed to be a homogeneous and incompressible fluid at constant temperature. Therefore, there are no temperature gradients inside the fluid, and there is no heat flux by conduction. We also assume that the heat generated by friction has a negligible effect and that there are no heat sources in the system. Eventually, we assume that the wall displacement is small so that the work done on the fluid is negligible.

Due to the assumption of incompressibility (i.e. ρ =const.) the continuity and momentum equations in cylindrical coordinates (Landau and Lifshitz, 1959) read

$$\frac{\partial v_z}{\partial z} + \frac{1}{r}\frac{\partial (r v_r)}{\partial r} + \frac{1}{r}\frac{\partial v_\varphi}{\partial \varphi} = 0, \tag{A.3}$$

$$\frac{\partial v_z}{\partial t} + v_z\frac{\partial v_z}{\partial z} + v_r\frac{\partial v_z}{\partial r} + \frac{v_\varphi}{r}\frac{\partial v_z}{\partial \varphi} = - \frac{1}{\rho}\frac{\partial P}{\partial z} + \frac{\mu}{\rho}\left[\frac{\partial^2 v_z}{\partial z^2} + \frac{\partial^2 v_z}{\partial r^2} + \frac{1}{r}\frac{\partial v_z}{\partial r} + \frac{1}{r^2}\frac{\partial^2 v_z}{\partial \varphi^2}\right], \tag{A.4}$$

$$\frac{\partial v_r}{\partial t} + v_z\frac{\partial v_r}{\partial z} + v_r\frac{\partial v_r}{\partial r} + \frac{v_\varphi}{r}\frac{\partial v_r}{\partial \varphi} - \frac{v_\varphi^2}{r} = - \frac{1}{\rho}\frac{\partial P}{\partial r} + \frac{\mu}{\rho}\left[\frac{\partial^2 v_r}{\partial z^2} + \frac{\partial^2 v_r}{\partial r^2} + \frac{1}{r}\frac{\partial v_r}{\partial r} + \frac{1}{r^2}\frac{\partial^2 v_r}{\partial \varphi^2} - \frac{2}{r^2}\frac{\partial v_\varphi}{\partial \varphi} - \frac{v_r}{r^2}\right], \tag{A.5}$$

$$\frac{\partial v_\varphi}{\partial t} + v_z\frac{\partial v_\varphi}{\partial z} + v_r\frac{\partial v_\varphi}{\partial r} + \frac{v_\varphi}{r}\frac{\partial v_\varphi}{\partial \varphi} - \frac{v_r v_\varphi}{r} = - \frac{1}{\rho}\frac{\partial P}{\partial \varphi} + \frac{\mu}{\rho}\left[\frac{\partial^2 v_\varphi}{\partial z^2} + \frac{\partial^2 v_\varphi}{\partial r^2} + \frac{1}{r}\frac{\partial v_\varphi}{\partial r} + \frac{1}{r^2}\frac{\partial^2 v_\varphi}{\partial \varphi^2} - \frac{2}{r^2}\frac{\partial v_r}{\partial \varphi} - \frac{v_\varphi}{r^2}\right]. \tag{A.6}$$

By assuming axisymmetric flow, the φ -wise velocity component was neglected,

$v_\varphi = 0$. The φ -momentum equation (A.6) was discarded, and the continuity (A.3), the z - (A.4) and r -momentum (A.5) equations read

$$\frac{\partial v_z}{\partial z} + \frac{1}{r}\frac{\partial (r v_r)}{\partial r} = 0, \tag{A.7}$$

$$\frac{\partial v_z}{\partial t} + v_z\frac{\partial v_z}{\partial z} + v_r\frac{\partial v_z}{\partial r} = -\frac{1}{\rho}\frac{\partial P}{\partial z} + \frac{\mu}{\rho}\left[\frac{\partial^2 v_z}{\partial z^2} + \frac{\partial^2 v_z}{\partial r^2} + \frac{1}{r}\frac{\partial v_z}{\partial r}\right], \tag{A.8}$$

$$\frac{\partial v_r}{\partial t} + v_z\frac{\partial v_r}{\partial z} + v_r\frac{\partial v_r}{\partial r} = -\frac{1}{\rho}\frac{\partial P}{\partial r} + \frac{\mu}{\rho}\left[\frac{\partial^2 v_r}{\partial z^2} + \frac{\partial^2 v_r}{\partial r^2} + \frac{1}{r}\frac{\partial v_r}{\partial r} - \frac{v_r}{r^2}\right], \tag{A.9}$$

respectively.

In order to simplify the mathematical procedure, it is convenient to express (A.7-A.9) in non-dimensional form (Barnard et al., 1966). Let us introduce the characteristic radial and axial velocities, the characteristic vessel length, and the characteristic lumen radius V_r, V_z, ℓ_0, and R_0, respectively. Non-dimensional quantities are defined as follows:

$$\tilde{r} = \frac{r}{R_0}, \quad \tilde{z} = \frac{z}{\ell_0}, \quad \tilde{t} = t\frac{V_z}{\ell_0}, \quad \tilde{v}_z = \frac{v_z}{V_z}, \quad \tilde{v}_r = \frac{v_r}{V_r}, \quad \tilde{P} = \frac{P}{\rho V_z^2}. \tag{A.10}$$

The non-dimensional term ε was defined as the ratio of the width and the length of the vessel,

$$\varepsilon = \frac{R_0}{\ell_0} = \frac{V_r}{V_z} \Rightarrow \frac{V_z R_0}{V_r \ell_0} = 1, \tag{A.11}$$

Take as reference the case of the abdominal aorta ($\ell_0 = 10$ cm, $R_0 = 8.2$ mm, $V = 0.1\ \mathrm{m\cdot s^{-1}}$, and $\mu/\rho 3.2 \times 10^{-6}\ \mathrm{m^2\cdot s^{-1}}$) for which $\varepsilon = 0.082$. Hence $\varepsilon \ll 1$ meaning that the radial velocity is small with respect to the axial velocity. Therefore, all the terms of order ε^2 and higher can be neglected.

The continuity equation (A.7) and the z -momentum equation (A.8) in non-dimensional variables read

$$\frac{\partial (\tilde{r}\tilde{v}_r)}{\partial \tilde{r}} + \frac{\partial (\tilde{r}\tilde{v}_z)}{\partial \tilde{z}} = 0, \tag{A.12}$$

$$\frac{V_z}{\ell_0}\frac{\partial(V_z\tilde{v}_z)}{\partial\tilde{t}} + \frac{V_z\tilde{v}_z}{\ell_0}\frac{\partial(V_z\tilde{v}_z)}{\partial\tilde{z}} + \frac{V_r\tilde{v}_r}{R_0}\frac{\partial(V_z\tilde{v}_z)}{\partial\tilde{r}} + \frac{V_z^2\rho}{\rho\ell_0}\frac{\partial\tilde{P}}{\partial\tilde{z}} = \frac{\mu}{\rho}\left[\frac{V_z}{\ell_0^2}\frac{\partial^2\tilde{v}_z}{\partial\tilde{z}^2} + \frac{V_z}{R_0^2}\frac{\partial^2\tilde{v}_z}{\partial\tilde{r}^2} + \frac{V_z}{\tilde{r}R_0^2}\frac{\partial\tilde{v}_z}{\partial\tilde{r}}\right], \quad \text{(A.13)}$$

respectively. By re-arranging the terms, dividing by V_z^2 and multiplying by $\ell_0\tilde{r}$ we obtain

$$\tilde{r}\frac{\partial\tilde{v}_z}{\partial\tilde{t}} + \tilde{r}\tilde{v}_z\frac{\partial\tilde{v}_z}{\partial\tilde{z}} + \tilde{r}\tilde{v}_r\frac{\partial\tilde{v}_z}{\partial\tilde{r}} + \tilde{r}\frac{\partial\tilde{P}}{\partial\tilde{z}} = \frac{\mu}{\rho}\frac{\ell_0}{V_zR_0^2}\frac{\partial}{\partial\tilde{r}}\left(\tilde{r}\frac{\partial\tilde{v}_z}{\partial\tilde{r}}\right). \quad \text{(A.14)}$$

Note that

$$\frac{\partial(\tilde{r}\tilde{v}_z^2)}{\partial\tilde{z}} = \tilde{v}_z\frac{\partial(\tilde{r}\tilde{v}_z)}{\partial\tilde{z}} + \tilde{r}\tilde{v}_z\frac{\partial\tilde{v}_z}{\partial\tilde{z}} \quad \text{(A.15)}$$

and

$$\frac{\partial}{\partial\tilde{r}}(\tilde{r}\tilde{v}_z\tilde{v}_r) = \tilde{v}_z\frac{\partial(\tilde{r}\tilde{v}_r)}{\partial\tilde{r}} + \tilde{r}\tilde{v}_r\frac{\partial\tilde{v}_z}{\partial\tilde{r}}. \quad \text{(A.16)}$$

Hence, by substituting in (A.14), we obtain

$$\tilde{r}\frac{\partial\tilde{v}_z}{\partial\tilde{t}} + \frac{\partial(\tilde{r}\tilde{v}_z^2)}{\partial\tilde{z}} + \frac{\partial}{\partial\tilde{r}}(\tilde{r}\tilde{v}_z\tilde{v}_r) + \tilde{r}\frac{\partial\tilde{P}}{\partial\tilde{z}} = \frac{\mu}{\rho}\frac{\ell_0}{V_zR_0^2}\frac{\partial}{\partial\tilde{r}}\left(\tilde{r}\frac{\partial\tilde{v}_z}{\partial\tilde{r}}\right), \quad \text{(A.17)}$$

The z -momentum equation reads

$$\tilde{r}\frac{\partial\tilde{v}_z}{\partial\tilde{t}} + \frac{\partial(\tilde{r}\tilde{v}_z^2)}{\partial\tilde{z}} + \frac{\partial}{\partial\tilde{r}}(\tilde{r}\tilde{v}_z\tilde{v}_r) + \tilde{r}\frac{\partial\tilde{P}}{\partial\tilde{z}} = \frac{\mu}{\rho}\frac{\ell_0}{V_zR_0^2}\frac{\partial}{\partial\tilde{r}}\left(\tilde{r}\frac{\partial\tilde{v}_z}{\partial\tilde{r}}\right). \quad \text{(A.18)}$$

The r -wise momentum equation (A.9) in non-dimensional variables reads

$$\frac{V_z}{\ell_0}\left[\frac{\partial(V_r\tilde{v}_r)}{\partial\tilde{t}} + \tilde{v}_z\frac{\partial(V_r\tilde{v}_r)}{\partial\tilde{z}}\right] + \frac{V_r\tilde{v}_r}{R_0}\frac{\partial(V_r\tilde{v}_r)}{\partial\tilde{r}} + \frac{1}{\rho R_0}\frac{\partial}{\partial\tilde{r}}\left(\rho V_r^2\tilde{P}\right) = \frac{\mu}{\rho}\left\{\frac{1}{\ell_0^2}\frac{\partial^2(V_r\tilde{v}_r)}{\partial\tilde{z}^2} + \frac{1}{R_0^2}\left[\frac{\partial^2(V_r\tilde{v}_r)}{\partial\tilde{r}^2} + \frac{1}{\tilde{r}}\frac{\partial(V_r\tilde{v}_r)}{\partial\tilde{r}} - \frac{V_r\tilde{v}_r}{\tilde{r}^2}\right]\right\}. \quad \text{(A.19)}$$

By multiplying (A.19) by R_0/V_z^2 and by neglecting the terms of order $\leq \varepsilon^2$, we obtain

$$\frac{\partial \tilde{P}}{\partial \tilde{r}} = 0, \tag{A.20}$$

hence the pressure is constant along the radial direction.

Introduce the average axial velocity

$$\tilde{U} = \frac{1}{\tilde{R}^2} \int_0^{\tilde{R}} 2\tilde{v}_z \tilde{r} d\tilde{r}, \tag{A.21}$$

and the Coriolis coefficient

$$\alpha = \frac{1}{\tilde{R}^2 \tilde{U}^2} \int_0^{\tilde{R}} 2\tilde{v}_z^2 \tilde{r} d\tilde{r}. \tag{A.22}$$

We then expressed equations (A.12) and (A.18) in terms of the averaged quantities across the cross-sectional area by integrating from $\tilde{r} = 0$ to $\tilde{r} = \tilde{R}$, with $\tilde{R}$ non-dimensional vessel inner radius. The continuity equation (A.12) reads

$$\int_0^{\tilde{R}} \frac{\partial \tilde{r}\tilde{v}_z}{\partial \tilde{z}} d\tilde{r} + \int_0^{\tilde{R}} \frac{\partial \tilde{r}\tilde{v}_r}{\partial \tilde{r}} d\tilde{r} = \frac{\partial}{\partial \tilde{z}} \underbrace{\int_0^{\tilde{R}} \tilde{r}\tilde{v}_z d\tilde{r}}_{\tilde{U}\frac{\tilde{R}_0^2}{2}} + \tilde{r}\tilde{v}_r\big|_{\tilde{R}}, \tag{A.23}$$

$$\frac{\partial}{\partial \tilde{z}} \left(\tilde{U} \frac{\tilde{R}_0^2}{2} \right) + \tilde{R}\tilde{v}_r\big|_{\tilde{R}} = 0, \tag{A.24}$$

The no-slip boundary condition was expressed by the streamline condition

$$\tilde{v}_r\big|_{\tilde{r}=\tilde{R}} = \frac{\partial \tilde{R}}{\partial \tilde{t}} + \tilde{v}_z\big|_{\tilde{r}=\tilde{R}} \frac{\partial \tilde{R}}{\partial \tilde{z}}, \tag{A.25}$$

which, by assuming negligible longitudinal displacement of the wall (i.e. $v_z\big|_{\tilde{r}=\tilde{R}} = 0$), reads

$$\tilde{v}_r\big|_{\tilde{r}=\tilde{R}} = \frac{\partial \tilde{R}}{\partial \tilde{t}}. \tag{A.26}$$

By substituting (A.26) in equation (A.24), the continuity equation results

$$\tilde{R} \frac{\partial \tilde{R}}{\partial \tilde{t}} + \frac{\partial}{\partial \tilde{z}} \left(\tilde{U} \frac{\tilde{R}_0^2}{2} \right) = 0. \tag{A.27}$$

The z -momentum equation (A.18) was integrated as

$$\frac{\partial}{\partial \tilde{t}} \int_0^{\tilde{R}} \tilde{r}\tilde{v}_z d\tilde{r} + \frac{\partial}{\partial \tilde{z}} \int_0^{\tilde{R}} \tilde{r}\tilde{v}_z^2 d\tilde{r} + \frac{\tilde{R}^2}{2}\frac{\partial \tilde{P}}{\partial \tilde{z}} = \frac{\mu}{\rho}\frac{\ell_0}{V_z R_0^2}\tilde{R}\frac{\partial \tilde{v}_z}{\partial \tilde{z}}\bigg|_{\tilde{R}}, \tag{A.28}$$

By using (A.21) and (A.22), equation (A.28) reads

$$\frac{\partial(\tilde{R}^2\tilde{U})}{\partial \tilde{t}} + \frac{\partial(\alpha\tilde{R}^2\tilde{U}^2)}{\partial \tilde{z}} + \tilde{R}^2\frac{\partial \tilde{P}}{\partial \tilde{z}} = \frac{\mu}{\rho}\frac{\ell_0}{V_z R_0^2} 2\tilde{R}\frac{\partial \tilde{v}_z}{\partial \tilde{z}}\bigg|_{\tilde{R}}. \tag{A.29}$$

The dimensional form of the reduced equations was obtained by applying the non-dimensional parameters definitions (A.10). The average axial velocity (A.21) reads

$$\tilde{U} = \frac{1}{\tilde{R}^2}\int_0^{\tilde{R}} 2\tilde{v}_z\tilde{r}d\tilde{r} = \frac{R_0^2}{R^2}\int_0^{R} 2\frac{v_z r}{V_z R_0^2}dr = \frac{2}{V_z R^2}\int_0^{R} r v_z dr, \tag{A.30}$$

where R is the inner vessel radius in dimensional variables. The dimensional average axial velocity was defined as

$$u = V_z\tilde{U} = \frac{1}{R^2}\int_0^{R} 2rv_z dr. \tag{A.31}$$

Similarly, for the Coriolis coefficient α (A.22) we obtain

$$\alpha = \frac{1}{\tilde{R}^2\tilde{U}^2}\int_0^{\tilde{R}} 2\tilde{v}_z^2\tilde{r}d\tilde{r} = \frac{1}{R^2u^2}\int_0^{R} 2rv_z^2 dr. \tag{A.32}$$

The continuity equation (A.27) became

$$\frac{\partial R^2}{\partial t} + \frac{\partial(R^2u)}{\partial z} = 0. \tag{A.33}$$

The z-wise momentum equation (A.29)

$$\frac{\partial(R^2u)}{\partial t} + \frac{\partial}{\partial z}(\alpha R^2u^2) + \frac{R^2}{\rho}\frac{\partial P}{\partial z} = 2\frac{\mu}{\rho}R\frac{\partial v_z}{\partial r}\bigg|_R. \tag{A.34}$$

In order to work out the viscous term on the right hand side of (A.34), the axial velocity profile v_z must be specified. By assuming that v_z is independent of the longitudinal coordinate z, a typical approximation is given by

$$v_z = \frac{\gamma_v + 2}{\gamma_v}u\left[1 - \left(\frac{r}{R}\right)^{\gamma_v}\right], \tag{A.35}$$

where γ_v is a non-dimensional parameter whose value defines the shape of the ve-

locity profile (Figure A.1.2). By substituting the velocity profile into the dimensional form of α (A.32), it leads to

$$\alpha = \frac{\gamma_v + 2}{\gamma_v + 1} \Rightarrow \gamma_v = \frac{\alpha - 2}{1 - \alpha}. \tag{A.36}$$

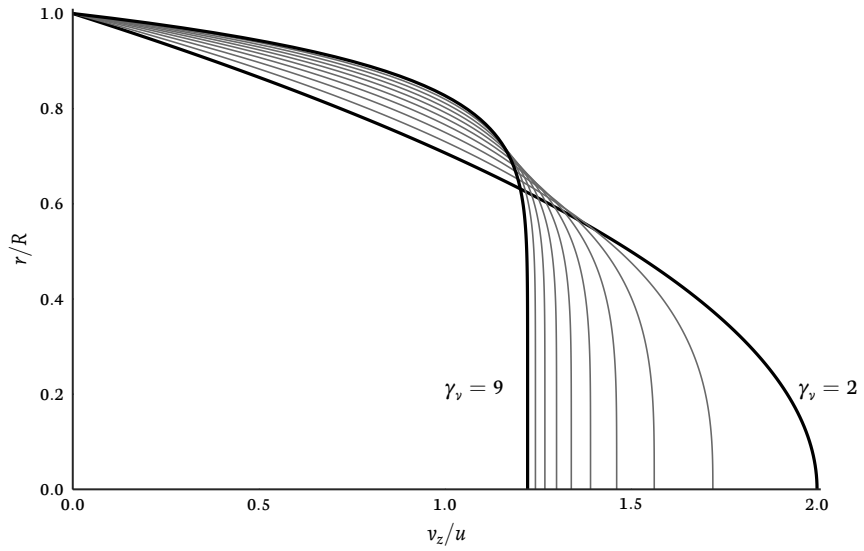

Figure A.1.2: Radial velocity profile for different values of γ_v. The parabolic profile is obtained for $\gamma_v = 2$, and the near plug-flow profile is obtained for $\gamma_v = 9$.

The viscous term in (A.34) reads

$$\left.\frac{2\mu R}{\rho}\frac{\partial v_z}{\partial r}\right|_R = -2\frac{\mu}{\rho}(\gamma_v + 2)u. \tag{A.37}$$

We can eventually express (A.33) and (A.34) in dimensional quantities as

$$\begin{cases} \dfrac{\partial A}{\partial t} + \dfrac{\partial Q}{\partial z} = 0, \\ \dfrac{\partial Q}{\partial t} + \dfrac{\partial}{\partial z}\left(\alpha\dfrac{Q^2}{A}\right) + \dfrac{A}{\rho}\dfrac{\partial P}{\partial z} = -2\dfrac{\mu}{\rho}(\gamma_v + 2)\dfrac{Q}{A}. \end{cases} \tag{A.38}$$

where $A = \pi R$ is the vessel cross-sectional area A and $Q = uA$ is the volumetric flow rate.

A.2 Constitutive equation for arterial wall mechanics

The system (A.38) consisted of two equations and three unknowns, i.e. (A, P, Q). To close the system of equations (A.38), a constitutive equation relating pressure and area needs to be specified (Formaggia et al., 2010). For this we used the independent ring model which is based on the assumption that the only force exerted by the fluid on the walls is in the radial direction, thus shear stress was ignored. The tube was treated as a series of thin rings and the circumferential stress was described by means of Laplace's law

$$\sigma_\varphi = P\frac{R}{h_0}, \tag{A.39}$$

where h_0 is the vessel walls thickness. The strain could be written as

$$\varepsilon_\varphi = \frac{2\pi R - 2\pi R_0}{2\pi R_0} = \frac{R}{R_0} - 1 = \sqrt{\frac{A}{A_0}} - 1. \tag{A.40}$$

By assuming that the longitudinal displacement of the tube is negligible, $v_z\big|_{r=R} = 0$, the wall is in a condition of plane strain, and by considering tube wall behaviour as linearly elastic, stress and strain were related as

$$\sigma_\varphi = \frac{E}{1-\nu^2}\varepsilon_\varphi, \tag{A.41}$$

where E is the Young's modulus and ν is the Poisson's ratio. Thus,

$$P\frac{R}{h_0} = P\frac{\sqrt{A}}{\sqrt{\pi}h_0} = \frac{E}{1-\nu^2}\left(\sqrt{\frac{A}{A_0}} - 1\right), \tag{A.42}$$

$$P = \sqrt{\pi}\frac{Eh_0}{1-\nu^2}\left(\frac{1}{\sqrt{A_0}} - \frac{1}{\sqrt{A}}\right). \tag{A.43}$$

The linear elastic theory employed works under the assumption of small displacements, and we can linearise (A.43) by applying the change of coordinates

$$\psi = \sqrt{A}, \qquad \psi_0 = \sqrt{A_0}, \tag{A.44}$$

$$P(\psi) = \sqrt{\pi}\frac{Eh_0}{1-\nu^2}\left(\frac{1}{\psi_0} - \frac{1}{\psi}\right). \tag{A.45}$$

The Taylor expansion of (A.45) read

$$P(\psi) = \xi_0 + \xi_1(\psi - \psi_0) + \dots, \tag{A.46}$$

where

$$\xi_0 = P(\psi_0) = 0, \tag{A.47}$$

and

$$\xi_1 = P'(\psi_0) = \sqrt{\pi}\frac{Eh_0}{1-\nu^2}\left.\frac{1}{\psi^2}\right|_{\psi_0} = \sqrt{\pi}\frac{Eh_0}{1-\nu^2}\frac{1}{\psi_0^2}. \tag{A.48}$$

Higher-orders terms were neglected and, by substituting back ψ and ψ_0, the pressure-area relation became

$$P(A) = \sqrt{\frac{\pi}{A_0}}\frac{Eh_0}{1-\nu^2}\left(\sqrt{\frac{A}{A_0}} - 1\right). \tag{A.49}$$

Eventually, the 1D reduced system read

$$\begin{cases} \dfrac{\partial A}{\partial t} + \dfrac{\partial Q}{\partial z} = 0, \\ \dfrac{\partial Q}{\partial t} + \dfrac{\partial}{\partial z}\left(\alpha\dfrac{Q^2}{A}\right) + \dfrac{A}{\rho}\dfrac{\partial P}{\partial z} = -2\dfrac{\mu}{\rho}(\gamma_\nu + 2)\dfrac{Q}{A}, \\ P(A) = P_{ext} + \beta\left(\sqrt{\dfrac{A}{A_0}} - 1\right), \quad \beta = \sqrt{\dfrac{\pi}{A_0}}\dfrac{Eh_0}{1-\nu^2}. \end{cases} \tag{A.50}$$

B Analytical solution

The 1D blood flow equations can be linearised around an equilibrium state and solved in the frequency domain. The wave equation in terms of P is

$$\frac{\partial^2 P}{\partial t^2} + \frac{8\mu}{\rho R^2}\frac{\partial P}{\partial t} - c^2\frac{\partial^2 P}{\partial z^2} = 0, \tag{B.1}$$

which has the general solution

$$\begin{aligned} P = e^{-Bz}\Big[P_1\cos(kz-\omega t) + P_2\sin(kz-\omega t)\Big] + \\ e^{Bz}\Big[P_3\cos(kz+\omega t) + P_4\sin(kz+\omega t)\Big], \end{aligned} \tag{B.2}$$

for a straight circular vessel.

Calculate derivatives

$$\begin{aligned} \frac{\partial P}{\partial t} = e^{-Bz}\Big[\omega P_1\sin(kz-\omega t) - \omega P_2\cos(kz-\omega t)\Big] + \\ e^{Bz}\Big[-\omega P_3\sin(kz+\omega t) + \omega P_4\cos(kz+\omega t)\Big], \end{aligned} \tag{B.3}$$

$$\begin{aligned} \frac{\partial^2 P}{\partial t^2} = e^{-Bz}\Big[-\omega^2 P_1\cos(kz-\omega t) - \omega^2 P_2\sin(kz-\omega t)\Big] + \\ e^{Bz}\Big[-\omega^2 P_3\cos(kz+\omega t) - \omega^2 P_4\sin(kz+\omega t)\Big], \end{aligned} \tag{B.4}$$

$$\begin{aligned}\frac{\partial P}{\partial z} = &-Be^{-Bz}\Big[P_1\cos(kz-\omega t)+P_2\sin(kz-\omega t)\Big]+\\ &e^{-Bz}\Big[-kP_1\sin(kz-\omega t)+kP_2\cos(kz-\omega t)\Big]+\\ &Be^{Bz}\Big[P_3\cos(kz+\omega t)+P_4\sin(kz+\omega t)\Big]+\\ &e^{Bz}\Big[-kP_3\sin(kz+\omega t)+kP_4\cos(kz+\omega t)\Big],\end{aligned} \tag{B.5}$$

$$\begin{aligned}\frac{\partial^2 P}{\partial z^2} = e^{-Bz}\Big\{&\left(B^2-k^2\right)\Big[P_1\cos(kz-\omega t)+P_2\sin(kz-\omega t)\Big]-\\ &2Bk\Big[-P_1\sin(kz-\omega t)+P_2\sin(kz-\omega t)\Big]\Big\}\\ e^{Bz}\Big\{&\left(B^2-k^2\right)\Big[P_3\cos(kz+\omega t)+P_4\sin(kz+\omega t)\Big]+\\ &2Bk\Big[-P_3\sin(kz+\omega t)+P_4\sin(kz+\omega t)\Big]\Big\}.\end{aligned} \tag{B.6}$$

Substitute in the general solution

$$\begin{aligned}e^{Bz}\Big\{&-\Big[\omega^2+c^2\left(B^2-k^2\right)\Big]\Big[P_3\cos(kz+\omega t)+P_4\sin(kz+\omega t)\Big]+\\ &\left(\frac{8\mu}{\rho R^2}\omega-2c^2Bk\right)\Big[-P_3\sin(kz+\omega t)+P_4\cos(kz+\omega t)\Big]\Big\}+\\ e^{-Bz}\Big\{&-\Big[\omega^2+c^2\left(B^2-k^2\right)\Big]\Big[P_1\cos(kz-\omega t)+P_2\sin(kz-\omega t)\Big]+\\ &\left(\frac{8\mu}{\rho R^2}\omega-2c^2Bk\right)\Big[P_1\sin(kz+\omega t)-P_2\cos(kz-\omega t)\Big]\Big\}=0,\end{aligned} \tag{B.7}$$

and solve as

$$\begin{cases}\omega^2+c^2\left(B^2-k^2\right)=0,\\ \dfrac{8\mu}{\rho R^2}\omega-2c^2Bk=0,\end{cases} \tag{B.8}$$

$$B = \omega \frac{4\mu}{c^2 k \rho R^2}, \qquad k = \frac{\sqrt{2}\omega}{2c} \left[1 \pm \sqrt{1 + \left(\frac{8\mu}{\omega \rho R^2} \right)^2} \right]^{1/2}. \tag{B.9}$$

Boundary conditions at the two vessel ends

$$P_0 = a_0 \cos(\omega t) + b_0 \sin(\omega t), \qquad P_\ell = a_\ell \cos(\omega t) + b_\ell \sin(\omega t), \tag{B.10}$$

$$P_0 = P(z = 0) = (P_1 + P_3) \cos(\omega t) + (P_4 - P_2) \sin(\omega t), \tag{B.11}$$

$$\begin{aligned} P_\ell = P(z = \ell) = & \Big\{ e^{-B\ell} \Big[P_1 \cos(k\ell) + P_2 \sin(k\ell) \Big] + \\ & e^{B\ell} \Big[P_3 \cos(k\ell) + P_4 \sin(k\ell) \Big] \Big\} \cos(\omega t) + \\ & \Big\{ e^{-B\ell} \Big[P_1 \sin(k\ell) - P_2 \cos(k\ell) \Big] + \\ & e^{B\ell} \Big[- P_3 \sin(k\ell) + P_4 \cos(k\ell) \Big] \Big\} \sin(\omega t), \end{aligned} \tag{B.12}$$

$$\begin{cases} P_1 + P_3 = a_0, \\ -P_2 + P_4 = b_0, \\ e^{-B\ell} P_1 \cos(k\ell) + e^{-B\ell} P_2 \sin(k\ell) + \\ \qquad e^{B\ell} P_3 \cos(k\ell) + e^{B\ell} P_4 \sin(k\ell) = a_\ell, \\ e^{-B\ell} P_1 \sin(k\ell) - e^{-B\ell} P_2 \cos(k\ell) - \\ \qquad e^{B\ell} P_3 \sin(k\ell) + e^{B\ell} P_4 \cos(k\ell) = b_\ell, \end{cases} \tag{B.13}$$

$$\mathbf{M}_P = \begin{bmatrix} 1 & 0 & 1 & 0 \\ 0 & -1 & 0 & 1 \\ e^{-B\ell} \cos(k\ell) & e^{-B\ell} \sin(k\ell) & e^{B\ell} \cos(k\ell) & e^{B\ell} \sin(k\ell) \\ e^{-B\ell} \sin(k\ell) & -e^{-B\ell} \cos(k\ell) & -e^{B\ell} \sin(k\ell) & e^{B\ell} \cos(k\ell) \end{bmatrix}, \tag{B.14}$$

$$\mathbf{P} = \left\{ \begin{array}{c} P_1 \\ P_2 \\ P_3 \\ P_4 \end{array} \right\}, \qquad \mathbf{A} = \left\{ \begin{array}{c} a_0 \\ b_0 \\ a_\ell \\ b_\ell \end{array} \right\}, \tag{B.15}$$

$$\mathbf{M}_P \mathbf{P}_z = \mathbf{A}, \tag{B.16}$$

for each harmonic n,

$$\mathbf{M}_P \mathbf{P}_z^{(n)} = \mathbf{A}^{(n)}. \tag{B.17}$$

The wave equation can be expressed also in terms of volumetric flow rate

$$\begin{aligned} Q = e^{-Bz}\Big[Q_1 \cos(kz - \omega t) + Q_2 \sin(kz - \omega t)\Big] + \\ e^{Bz}\Big[Q_3 \cos(kz + \omega t) + Q_4 \sin(kz + \omega t)\Big]. \end{aligned} \tag{B.18}$$

Eventually, one can couple a 0D model to the outlet. This is expressed by

$$\mathcal{C}\frac{\partial P}{\partial t} + \frac{\partial Q}{\partial z} = \mathbf{0}, \qquad \mathcal{C} = \frac{2(1-\sigma^2)A_0^{3/2}}{\sqrt{\pi}Eh_0}, \tag{B.19}$$

where

$$\begin{aligned} \frac{\partial Q}{\partial z} = -Be^{-Bz}\Big[Q_1 \cos(kz - \omega t) + Q_2 \sin(kz - \omega t)\Big] + \\ e^{-Bz}\Big[-kQ_1 \sin(kz - \omega t) + kQ_2 \cos(kz - \omega t)\Big] + \\ Be^{Bz}\Big[Q_3 \cos(kz + \omega t) + Q_4 \sin(kz + \omega t)\Big] + \\ e^{Bz}\Big[-kQ_3 \sin(kz + \omega t) + kQ_4 \cos(kz + \omega t)\Big]. \end{aligned} \tag{B.20}$$

Substitute derivatives into (B.19)

$$
\begin{aligned}
e^{-Bz}\Big\{ & \mathcal{C}\omega\Big[P_1\sin(kz-\omega t)-P_2\cos(kz-\omega t)\Big]- \\
& B\Big[Q_1\cos(kz-\omega t)+Q_2\sin(kz-\omega t)\Big]+ \\
& k\Big[-Q_1\sin(kz-\omega t)+Q_2\cos(kz-\omega t)\Big]\Big\}+ \\
e^{Bz}\Big\{ & \mathcal{C}\omega\Big[-P_3\sin(kz+\omega t)+P_4\cos(kz+\omega t)\Big]+ \\
& B\Big[Q_3\cos(kz+\omega t)+Q_4\sin(kz+\omega t)\Big]- \\
& k\Big[Q_3\sin(kz+\omega t)+Q_4\cos(kz+\omega t)\Big]\Big\}=\mathbf{0},
\end{aligned}
\tag{B.21}
$$

and solve as

$$
\begin{cases}
\mathcal{C}\omega P_1 - BQ_2 - kQ_1 = \mathbf{0}, \\
-\mathcal{C}\omega P_2 - BQ_1 + kQ_2 = \mathbf{0}, \\
-\mathcal{C}\omega P_3 + BQ_4 - kQ_3 = \mathbf{0}, \\
\mathcal{C}\omega P_4 + BQ_3 - kQ_4 = \mathbf{0},
\end{cases}
\tag{B.22}
$$

$$
\mathbf{M}_{\mathrm{Q}} = \begin{bmatrix} -k & -B & \mathbf{0} & \mathbf{0} \\ -B & k & \mathbf{0} & \mathbf{0} \\ \mathbf{0} & \mathbf{0} & -k & B \\ \mathbf{0} & \mathbf{0} & B & -k \end{bmatrix}, \tag{B.23}
$$

$$
\mathbf{Q} = \begin{Bmatrix} Q_1 \\ Q_2 \\ Q_3 \\ Q_4 \end{Bmatrix}, \qquad \mathbf{B} = \begin{Bmatrix} -P_1 \\ P_2 \\ P_3 \\ -P_4 \end{Bmatrix}, \tag{B.24}
$$

$$
\mathbf{M}_{\mathrm{Q}}\mathbf{Q}_{\ z} = \mathcal{C}\omega\mathbf{B}. \tag{B.25}
$$

C Continuity equation

C.1 Derivation in cylindrical coordinates

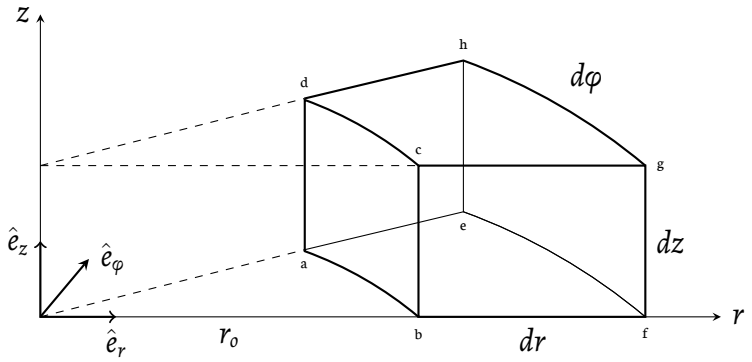

Figure C.1.1: Fluid control volume in cylindrical coordinates at distance r_o from the z axis.

The infinitesimal fluid element derivation method described in (Anderson Jr., 2001) and (Anderson Jr., 1995) has been used to obtain the continuity equation in cylindrical coordinates. In particular, the case of an infinitesimal fluid element fixed in space with the fluid moving through it is taken into account. The general geometric configuration is shown in Figure C.1.1. Let us introduce:

- the cylindrical coordinates (z, r, φ) and the unit vectors $(\hat{e}_z, \hat{e}_r, \hat{e}_\varphi)$;
- the infinitesimal volume $dV = dzdrd\varphi$;
- the velocity $\vec{V} = v_z\,\hat{e}_z + v_r\,\hat{e}_r + v_\varphi\,\hat{e}_\varphi$;
- the local fluid density $\rho = \rho(z, r, \varphi)$;

The principle of mass conservation may be expressed as: the *net* mass flow out of the element must equal the time rate of *decrease* of mass inside the element.

z direction faces

Let us assume that the flow comes in through face $abfe$ and exits via $dcgh$. The entering mass flow is

$$Q_{z,in} = \rho v_z A_{abfe}, \tag{C.1}$$

where $A_{abfe} = \frac{1}{2}\left[r_o d\varphi + (r_o + dr)d\varphi\right] dr$. The mass flow out is

$$Q_{z,out} = \left(\rho v_z + \frac{\partial(\rho v_z)}{\partial z} dz\right) A_{dcgh}, \tag{C.2}$$

where $A_{dcgh} = A_{abfe}$. Hence, the net mass flow in the z wise direction is given by

$$\begin{aligned} Q_z = Q_{z,out} - Q_{z,in} = \\ \left(\rho v_z + \frac{\partial(\rho v_z)}{\partial z} dz\right) A_{dcgh} - \rho v_z A_{abfe} = \\ \frac{1}{2}\frac{\partial(\rho v_z)}{\partial z}\Big[r_o d\varphi + (r_o + dr)d\varphi\Big] dr dz = \\ \left(\frac{1}{2} r dz dr d\varphi + \frac{1}{2} r dz dr d\varphi + \frac{1}{2} dz dr^2 d\varphi\right) \frac{\partial(\rho v_z)}{\partial z} = \\ \frac{\partial(\rho v_z)}{\partial z} dV + o(dr^2). \end{aligned} \tag{C.3}$$

r-direction faces

The mass flow entering through face $abcd$ is expressed by

$$Q_{r,in} = \rho v_r r_o d\varphi dz, \tag{C.4}$$

while for the outflow through $cghd$, the change of the area has to be taken into account as

$$Q_{r,out} = \left(\rho v_r + \frac{\partial(\rho v_r)}{\partial r} dr\right) (r_o + dr) d\varphi dz, \tag{C.5}$$

thus the net mass flow in the radial direction reads

$$Q_r = \left(\rho v_r + \frac{\partial(\rho v_r)}{\partial r} dr\right)(r_o + dr)d\varphi dz - \rho v_r r_o d\varphi dz = \rho v_r dz dr d\varphi + \frac{\partial(\rho v_r)}{\partial r} r_o dz dr d\varphi + o(dr^2) = \frac{1}{r_o}\rho v_z dV + \frac{\partial(\rho v_r)}{\partial r} dV + o(dr^2). \tag{C.6}$$

φ direction faces

In this case the inflow and outflow areas are the same, $bfgh = cghd$, hence the net mass flow is given by

$$Q_\varphi = \frac{\partial(\rho v_\varphi)}{\partial \varphi} dz dr d\varphi = \frac{1}{r_o}\frac{\partial(\rho v_\varphi)}{\partial \varphi} dV. \tag{C.7}$$

We now apply the mass conservation principle and re-write all the terms as

$$\begin{array}{l}\text{time rate of} \\ \textit{decrease} \\ \text{of mass inside} \\ \text{the element}\end{array} = \frac{\partial(\rho v_z)}{\partial z} dV + \frac{1}{r_o}\rho v_z dV + \frac{\partial(\rho v_r)}{\partial r} dV + \frac{1}{r_o}\frac{\partial(\rho v_\varphi)}{\partial \varphi} dV, \tag{C.8}$$

where the terms of order dr^2 have been neglected. Since rate of decrease of mass in the control volume is given by $-\frac{\partial \rho}{\partial t} dV$, the continuity equation reads

$$-\frac{\partial \rho}{\partial t} dV = \frac{\partial(\rho v_z)}{\partial z} dV + \frac{1}{r_o}\rho v_z dV + \frac{\partial(\rho v_r)}{\partial r} dV + \frac{1}{r_o}\frac{\partial(\rho v_\varphi)}{\partial \varphi} dV, \tag{C.9}$$

where the infinitesimal volume term dV can be simplified and the radial coordinate generalised in order to obtain

$$\frac{\partial \rho}{\partial t} + \frac{\partial(\rho v_z)}{\partial z} + \frac{\partial(\rho r v_r)}{\partial r} + \frac{1}{r}\frac{\partial(\rho v_\varphi)}{\partial \varphi} = 0. \tag{C.10}$$

Permissions

SPRINGER NATURE LICENSE TERMS AND CONDITIONS

Jan 11, 2018

This Agreement between The University of Sheffield -- Alessandro Melis ("You") and Springer Nature ("Springer Nature") consists of your license details and the terms and conditions provided by Springer Nature and Copyright Clearance Center.

License Number	4265990390110
License date	Jan 11, 2018
Licensed Content Publisher	Springer Nature
Licensed Content Publication	Medical & Biological Engineering & Computing
Licensed Content Title	Multi-branched model of the human arterial system
Licensed Content Author	A. P. Avolio
Licensed Content Date	Jan 1, 1980
Licensed Content Volume	18
Licensed Content Issue	6
Type of Use	Thesis/Dissertation
Requestor type	academic/university or research institute
Format	electronic
Portion	figures/tables/illustrations
Number of figures/tables/illustrations	1
Will you be translating?	no
Circulation/distribution	>50,000
Author of this Springer Nature content	no
Title	Gaussian process emulators for 1D vascular models
Instructor name	A. Marzo
Institution name	The University of Sheffield
Expected presentation date	Jan 2018
Portions	Figure 5
Requestor Location	The University of Sheffield Pam Liversidge Building Mappin Street Room E09 Sheffield, S13JD United Kingdom Attn: The University of Sheffield
Billing Type	Invoice
Billing Address	The University of Sheffield Pam Liversidge Building Mappin Street Room E09 Sheffield, United Kingdom S13JD Attn: The University of Sheffield
Total	**0.00 USD**
Terms and Conditions	

Springer Nature Terms and Conditions for RightsLink Permissions

Springer Customer Service Centre GmbH (the Licensor) hereby grants you a non-exclusive, world-wide licence to reproduce the material and for the purpose and requirements specified in the attached copy of your order form, and for no other use, subject to the conditions below:

1. The Licensor warrants that it has, to the best of its knowledge, the rights to license reuse of this material. However, you should ensure that the material you are requesting is original to the Licensor and does not carry the copyright of another entity (as credited in the published version).

If the credit line on any part of the material you have requested indicates that it was reprinted or adapted with permission from another source, then you should also seek permission from that source to reuse the material.

2. Where **print only** permission has been granted for a fee, separate permission must be obtained for any additional electronic re-use.

3. Permission granted **free of charge** for material in print is also usually granted for any electronic version of that work, provided that the material is incidental to your work as a whole and that the electronic version is essentially equivalent to, or substitutes for, the print version.

4. A licence for 'post on a website' is valid for 12 months from the licence date. This licence does not cover use of full text articles on websites.

5. Where **'reuse in a dissertation/thesis'** has been selected the following terms apply: Print rights for up to 100 copies, electronic rights for use only on a personal website or institutional repository as defined by the Sherpa guideline (www.sherpa.ac.uk/romeo/).

6. Permission granted for books and journals is granted for the lifetime of the first edition and does not apply to second and subsequent editions (except where the first edition permission was granted free of charge or for signatories to the STM Permissions Guidelines http://www.stm-assoc.org/copyright-legal-affairs/permissions/permissions-guidelines/), and does not apply for editions in other languages unless additional translation rights have been granted separately in the licence.

7. Rights for additional components such as custom editions and derivatives require additional permission and may be subject to an additional fee. Please apply to Journalpermissions@springernature.com/bookpermissions@springernature.com for these rights.

8. The Licensor's permission must be acknowledged next to the licensed material in print. In electronic form, this acknowledgement must be visible at the same time as the figures/tables/illustrations or abstract, and must be hyperlinked to the journal/book's homepage. Our required acknowledgement format is in the Appendix below.

9. Use of the material for incidental promotional use, minor editing privileges (this does not include cropping, adapting, omitting material or any other changes that affect the meaning, intention or moral rights of the author) and copies for the disabled are permitted under this licence.

10. Minor adaptations of single figures (changes of format, colour and style) do not require the Licensor's approval. However, the adaptation should be credited as shown in Appendix below.

Appendix — Acknowledgements:

For Journal Content:
Reprinted by permission from [**the Licensor**]: [**Journal Publisher** (e.g. Nature/Springer/Palgrave)] [**JOURNAL NAME**] [**REFERENCE CITATION** (Article name, Author(s) Name), [**COPYRIGHT**] (year of publication)

For **Advance Online Publication papers:**
Reprinted by permission from [**the Licensor**]: [**Journal Publisher** (e.g. Nature/Springer/Palgrave)] [**JOURNAL NAME**] [**REFERENCE CITATION** (Article name, Author(s) Name), [**COPYRIGHT**] (year of publication), advance online publication, day month year (doi: 10.1038/sj.[JOURNAL ACRONYM].)

For Adaptations/Translations:
Adapted/Translated by permission from [**the Licensor**]: [**Journal Publisher** (e.g. Nature/Springer/Palgrave)] [**JOURNAL NAME**] [**REFERENCE CITATION** (Article name, Author(s) Name), [**COPYRIGHT**] (year of publication)

Note: For any republication from the British Journal of Cancer, the following credit line style applies:

Reprinted/adapted/translated by permission from [**the Licensor**]: on behalf of Cancer Research UK: : [**Journal Publisher** (e.g. Nature/Springer/Palgrave)] [**JOURNAL NAME**] [**REFERENCE CITATION** (Article name, Author(s) Name), [**COPYRIGHT]** (year of publication)

For **Advance Online Publication** papers:
Reprinted by permission from The [**the Licensor**]: on behalf of Cancer Research UK: [**Journal Publisher** (e.g. Nature/Springer/Palgrave)] [**JOURNAL NAME**] [**REFERENCE CITATION** (Article name, Author(s) Name), [**COPYRIGHT**] (year of publication), advance online publication, day month year (doi: 10.1038/sj.[JOURNAL ACRONYM])

For Book content:
Reprinted/adapted by permission from [**the Licensor**]: [**Book Publisher** (e.g. Palgrave Macmillan, Springer etc) [**Book Title**] by [**Book author**(s)] [**COPYRIGHT**] (year of publication)

Other Conditions:

Version 1.0

Questions? customercare@copyright.com or +1-855-239-3415 (toll free in the US) or +1-978-646-2777.

ELSEVIER LICENSE
TERMS AND CONDITIONS

Jan 11, 2018

This Agreement between The University of Sheffield -- Alessandro Melis ("You") and Elsevier ("Elsevier") consists of your license details and the terms and conditions provided by Elsevier and Copyright Clearance Center.

License Number	4266000693588
License date	Jan 11, 2018
Licensed Content Publisher	Elsevier
Licensed Content Publication	Journal of Biomechanics
Licensed Content Title	Modelling the circle of Willis to assess the effects of anatomical variations and occlusions on cerebral flows
Licensed Content Author	J. Alastruey,K.H. Parker,J. Peiró,S.M. Byrd,S.J. Sherwin
Licensed Content Date	Jan 1, 2007
Licensed Content Volume	40
Licensed Content Issue	8
Licensed Content Pages	12
Start Page	1794
End Page	1805
Type of Use	reuse in a thesis/dissertation
Portion	figures/tables/illustrations
Number of figures/tables/illustrations	1
Format	electronic
Are you the author of this Elsevier article?	No
Will you be translating?	No
Original figure numbers	Figure 5
Title of your thesis/dissertation	Gaussian process emulators for 1D vascular models
Expected completion date	Jan 2018
Estimated size (number of pages)	190
Requestor Location	The University of Sheffield Pam Liversidge Building Mappin Street Room E09 Sheffield, Please choose a State S13JD United Kingdom Attn: The University of Sheffield
Publisher Tax ID	GB 494 6272 12
Total	0.00 GBP
Terms and Conditions	

INTRODUCTION

1. The publisher for this copyrighted material is Elsevier. By clicking "accept" in connection with completing this licensing transaction, you agree that the following terms and conditions apply to this transaction (along with the Billing and Payment terms and conditions

established by Copyright Clearance Center, Inc. ("CCC"), at the time that you opened your Rightslink account and that are available at any time at http://myaccount.copyright.com).

GENERAL TERMS

2. Elsevier hereby grants you permission to reproduce the aforementioned material subject to the terms and conditions indicated.

3. Acknowledgement: If any part of the material to be used (for example, figures) has appeared in our publication with credit or acknowledgement to another source, permission must also be sought from that source. If such permission is not obtained then that material may not be included in your publication/copies. Suitable acknowledgement to the source must be made, either as a footnote or in a reference list at the end of your publication, as follows:

"Reprinted from Publication title, Vol /edition number, Author(s), Title of article / title of chapter, Pages No., Copyright (Year), with permission from Elsevier [OR APPLICABLE SOCIETY COPYRIGHT OWNER]." Also Lancet special credit - "Reprinted from The Lancet, Vol. number, Author(s), Title of article, Pages No., Copyright (Year), with permission from Elsevier."

4. Reproduction of this material is confined to the purpose and/or media for which permission is hereby given.

5. Altering/Modifying Material: Not Permitted. However figures and illustrations may be altered/adapted minimally to serve your work. Any other abbreviations, additions, deletions and/or any other alterations shall be made only with prior written authorization of Elsevier Ltd. (Please contact Elsevier at permissions@elsevier.com). No modifications can be made to any Lancet figures/tables and they must be reproduced in full.

6. If the permission fee for the requested use of our material is waived in this instance, please be advised that your future requests for Elsevier materials may attract a fee.

7. Reservation of Rights: Publisher reserves all rights not specifically granted in the combination of (i) the license details provided by you and accepted in the course of this licensing transaction, (ii) these terms and conditions and (iii) CCC's Billing and Payment terms and conditions.

8. License Contingent Upon Payment: While you may exercise the rights licensed immediately upon issuance of the license at the end of the licensing process for the transaction, provided that you have disclosed complete and accurate details of your proposed use, no license is finally effective unless and until full payment is received from you (either by publisher or by CCC) as provided in CCC's Billing and Payment terms and conditions. If full payment is not received on a timely basis, then any license preliminarily granted shall be deemed automatically revoked and shall be void as if never granted. Further, in the event that you breach any of these terms and conditions or any of CCC's Billing and Payment terms and conditions, the license is automatically revoked and shall be void as if never granted. Use of materials as described in a revoked license, as well as any use of the materials beyond the scope of an unrevoked license, may constitute copyright infringement and publisher reserves the right to take any and all action to protect its copyright in the materials.

9. Warranties: Publisher makes no representations or warranties with respect to the licensed material.

10. Indemnity: You hereby indemnify and agree to hold harmless publisher and CCC, and their respective officers, directors, employees and agents, from and against any and all claims arising out of your use of the licensed material other than as specifically authorized pursuant to this license.

11. No Transfer of License: This license is personal to you and may not be sublicensed, assigned, or transferred by you to any other person without publisher's written permission.

12. No Amendment Except in Writing: This license may not be amended except in a writing signed by both parties (or, in the case of publisher, by CCC on publisher's behalf).

13. Objection to Contrary Terms: Publisher hereby objects to any terms contained in any purchase order, acknowledgment, check endorsement or other writing prepared by you, which terms are inconsistent with these terms and conditions or CCC's Billing and Payment terms and conditions. These terms and conditions, together with CCC's Billing and Payment terms and conditions (which are incorporated herein), comprise the entire agreement between you and publisher (and CCC) concerning this licensing transaction. In the event of

any conflict between your obligations established by these terms and conditions and those established by CCC's Billing and Payment terms and conditions, these terms and conditions shall control.

14. Revocation: Elsevier or Copyright Clearance Center may deny the permissions described in this License at their sole discretion, for any reason or no reason, with a full refund payable to you. Notice of such denial will be made using the contact information provided by you. Failure to receive such notice will not alter or invalidate the denial. In no event will Elsevier or Copyright Clearance Center be responsible or liable for any costs, expenses or damage incurred by you as a result of a denial of your permission request, other than a refund of the amount(s) paid by you to Elsevier and/or Copyright Clearance Center for denied permissions.

LIMITED LICENSE

The following terms and conditions apply only to specific license types:

15. **Translation**: This permission is granted for non-exclusive world **English** rights only unless your license was granted for translation rights. If you licensed translation rights you may only translate this content into the languages you requested. A professional translator must perform all translations and reproduce the content word for word preserving the integrity of the article.

16. **Posting licensed content on any Website**: The following terms and conditions apply as follows: Licensing material from an Elsevier journal: All content posted to the web site must maintain the copyright information line on the bottom of each image; A hyper-text must be included to the Homepage of the journal from which you are licensing at http://www.sciencedirect.com/science/journal/xxxxx or the Elsevier homepage for books at http://www.elsevier.com; Central Storage: This license does not include permission for a scanned version of the material to be stored in a central repository such as that provided by Heron/XanEdu.

Licensing material from an Elsevier book: A hyper-text link must be included to the Elsevier homepage at http://www.elsevier.com . All content posted to the web site must maintain the copyright information line on the bottom of each image.

Posting licensed content on Electronic reserve: In addition to the above the following clauses are applicable: The web site must be password-protected and made available only to bona fide students registered on a relevant course. This permission is granted for 1 year only. You may obtain a new license for future website posting.

17. **For journal authors:** the following clauses are applicable in addition to the above:

Preprints:

A preprint is an author's own write-up of research results and analysis, it has not been peer-reviewed, nor has it had any other value added to it by a publisher (such as formatting, copyright, technical enhancement etc.).

Authors can share their preprints anywhere at any time. Preprints should not be added to or enhanced in any way in order to appear more like, or to substitute for, the final versions of articles however authors can update their preprints on arXiv or RePEc with their Accepted Author Manuscript (see below).

If accepted for publication, we encourage authors to link from the preprint to their formal publication via its DOI. Millions of researchers have access to the formal publications on ScienceDirect, and so links will help users to find, access, cite and use the best available version. Please note that Cell Press, The Lancet and some society-owned have different preprint policies. Information on these policies is available on the journal homepage.

Accepted Author Manuscripts: An accepted author manuscript is the manuscript of an article that has been accepted for publication and which typically includes author-incorporated changes suggested during submission, peer review and editor-author communications.

Authors can share their accepted author manuscript:

- immediately
    - via their non-commercial person homepage or blog
    - by updating a preprint in arXiv or RePEc with the accepted manuscript

- via their research institute or institutional repository for internal institutional uses or as part of an invitation-only research collaboration work-group
- directly by providing copies to their students or to research collaborators for their personal use
- for private scholarly sharing as part of an invitation-only work group on commercial sites with which Elsevier has an agreement

- After the embargo period
  - via non-commercial hosting platforms such as their institutional repository
  - via commercial sites with which Elsevier has an agreement

In all cases accepted manuscripts should:

- link to the formal publication via its DOI
- bear a CC-BY-NC-ND license - this is easy to do
- if aggregated with other manuscripts, for example in a repository or other site, be shared in alignment with our hosting policy not be added to or enhanced in any way to appear more like, or to substitute for, the published journal article.

Published journal article (JPA): A published journal article (PJA) is the definitive final record of published research that appears or will appear in the journal and embodies all value-adding publishing activities including peer review co-ordination, copy-editing, formatting, (if relevant) pagination and online enrichment.
Policies for sharing publishing journal articles differ for subscription and gold open access articles:
Subscription Articles: If you are an author, please share a link to your article rather than the full-text. Millions of researchers have access to the formal publications on ScienceDirect, and so links will help your users to find, access, cite, and use the best available version.
Theses and dissertations which contain embedded PJAs as part of the formal submission can be posted publicly by the awarding institution with DOI links back to the formal publications on ScienceDirect.
If you are affiliated with a library that subscribes to ScienceDirect you have additional private sharing rights for others' research accessed under that agreement. This includes use for classroom teaching and internal training at the institution (including use in course packs and courseware programs), and inclusion of the article for grant funding purposes.
Gold Open Access Articles: May be shared according to the author-selected end-user license and should contain a CrossMark logo, the end user license, and a DOI link to the formal publication on ScienceDirect.
Please refer to Elsevier's posting policy for further information.
18. **For book authors** the following clauses are applicable in addition to the above:
Authors are permitted to place a brief summary of their work online only. You are not allowed to download and post the published electronic version of your chapter, nor may you scan the printed edition to create an electronic version. **Posting to a repository:** Authors are permitted to post a summary of their chapter only in their institution's repository.
19. **Thesis/Dissertation**: If your license is for use in a thesis/dissertation your thesis may be submitted to your institution in either print or electronic form. Should your thesis be published commercially, please reapply for permission. These requirements include permission for the Library and Archives of Canada to supply single copies, on demand, of the complete thesis and include permission for Proquest/UMI to supply single copies, on demand, of the complete thesis. Should your thesis be published commercially, please reapply for permission. Theses and dissertations which contain embedded PJAs as part of the formal submission can be posted publicly by the awarding institution with DOI links back to the formal publications on ScienceDirect.

Elsevier Open Access Terms and Conditions
You can publish open access with Elsevier in hundreds of open access journals or in nearly 2000 established subscription journals that support open access publishing. Permitted third party re-use of these open access articles is defined by the author's choice of Creative Commons user license. See our open access license policy for more information.

JOHN WILEY AND SONS LICENSE TERMS AND CONDITIONS

Jan 11, 2018

This Agreement between The University of Sheffield -- Alessandro Melis ("You") and John Wiley and Sons ("John Wiley and Sons") consists of your license details and the terms and conditions provided by John Wiley and Sons and Copyright Clearance Center.

License Number	4265990092795
License date	Jan 11, 2018
Licensed Content Publisher	John Wiley and Sons
Licensed Content Publication	International Journal of Numerical Methods in Biomedical Engineering
Licensed Content Title	A global multiscale mathematical model for the human circulation with emphasis on the venous system
Licensed Content Author	Lucas O. Müller,Eleuterio F. Toro
Licensed Content Date	Jan 15, 2014
Licensed Content Pages	45
Type of use	Dissertation/Thesis
Requestor type	University/Academic
Format	Electronic
Portion	Figure/table
Number of figures/tables	1
Original Wiley figure/table number(s)	Figure 5
Will you be translating?	No
Title of your thesis / dissertation	Gaussian process emulators for 1D vascular models
Expected completion date	Jan 2018
Expected size (number of pages)	1
Requestor Location	The University of Sheffield Pam Liversidge Building Mappin Street Room E09 Sheffield, S13JD United Kingdom Attn: The University of Sheffield
Publisher Tax ID	EU826007151
Total	0.00 GBP
Terms and Conditions	

TERMS AND CONDITIONS

This copyrighted material is owned by or exclusively licensed to John Wiley & Sons, Inc. or one of its group companies (each a"Wiley Company") or handled on behalf of a society with which a Wiley Company has exclusive publishing rights in relation to a particular work (collectively "WILEY"). By clicking "accept" in connection with completing this licensing transaction, you agree that the following terms and conditions apply to this transaction (along with the billing and payment terms and conditions established by the Copyright Clearance Center Inc., ("CCC's Billing and Payment terms and conditions"), at the time that

you opened your RightsLink account (these are available at any time at http://myaccount.copyright.com).

Terms and Conditions

- The materials you have requested permission to reproduce or reuse (the "Wiley Materials") are protected by copyright.

- You are hereby granted a personal, non-exclusive, non-sub licensable (on a stand-alone basis), non-transferable, worldwide, limited license to reproduce the Wiley Materials for the purpose specified in the licensing process. This license, **and any CONTENT (PDF or image file) purchased as part of your order,** is for a one-time use only and limited to any maximum distribution number specified in the license. The first instance of republication or reuse granted by this license must be completed within two years of the date of the grant of this license (although copies prepared before the end date may be distributed thereafter). The Wiley Materials shall not be used in any other manner or for any other purpose, beyond what is granted in the license. Permission is granted subject to an appropriate acknowledgement given to the author, title of the material/book/journal and the publisher. You shall also duplicate the copyright notice that appears in the Wiley publication in your use of the Wiley Material. Permission is also granted on the understanding that nowhere in the text is a previously published source acknowledged for all or part of this Wiley Material. Any third party content is expressly excluded from this permission.

- With respect to the Wiley Materials, all rights are reserved. Except as expressly granted by the terms of the license, no part of the Wiley Materials may be copied, modified, adapted (except for minor reformatting required by the new Publication), translated, reproduced, transferred or distributed, in any form or by any means, and no derivative works may be made based on the Wiley Materials without the prior permission of the respective copyright owner.**For STM Signatory Publishers clearing permission under the terms of the STM Permissions Guidelines only, the terms of the license are extended to include subsequent editions and for editions in other languages, provided such editions are for the work as a whole in situ and does not involve the separate exploitation of the permitted figures or extracts,** You may not alter, remove or suppress in any manner any copyright, trademark or other notices displayed by the Wiley Materials. You may not license, rent, sell, loan, lease, pledge, offer as security, transfer or assign the Wiley Materials on a stand-alone basis, or any of the rights granted to you hereunder to any other person.

- The Wiley Materials and all of the intellectual property rights therein shall at all times remain the exclusive property of John Wiley & Sons Inc, the Wiley Companies, or their respective licensors, and your interest therein is only that of having possession of and the right to reproduce the Wiley Materials pursuant to Section 2 herein during the continuance of this Agreement. You agree that you own no right, title or interest in or to the Wiley Materials or any of the intellectual property rights therein. You shall have no rights hereunder other than the license as provided for above in Section 2. No right, license or interest to any trademark, trade name, service mark or other branding ("Marks") of WILEY or its licensors is granted hereunder, and you agree that you shall not assert any such right, license or interest with respect thereto

- NEITHER WILEY NOR ITS LICENSORS MAKES ANY WARRANTY OR REPRESENTATION OF ANY KIND TO YOU OR ANY THIRD PARTY, EXPRESS, IMPLIED OR STATUTORY, WITH RESPECT TO THE MATERIALS OR THE ACCURACY OF ANY INFORMATION CONTAINED IN THE MATERIALS, INCLUDING, WITHOUT LIMITATION, ANY IMPLIED WARRANTY OF MERCHANTABILITY, ACCURACY, SATISFACTORY QUALITY, FITNESS FOR A PARTICULAR PURPOSE, USABILITY, INTEGRATION OR NON-INFRINGEMENT AND ALL SUCH WARRANTIES

ARE HEREBY EXCLUDED BY WILEY AND ITS LICENSORS AND WAIVED BY YOU.

- WILEY shall have the right to terminate this Agreement immediately upon breach of this Agreement by you.
- You shall indemnify, defend and hold harmless WILEY, its Licensors and their respective directors, officers, agents and employees, from and against any actual or threatened claims, demands, causes of action or proceedings arising from any breach of this Agreement by you.
- IN NO EVENT SHALL WILEY OR ITS LICENSORS BE LIABLE TO YOU OR ANY OTHER PARTY OR ANY OTHER PERSON OR ENTITY FOR ANY SPECIAL, CONSEQUENTIAL, INCIDENTAL, INDIRECT, EXEMPLARY OR PUNITIVE DAMAGES, HOWEVER CAUSED, ARISING OUT OF OR IN CONNECTION WITH THE DOWNLOADING, PROVISIONING, VIEWING OR USE OF THE MATERIALS REGARDLESS OF THE FORM OF ACTION, WHETHER FOR BREACH OF CONTRACT, BREACH OF WARRANTY, TORT, NEGLIGENCE, INFRINGEMENT OR OTHERWISE (INCLUDING, WITHOUT LIMITATION, DAMAGES BASED ON LOSS OF PROFITS, DATA, FILES, USE, BUSINESS OPPORTUNITY OR CLAIMS OF THIRD PARTIES), AND WHETHER OR NOT THE PARTY HAS BEEN ADVISED OF THE POSSIBILITY OF SUCH DAMAGES. THIS LIMITATION SHALL APPLY NOTWITHSTANDING ANY FAILURE OF ESSENTIAL PURPOSE OF ANY LIMITED REMEDY PROVIDED HEREIN.
- Should any provision of this Agreement be held by a court of competent jurisdiction to be illegal, invalid, or unenforceable, that provision shall be deemed amended to achieve as nearly as possible the same economic effect as the original provision, and the legality, validity and enforceability of the remaining provisions of this Agreement shall not be affected or impaired thereby.
- The failure of either party to enforce any term or condition of this Agreement shall not constitute a waiver of either party's right to enforce each and every term and condition of this Agreement. No breach under this agreement shall be deemed waived or excused by either party unless such waiver or consent is in writing signed by the party granting such waiver or consent. The waiver by or consent of a party to a breach of any provision of this Agreement shall not operate or be construed as a waiver of or consent to any other or subsequent breach by such other party.
- This Agreement may not be assigned (including by operation of law or otherwise) by you without WILEY's prior written consent.
- Any fee required for this permission shall be non-refundable after thirty (30) days from receipt by the CCC.
- These terms and conditions together with CCC's Billing and Payment terms and conditions (which are incorporated herein) form the entire agreement between you and WILEY concerning this licensing transaction and (in the absence of fraud) supersedes all prior agreements and representations of the parties, oral or written. This Agreement may not be amended except in writing signed by both parties. This Agreement shall be binding upon and inure to the benefit of the parties' successors, legal representatives, and authorized assigns.
- In the event of any conflict between your obligations established by these terms and conditions and those established by CCC's Billing and Payment terms and conditions, these terms and conditions shall prevail.

- WILEY expressly reserves all rights not specifically granted in the combination of (i) the license details provided by you and accepted in the course of this licensing transaction, (ii) these terms and conditions and (iii) CCC's Billing and Payment terms and conditions.

- This Agreement will be void if the Type of Use, Format, Circulation, or Requestor Type was misrepresented during the licensing process.

- This Agreement shall be governed by and construed in accordance with the laws of the State of New York, USA, without regards to such state's conflict of law rules. Any legal action, suit or proceeding arising out of or relating to these Terms and Conditions or the breach thereof shall be instituted in a court of competent jurisdiction in New York County in the State of New York in the United States of America and each party hereby consents and submits to the personal jurisdiction of such court, waives any objection to venue in such court and consents to service of process by registered or certified mail, return receipt requested, at the last known address of such party.

WILEY OPEN ACCESS TERMS AND CONDITIONS

Wiley Publishes Open Access Articles in fully Open Access Journals and in Subscription journals offering Online Open. Although most of the fully Open Access journals publish open access articles under the terms of the Creative Commons Attribution (CC BY) License only, the subscription journals and a few of the Open Access Journals offer a choice of Creative Commons Licenses. The license type is clearly identified on the article.

The Creative Commons Attribution License

The Creative Commons Attribution License (CC-BY) allows users to copy, distribute and transmit an article, adapt the article and make commercial use of the article. The CC-BY license permits commercial and non-

Creative Commons Attribution Non-Commercial License

The Creative Commons Attribution Non-Commercial (CC-BY-NC)License permits use, distribution and reproduction in any medium, provided the original work is properly cited and is not used for commercial purposes.(see below)

Creative Commons Attribution-Non-Commercial-NoDerivs License

The Creative Commons Attribution Non-Commercial-NoDerivs License (CC-BY-NC-ND) permits use, distribution and reproduction in any medium, provided the original work is properly cited, is not used for commercial purposes and no modifications or adaptations are made. (see below)

Use by commercial "for-profit" organizations

Use of Wiley Open Access articles for commercial, promotional, or marketing purposes requires further explicit permission from Wiley and will be subject to a fee.

Further details can be found on Wiley Online Library

http://olabout.wiley.com/WileyCDA/Section/id-410895.html

Other Terms and Conditions:

v1.10 Last updated September 2015

Questions? customercare@copyright.com or +1-855-239-3415 (toll free in the US) or +1-978-646-2777.

JOHN WILEY AND SONS LICENSE TERMS AND CONDITIONS

Jan 11, 2018

This Agreement between The University of Sheffield -- Alessandro Melis ("You") and John Wiley and Sons ("John Wiley and Sons") consists of your license details and the terms and conditions provided by John Wiley and Sons and Copyright Clearance Center.

License Number	4265981415212
License date	Jan 11, 2018
Licensed Content Publisher	John Wiley and Sons
Licensed Content Publication	International Journal of Numerical Methods in Biomedical Engineering
Licensed Content Title	Issue Information
Licensed Content Author	
Licensed Content Date	Dec 4, 2017
Licensed Content Pages	2
Type of use	Dissertation/Thesis
Requestor type	Author of this Wiley article
Format	Electronic
Portion	Full article
Will you be translating?	No
Title of your thesis / dissertation	Gaussian process emulators for 1D vascular models
Expected completion date	Jan 2018
Expected size (number of pages)	1
Requestor Location	The University of Sheffield Pam Liversidge Building Mappin Street Room E09 Sheffield, S13JD United Kingdom Attn: The University of Sheffield
Publisher Tax ID	EU826007151
Total	0.00 GBP
Terms and Conditions	

TERMS AND CONDITIONS

This copyrighted material is owned by or exclusively licensed to John Wiley & Sons, Inc. or one of its group companies (each a"Wiley Company") or handled on behalf of a society with which a Wiley Company has exclusive publishing rights in relation to a particular work (collectively "WILEY"). By clicking "accept" in connection with completing this licensing transaction, you agree that the following terms and conditions apply to this transaction (along with the billing and payment terms and conditions established by the Copyright Clearance Center Inc., ("CCC's Billing and Payment terms and conditions"), at the time that you opened your RightsLink account (these are available at any time at http://myaccount.copyright.com).

Terms and Conditions

- The materials you have requested permission to reproduce or reuse (the "Wiley Materials") are protected by copyright.

- You are hereby granted a personal, non-exclusive, non-sub licensable (on a stand-alone basis), non-transferable, worldwide, limited license to reproduce the Wiley Materials for the purpose specified in the licensing process. This license, **and any CONTENT (PDF or image file) purchased as part of your order,** is for a one-time use only and limited to any maximum distribution number specified in the license. The first instance of republication or reuse granted by this license must be completed within two years of the date of the grant of this license (although copies prepared before the end date may be distributed thereafter). The Wiley Materials shall not be used in any other manner or for any other purpose, beyond what is granted in the license. Permission is granted subject to an appropriate acknowledgement given to the author, title of the material/book/journal and the publisher. You shall also duplicate the copyright notice that appears in the Wiley publication in your use of the Wiley Material. Permission is also granted on the understanding that nowhere in the text is a previously published source acknowledged for all or part of this Wiley Material. Any third party content is expressly excluded from this permission.

- With respect to the Wiley Materials, all rights are reserved. Except as expressly granted by the terms of the license, no part of the Wiley Materials may be copied, modified, adapted (except for minor reformatting required by the new Publication), translated, reproduced, transferred or distributed, in any form or by any means, and no derivative works may be made based on the Wiley Materials without the prior permission of the respective copyright owner.**For STM Signatory Publishers clearing permission under the terms of the STM Permissions Guidelines only, the terms of the license are extended to include subsequent editions and for editions in other languages, provided such editions are for the work as a whole in situ and does not involve the separate exploitation of the permitted figures or extracts,** You may not alter, remove or suppress in any manner any copyright, trademark or other notices displayed by the Wiley Materials. You may not license, rent, sell, loan, lease, pledge, offer as security, transfer or assign the Wiley Materials on a stand-alone basis, or any of the rights granted to you hereunder to any other person.

- The Wiley Materials and all of the intellectual property rights therein shall at all times remain the exclusive property of John Wiley & Sons Inc, the Wiley Companies, or their respective licensors, and your interest therein is only that of having possession of and the right to reproduce the Wiley Materials pursuant to Section 2 herein during the continuance of this Agreement. You agree that you own no right, title or interest in or to the Wiley Materials or any of the intellectual property rights therein. You shall have no rights hereunder other than the license as provided for above in Section 2. No right, license or interest to any trademark, trade name, service mark or other branding ("Marks") of WILEY or its licensors is granted hereunder, and you agree that you shall not assert any such right, license or interest with respect thereto

- NEITHER WILEY NOR ITS LICENSORS MAKES ANY WARRANTY OR REPRESENTATION OF ANY KIND TO YOU OR ANY THIRD PARTY, EXPRESS, IMPLIED OR STATUTORY, WITH RESPECT TO THE MATERIALS OR THE ACCURACY OF ANY INFORMATION CONTAINED IN THE MATERIALS, INCLUDING, WITHOUT LIMITATION, ANY IMPLIED WARRANTY OF MERCHANTABILITY, ACCURACY, SATISFACTORY QUALITY, FITNESS FOR A PARTICULAR PURPOSE, USABILITY, INTEGRATION OR NON-INFRINGEMENT AND ALL SUCH WARRANTIES ARE HEREBY EXCLUDED BY WILEY AND ITS LICENSORS AND WAIVED BY YOU.

- WILEY shall have the right to terminate this Agreement immediately upon breach of this Agreement by you.

- You shall indemnify, defend and hold harmless WILEY, its Licensors and their respective directors, officers, agents and employees, from and against any actual or threatened claims, demands, causes of action or proceedings arising from any breach of this Agreement by you.

- IN NO EVENT SHALL WILEY OR ITS LICENSORS BE LIABLE TO YOU OR ANY OTHER PARTY OR ANY OTHER PERSON OR ENTITY FOR ANY SPECIAL, CONSEQUENTIAL, INCIDENTAL, INDIRECT, EXEMPLARY OR PUNITIVE DAMAGES, HOWEVER CAUSED, ARISING OUT OF OR IN CONNECTION WITH THE DOWNLOADING, PROVISIONING, VIEWING OR USE OF THE MATERIALS REGARDLESS OF THE FORM OF ACTION, WHETHER FOR BREACH OF CONTRACT, BREACH OF WARRANTY, TORT, NEGLIGENCE, INFRINGEMENT OR OTHERWISE (INCLUDING, WITHOUT LIMITATION, DAMAGES BASED ON LOSS OF PROFITS, DATA, FILES, USE, BUSINESS OPPORTUNITY OR CLAIMS OF THIRD PARTIES), AND WHETHER OR NOT THE PARTY HAS BEEN ADVISED OF THE POSSIBILITY OF SUCH DAMAGES. THIS LIMITATION SHALL APPLY NOTWITHSTANDING ANY FAILURE OF ESSENTIAL PURPOSE OF ANY LIMITED REMEDY PROVIDED HEREIN.

- Should any provision of this Agreement be held by a court of competent jurisdiction to be illegal, invalid, or unenforceable, that provision shall be deemed amended to achieve as nearly as possible the same economic effect as the original provision, and the legality, validity and enforceability of the remaining provisions of this Agreement shall not be affected or impaired thereby.

- The failure of either party to enforce any term or condition of this Agreement shall not constitute a waiver of either party's right to enforce each and every term and condition of this Agreement. No breach under this agreement shall be deemed waived or excused by either party unless such waiver or consent is in writing signed by the party granting such waiver or consent. The waiver by or consent of a party to a breach of any provision of this Agreement shall not operate or be construed as a waiver of or consent to any other or subsequent breach by such other party.

- This Agreement may not be assigned (including by operation of law or otherwise) by you without WILEY's prior written consent.

- Any fee required for this permission shall be non-refundable after thirty (30) days from receipt by the CCC.

- These terms and conditions together with CCC's Billing and Payment terms and conditions (which are incorporated herein) form the entire agreement between you and WILEY concerning this licensing transaction and (in the absence of fraud) supersedes all prior agreements and representations of the parties, oral or written. This Agreement may not be amended except in writing signed by both parties. This Agreement shall be binding upon and inure to the benefit of the parties' successors, legal representatives, and authorized assigns.

- In the event of any conflict between your obligations established by these terms and conditions and those established by CCC's Billing and Payment terms and conditions, these terms and conditions shall prevail.

- WILEY expressly reserves all rights not specifically granted in the combination of (i) the license details provided by you and accepted in the course of this licensing transaction, (ii) these terms and conditions and (iii) CCC's Billing and Payment terms and conditions.

- This Agreement will be void if the Type of Use, Format, Circulation, or Requestor Type was misrepresented during the licensing process.

- This Agreement shall be governed by and construed in accordance with the laws of the State of New York, USA, without regards to such state's conflict of law rules. Any legal action, suit or proceeding arising out of or relating to these Terms and Conditions or the breach thereof shall be instituted in a court of competent jurisdiction in New York County in the State of New York in the United States of America and each party hereby consents and submits to the personal jurisdiction of such court, waives any objection to venue in such court and consents to service of process by registered or certified mail, return receipt requested, at the last known address of such party.

WILEY OPEN ACCESS TERMS AND CONDITIONS

Wiley Publishes Open Access Articles in fully Open Access Journals and in Subscription journals offering Online Open. Although most of the fully Open Access journals publish open access articles under the terms of the Creative Commons Attribution (CC BY) License only, the subscription journals and a few of the Open Access Journals offer a choice of Creative Commons Licenses. The license type is clearly identified on the article.

The Creative Commons Attribution License

The Creative Commons Attribution License (CC-BY) allows users to copy, distribute and transmit an article, adapt the article and make commercial use of the article. The CC-BY license permits commercial and non-

Creative Commons Attribution Non-Commercial License

The Creative Commons Attribution Non-Commercial (CC-BY-NC)License permits use, distribution and reproduction in any medium, provided the original work is properly cited and is not used for commercial purposes.(see below)

Creative Commons Attribution-Non-Commercial-NoDerivs License

The Creative Commons Attribution Non-Commercial-NoDerivs License (CC-BY-NC-ND) permits use, distribution and reproduction in any medium, provided the original work is properly cited, is not used for commercial purposes and no modifications or adaptations are made. (see below)

Use by commercial "for-profit" organizations

Use of Wiley Open Access articles for commercial, promotional, or marketing purposes requires further explicit permission from Wiley and will be subject to a fee.

Further details can be found on Wiley Online Library

http://olabout.wiley.com/WileyCDA/Section/id-410895.html

Other Terms and Conditions:

v1.10 Last updated September 2015

Questions? customercare@copyright.com or +1-855-239-3415 (toll free in the US) or +1-978-646-2777.